

Crosslinked Polyimide Hollow Fiber Membranes for Aggressive Natural Gas Feed Streams

A Dissertation
Presented to
The Academic Faculty

By

Imona C. Omole

In Partial Fulfillment
Of the Requirements for the Degree
Doctor of Philosophy in
Chemical & Biomolecular Engineering

Georgia Institute of Technology
December 2008

Copyright 2008 by Imona C. Omole

Crosslinked Polyimide Hollow Fiber Membranes for Aggressive Natural Gas Feed Streams

Approved by:

Dr. William J. Koros, Advisor
School of Chemical & Biomolecular Engineering
Georgia Institute of Technology

Dr. Haskell W. Beckham
School of Polymer, Textile, & Fiber Engineering
Georgia Institute of Technology

Dr. Christopher W. Jones
School of Chemical & Biomolecular Engineering
Georgia Institute of Technology

Dr. Stephen J. Miller
Chevron Fellow
Chevron Energy Technology Company

Dr. Aryn Teja
School of Chemical & Biomolecular Engineering
Georgia Institute of Technology

Date Approved: September 30, 2008

ACKNOWLEDGEMENTS

First and foremost, I would like to express my sincerest gratitude to my advisor Prof. Bill Koros for his unwavering support and guidance through the years, despite his very busy schedule. He has been the best mentor and teacher I've had.

My committee members deserve much appreciation as well. Dr. Steve Miller's guidance has been exceptionally helpful especially when it comes to looking at things from an industrial perspective. His constructive feedback on results was very useful and encouraging. Dr. Haskell Beckham, Dr. Chris Jones, and Dr. Aryn Teja were also very supportive and earn much appreciation.

The members of the Koros group, past and present, have been great and exciting to work with. The technical contributions from Dr. John Wind, Dr. David Wallace, and Dr. Alexis (Hillock) McKittrick were very beneficial. I thank Dr. Bill Madden and Dr. Fangbin Zhou for teaching me to spin hollow fibers and also Dr. Shabbir Husain for the technical discussions and critique especially concerning spinning. Dr. Adam Kratochvil's help during my first synthesis experiments were invaluable. The comradeship of the group has also kept me sane through the years and I really thank God for these wonderful people.

TABLE OF CONTENTS

ACKNOWLEDGEMENTS.....	iii
LIST OF TABLES.....	xi
LIST OF FIGURES.....	xiii
SUMMARY.....	xxiii
CHAPTER 1: INTRODUCTION.....	1
1.1 Natural gas processing.....	1
1.2 Membranes for natural gas separations.....	3
1.3 Membrane technology overview.....	5
1.4 Research objectives.....	8
1.5 Dissertation overview.....	9
1.6 References.....	10
CHAPTER 2: BACKGROUND AND THEORY.....	11
2.1 Small molecule transport in membranes.....	11
2.1.1 Solution diffusion.....	15
2.1.2 Characterizing solution diffusion membranes.....	18
2.2 Glassy polymers.....	25
2.2.1 Physical ageing in glassy polymers.....	26
2.2.2 Sorption in glassy polymers.....	28
2.3 Permeation modeling in glassy polymers.....	31
2.3.1 Partial immobilization model (dual mode extension).....	31

2.3.2	Frame of reference model/Bulk flow model.....	33
2.4	Penetrant-polymer interaction effects on transport.....	36
2.4.1	Plasticization.....	36
2.4.1.1	Overview of plasticization.....	36
2.4.1.2	Strategy for stabilization against plasticization.....	42
2.4.2	Antiplasticization.....	44
2.4.3	Conditioning.....	47
2.5	References.....	49
 CHAPTER 3: EXPERIMENTAL PROCEDURES AND		
MATERIALS.....		
3.1	Introduction.....	58
3.2	Experimental methods.....	58
3.2.1	Dense film permeation.....	58
3.2.1.1	Dense film preparation.....	58
3.2.1.2	Dense film permeation.....	59
3.2.2	Asymmetric hollow fiber permeation.....	62
3.2.2.1	Asymmetric hollow fiber membrane preparation: spinning.....	62
3.2.2.2	Hollow fiber permeation.....	65
3.2.2.2.1	Hollow fiber pure gas permeation.....	66

3.2.2.2.2	Hollow fiber mixed gas permeation.....	69
3.2.3	Sorption.....	71
3.2.3.1	Pressure decay sorption.....	71
3.2.3.2	Quartz-spring sorption.....	73
3.2.4	Scanning electron microscopy (SEM).....	74
3.2.5	Gel permeation chromatography (GPC).....	74
3.2.6	Fourier transform infra-red spectroscopy (FTIR).....	75
3.2.7	Nuclear magnetic resonance imaging (NMR).....	75
3.3	Materials.....	75
3.3.1	Polymer synthesis.....	78
3.3.2	Imidization.....	80
3.3.3	Crosslinking.....	84
3.3.3.1	Monoesterification.....	85
3.3.3.2	Transesterification.....	87
3.3.4	Monoesterification effects on polymer.....	88
3.3.5	Reaction scale-up.....	100
3.4	Summary.....	103
3.5	References.....	104
CHAPTER 4: SPINNING A DEFECT-FREE CROSSLINKABLE POLYIMIDE: A STUDY ON PDMC (3:2).....		
4.1	Review.....	108

4.1.1	Defect-free asymmetric hollow fiber membranes.....	108
4.1.2	Other non-ideal morphologies.....	114
4.1.2.1	External mass transfer resistance.....	114
4.1.2.2	Substructure resistance.....	120
4.2	Hollow fiber spinning.....	124
4.2.1	Dope development.....	127
4.2.2	Spinning parameters.....	130
4.2.2.1	Spin dope.....	130
4.2.2.2	Bore fluid.....	131
4.2.2.3	Quench medium.....	132
4.2.2.4	Air gap.....	133
4.2.2.5	Spinneret temperature.....	134
4.2.2.6	Extrusion rate and draw ratio.....	134
4.2.2.7	Drying.....	135
4.2.3	Skin layer formation.....	136
4.2.3.1	Overview.....	136
4.2.3.2	Current understanding.....	141
4.3	Case studies on PDMC material.....	143
4.3.1	PDMC spinning – spinnability and macroscopic properties.....	143
4.3.2	PDMC spinning – skin integrity.....	148
4.3.2.1	First iteration spinning.....	148

4.3.2.2	High pressure defect-free fibers.....	151
4.3.3	Preliminary characterization of defect-free fibers with a model natural gas feed and summary of Chapter 4.....	157
4.4	References.....	159
CHAPTER 5: CROSSLINKABLE ASYMMETRIC HOLLOW FIBER MEMBRANES FOR NATURAL GAS (CO ₂ /CH ₄) SEPARATION AND PLASTICIATION RESISTANCE.....		
5.1	Introduction.....	164
5.2	Natural gas permeation and stability for high CO ₂ content feeds.....	165
5.2.1	Effect of crosslinking temperature on separation performance of defect-free membranes.....	165
5.2.2	Effect of CO ₂ concentration in feed.....	173
5.2.2.1	Permeation experiments on defect-free crosslinked PDMC.....	173
5.2.2.2	Sorption analysis on crosslinked PDMC.....	176
5.2.2.3	Practical considerations in separation.....	187
5.2.3	Hollow fiber performance stability over time.....	192
5.2.4	Effect of gas phase non-idealities (fugacity).....	195
5.2.5	Effect of ageing on separation performance.....	197

5.2.5.1	Effect of ageing on absolute separation performance values.....	197
5.2.5.2	Effect of ageing on pressure dependence of separation performance.....	203
5.2.6	Effect of temperature on separation performance.....	207
5.2.7	Permeation characterization of non-defect-free PDMC fibers.....	211
5.3	Summary.....	216
5.4	References.....	218

CHAPTER 6: PERFORMANCE OF CROSSLINKABLE HOLLOW FIBER

MEMBRANES IN THE PRESENCE OF TOLUENE

CONTAMINANTS.....	221	
6.1	Introduction.....	221
6.2	Sorption with toluene vapors.....	222
6.3	Stability against natural gas feed with toluene impurity.....	225
6.3.1	Preliminary studies.....	225
6.3.1.1	First exposure.....	226
6.3.1.2	Second exposure.....	230
6.3.2	More aggressive feeds.....	231
6.3.2.1	Effect of increasing concentration of toluene on crosslinked PDMC fibers.....	232

6.3.2.2	Effect of toluene contamination on uncrosslinked PDMC hollow fibers.....	248
6.4	Summary.....	255
6.5	References.....	256
CHAPTER 7: SUMMARY AND RECOMMENDATIONS.....		257
APPENDIX A: MANUFACTURE OF LAB SCALE HOLLOW FIBER MODULES.....		
		267
APPENDIX B: PERMEATION TESTING OF HOLLOW FIBER MODULES.....		
		273
APPENDIX C: HOLLOW FIBER POST-TREATMENT.....		
		280

LIST OF TABLES

Table 1.1: Natural gas composition specifications for delivery to the U.S. national pipeline grid [1, 2].....	2
Table 2.1 Kinetic diameters [22] and critical temperatures of gases used in this work...16	
Table 2.2: Permeabilities and selectivities for poly(phelylene oxide) containing different amounts of various diluents. Measurements made at 35 °C and 10 atm except where noted [72].....	45
Table 4.1 Potential non-solvents for fluid exchanging before drying asymmetric hollow fibers [23, 40].....	136
Table 4.2 Hollow fiber spinning dope compositions.....	145
Table 4.3 Hollow fiber spinning conditions.....	145
Table 4.4 Hollow fiber permeation properties.....	147
Table 4.5 Hollow fiber spinning dope compositions.....	149
Table 4.6 Hollow fiber spinning conditions.....	149
Table 4.7 Hollow fiber permeation properties.....	151
Table 4.8 Hollow fiber spinning dope compositions.....	153
Table 4.9 Hollow fiber spinning conditions.....	153
Table 4.10 Hollow fiber permeation properties.....	154
Table 5.1: <u>Pure gas</u> permeation properties due to crosslinking the PDMC films from Hillock’s work [1]. Test temperature 35 °C, pressure 65 psia.....	165
Table 5.2: <u>Mixed gas permeation</u> properties due to crosslinking the PDMC fibers used in this work. Feed: 20/80 CO ₂ /CH ₄ gas at 200 psia, 35 °C.....	167
Table 5.3 Dual mode sorption parameters for CO ₂ and CH ₄ at 35 °C.....	179
Table 5.4: Transport model parameters for crosslinked PDMC.....	183
Table 5.5: Linear correlation coefficients for permselectivity data from Figure 5.9.....	189

Table 5.6 Fugacity effects on performance.....	196
Table 5.7 Ageing effects on performance.....	199
Table 6.1 Dual mode sorption parameters for CO ₂ , CH ₄ , and toluene at 35 °C in PDMC hollow fibers crosslinked at 200 °C.....	225
Table 6.2: Description of numbered points in Figure 6.4.....	227
Table 6.3: Description of numbered points in Figure 6.5.....	231

LIST OF FIGURES

Figure 1.1: Schematic showing a two stage membrane process to purify a natural gas stream using a cellulose acetate membrane (left) and a yet to be developed high performance membrane (right) [6].....4

Figure 1.2: A schematic showing a hollow fiber membrane module (top) and a bar graph illustration of the surface are/volume achievable in various module types.....6

Figure 2.1: Schematic showing the various transport mechanisms for small molecules through membranes [2].....11

Figure 2.2: Transient gap formation for molecular diffusion in dense polymer membranes.....14

Figure 2.3: Depiction illustrating the relative sizes (kinetic diameters) and condensability (boiling points) of a few natural gas components [21].....16

Figure 2.4: Schematic illustrating the separation process of CO₂ and CH₄ through a dense polymer membrane.....18

Figure 2.5: Schematic showing excess free volume or “unrelaxed volume ($V_g - V_l$) in glassy polymers as a function of temperature [26].....25

Figure 2.6: Ageing polyimide films in separating He/N₂, showing decreases in permeance (top) and increases in selectivity (bottom) using various film thicknesses: (●) thick, 28.45 μm; (○) intermediate, 2.54 μm; (Δ) thin, 0.5 μm–5000 Å; (▲) thin, air dried at room temperature only. Arrows: storage at 35 °C, 1 atm, dry air [36].....27

Figure 2.7: Schematic illustrating dual mode sorption in glassy polymers.....29

Figure 2.8: Pure and mixed gas (50/50 CO₂/CH₄) sorption isotherms [42, 43].....30

Figure 2.9: Schematic showing plasticization effects on membrane separation performance. Plasticization causes an increase in permeability and decrease in selectivity as pressure of sorbed penetrant increases.....38

Figure 2.10: Schematic illustrating dual mode and plasticization effects on sorption and diffusion coefficients as pressure of plasticizer is increased.....39

Figure 2.11: Graph illustrating the difference between pure gas and mixed gas determined selectivities using cellulose acetate, with different CO₂ content in the feed. The separation

performance using the pure gas feeds is overestimated since the permeability of CO ₂ is increased by plasticization [21, 62].....	41
Figure 2.12: Permeation isotherms for crosslinked polyimide and uncrosslinked polyimide, illustrating the efficacy of the crosslinking approach in stabilizing the membrane against CO ₂ induced plasticization [67].....	43
Figure 2.13: Selectivity for CO ₂ /CH ₄ (top) and He/N ₂ (bottom) using different diluent types and amounts in poly(phenylene oxide).....	46
Figure 2.14: Conditioning loop (pressurization/depressurization with CO ₂) showing hysteresis in 6FDA-6FmDA solubility coefficient (top) and 6FDA-6FpDA permeability (bottom) [83].....	48
Figure 3.1: A schematic showing a dense film cast on a Teflon casting plate.....	59
Figure 3.2: Schematic of a permeation cell. A cross section through the cell is shown with a “sandwich” type masked membrane. The membrane assembly is composed of: membrane, yellow; filter paper, light gray; epoxy, brown; adhesive backed aluminum, checkered. Bolts, shown at left and right, and o-rings, solid black circles, assure a leak tight seal [1].....	60
Figure 3.3: Isochoric (constant volume), variable pressure permeation system with dual upstream and downstream volumes. (1) Large (1000 cc) upstream reservoir; (2) Downstream pressure transducer; (3) Large (500 cc) downstream reservoir; (4) Upstream pressure gauge; (5) Permeation cell; (6) Small (10 cc) downstream reservoir; (7) Small (150 cc) upstream reservoir; (8) Fan; (9) Heat source (heat tape) with temperature control. Adapted from reference [4].....	61
Figure 3.4: An asymmetric hollow fiber membrane with an outer selective skin layer on a porous support substructure.....	63
Figure 3.5: Spinning process for producing asymmetric hollow fiber membranes.....	64
Figure 3.6: Schematic showing a hollow fiber membrane in a module housing, which interfaces the membrane with the permeation system.....	66
Figure 3.7: Schematic showing a variable volume system with the permeate stream at atmospheric pressure, set up for pure gas permeation experiments.....	68
Figure 3.8: Schematic showing a variable volume system with the permeate stream at atmospheric pressure, set up for mixed gas permeation experiments. The syringe pump was used when the pressure in the feed gas cylinder was below the desired membrane feed pressure.....	70
Figure 3.9: Pressure decay sorption apparatus used for gas sorption experiments.....	72

Figure 3.10: Quartz spring sorption apparatus used for vapor sorption experiments.....	73
Figure 3.11: A schematic showing two PDMC (3:2) variants with two different backbone structures: 6FDA-DAM:DABA (3:2) (top) and 6FDA-mPDA:DABA (3:2).....	76
Figure 3.12: Robeson’s 1991 upper bound showing the tradeoff between permeability and selectivity using different polymers (black dots) [15], along with the permeability and selectivity values for the two PDMC (3:2) variants: using “DAM” prepared and measured by Hillock using a 10/90 CO ₂ /CH ₄ feed at 65 psia, 35 °C [14], and using “mPDA” made and measured in this work and tested under the same conditions.....	77
Figure 3.13: Pictures of the sublimation set-up and sublimed monomers used in this work.....	79
Figure 3.14: Effect of imidization temperature and time on intrinsic viscosity and residual % amic acid. Adapted from reference [19].....	82
Figure 3.15: Synthesis steps for 6FDA-DAM:DABA (3:2) polyimide.....	84
Figure 3.16: Monoesterification reaction for synthesizing 1,3-propanediol <u>mono</u> esterified <u>crosslinkable</u> (PDMC) polyimide (3:2).....	86
Figure 3.17: Crosslinking/transesterification reaction between two PDMC (3:2) polyimide chain segments.....	88
Figure 3.18: Schematic showing an irregular crosslinked network from a lower molecular weight backbone (left) and an improved network from a higher molecular weight backbone (right).....	89
Figure 3.19: Solution ¹ H NMR spectra of a PDMC (3:2) polyimide that experienced molecular weight loss.....	90
Figure 3.20: Reaction steps of a PDMC (3:2) chain segment undergoing chain scissioning on the imide ring.....	91
Figure 3.21: ATR-IR spectrum of a PDMC (3:2) polyimide that experienced molecular weight loss (red) and the precursor untreated/unesterified polyimide (blue).....	93
Figure 3.22: Monoesterification yield and weight average molecular weight trends of a PDMC (3:2) polyimide, showing no molecular weight loss and high ester yields. Increased molecular weights indicate the addition of the esters on the polymer chain from the diol crosslinking agent.....	95

Figure 3.23: ATR-IR spectra of PDMC (3:2) polyimide samples that experienced no molecular weight loss, but show the resurgence of amide peaks (top) and the precursor untreated/unesterified polyimide (bottom/blue).....	96
Figure 3.24: ATR-IR spectra of the precursor untreated/unesterified polyimide; a PDMC (3:2) polyimide (monoesterified) sample made from it that experienced no molecular weight loss, but shows the resurgence of amide peaks; and an annealed/crosslinked polyimide showing recyclization of the imide ring.....	98
Figure 3.25: ATR-IR spectra of the precursor untreated/unesterified polyimide; a PDMC (3:2) polyimide (monoesterified) sample made from it that experienced no molecular weight loss, but shows the appearance of alcohols from propane-diol; and an annealed/crosslinked polyimide showing disappearance of the alcohol.....	99
Figure 3.26: Schematic showing the set-up for polymer synthesis used in this work....	101
Figure 3.27: Picture showing precipitated PDMC polymer after large scale synthesis.....	102
Figure 4.1: A membrane with pin-hole defects (top) and a composite membrane showing a post-treatment (PT) layer used to “heal” defects (bottom).....	111
Figure 4.2: A post-treated PDMC hollow fiber membrane tested against high pressure feed containing 20% CO ₂ in CH ₄ , showing the short-comings of the post-treatment process [22].....	113
Figure 4.3: A membrane showing the boundary layer (BL) region during mixed gas permeation of CO ₂ and CH ₄	115
Figure 4.4: Effects of external mass transfer resistances on PDMC membrane performance. Parameters: 200 μm fiber OD, viscosity (μ) and density (ρ) at 1000 psi, 35 °C, diffusion coefficient (D) using Fuller equation [29].....	119
Figure 4.5: Schematic showing resistances from boundary layer, membrane, and substructure.....	120
Figure 4.6: Analysis showing the effect of substructure resistance on permselectivity.....	122
Figure 4.7: Schematic showing the steps involved in the development of a hollow fiber membrane, starting with spinnability: the ability to spin the fibers under realistic conditions; followed by macroscopic properties: including fiber size (>300 μm), concentricity, and openness of substructure; and final skin integrity [30].....	125
Figure 4.8: Ternary phase diagram showing the binodal (thick curve) that can be obtained from a Gibbs free energy of mixing equation [36].....	128

Figure 4.9: Ternary phase diagrams of polymer, solvent, and non-solvent for spinning hollow fibers demonstrating how to obtain the binodal. Filled (red) and unfilled (partially red) circles represent 1 and 2 phase compositions achieved at constant polymer concentration with increasing non-solvent addition.....	129
Figure 4.10: Determination of bore fluid composition by extrapolation of binodal towards solvent/non-solvent axis on ternary phase diagram. The bore fluid composition is indicated by the blue star.....	132
Figure 4.11: Schematic showing the spinning apparatus, with an air-gap and the critical quench bath height for phase separation.....	134
Figure 4.12: Ternary phase diagram showing the trajectory of the spinning dope as it undergoes phase separation to form polymer rich and poor phases.....	140
Figure 4.13: Ternary phase diagram showing the trajectory of the outer layer of a spinning dope as it undergoes vitrification to form a skin layer prior to quenching.....	142
Figure 4.14: Scanning Electron Micrographs (SEM) of hollow fibers from states 2 (top) and 4 (bottom) of the PDMC (3:2) polyimide.....	146
Figure 4.15: Schematic showing the differences in fiber sizes from using higher draw ratios (left) and lower draw ratios (right) as obtained from a spinneret with relatively large annulus (~1270 μm).....	150
Figure 4.16: Schematic illustrating the sizes of the annulus and bore needle of the spinneret designed in this work for developing smaller OD fibers for high pressure applications.....	152
Figure 4.17: Scanning Electron Micrographs of a cross-section of the PDMC hollow fiber, showing the skin layer (top) and the porous fiber wall (bottom) that acts mostly as a support for the skin layer.....	156
Figure 4.18: Scanning Electron Micrograph of a cross-section of the PDMC hollow fiber, showing the porosity of the substructure adjacent to the bore.....	157
Figure 5.1: Effect of crosslinking agent and crosslinking temperature on permeability in dense film membranes [2]. Note that these polymers have different backbone structures from the ones used in this work so their absolute permeability values are not directly comparable.....	166
Figure 5.2: Effect of crosslinking temperature on CO ₂ permeance using a mixed gas feed with 50% CO ₂ . Test temperature was 35 °C.....	169

Figure 5.3: Effect of crosslinking temperature on CH ₄ permeance using a mixed gas feed with 50% CO ₂ . Test temperature was 35 °C.....	169
Figure 5.4: Effect of crosslinking temperature on permselectivity for CO ₂ /CH ₄ mixed gas with 50% CO ₂ . Test temperature was 35 °C.....	170
Figure 5.5: Effect of crosslinking temperature on separation factor for CO ₂ /CH ₄ mixed gas with 50% CO ₂ . Test temperature was 35 °C.....	170
Figure 5.6: Solid state ¹³ C NMR spectrum of an uncrosslinked PDMC polymer (lower) and a 200 °C crosslinked PDMC polymer (above). The green arrow indicates the middle aliphatic carbon from the propane diol crosslinking agent.....	173
Figure 5.7: Carbon dioxide permeance versus feed pressure for 200 °C crosslinked PDMC hollow fibers tested using different feed concentrations of CO ₂ at 35 °C.....	174
Figure 5.8: Methane permeance versus feed pressure for 200 °C crosslinked PDMC hollow fibers tested using different feed concentrations of CO ₂ at 35 °C.....	174
Figure 5.9: CO ₂ /CH ₄ permselectivity versus feed pressure for 200 °C crosslinked PDMC hollow fibers tested using different feed concentrations of CO ₂ at 35 °C.....	175
Figure 5.10: CO ₂ /CH ₄ separation factor versus feed pressure for 200 °C crosslinked PDMC hollow fibers tested using different feed concentrations of CO ₂ at 35 °C.....	175
Figure 5.11: Carbon dioxide and methane sorption isotherms for 200 °C crosslinked PDMC hollow fibers tested at 35 °C. Solid lines are dual mode fit.....	178
Figure 5.12: Carbon dioxide sorption coefficients calculated using dual mode model at different CO ₂ concentrations in the feed.....	179
Figure 5.13: CO ₂ /CH ₄ sorption selectivities calculated using dual mode model at different CO ₂ concentrations in the feed.....	180
Figure 5.14: Pure gas CO ₂ permeation isotherm used to obtain model parameters from a dense film crosslinked PDMC.....	183
Figure 5.15: Bulk flow and dual mode model predictions of CO ₂ permeance isotherm using a 50/50 CO ₂ /CH ₄ mixture at 35 °C in a crosslinked PDMC hollow fiber.....	185
Figure 5.16: Bulk flow and dual mode model predictions of CH ₄ permeance isotherm using a 50/50 CO ₂ /CH ₄ mixture at 35 °C in a crosslinked PDMC hollow fiber.....	186
Figure 5.17: CO ₂ /CH ₄ separation factors calculated using Equation 5.8–10 at a 14.7 psia permeate pressure using different CO ₂ concentrations in the feed.....	189

Figure 5.18: CO ₂ /CH ₄ separation factors calculated using Equation 5.8–10 at a 40 psia permeate pressure using different CO ₂ concentrations in the feed.....	190
Figure 5.19: CO ₂ /CH ₄ separation factors calculated using Equation 5.8–10 at a 60 psia permeate pressure using different CO ₂ concentrations in the feed.....	190
Figure 5.20: Stability over time of the CO ₂ and CH ₄ permeances using 200 °C crosslinked PDMC hollow fibers in a feed with 20% CO ₂	192
Figure 5.21: Stability over time of the CO ₂ /CH ₄ permselectivity and separation factor using 200 °C crosslinked PDMC hollow fibers in a feed with 20% CO ₂	193
Figure 5.22: Stability over time of the CO ₂ and CH ₄ permeances using 200 °C crosslinked PDMC hollow fibers in a feed with 50% CO ₂	194
Figure 5.23: Stability over time of the CO ₂ /CH ₄ permselectivity and separation factor using 200 °C crosslinked PDMC hollow fibers in a feed with 50% CO ₂	194
Figure 5.24: Carbon dioxide and methane fugacity coefficients as a function of feed pressure from the virial equation of state using a binary mixture with 50% CO ₂ at 35 °C.....	196
Figure 5.25: Ageing effects on separation performance using an uncrosslinked PDMC hollow fiber. CO ₂ /CH ₄ permeation using mixed gas at 200 psia with 20% CO ₂ at 35 °C. O ₂ , N ₂ , He tests using pure gases at 100 psia, 35 °C.....	198
Figure 5.26: Ageing effects on separation performance using a crosslinked PDMC hollow fiber. CO ₂ /CH ₄ permeation using mixed gas at 200 psia with 20% CO ₂ at 35 °C.....	202
Figure 5.27: Effect of fiber age on CO ₂ permeance versus feed pressure.....	204
Figure 5.28: Effect of fiber age on CH ₄ permeance versus feed pressure.....	204
Figure 5.29: Effect of fiber age on CO ₂ /CH ₄ permselectivity versus feed pressure.....	205
Figure 5.30: Effect of fiber age on CO ₂ /CH ₄ separation factor versus feed pressure.....	205
Figure 5.31: Permeances for CO ₂ for a crosslinked PDMC fiber using a 20/80 CO ₂ /CH ₄ feed at 35 °C, 50 °C, and 80 °C.....	207
Figure 5.32: Permeances for CH ₄ for a PDMC fiber using a 20/80 CO ₂ /CH ₄ feed at 35 °C, 50 °C, and 80 °C.....	208
Figure 5.33: Permselectivity for a PDMC fiber using a 20/80 CO ₂ /CH ₄ feed at 35 °C, 50 °C, and 80 °C.....	208

Figure 5.34: Separation factor for a PDMC fiber using a 20/80 CO ₂ /CH ₄ feed at 35 °C, 50 °C, and 80 °C.....	209
Figure 5.35: PDMC hollow fiber stability against a high pressure CO ₂ feed, using 200 °C crosslinking for 24 h [16] and 1 h. Normalized permeance is the permeance at each pressure versus permeance at 100 psia.....	212
Figure 5.36: Mixed gas permeation using a 20/80 CO ₂ /CH ₄ feed at 35 °C demonstrating the CO ₂ permeance of a crosslinked PDMC (3:2) hollow fiber membrane at elevated feed pressures.....	213
Figure 5.37: Mixed gas permeation using a 20/80 CO ₂ /CH ₄ feed at 35 °C demonstrating the permselectivity of a crosslinked PDMC (3:2) hollow fiber membrane at elevated feed pressures.....	213
Figure 5.38: Plasticization curves for a crosslinked and uncrosslinked PDMC (3:2) polyimide. Test temperature was 35 °C.....	216
Figure 6.1: Graph illustrating the extent to which a natural gas feed may be pretreated before being fed to a membrane [1].....	221
Figure 6.2: Toluene sorption and desorption isotherms in 200 °C crosslinked PDMC hollow fibers tested at 35 °C. For each point, measurements were made after ~24 h....	223
Figure 6.3: Sorption isotherm for toluene in PDMC hollow fiber membranes crosslinked at 200 °C.....	224
Figure 6.4: Performance of crosslinked fibers tested under various conditions with and without impurities. The numbers beside each point indicate a test condition as described in Table 6.2. The red arrow between points 4 and 5 represents a 2 week interval.....	226
Figure 6.5: Schematic illustrating the occupation of a chain packing defect or excess free volume (or Langmuir domain) by the toluene molecule, which may causes declines in permeance of CO ₂ and CH ₄ even at low feed pressures and low toluene concentrations.....	228
Figure 6.6: Performance of crosslinked fibers tested under various conditions with and without impurities after first exposure shown in Figure 6.4 and Table 6.2. The numbers beside each point indicate a test condition as described in Table 6.3.....	231
Figure 6.7: Effect of toluene at different feed pressures on the CO ₂ permeance using a 200 °C crosslinked PDMC hollow fiber membrane. Test temperature: 35 °C.....	234
Figure 6.8: Effect of toluene at different feed pressures on the CH ₄ permeance using a 200 °C crosslinked PDMC hollow fiber membrane. Test temperature: 35 °C.....	234

Figure 6.9: Effect of toluene at different feed pressures on the CO ₂ /CH ₄ permselectivity using a 200 °C crosslinked PDMC hollow fiber membrane. Test temperature: 35 °C...	235
Figure 6.10: Effect of toluene at different feed pressures on the CO ₂ /CH ₄ separation factor using a 200 °C crosslinked PDMC hollow fiber membrane. Test temperature: 35 °C.....	235
Figure 6.11: Schematic illustrating the effect of antiplasticization on the molecular motions of the polymer and on the gas diffusion.....	238
Figure 6.12: Effect of toluene concentration on normalized CO ₂ permeance of Matrimid [®] and PDMC crosslinked at 200 °C. Feed pressure ~400 psia, temperature ~35 °C.....	239
Figure 6.13: Effect of toluene concentration on normalized CH ₄ permeance of Matrimid [®] and PDMC crosslinked at 200 °C. Feed pressure ~400 psia, temperature ~35 °C.....	240
Figure 6.14: Effect of toluene concentration on normalized CH ₄ permeance of Matrimid [®] and PDMC crosslinked at 200 °C. Feed pressure ~400 psia, temperature ~35 °C.....	241
Figure 6.15: Effect of toluene level on normalized CO ₂ permeance of PDMC crosslinked at 200 °C. Feed pressure ~1000 psia, temperature ~35 °C.....	242
Figure 6.16: Effect of toluene level on normalized CH ₄ permeance of PDMC crosslinked at 200 °C. Feed pressure ~1000 psia, temperature ~35 °C.....	243
Figure 6.17: Effect of toluene level on CO ₂ /CH ₄ permselectivity of PDMC crosslinked at 200 °C. Feed pressure ~1000 psia, temperature ~35 °C.....	244
Figure 6.18: Sorption of toluene in crosslinked PDMC hollow fiber membranes and Matrimid [®] . (Matrimid courtesy of Madden).....	246
Figure 6.19: Chemical backbone structure of Matrimid [®] polyimide (top) and the PDMC polyimide (bottom).....	247
Figure 6.20: CO ₂ permeance for uncrosslinked and crosslinked PDMC hollow fiber membranes in the presence of toluene contamination (feed pressure ~800 psia, temperature ~ 35 °C, CO ₂ content ~ 10%, CH ₄ content ~ balance).....	249
Figure 6.21: CH ₄ permeance for uncrosslinked and crosslinked PDMC hollow fiber membranes in the presence of toluene contamination (feed pressure ~800 psia, temperature ~ 35 °C, CO ₂ content ~ 10%, CH ₄ content ~ balance).....	250
Figure 6.22: CO ₂ /CH ₄ permselectivity for uncrosslinked and crosslinked PDMC hollow fiber membranes in the presence of toluene contamination (feed pressure ~800 psia, temperature ~ 35 °C, CO ₂ content ~ 10%, CH ₄ content ~ balance).....	251

Figure 6.23: CO ₂ and CH ₄ permeances for uncrosslinked PDMC hollow fiber membranes showing plasticization occurring (Temperature ~ 35 °C, CO ₂ content ~ 50%, CH ₄ content ~ balance).....	253
Figure 6.24: CO ₂ /CH ₄ permselectivity for uncrosslinked PDMC hollow fiber membranes from corresponding permeances shown in Figure 6.23, which indicate plasticization (Temperature ~ 35 °C, CO ₂ content ~ 50%, CH ₄ content ~ balance).....	254
Figure 7.1: A depiction showing catalysts imbibed into uncrosslinked hollow fibers in a module, useful for permeation testing.....	261
Figure 7.2: Schematic illustrating a dual layer hollow fiber showing the sheath and core layers.....	263
Figure 7.3: Illustration showing effects of mixing various polymers in solution with PDMC (tests performed in February 2007).....	264

SUMMARY

Natural gas is one of the fastest growing primary energy sources in the world today. The increasing world demand for energy requires increased production of high quality natural gas. For the natural gas to be fed into the mainline gas transportation system, it must meet the pipe-line quality standards. Natural gas produced at the wellhead is usually “sub-quality” and contains various impurities such as CO₂, H₂S, and higher hydrocarbons, which must be removed to meet specifications.

Carbon dioxide is usually the most abundant impurity in natural gas feeds and high CO₂ partial pressures in the feed can lead to plasticization, which causes loss of some methane product and may ultimately render the membrane ineffective. Moreover, the presence of highly sorbing higher hydrocarbons in the feed can further reduce membrane performance.

Covalent crosslinking has been shown to increase plasticization resistance in dense films by suppressing the degree of swelling and segmental chain mobility in the polymer, thereby preserving the selectivity of the membrane. This research focuses on extending the dense film success to asymmetric hollow fibers.

In this work, the effect of high pressure CO₂ (up to 400 psia CO₂ partial pressure) on CO₂/CH₄ mixed gas separation performance was investigated on defect-free the hollow fiber membrane at different degrees of crosslinking. All the crosslinked fibers were

shown to exhibit good resistance to selectivity losses from CO₂ induced plasticization, significantly more than the uncrosslinked fibers. Robust resistance of the hollow fiber membranes in the presence of toluene (a highly sorbing contaminant) was also demonstrated as the membranes showed no plasticization. Antiplasticization was found to occur in the presence of toluene feeds with the crosslinkable fibers used in this work.

CHAPTER 1

INTRODUCTION

1.1 Natural gas processing

Due to growing population around the world and increased global development, it is quite clear that energy is becoming a scarce resource. The increasing demand for energy and the depletion of liquid fossil fuels has created interests in natural gas. For these reasons, natural gas (primarily CH_4) has become one of the fastest growing sources of energy because it is abundant and relatively cleaner than current liquid fossil fuels or coal. The consumption of natural gas is now ~22 trillion scf/yr in the U.S. and ~95 trillion scf/yr globally [1] (scf is defined as standard cubic feet, and 359 scf ~ 1 lbmole).

Raw natural gas contains various amounts of different impurities such as CO_2 , H_2S , H_2O , N_2 , and some heavy hydrocarbons, which must be reduced to certain limits to meet pipe-line specifications as shown in Table 1 [1, 2].

Table 1.1: Natural gas composition specifications for delivery to the U.S. national pipeline grid [1, 2].

<i>component</i>	<i>specification</i>
CO ₂	<2%
H ₂ O	<120 ppm
H ₂ S	<4 ppm
C ₃₊ content	950–1050 Btu/scf; dew point: < -20 °C
Total inert gases (N ₂ , He)	<4%

Carbon dioxide is usually the most abundant impurity in natural gas and although most of the wells in the U.S. contain between 1–10% CO₂ [1, 2], concentrations can vary from <1% to >50%. In enhanced oil recovery applications, CO₂ contents can be >70% of the natural gas stream [3]. Therefore, in natural gas purification processes, the removal of CO₂ is usually an important step. The presence of H₂O and acid gases such as CO₂ and H₂S may cause corrosion in pipelines; thus their removal is essential to the functioning of a stable pipeline network grid. Moreover, removal of non fuel gases such as CO₂, and N₂ increases the heating value of the natural gas and also reduces costs for the compression required to transport the gas.

Separation technologies that exist currently for natural gas purification applications include cryogenic distillation, amine absorption, and membranes. Cryogenic distillation is an energy intensive process since the gas must be cooled to very low temperatures to achieve a separation. Amine absorption processes are currently well accepted and are considered the standard [1, 4] for such applications because they have

been used extensively in the past with some success. Despite these facts, the capital and maintenance costs associated with these absorption units can be high since the size of the absorption tower and the amount absorbent liquid required scales with the amount of CO₂ that must be removed [1]. Moreover, there are additional costs associated with regeneration of the solvents used in the absorption processes; and the environmental restrictions on the disposal of such solvents make the processes more cumbersome especially where the level of CO₂ to be removed is high. Membrane processes are a growing technological area. Most of the growth in the natural gas market using membranes has been for CO₂ removal [1] since the high CO₂ content typical of raw natural gas wells makes the current amine technologies less competitive and gives membranes an opportunity to prove itself as a viable technology for the future.

1.2 Membranes for natural gas separations

The recent advancement in the application of membranes versus amine absorption processes is due to a number of factors. Some of these are the size and weight advantage that membranes offer, the reduced environmental effects, the lower energy requirements capable, the ease of operation (no moving parts), and the ability to do well with high CO₂ contents since productivity can be scaled with membrane thickness (inversely), transmembrane pressure difference, and area/volume (not just size alone). Moreover, the pressure driving force that makes membranes operational usually already exists in natural gas wells. Site specific reasons ultimately determine the separation process of choice. For instance, in offshore applications where space and weight are at a premium, membranes

are more attractive. Some current processes use a combination of membranes and amine absorption units, particularly where CO₂ contents are high since membranes are more suited for the bulk removal of CO₂ while the amines may be used for final polishing [1]. These are usually referred to as hybrid systems [5]. The disadvantage of using current membranes alone is due to the relatively high methane loss associated with removing high amounts of CO₂ with membranes with moderate separation efficiencies. Even in non-hybrid processes, more than one membrane unit (usually two) is typically used to alleviate this problem and requires the use of expensive compressors for recycle. The development of membranes that demonstrate high fluxes and exhibit and maintain high separation efficiencies may reduce these shortcomings of membrane technology. A typical two stage membrane process using a current (less efficient) membrane material and a yet to be discovered, more advanced membrane is shown in Figure 1.1 [6].

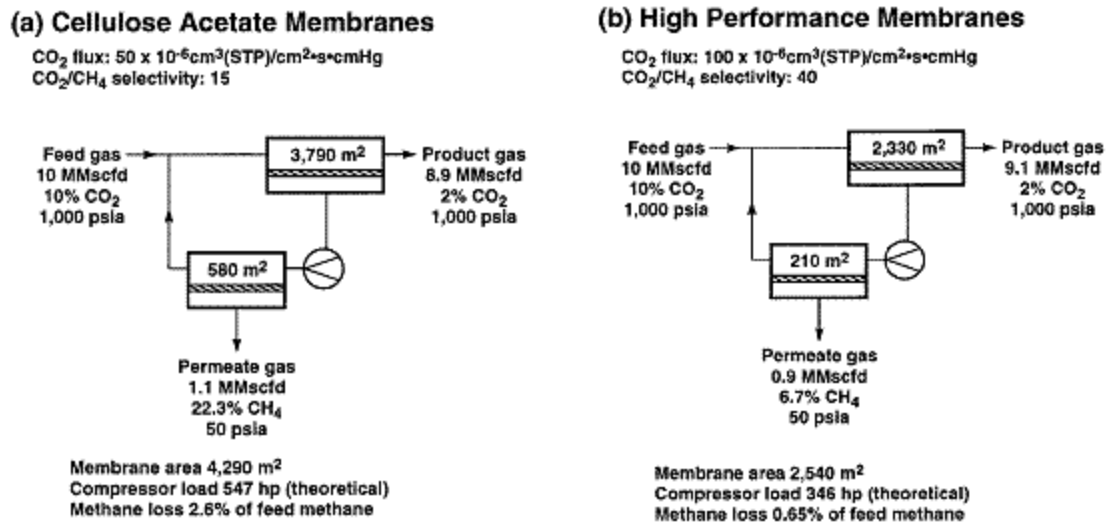


Figure 1.1: Schematic showing a two stage membrane process to purify a natural gas stream using a cellulose acetate membrane (left) and a yet to be developed high performance membrane (right) [6].

As can be seen from the analysis shown in Figure 1.1, there is a huge benefit from using membranes with high fluxes (productivities) and high separation efficiencies (selectivity). The higher flux reduces the membrane area required to achieve the separation requirements and the higher separation efficiency reduces the compression required to recycle the methane that would otherwise be lost to the permeate stream in the first stage. Moreover, such higher methane recoveries translate to higher returns on investment as well. For these reasons, a motivation exists for a materials science approach to address these issues that make membrane processes less competitive.

1.3 Membrane technology overview

To develop a membrane for commercial application, a number of practical requirements must be met. An article written by Koros [7] identifies four key elements for advancement of membrane technology. They are: (1) development of high-efficiency modules with high surface area/volume for large scale processes, (2) development of advanced materials, (3) development of a capability to tailor morphologies at multiple levels along the cross section of a membrane, and lastly, (4) development of manufacturing methods to rapidly and efficiently link the previous three elements.

To meet such requirements, the asymmetric hollow fiber membrane morphology was chosen for the basis of the membrane work in this research. Asymmetric hollow fibers are tubular forms of a membrane and provide high fluxes required for productive separations due to the ability to reduce the separating layer to a thin integral “skin” on the

outer surface of the membrane [8]. Such small diameter, cylindrical morphologies also can provide high surface area to volume ratios and high packing densities, with the ability to withstand large transmembrane driving force pressure differences.

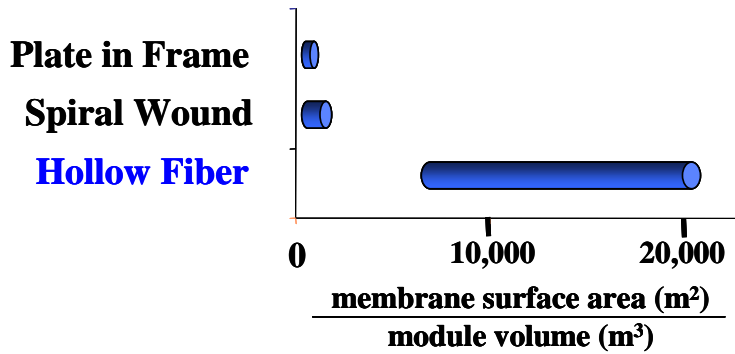
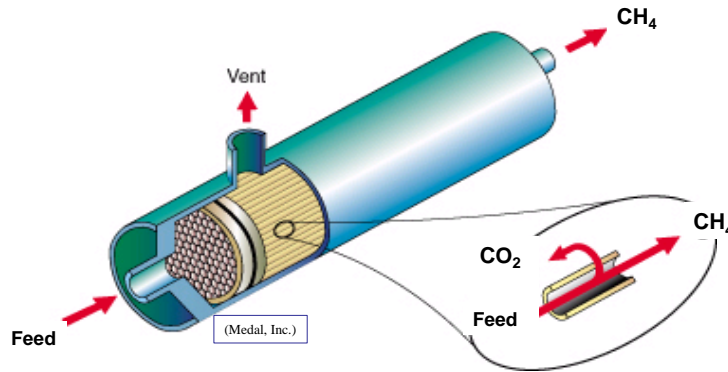


Figure Courtesy of Baker R. W., Membrane Technology and Applications.

Figure 1.2: A schematic showing a hollow fiber membrane module (top) and a bar graph illustration of the surface are/volume achievable in various module types.

The membrane skin on an asymmetric hollow fiber membrane can be on the order of 100 nm. Figure 1.2 above shows a schematic of a hollow fiber membrane module (top) and a bar chart showing the surface area to volume ratio advantages of hollow fiber modules

compared to other module configurations (below). More details on asymmetric hollow fiber design are discussed in Chapters 3 and 4. The first, third, and fourth element described above may be addressed directly within the framework of the chosen membrane type, which in this research is the asymmetric hollow fiber. The second element, advanced material development, is a more obvious factor within the four elements described. Most of the work published in the literature in developing membrane technology has focused on this particular aspect. Some of the challenges include the ability to tailor materials for specific separations that achieve high separation efficiencies and high fluxes. Another aspect has been in the area of stability and maintenance of membrane performance under realistic conditions with aggressive streams that have typically caused many new materials to fail. One of the main problems with current membranes for natural gas purification applications has been the issue of plasticization caused by the presence of high CO₂ contents. Although high CO₂ content streams make membranes favorable as a process option, high CO₂ content causes current membranes to swell and lose separation performance. The phenomenon of plasticization is discussed further in the next chapter. There is a maximum CO₂ partial pressure allowed by current membranes [9] due to these material limitations in maintaining stability. The overarching goal in this research focuses on bridging the gap between the material stability requirements and hollow fiber membrane technology. The following are the main research objectives for this dissertation.

1.4 Research objectives

1. To synthesize a high molecular weight polymer from a propane-diol crosslinkable polyimide (PDMC) for spinning asymmetric hollow fibers.

Crosslinkable polymers have been shown to stabilize membrane performance against plasticization in dense films. Identification of a crosslinkable material (PDMC) and synthesizing the material to meet spinnability requirements is addressed in this objective.

2. To spin defect-free asymmetric hollow fiber membranes from the PDMC material for separation of CO₂/CH₄

The feasibility of producing defect-free hollow fiber membranes from the crosslinkable material mentioned in objective 1, that can separate CO₂ from CH₄ at separation efficiencies equivalent to those found in dense film analogues is addressed in this objective.

3. To characterize the performance of the crosslinked PDMC hollow fiber membranes in the presence of high CO₂ content.

The evaluation of the performance of such defect-free crosslinkable hollow fiber membranes in the presence of plasticizing feeds (high CO₂ content) is addressed in this objective.

4. To demonstrate the efficacy of the PDMC hollow fiber membranes for the separation of CO₂/CH₄ in the presence of toluene, a highly sorbing contaminant.

The performance of the crosslinkable hollow fiber membrane in the presence of a heavy hydrocarbon, toluene, is determined.

1.5 Dissertation overview

Chapter 2 presents background and theory of the concepts referred to in this dissertation; Chapter 3 contains the material development details and description of the experimental methods used; Chapter 4 describes the method used to create a defect-free asymmetric hollow fiber membrane from the PDMC polymer; Chapter 5 contains the characterization results from using crosslinked and uncrosslinked PDMC hollow fiber membranes to demonstrate the viability of the membranes; Chapter 6 contains results from characterizing the membrane performance in the presence of toluene containing natural gas feeds; and Chapter 7 summarizes the results and scientific contributions made from this work and recommendations for future work are also mentioned.

1.6 References

1. Baker, R.W. and K. Lokhandwala, *Natural Gas Processing with Membranes: An Overview*. Ind. Eng. Chem. Res., 2008. **47**: p. 2109-2121.
2. Hugman, R.H., P.S. Springer, and E.H. Vidas, *Chemical Composition in Discovered and Undiscovered Natural Gas in the Lower-48 United States*. 1990, Energy and Environmental Analysis, Inc.: Arlington, VA.
3. Tatarzyn, J. and A. Brimm, *Salt Creek CO2 Enhanced Oil Recovery (EOR) Project*, in *74th Annual GPA Convention*. 1995: San Antonio, Texas. p. 12.
4. Kohl, A.L. and R.B. Nielsen, *Gas Purification*. 5th ed. 1997, Houston, TX: Gulf Publishing.
5. (<http://www.uop.com/objects/86MembrnAmineHybSys.pdf>). 2008 [cited 8/29/08].
6. Baker, R.W., *Future Directions of Membrane Gas Separation Technology*. Ind. Eng. Chem. Res., 2002. **41**: p. 1393-1411.
7. Koros, W.J., *Evolving beyond the thermal age of separation processes: Membranes can lead the way*. AIChE Journal, 2004. **50**(10): p. 2326-2334.
8. Baker, R.W., *Membrane Technology and Applications*. 2nd ed. 2004: John Wiley & Sons, Ltd. 538 pp.
9. Peters, R., *Hollow fiber membrane materials: applications and limitations*, I. Omole, Editor. 2008: Houston, TX.

CHAPTER 2

BACKGROUND AND THEORY

2.1 Small molecule transport in membranes

A membrane can be defined as a selective barrier between two phases [1]. There are several mechanisms for the transport of small molecules through a membrane. When the membrane consists of pores, the size of the pores and the mean free path of the penetrant govern the transport process. Under these circumstances, a number of diffusion mechanisms may exist as shown in Figure 2.1 [2].

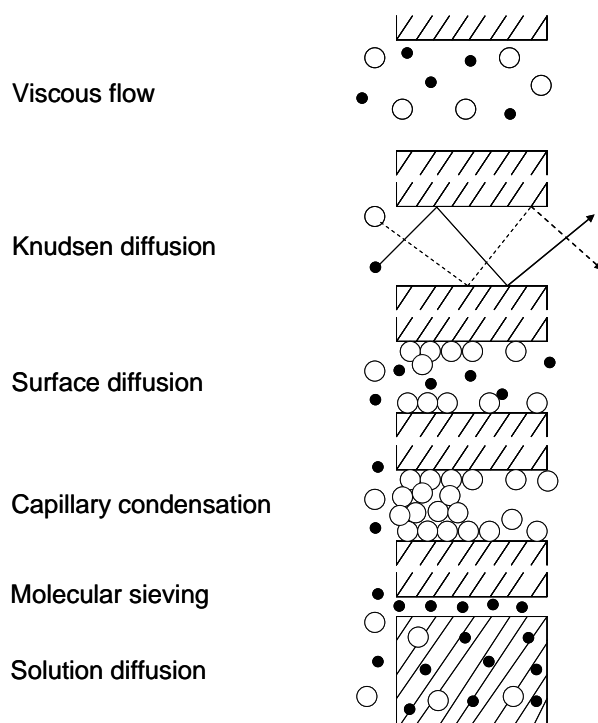


Figure 2.1: Schematic showing the various transport mechanisms for small molecules through membranes [2].

When the pore radius is much larger than the mean free path of the penetrant molecule at a given temperature and pressure, viscous flow occurs. In this case, there is no discrimination between the penetrants. Such pore sizes may be useful for hydrodynamic sieving applications, where the small molecule penetrants can be separated from much larger species. As the pore size reduces to the point where it is less than the mean free path of the penetrant molecules, Knudsen flow can occur [3]. In this case, there may be discrimination between the small penetrants depending on their molecular weights and temperature. The diffusion coefficient of component i during Knudsen type transport is represented by Equation 2.1, when the pores are straight and round [4].

$$D_{i,K} = 97.0 \cdot r \cdot \left(\frac{T}{M_i} \right)^{0.5} \quad (2.1)$$

In Equation 2.1, r is the pore radius in meters, T is the absolute temperature in Kelvin, and M is the molecular weight.

Other mechanisms may exist when the pore sizes are smaller than the mean free path of the penetrants. Some of which are surface diffusion, capillary condensation, and molecular sieving. All of these processes may cause separations due to their various molecular discrimination capabilities. However, as the size of the penetrant becomes smaller or closer to each other, these pore driven separations become more difficult since such pore dimensions may be hard to tailor for these harder separations. Molecular sieves in the form of zeolites and carbons are promising for their discrimination capabilities for small molecules [5-10], but the large scale manufacture of modules with these materials

can be costly [11]. In this work, the materials under investigation are dense (non-porous) polymers that undergo a solution diffusion mechanism.

Polymer membrane based separation technology has attracted attention due to the processability of polymers and their inherent permselectivity for different molecules. Polymer materials have been applied for various gas separations including nitrogen from air, hydrogen from ammonia purge gas streams, and for natural gas purification [12, 13]. Robust polymeric materials can also be applied in conjunction with other high performance materials like zeolites to form hybrid “mixed matrix membranes” [14-19]. Polyimides are a class of polymer materials that have been widely used in conventional membranes because of their transport properties, as well as chemical and thermal durability. Polyimides show separation properties that are superior to most other polymers due to their stiff backbone chains which can be tailored by incorporating different functional groups so as to engineer the free volume distributions needed to achieve attractive separation properties [13, 20]. These free volume elements, in a way, act as the sieving property in such dense materials. This makes the materials capable of discriminating between molecules of different sizes and shapes. Due to these features, the applications of polyimide membranes have grown and one of the major markets is in natural gas processing [12, 21], the chief area of interest for this research. The mechanism for transport of gas molecules through such polymers, as mentioned previously, can be modeled using a solution diffusion mechanism. Here, the transport is governed by the polymer/penetrant thermodynamic partitioning and by thermally activated transient gaps between polymer chains which creates free volume for molecular diffusion through the dense polymer. The diffusion of a penetrant molecule in an

isotropic medium can be described as a function of the frequency of the diffusion jumps and the average jump length created by the transient gap according to Equation 2.2 [13]. These transient gaps are illustrated in Figure 2.2.

$$D_i = \frac{f_i \cdot \lambda_i^2}{6} \quad (2.2)$$

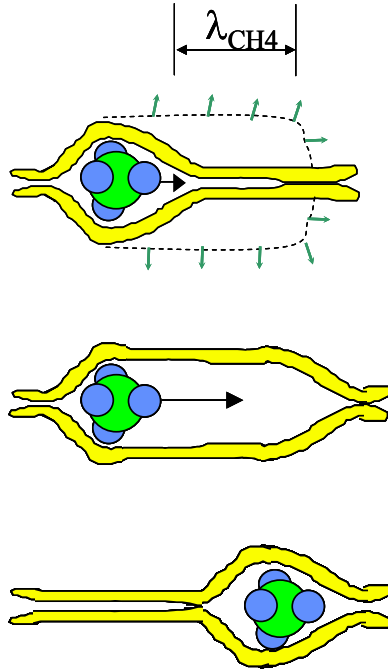


Figure 2.2: Transient gap formation for molecular diffusion in dense polymer membranes.

2.1.1 Solution diffusion

In solution diffusion membranes, the thermodynamic partitioning between the membrane and the penetrants is influenced by the condensability of the penetrant gas and the polymer/penetrant chemical affinity. The critical temperature or boiling point of penetrant gases correlates well with their condensabilities; and gases with higher critical temperatures tend to have higher partitioning [2] and thus permeate faster through dense membranes where sorption is the dominating mechanism for transport. This is usually the case for rubbery polymers. On the other hand, the diffusivity of the gas is dependent on the kinetic diameter of the penetrant gas molecules; thus, smaller molecules tend to have higher permeation rates through dense membranes where diffusion is the dominant mechanism such as in glassy polymers. However, since sorption and diffusion are both important in glassy polymers, both mechanisms play important roles in effecting a separation using dense polymeric membranes. The tailoring of functional groups within polymer chains can impart increased affinities between the penetrant and polymer and thus increase contributions from sorption. In separating CO₂ from CH₄ using glassy polyimides, CO₂ is usually considered the fast gas because it is more condensable and also has a smaller kinetic diameter than CH₄. Therefore, the CO₂/CH₄ pair is a favorable separation using these dense glassy polyimide materials as illustrated in the schematic in Figure 2.3.

In such a solution diffusion driven process using glassy polyimides, a separation can be implemented by maintaining a chemical potential (μ) gradient between the upstream and downstream sides of the membrane. This can be achieved by maintaining lower pressures on the permeate side of the membrane compared to the feed side. Hence, as the permeate pressure is reduced, the chemical potential gradient is maximized; therefore, with a permselective membrane and a sufficient stage cut, enrichment in the CH₄ product can be achieved as illustrated in Figure 2.4. In membrane processes, the stage cut is defined as the ratio of the permeate flow rate to the feed flow rate and can be adjusted to achieve the desired product purity. Practically, the intrinsic separation capability of the membrane material largely determines the amount of product lost in the permeate stream.

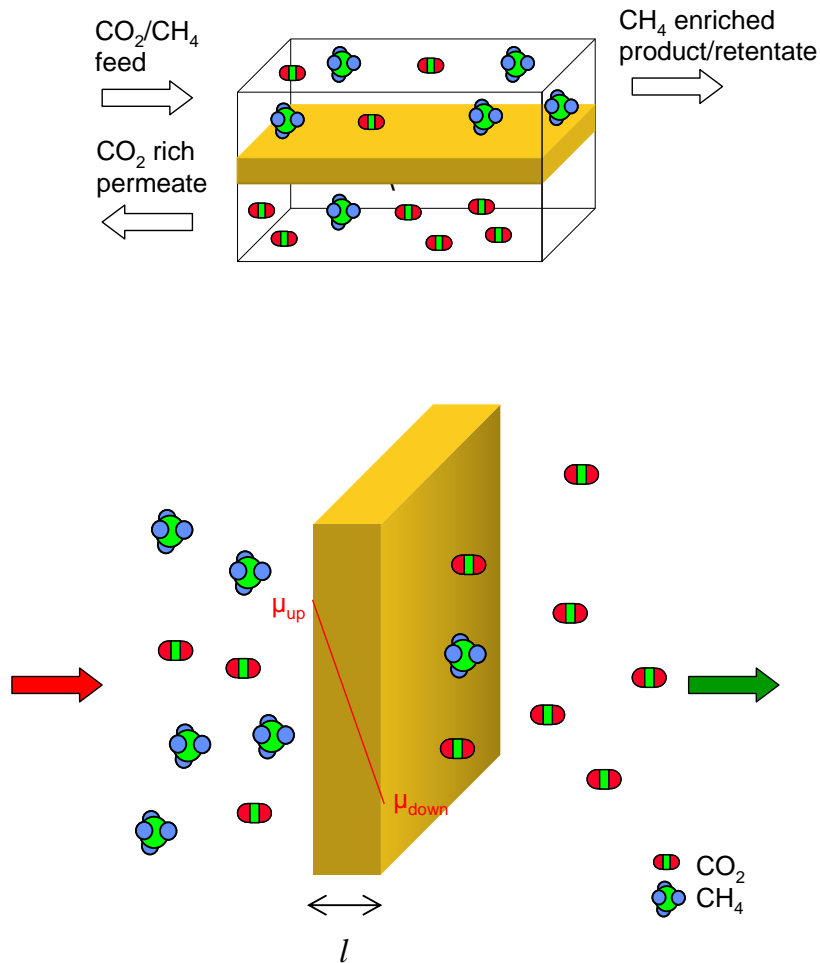


Figure 2.4: Schematic illustrating the separation process of CO₂ and CH₄ through a dense polymer membrane.

2.1.2 Characterizing solution diffusion membranes

In the transport of gas molecules through the solution diffusion mechanism described previously, gas molecules dissolve into the polymer at the upstream, then diffuse under the influence of an established chemical potential gradient, and finally desorb out of the polymer at the downstream. Two key intrinsic properties, the so called

“permeability” and “selectivity” are commonly used to evaluate the performance of membranes. Permeability is a measure of the membrane’s productivity; more specifically, it is the pressure and thickness normalized flux, described mathematically by Equation 2.3 below:

$$P_i = \frac{n_i \cdot l}{\Delta p_i} \quad (2.3)$$

In Equation 2.3, n_i represents the flux of component “ i ” gas molecules through the membrane, l represents the membrane thickness, and Δp_i is the transmembrane pressure or fugacity difference that acts as the driving force across the membrane. In asymmetric hollow fibers, which will be considered later, the actual membrane thickness is not readily known, so the productivity in these membranes is described by the permeance, which is simply the pressure (or fugacity) normalized flux as written in Equation 2.4 as follows:

$$\left(\frac{P}{l} \right)_i = \frac{n_i}{\Delta p_i} \quad (2.4)$$

The most common unit for permeability is the Barrer which is defined as

$$\text{Barrer} = 10^{-10} \frac{\text{cm}^3 (\text{STP}) \cdot \text{cm}}{\text{cm}^2 \cdot \text{s} \cdot \text{cmHg}} \quad (2.5)$$

and the permeance unit is the GPU, which is defined as

$$GPU = 10^{-6} \frac{cm^3 (STP)}{cm^2 \cdot s \cdot cmHg} \quad (2.6)$$

From Fick's first law of diffusion, the diffusion coefficient is assumed to be independent of the penetrant concentration and the flux is defined as follows.

$$n_i = -D_{i,m} \cdot \frac{dC_i}{dx} \quad (2.7)$$

Using the definition of flux and substituting into the equation for permeability or permeance, the following expression can be obtained

$$\frac{P_i}{l} = \frac{-D_{i,m} \cdot \frac{dC_i}{dx}}{\Delta p_i} \quad (2.8)$$

Integrating Equation 2.8 over the membrane thickness, l , and representing the concentrations of component i in the upstream and downstream faces of the membrane as $C_{i,up}$ and $C_{i,d}$, the following terms are obtained.

$$\int_0^l \frac{P_i}{l} \cdot dx = - \int_{C_{i,up}}^{C_{i,d}} \frac{D_{i,m}}{\Delta p_i} \cdot dC_i = \int_{C_{i,d}}^{C_{i,up}} \frac{D_{i,m}}{\Delta p_i} \cdot dC_i \quad (2.9)$$

The average diffusion coefficient in the membrane is defined by Equation 2.10, and can be substituted into Equation 2.9 to yield Equation 2.11.

$$\bar{D}_{i,m} = \frac{\int_{C_{i,d}}^{C_{i,up}} D_{i,m} \cdot dC_i}{C_{i,up} - C_{i,d}} \quad (2.10)$$

$$P_i = \bar{D}_{i,m} \cdot \frac{C_{i,up} - C_{i,d}}{\Delta p_i} \quad (2.11)$$

Also, the average solubility or sorption coefficient can be defined by Equation 2.12.

$$\bar{S}_i = \frac{C_{i,up} - C_{i,d}}{\Delta p_i} \quad (2.12)$$

Therefore, the permeability can also be described in terms of the governing kinetic and thermodynamic parameters, namely the diffusion coefficient and the solubility coefficient, by Equation 2.13, when the diffusion process is Fickian.

$$P_i = \bar{D}_i \cdot \bar{S}_i \quad (2.13)$$

The temperature dependence of the penetrant transport can be modeled using an Arrhenius relation. Here, the diffusivity is correlated with temperature by the energy of activation for the diffusive jump [23]. This is represented by the Equation 2.14 below.

$$D_i = D_{o,i} \cdot \exp\left(\frac{-E_d}{R \cdot T}\right) \quad (2.14)$$

The sorption temperature dependence is represented by a van't Hoff relation shown below [24].

$$S_i = S_{o,i} \cdot \exp\left(\frac{-\Delta H_s}{R \cdot T}\right) \quad (2.15)$$

In Equations 2.14 and 2.15, D_i and S_i are the diffusion and sorption coefficients of component i respectively. The terms $D_{o,i}$ and $S_{o,i}$ represent the pre-exponential factors in the correlations for the diffusion and sorption coefficient respectively. E_d represents the activation energy for the diffusion jump, and ΔH_s represents the heat of sorption for the penetrant, which is usually negative since sorption is usually exothermic. Lastly, T and R represent the absolute temperature and gas constant respectively.

Since the permeability is a product of the diffusion and sorption coefficients, the permeability may be represented by an Arrhenius expression as follows.

$$P_i = D_{o,i} \cdot S_{o,i} \cdot \exp\left(\frac{-E_d + \Delta H_s}{R \cdot T}\right) \quad (2.16)$$

The pre-exponential factor for the expression for temperature dependence of the permeability, $P_{o,i}$, and the activation energy for permeation, E_p , can be defined as follows,

$$P_{o,i} = D_{o,i} \cdot S_{o,i} \quad (2.17)$$

$$E_p = E_d + \Delta H_s \quad (2.18)$$

A simple expression for permeability temperature dependence can thus be obtained as shown in Equation 2.19.

$$P_i = P_{o,i} \cdot \exp\left(\frac{-E_p}{R \cdot T}\right) \quad (2.19)$$

The selectivity is a measure of the membrane's separation efficiency. The "ideal selectivity" (for pure gas feeds) of a membrane is described by the ratio of the component permeabilities or permeances:

$$\alpha_{i/j} = \frac{P_i}{P_j} = \frac{(P/l)_i}{(P/l)_j} = \frac{\bar{D}_i \cdot \bar{S}_i}{\bar{D}_j \cdot \bar{S}_j} \quad (2.20)$$

In the case of mixed gas feeds where there may be plasticization as well as competitive interactions between the permeating gases and the polymer, the separation factor is used to describe the separation by:

$$S.F. = \frac{y_i/y_j}{x_i/x_j} \quad (2.21)$$

In Equation 2.21, x and y represent the mole fractions of the gas components in the downstream and upstream sections of the membrane. The mixed gas separation factor (Equation 2.21) could also be written in terms of the diffusion and solubility coefficients by including a driving force controlled factor, viz. [13]:

$$S.F. = \frac{\bar{D}_i}{\bar{D}_j} \cdot \frac{\bar{S}_i}{\bar{S}_j} \cdot \frac{\Delta p_i / (p_i)_U}{\Delta p_j / (p_j)_U} \quad (2.22)$$

Therefore, the ideal selectivity or permselectivity can still be obtained using mixed gases once the downstream compositions and pressures are known. Thus, the permselectivity is more reflective of the membrane's intrinsic separation capability since the separation factor is dependent of the downstream pressure. The separation factor in Equation 2.22 approaches the ideal selectivity in Equation 2.20 as the downstream partial pressure approaches zero. Generally, in commercial applications of polymer membranes, the permeability and permselectivity must be balanced, since there is usually a trade-off between the two parameters [25].

2.2 Glassy polymers

Glassy polymers are non-equilibrium materials in the sense that they undergo chain relaxations under very long timescales. At room temperature, the mobility of a glassy polymer is highly restricted and the packing configuration of an amorphous glass gives rise to the presence of “micro-defects” in the chain conformations. These packing defects are temporarily trapped into the polymer matrix and are called “excess free volume”, defined as $V_g - V_l$ from Figure 2.5 [26], where V_g is the actual glassy volume and V_l is the volume of the densified glass at a hypothetical equilibrium.

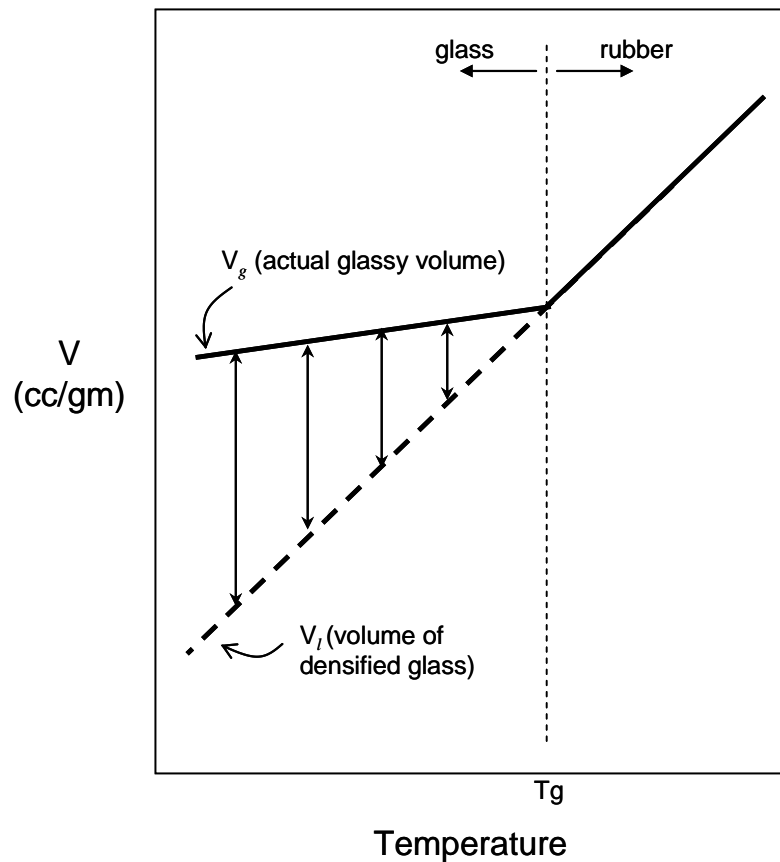


Figure 2.5: Schematic showing excess free volume or “unrelaxed volume ($V_g - V_l$) in glassy polymers as a function of temperature [26].

As the temperature of the glassy polymer is increased, the mobility of the rigid matrix is increased as the chains begin to possess increased rotational and torsional flexibility; and ultimately the free volume (and specific volume) increases. The glass transition temperature (T_g) defines the point where the glass transitions to a rubber as the temperature is increased further. This is exemplified by rapid chain motions and a steeper increase in the specific volume of the polymer. The high specific volume in the rubber is indicative of the high free volume from the increased mobility. It must be noted that the increased volume caused by increased chain mobility is simply called free volume or fractional free volume, while that which is present due to the glassy nature of the polymer is called excess free volume.

2.2.1 Physical ageing in glassy polymers

The relaxation process that takes place in a glassy polymer results in an elimination of the excess free volume or “unrelaxed volume”. This process is known as *physical ageing* and has been studied to some extent by a number of researchers mostly in flat films [27-32]. Physical ageing results in a decrease in the permeability of penetrant molecules and an increase in selectivity. The amount of unrelaxed volume present in a polymer may depend on the polymer material as well as the sample processing conditions, thermal history, and previous gas exposure [31-35]. In casting dense films, as the solvent evaporates, the polymer vitrifies. As the polymer transitions from a highly plasticized matrix to a dense glass, unrelaxed volume is created in the matrix. As the polymer slowly relaxes to its equilibrium conformation, the matrix becomes densified like a liquid, but molecular motions are still hindered as the polymer is still below its

glass transition temperature. This results in drastic time dependence of permeation properties in glassy polymeric membranes. The mechanism driving the physical ageing process has been shown to be dependent on the thickness of the sample [36]. Thinner membrane samples age faster than thicker membranes. Thus, physical ageing is worthy of investigation, since commercial membranes are usually preferred to be very thin. In Figure 2.6, the performance of ageing dense membranes of different thicknesses, in the separation of helium and nitrogen, are shown [36].

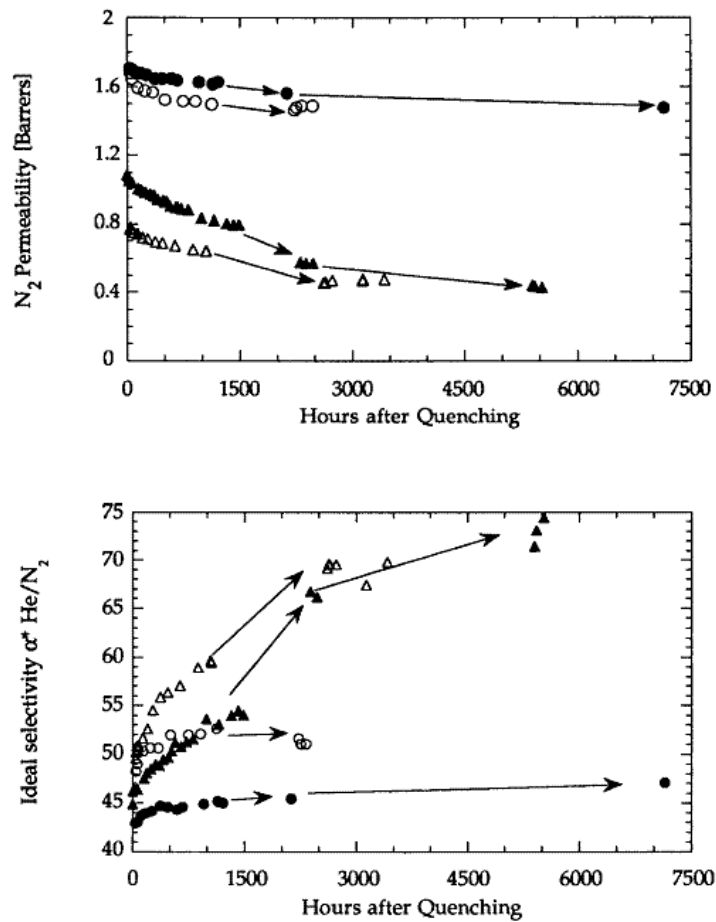


Figure 2.6: Ageing polyimide films in separating He/N₂, showing decreases in permeance (top) and increases in selectivity (bottom) using various film thicknesses: (●) thick, 28.45 μm ; (○) intermediate, 2.54 μm ; (△) thin, 0.5 μm –5000 Å; (▲) thin, air dried at room temperature only. Arrows: storage at 35 °C, 1 atm, dry air [36].

2.2.2 Sorption in glassy polymers

Due to the non-equilibrium nature of glassy polymers, the sorption of gas molecules in these materials do not follow Henry's law as is the case for rubbery polymers (elastomers). The presence of the excess free volume or holes in the matrix cause the glassy polymers to exhibit a combination of a Langmuir type sorption isotherm and a Henry's type, in two distinct modes. This phenomenon is well described by the dual-mode sorption theory [37-39]. Here, the sorbed concentration is a combination of that from the Henry's mode C_D and the hole filling mode (Langmuir type) C_H , as shown in Equation 2.23 for component i .

$$C_i = C_{D,i} + C_{H,i} \quad (2.23)$$

Figure 2.7 below shows a schematic illustrating the combination of the two modes of sorption, which results in a sorption isotherm typically seen in the case of glassy polymers.

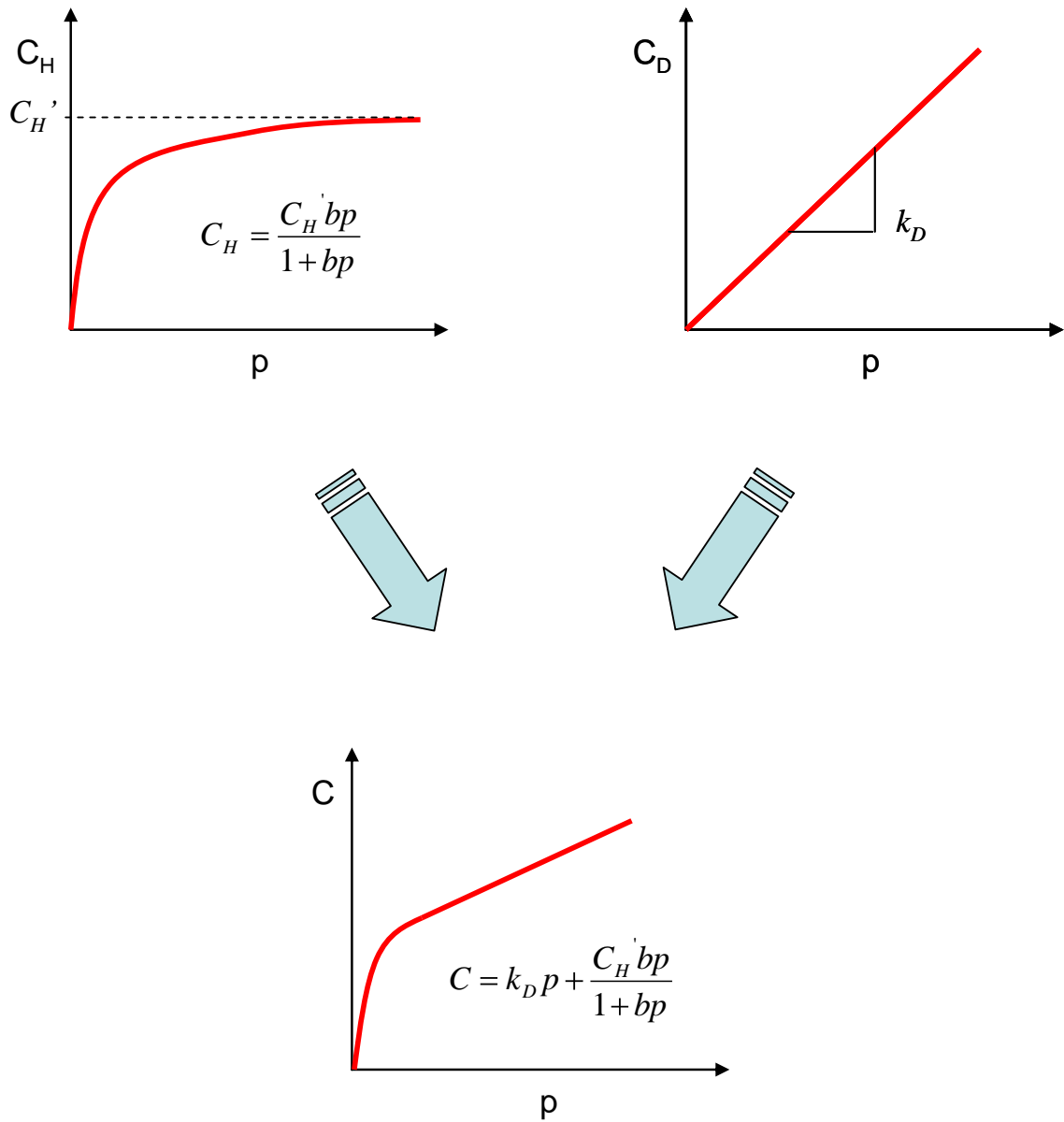


Figure 2.7: Schematic illustrating dual mode sorption in glassy polymers.

The dual-mode theory can be used as a model for sorption in glassy polymers. This is usually treated by curve fitting the pure gas experimental sorption data with the model. Using this model, three parameters can be obtained; namely, the Hole filling or Langmuir

capacity constant (C_H), the Langmuir affinity constant (b), and the Henry's constant (k_D). An interesting feature of the model is that these parameters can describe the sorption behavior of the penetrant and polymer and can be simply obtained for a variety of penetrants. The Langmuir affinity constant usually correlates with the condensability of the gas, the Langmuir capacity constant usually describes the capacity for sorption between different penetrants, and the Henry's constant describes the level of dissolution capable by the gas. Another interesting aspect of the model is that it can be extended to mixed gases as treated by Koros et al. [40, 41]. An illustration of this is shown in Figure 2.8 [42, 43].

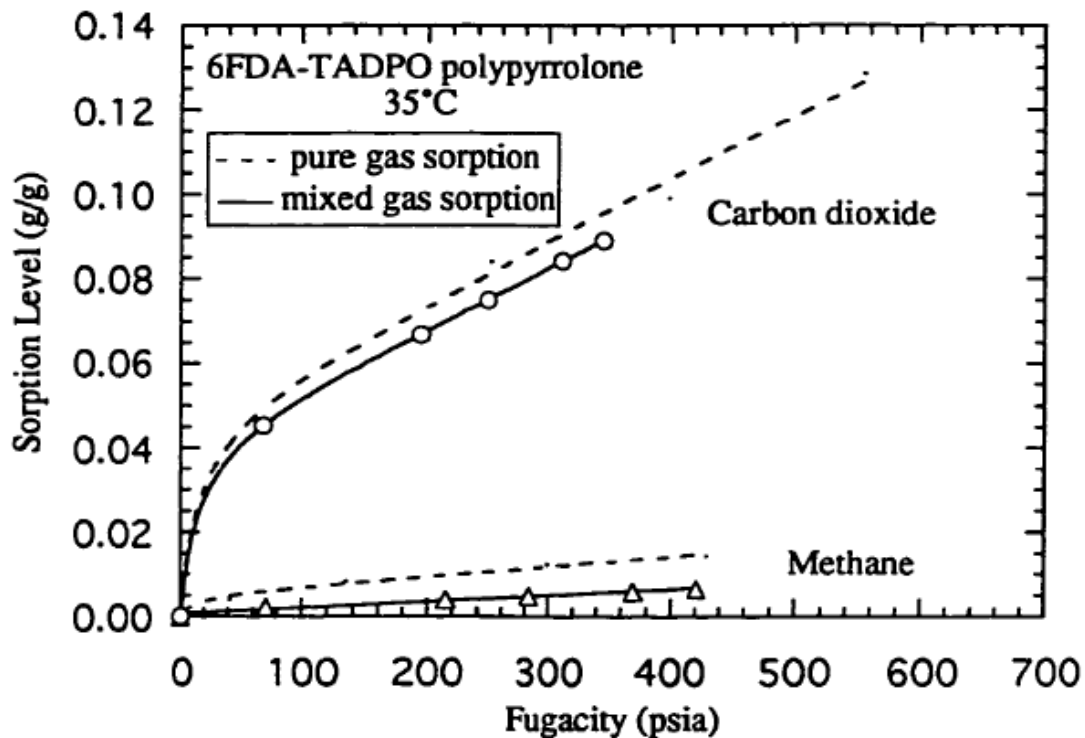


Figure 2.8: Pure and mixed gas (50/50 CO₂/CH₄) sorption isotherms [42, 43].

The prediction of mixed gas sorption using the dual-mode is treated by reflecting the competition for the Langmuir sorption sites, and can be represented using the Equations 2.24 and 2.25 below for the equilibrium sorbed concentrations of components i and j respectively.

$$C_i = k_{D,i} \cdot p_i + \frac{C_H' \cdot b_i \cdot p_i}{1 + b_i \cdot p_i + b_j \cdot p_j} \quad (2.24)$$

$$C_j = k_{D,j} \cdot p_j + \frac{C_H' \cdot b_j \cdot p_j}{1 + b_i \cdot p_i + b_j \cdot p_j} \quad (2.25)$$

2.3 Permeation modeling in glassy polymers

2.3.1 Partial immobilization model (dual-mode extension)

The dual-mode model can be extended to the analysis of permeation data [40], by expressing the steady state flux in terms of concentrations in the Henry's law and Langmuir environments. The expression for the flux of component i is given below.

$$N_i = -D_{D,i} \cdot \frac{dC_{D,i}}{dx} - D_{H,i} \cdot \frac{dC_{H,i}}{dx} \quad (2.26)$$

A simpler form of this expression can be written as shown in Equation 2.27.

$$N_i = -D_{D,i} \cdot \frac{dC_{M,i}}{dx} \quad (2.27)$$

Equation 2.27 is a mathematically more convenient expression obtained by defining the mobile concentration (C_M), an expression representing the concentrations and diffusion coefficients in the Henry's and Langmuir populations as seen in Equations 2.28 and 2.29,

$$C_{M,i} \equiv C_{D,i} + F_i \cdot C_{H,i} \quad (2.28)$$

$$F_i \equiv \frac{D_{H,i}}{D_{D,i}} \quad (2.29)$$

In Equations 2.28 and 2.29, $D_{H,i}$ represents the diffusion coefficient for penetrant diffusion from the Langmuir (hole) region to the dissolved region, and $D_{D,i}$ represents the diffusion from one dissolved region to another [39].

Ultimately, the permeability or permeance is given as a function of the boundary conditions, namely the fugacities of the penetrant in the upstream and downstream sections of the membrane as shown in Equation 2.30. A complete derivation can be found in the reference [40].

$$\frac{P_i}{l} = \frac{D_{D,i} \cdot k_{D,i}}{l} \cdot \left(1 + \frac{F_i \cdot K_i \cdot \frac{f_{i,up}}{f_{i,up} - f_{i,d}}}{1 + b_i \cdot f_{i,up} + b_j \cdot f_{j,up}} - \frac{F_i \cdot K_i \cdot \frac{f_{i,d}}{f_{i,up} - f_{i,d}}}{1 + b_i \cdot f_{i,d} + b_j \cdot f_{j,d}} \right) \quad (2.30)$$

Under negligible downstream pressures, as is the case for most of the work reported in the literature, the Equation 2.30 reduces to Equation 2.31, a more common form of the equation.

$$\frac{P_i}{l} = \frac{D_{D,i} \cdot k_{D,i}}{l} \cdot \left(1 + \frac{F_i \cdot K_i}{1 + b_i \cdot f_{i,up} + b_j \cdot f_{j,up}} \right) \quad (2.31)$$

In Equation 2.30 and 2.31, K is defined as the equilibrium relationship between the dissolved mode (Henry's region) and the hole filling mode (Langmuir region), given mathematically as $C_H'/b \cdot k_D$.

2.3.2 Frame of reference model/Bulk flow model [43, 44]

In the derivations for permeability using Fick's law in the previous sections, the frame of reference terms were not included. This is valid when the sorbed concentrations are low and the flux depends only on a Fickian diffusion driven process. However, in mixed gas permeation, the flux of each component can be very dependent on the concentrations of each other [43]. The flux of each component (i and j) is actually a sum of the diffusive flux and the bulk (convective) flux in polymer membrane (j) according to the expressions in Equations 2.32–35. This means that when the flux of component i (CO_2) is large, it's coupling with CH_4 can cause the convective flux and diffusive flux of CH_4 to be of the same magnitude.

$$n_A = n_A^{bulk} + n_A^{diff} \quad (2.32)$$

$$n_i = \left(n_i + n_j + n_p \right) \omega_i - \rho \cdot D_{i,m} \cdot \frac{d\omega_i}{dx} \quad (2.33)$$

$$n_j = \left(n_i + n_j + n_p \right) \omega_j - \rho \cdot D_{j,m} \cdot \frac{d\omega_j}{dx} \quad (2.34)$$

$$n_p = \left(n_i + n_j + n_p \right) \omega_p - \rho \cdot D_{p,m} \cdot \frac{d\omega_p}{dx} \quad (2.35)$$

Since the membrane is stationary, the flux term for the polymer (n_p) is zero. Therefore, the mutually dependent flux of components i and j can be expressed using Equation 2.36–2.38.

$$n_i = \frac{-\rho \cdot D_{D,i} \cdot \frac{d\omega_i}{dx}}{\left[1 - \left(1 + \frac{1}{r} \right) \cdot \omega_i \right]} \quad (2.36)$$

$$n_j = \frac{-\rho \cdot D_{D,j} \cdot \frac{d\omega_j}{dx}}{\left[1 - \left(1 + r \right) \omega_j \right]} \quad (2.37)$$

$$r = \frac{n_i}{n_j} \quad (2.38)$$

In these equations, ω is the mobile concentration of the penetrant defined by the equations below for component i and j [43].

$$\omega_i = \omega_i^{mobile} = \frac{k_{D,i} \cdot f_i \cdot M_i}{22400 \cdot \rho} \cdot \left(1 + \frac{F_i \cdot K_i}{1 + b_i \cdot f_i + b_j \cdot f_j} \right) \quad (2.39)$$

$$\omega_j = \omega_j^{mobile} = \frac{k_{D,j} \cdot f_j \cdot M_j}{22400 \cdot \rho} \cdot \left(1 + \frac{F_j \cdot K_j}{1 + b_i \cdot f_i + b_j \cdot f_j} \right) \quad (2.40)$$

In Equation 2.39 and 2.40, M is the molecular weight, ρ is the polymer density. The following boundary conditions can be defined for fugacity and mobile concentrations for i and j in the upstream and downstream sections of the membrane.

$$x = 0; \quad f_i = f_{i,up}; \quad f_j = f_{j,up}; \quad \omega_i = \omega_{i,up}; \quad \omega_j = \omega_{j,up}$$

$$x = l; \quad f_i = f_{i,d}; \quad f_j = f_{j,d}; \quad \omega_i = \omega_{i,d}; \quad \omega_j = \omega_{j,d}$$

The following expressions can thus be obtained for the flux of i and j , accounting for these bulk flow or frame of reference effects [43].

$$n_i = \frac{\rho \cdot D_{D,i}}{l} \cdot \frac{\ln \left[\frac{1 - \omega_{i,d} \cdot \left(1 + \frac{1}{r} \right)}{1 - \omega_{i,up} \cdot \left(1 + \frac{1}{r} \right)} \right]}{\left(1 + \frac{1}{r} \right)} \quad (2.41)$$

$$n_j = \frac{\rho \cdot D_{D,j}}{l} \cdot \frac{\ln \left[\frac{1 - \omega_{j,d} \cdot (+r)}{1 - \omega_{j,\mu\varphi} \cdot (+r)} \right]}{(+r)} \quad (2.42)$$

Therefore, using Equations 2.41 and 2.42 and the definition for r (Equation 2.38), the flux can be obtained iteratively and can be used to predict the permeability or permeance using the equation below, accounting for frame of reference effects. To start the iteration, an initial value of r is guessed, and used to solve for n_i and n_j . This is repeated until the calculated value for r converges to the previous value. A good initial value for r is the ratio of n_i and n_j , neglecting the r term in equations 2.41 and 2.42.

$$\frac{P_A}{l} = \frac{22400 \cdot n_A}{M_A \cdot \Delta f_A} \quad (2.43)$$

2.4 Penetrant-polymer interaction effects on transport

2.4.1 Plasticization

2.4.1.1 Overview of plasticization

Plasticization occurs when a sorbed penetrant causes a glassy polymer to increase segmental mobility and thus free volume, thereby significantly increasing the diffusion coefficients of all penetrants in the membrane. Plasticization has been investigated by a number of researchers [45-58]. This usually occurs when the concentration of the sorbing

penetrant is high or at high pressures of a highly sorbing species. The dual-mode model does predict increases in diffusion coefficients with increasing pressure, not associated with swelling, according to Equation 2.44 [59, 60].

$$D_{eff} = D_D \cdot \frac{\left[1 + \frac{F \cdot K}{\left(1 + C_D \cdot \frac{b}{k_D} \right)^2} \right]}{\left[1 + \frac{K}{\left(1 + C_D \cdot \frac{b}{k_D} \right)^2} \right]} \quad (2.44)$$

However, increases in D_{eff} beyond that predicted by the dual-mode model are reflective of non-idealities in the transport mechanism induced by the sorbed penetrant, such as swelling or plasticization. The increased molecular motions reduce the size discriminating ability of the polymer. An upswing in the permeability of the penetrants and a corresponding decrease in permselectivity are seen. Macroscopically, plasticization has been evidenced by a decrease in the glass transition temperature and a softening of the material [45, 46]. Since the membrane loses its mobility selectivity, the permeation of the slower gas is increased more than that for the fast gas. The plasticization effect is depicted in a schematic shown in Figure 2.9.

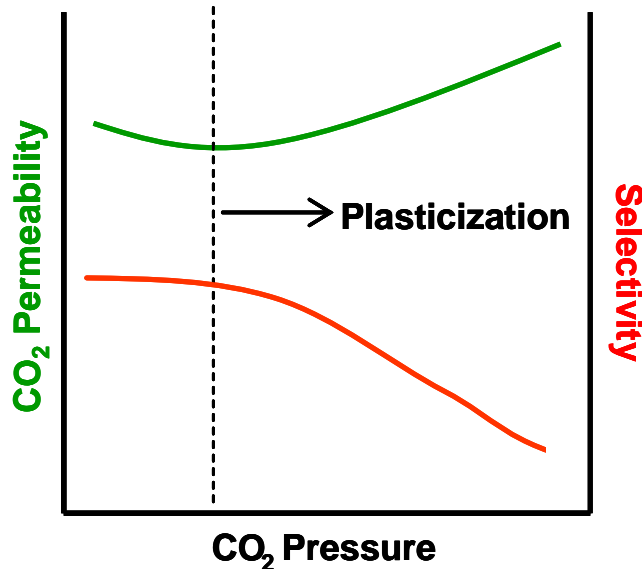


Figure 2.9: Schematic showing plasticization effects on membrane separation performance. Plasticization causes an increase in permeability and decrease in selectivity as pressure of sorbed penetrant increases.

The plasticization pressure is the pressure at which the permeability starts to increase with increasing penetrant concentration or pressure [47] as illustrated in Figure 2.9. This usually is defined in terms of a zero downstream pressure, and when a non zero downstream pressure exists, the observed plasticization pressure can be reduced. Initially, as the pressure is increased, there is a decrease in permeability, reflective of sorption in the Langmuir mode. As the Langmuir sorption sites saturate with penetrant molecules, the permeability decreases according to the dual-mode model. As the pressure is increased further, sorption in the Henry's mode begins to dominate and further increases

in concentration causes swelling in the densely packed regions. When the level of swelling is high, segmental motions are facilitated and leads to a plasticizing effect. Therefore it is understood that the key to controlling plasticization is to control excessive swelling and not necessarily the sorption level per se [51, 52, 61]. Figure 2.10 illustrates the effect of dual mode sorption effects and plasticization on the sorption and diffusion coefficients.

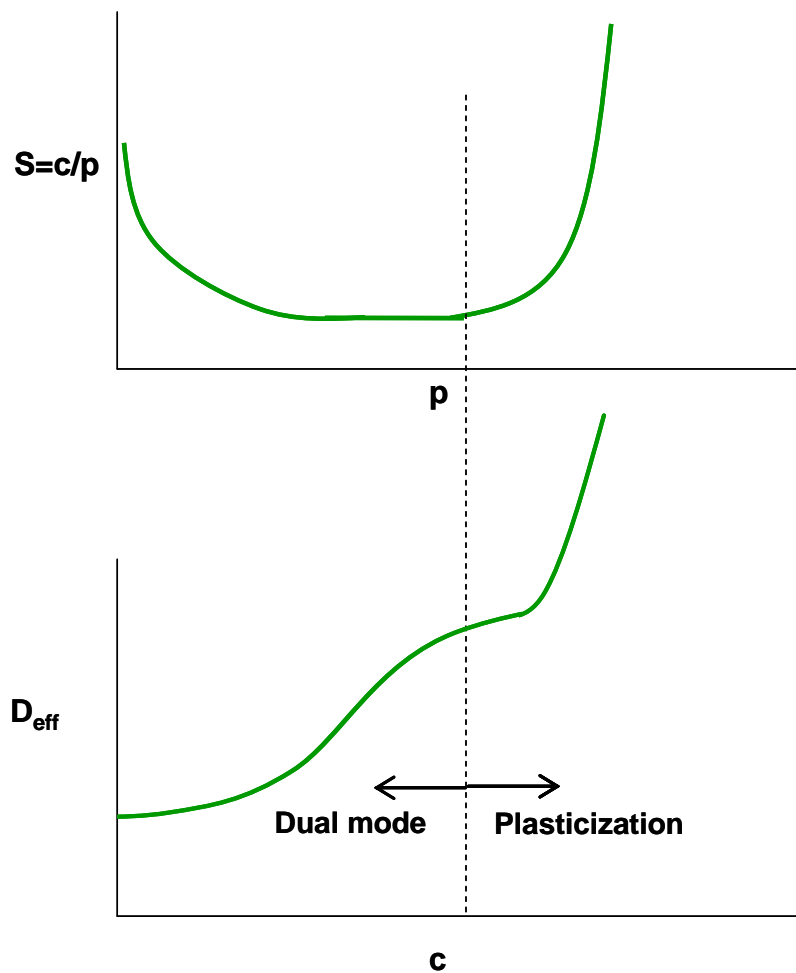


Figure 2.10: Schematic illustrating dual mode and plasticization effects on sorption and diffusion coefficients as pressure of plasticizer is increased.

During permeation there can be competing effects of sorption and swelling, both of which can cause depressions in separation performance but sorption can be predicted well enough that its effects are usually not considered a problem. Plasticization, on the other hand, signifies a continuous deterioration of the membrane resulting from excessive swelling stresses and is much harder to control. It has also been noticed that thinner membranes tend to plasticize more easily [50]. In asymmetric membranes, where the membrane thickness can be less than 500 nm, plasticization usually occurs immediately (without a minimum in the permeability versus pressure plot) and there may be no apparent plasticization pressure. In fact, part of the source of this tendency for asymmetric membranes to plasticize more easily may be due to the large excess volume fractions trapped in the matrix during the rapid quenching process used to form asymmetric membranes. In any case, the suppression of plasticization is important for membrane stability and for predicting membrane performance, especially in thin membrane structures.

A plasticized membrane tends to be unstable; thus, it is important to test membranes with mixed gas feeds when using penetrants that can act as plasticizers such as CO₂. Figure 2.11 shows permeation data from pure and mixed gas CO₂/CH₄ feeds to illustrate the importance of mixed gas testing in the presence of CO₂ [21, 62]. As can be seen from the figure, the pure gas CO₂/CH₄ permselectivity is gravely overestimated as the membrane plasticizes in the presence of pure CO₂ and not with pure CH₄.

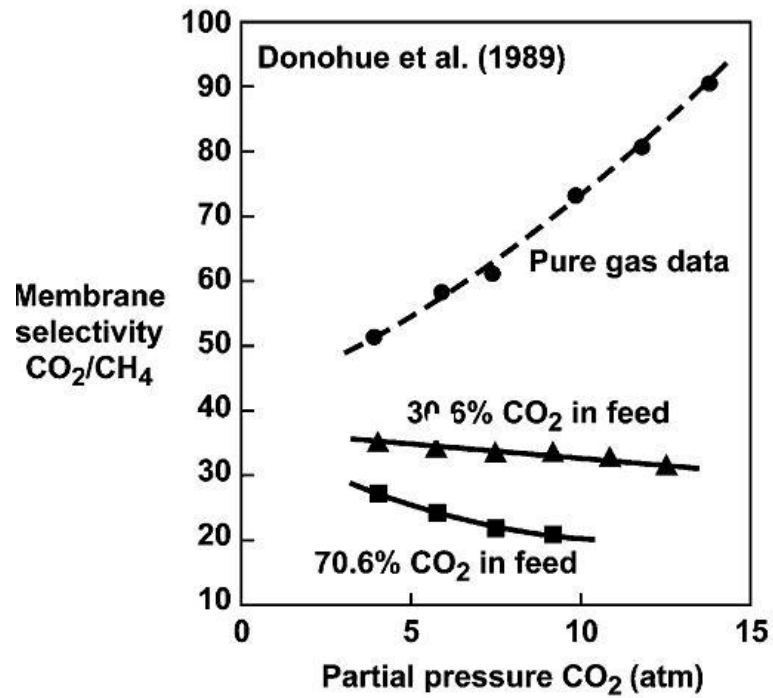


Figure 2.11: Graph illustrating the difference between pure gas and mixed gas determined selectivities using cellulose acetate, with different CO_2 content in the feed. The separation performance using the pure gas feeds is overestimated since the permeability of CO_2 is increased by plasticization [21, 62].

2.4.1.2 Strategy for stabilization against plasticization

Covalent crosslinking using a class of crosslinkable polyimides [28, 51, 52, 61, 63-71] has been shown to increase plasticization resistance mostly in dense films [28, 51, 52, 61, 63-68] by suppressing the degree of swelling and segmental chain mobility in the polymer, thereby preserving the selectivity of the membrane. This class of crosslinkable polyimides utilizes a diaminobenzoic acid (DABA) group in the polyimide backbone as a site for inter-chain crosslinking. The crosslinking agent is a diol such as ethylene glycol, 1,3-propanediol, propylene glycol, 1,4-butanediol, or 1,4-cyclohexanedimethanol. The choice of the diol is dependent on its reactivity and effects on the separation properties of the membrane made from it. The effects of the crosslinking agent has been studied by previous researchers,[61, 65] and the choice for this study was 1,3-propanediol based on work done by Hillock et al. [65]. Hillock showed that crosslinked “PDMC” (propanediol monoester crosslinkable) polyimide could be used to suppress plasticization in flat dense films. Wind also showed some success in crosslinking dense films as shown in Figure 2.12 [67]. This research focuses on extending the dense film success to much thinner membrane structures and characterizing the performance in high CO₂ content mixed gas feeds.

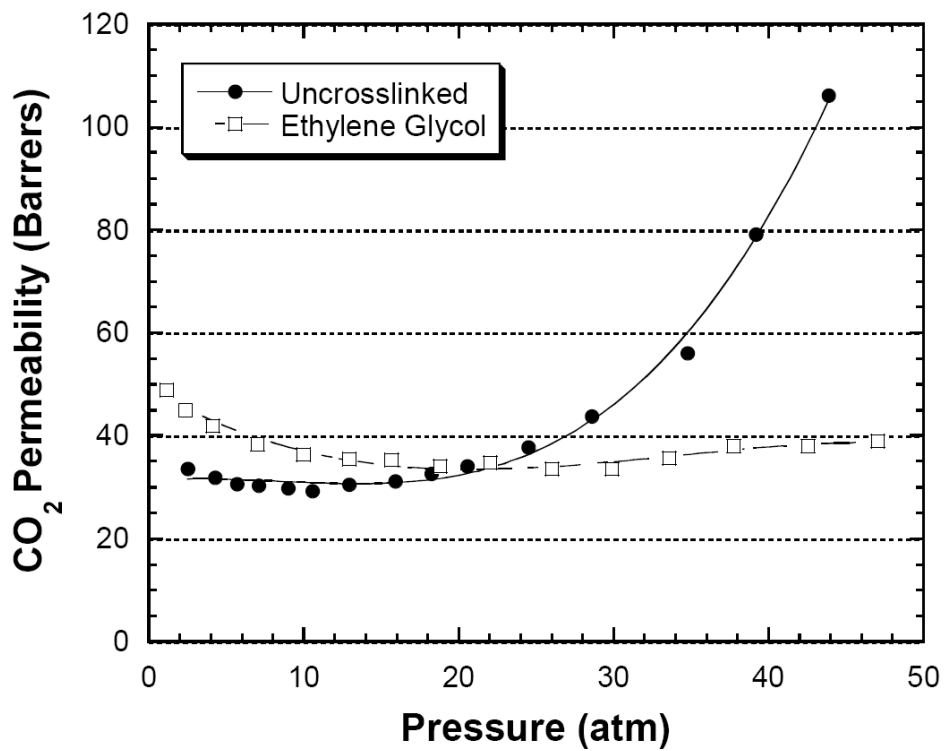


Figure 2.12: Permeation isotherms for crosslinked polyimide and uncrosslinked polyimide, illustrating the efficacy of the crosslinking approach in stabilizing the membrane against CO₂ induced plasticization [67].

2.4.2 Antiplasticization

In the literature, it has been reported that certain low molecular weight compounds mixed into to a polymer matrix at low concentrations (10 – 20 wt%) may retard the segmental motions of the polymer matrix [72]. Increases in modulus and strength and losses in elongation at break and impact resistance, contrary to what is seen in the case for a plasticized matrix, suggest evidence for the opposite phenomena under these conditions. This phenomena is referred to as *antiplasticization* and the penetrant is referred to as the *antiplasticizer*. Antiplasticization has been studied by a number of researchers [72-81]. In polymer membrane science, in applications for gas separations, the result of such an occurrence leads to a decrease in permeability with mixed effects on selectivity. It was found by Maeda and Paul that some low molecular weight aromatic compounds, at low concentrations, can cause an increase in selectivity through antiplasticization. However, further increases in the additive concentrations caused declines in selectivity. Table 2.2 and Figure 2.13 show some of the trends observed by Maeda and Paul using poly(phelylene oxide) and polysulfone.

Table 2.2: Permeabilities and selectivities for poly(phelylene oxide) containing different amounts of various diluents. Measurements made at 35 °C and 10 atm except where noted [72].

Material	P_{He}	P_{CO_2}	P_{CH_4}	$P_{\text{He}}/P_{\text{CH}_4}$	$P_{\text{He}}/P_{\text{CO}_2}$	$P_{\text{CO}_2}/P_{\text{CH}_4}$
PPO	78.5	60.4	3.78	20.8	1.30	15.6
TCP 10%	39.3	19.6	1.28	30.7	2.01	15.3
TCP 20%	19.7	8.75	0.56	35.5	2.25	15.8
TCP 30% ^a	12.4	5.71	0.37	33.5	2.17	15.5
K-50 10%	39.5	22.20	1.45	27.3	1.78	15.3
K-50 20%	20.4	9.24	0.55	37.0	2.21	16.8
K-50 30% ^a	13.3	7.10	0.52	25.2	1.87	14.8
DOS 10%	36.5	22.8	1.84	19.8	1.60	12.4
DOS 20%	27.1	16.5	0.54	3.0	1.64	5.0
DMS 5%	52.7	36.0	2.54	20.8	1.46	14.2
DMS 10%	39.5	31.5	2.45	16.2	1.25	12.9
DBS 5%	51.9	35.1	2.49	20.9	1.48	14.1
DBS 10%	37.4	25.7	2.11	17.7	1.46	12.2
DOP 10%	35.3	16.7	1.20	29.7	2.11	14.0
DOP 20%	22.5	10.4	1.19	18.9	2.16	8.7
DDS 20%	23.2	8.2	0.50	46.1	2.84	16.3

^aDriving pressure = 5 atm; Abbreviations: PPO is poly(phenylene oxide); K-50 is Kronitex; DOS is dioctyl sebacate; DMS is dimethyl sebacate; DBS is dibutyl sebacate; and DOP is di-2-ethylhexyl phthalate. More information can be found in the reference [72].

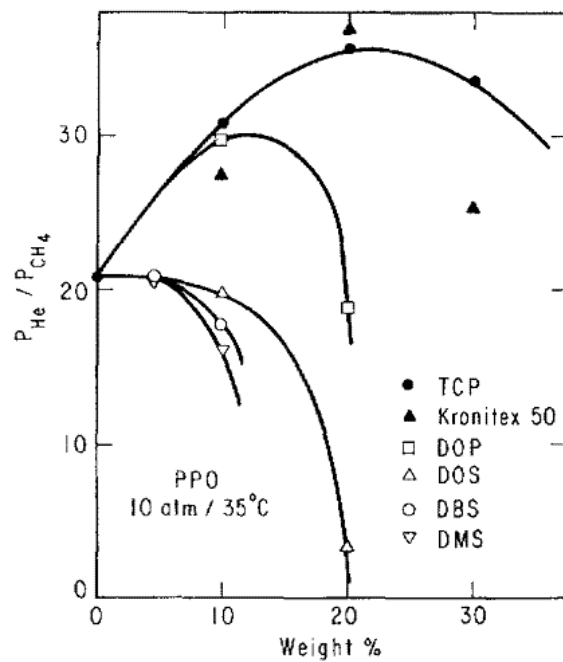
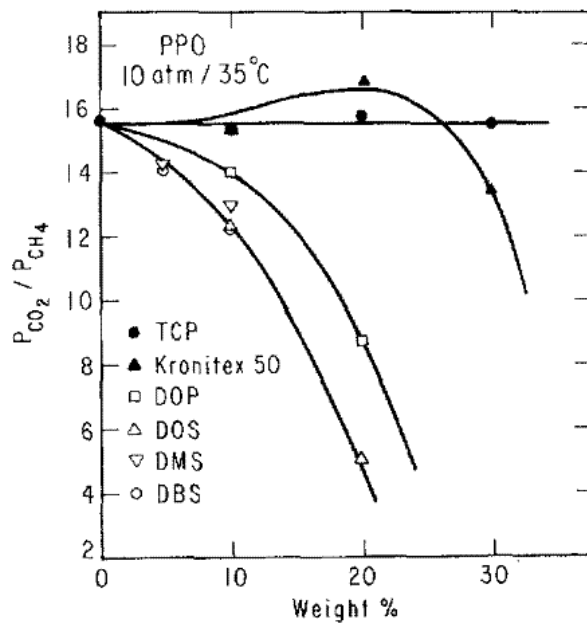


Figure 2.13: Selectivity for CO₂/CH₄ (top) and He/N₂ (bottom) using different diluent types and amounts in poly(phenylene oxide).

2.4.3 Conditioning

When a polymer is exposed to a sorbing penetrant and swelling occurs, the polymer chain configuration is altered to accommodate for the sorbed penetrants. When the sorbed penetrant is removed, the polymer slowly relaxes back to its original state. A membrane material is said to be conditioned during this “post-exposure” relaxation process [27, 82-86]. Such a conditioning process causes hysteresis in sorption and permeation isotherms [83] as shown in Figure 2.14.

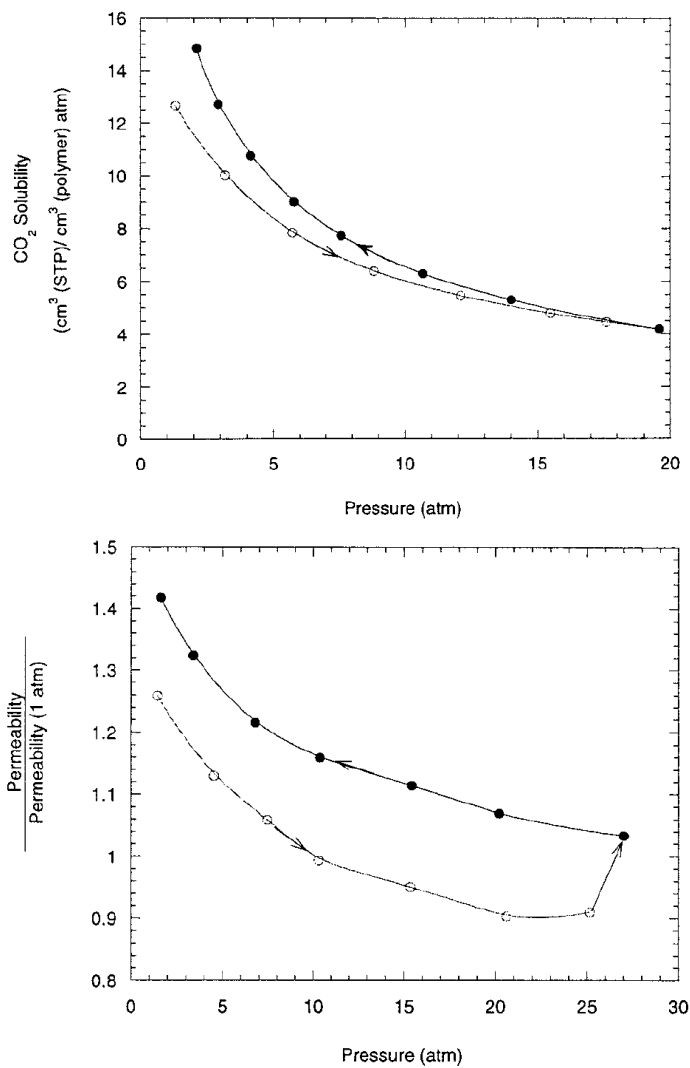


Figure 2.14: Conditioning loop (pressurization/depressurization with CO₂) showing hysteresis in 6FDA-6FmDA solubility coefficient (top) and 6FDA-6FpDA permeability (bottom) [83].

2.5 References

1. Mulder, M. and Editor, *Basic Principles of Membrane Technology, Second Edition*. 1996. 564 pp.
2. Cussler, E.L., *Diffusion, Mass Transfer in Fluid Systems*. 2nd ed. 1997, Cambridge, UK: Cambridge University Press. 580.
3. Knudsen, M., *The Law of the Molecular Flow and Viscosity of Gases Moving through Tubes*. Annalen der Physik (Weinheim, Germany), 1909. **28**: p. 75-130.
4. Hines, A.L. and R.N. Maddox, *Mass Transfer: Fundamentals and Applications*. 1985, Englewood Cliffs: Prentice-Hall, Inc. 542.
5. Bird, A.J. and D.L. Trimm, *Carbon molecular sieves used in gas separation membranes*, in *Carbon*. 1983. p. 177-80.
6. Barton, T.J., et al., *Tailored Porous Materials*. Chem. Mater., 1999. **11**(10): p. 2633-2656.
7. Chen, Y.D. and R.T. Yang, *Preparation of Carbon Molecular Sieve Membrane and Diffusion of Binary Mixtures in the Membrane*. Ind. Engr. Chem. Res., 1994. **33**(12): p. 3146-53.
8. Koresh, J. and A. Soffer, *Study of molecular sieve carbons. Part 1. Pore structure, gradual pore opening, and mechanism of molecular sieving*. J. Chem. Soc., Faraday Trans. 1, 1980. **76**(12): p. 2457-71, 1 plate.
9. Vu, D.Q., *Formation and Characterization of Asymmetric Carbon Molecular Sieve and Mixed Matrix Membranes for Natural Gas Purification*, in *Chemical Engineering*. 2001, The University of Texas at Austin: Austin, Texas. p. 334.
10. Ruthven, D.M., *Diffusion of oxygen and nitrogen in carbon molecular sieve*. Chemical Engineering Science, 1992. **47**(17-18): p. 4305-8.

11. Koros, W.J. and R. Mahajan, *Pushing the limits on possibilities for large scale gas separation: which strategies?* J. Membr. Sci., 2000. **175**(2): p. 181-196.
12. Baker, R.W., *Future Directions of Membrane Gas Separation Technology*. Ind. Eng. Chem. Res., 2002. **41**: p. 1393-1411.
13. W.J. Koros, G.K.F., *Membrane-based gas separation*. Journal of Membrane Science, 1993. **83**: p. 1-80.
14. Li, Y., et al., *Dual-layer polyethersulfone (PES)/BTDA-TDI/MDI co-polyimide (P84) hollow fiber membranes with a submicron PES-zeolite beta mixed matrix dense-selective layer for gas separation*. Journal of Membrane Science, 2006. **277**(1-2): p. 28-37.
15. Boom, J.P., et al., *Transport through zeolite filled polymeric membranes*. J. Membr. Sci., 1998. **138**(2): p. 237-258.
16. Cussler, E.L., *Membranes containing selective flakes*. J. Membr. Sci., 1990. **52**(3): p. 275-88.
17. Koros, W.J. and R. Mahajan, *Mixed matrix gas separation membranes*. Book of Abstracts, 219th ACS National Meeting, San Francisco, CA, March 26-30, 2000, 2000: p. IEC-187.
18. Mahajan, R. and W.J. Koros, *Mixed matrix membrane materials with glassy polymers. Part I*. Polymer Engineering and Science, 2002. **42**(7): p. 1420-1431.
19. Vu, D.Q., W.J. Koros, and S.J. Miller, *Mixed matrix membranes using carbon molecular sieves. I. Preparation and experimental results*. Journal of Membrane Science, 2003. **211**(2): p. 311-334.
20. Ohya, H., V.V. Kudryavtsev, and S.I. Semenova, *Polyimide Membranes: Applications, Fabrications, and Properties*. 1996, Tokyo, Japan: Gordon and Breach Publishers. 324 pp.
21. Baker, R.W. and K. Lokhandwala, *Natural Gas Processing with Membranes: An Overview*. Ind. Eng. Chem. Res., 2008. **47**: p. 2109-2121.

22. Breck, D.W., *Zeolite Molecular Sieves: Structure, Chemistry, and Use*. 1974, Malabar, FL: Robert E. Krieger Publishing Co, Inc. 771.
23. Crank, J. and G.S. Park, eds. *Diffusion in Polymers*. 1968, Academic Press: New York. 452 pp.
24. Costello, L.M., *Temperature dependence of gas sorption and transport properties in glassy polymers*, in *Department of Chemical Engineering*. 1994, University of Texas: Austin. p. 247 pp.
25. Robeson, L.M., *Correlation of separation factor versus permeability for polymeric membranes*. *Journal of Membrane Science*, 1991. **62**: p. 165-185.
26. Koros, W.J., et al., *A model for permeation of mixed gases and vapors in glassy polymers*. *J. Polym. Sci., Polym. Phys. Ed.*, 1981. **19**(10): p. 1513-30.
27. Adam, K., *THICKNESS DEPENDENT PHYSICAL AGING AND SUPERCRITICAL CARBON DIOXIDE CONDITIONING EFFECTS ON CROSSLINKABLE POLYIMIDE MEMBRANES FOR NATURAL GAS PURIFICATION*, in *Chemical & Biomolecular Engineering*. 2008, Georgia Institute of Technology: Atlanta. p. 200.
28. Kim, J.H., W.J. Koros, and D.R. Paul, *Effects of CO₂ exposure and physical aging on the gas permeability of thin 6FDA-based polyimide membranes: Part 2. with crosslinking*. *Journal of Membrane Science*, 2006. **282**(1-2): p. 32-43.
29. Kim, J.H., W.J. Koros, and D.R. Paul, *Physical aging of thin 6FDA-based polyimide membranes containing carboxyl acid groups. Part I. Transport properties*. *Polymer*, 2006. **47**(9): p. 3094-3103.
30. Kim, J.H., W.J. Koros, and D.R. Paul, *Physical aging of thin 6FDA-based polyimide membranes containing carboxyl acid groups. Part II. Optical properties*. *Polymer*, 2006. **47**(9): p. 3104-3111.
31. Moe, M.B., W.J. Koros, and D.R. Paul, *Effects of molecular structure and thermal annealing on gas transport in two tetramethylbisphenol A polymers*. *J. Polym. Sci., Part B: Polym. Phys.*, 1988. **26**(9): p. 1931-45.

32. Jordan, S.M., W.J. Koros, and G.K. Fleming, *The effects of carbon dioxide exposure on pure and mixed gas permeation behavior: comparison of glassy polycarbonate and silicone rubber*. J. Membr. Sci., 1987. **30**(2): p. 191-212.
33. Moe, M., et al., *Effects of film history on gas transport in a fluorinated aromatic polyimide*. J. Appl. Polym. Sci., 1988. **36**(8): p. 1833-46.
34. Pope, D.S., G.K. Fleming, and W.J. Koros, *Effect of various exposure histories on sorption and dilation in a family of polycarbonates*. Macromolecules, 1990. **23**(11): p. 2988-94.
35. Madden, W.C., *The Performance of Hollow Fiber Gas Separation Membranes in the Presence of an Aggressive Feed Stream*, in *Chemical Engineering*. 2005, Georgia Institute of Technology: Atlanta, Georgia. p. 219.
36. Pfromm, P.H. and W.J. Koros, *Accelerated physical ageing of thin glassy polymer films: evidence from gas transport measurements*. Polymer, 1995. **36**(12): p. 2379-2387.
37. Vieth, W.R., J.M. Howell, and J.H. Hsieh, *Dual sorption theory*. Journal of Membrane Science, 1976. **1**: p. 177-220.
38. Barrer, R.M., J.A. Barrie, and J. Slater, *Sorption and Diffusion in Ethyl Cellulose. Part III. Comparison Between Ethyl Cellulose and Rubber*. Journ. Polymer Sci., 1958. **27**: p. 177-197.
39. Koros, W.J., *Sorption and Transport in Glassy Polymers*, in *Department of Chemical Engineering*. 1977, The University of Texas at Austin: Austin.
40. Koros, W.J., et al., *Model For Permeation of Mixed Gases and Vapors in Glassy Polymers*. Journal of Polymer Science, Polymer Physics Edition, 1981. **19**(10): p. 1513-1530.
41. Koros, W.J., *Model for sorption of mixed gases in glassy polymers*. J. Polym. Sci., Polym. Phys. Ed., 1980. **18**(5): p. 981-92.
42. Kamaruddin, H.D., *Analysis of methanol/methyl tert-butyl ether (MTBE) separations using pervaporation*, in *Department of Chemical Engineering*. 1997, The University of Texas at Austin: Austin, TX. p. 215.

43. Kamaruddin, H.D. and W.J. Koros, *Some observations about the application of Fick's first law for membrane separation of multicomponent mixtures*. Journal of Membrane Science, 1997. **135**: p. 147-159.
44. Thundyil, M.J., Y.H. Jois, and W.J. Koros, *Effect of permeate pressure on the mixed gas permeation of carbon dioxide and methane in a glassy polyimide*. Journal of Membrane Science, 1999. **152**(1): p. 29-40.
45. Kesting, R. and A. Fritzsche, *Polymeric Gas Separation Membranes*. 1993, New York: John Wiley & Sons.
46. Ismail, A.F. and W. Lorna, *Penetrant-induced plasticization phenomenon in glassy polymers for gas separation membrane*. Separation and Purification Technology, 2002. **27**(3): p. 173-194.
47. Bos, A., et al., *CO₂-induced plasticization phenomena in glassy polymers*. Journal of Membrane Science, 1999. **155**(1): p. 67-78.
48. Bos, A., et al., *Plasticization-resistant glassy polyimide membranes for CO₂/CO₄ separations*. Separation and Purification Technology, 1998. **14**(1-3): p. 27-39.
49. Sanders, E.S., S.M. Jordan, and R. Subramanian, *Penetrant-plasticized permeation in polymethylmethacrylate*. Journal of Membrane Science, 1992. **74**(1-2): p. 29-36.
50. Wessling, M., M. Lidon Lopez, and H. Strathmann, *Accelerated plasticization of thin-film composite membranes used in gas separation*. Separation and Purification Technology, 2001. **24**(1-2): p. 223-233.
51. Wind, J.D., et al., *Carbon Dioxide-Induced Plasticization of Polyimide Membranes: Pseudo-Equilibrium Relationships of Diffusion, Sorption, and Swelling*. Macromolecules, 2003. **36**: p. 6433-6441.
52. Wind, J.D., et al., *Relaxation Dynamics of CO₂ Diffusion, Sorption, and Polymer Swelling for Plasticized Polyimide Membranes*. Macromolecules, 2003. **36**(17): p. 6442-6448.
53. Visser, T., G.H. Koops, and M. Wessling, *On the subtle balance between competitive sorption and plasticization effects in asymmetric hollow fiber gas*

- separation membranes*. Journal of Membrane Science, 2005. **252**(1-2): p. 265-277.
54. Visser, T., N. Masetto, and M. Wessling, *Materials dependence of mixed gas plasticization behavior in asymmetric membranes*. Journal of Membrane Science, 2007. **306**(1-2): p. 16-28.
 55. Houde, A.Y., S.S. Kulkarni, and M.G. Kulkarni, *Permeation and plasticization behavior of glassy polymers: a WAXD interpretation*. Journal of Membrane Science, 1992. **71**(1-2): p. 117-128.
 56. Wessling, M., et al., *Plasticization of gas separation membranes*. Gas Separation & Purification, 1991. **5**(4): p. 222-228.
 57. Chiou, J.S., J.W. Barlow, and D.R. Paul, *Plasticization of glassy polymers by carbon dioxide*. J. Appl. Polym. Sci., 1985. **30**(6): p. 2633-42.
 58. Zhou, S. and S.A. Stern, *The effect of plasticization on the transport of gases in and through glassy polymers*, in *J. Polym. Sci., Part B: Polym. Phys.* 1989. p. 205-22.
 59. Barrer, R.M., *Nature of diffusion process in rubber*. Nature, 1937. **140**: p. 106.
 60. Crank, J. and G.S. Park, *Diffusion in polymers*. 1971, New York: John Wiley & Sons.
 61. Wind, J.D., et al., *Solid-State Covalent Cross-Linking of Polyimide Membranes for Carbon Dioxide Plasticization Reduction*. Macromolecules, 2003. **36**: p. 1882-1888.
 62. Donohue, M.D., B.S. Minhas, and S.Y. Lee, *Permeation behavior of carbon dioxide-methane mixtures in cellulose acetate membranes*. Journal of Membrane Science, 1989. **42**(3): p. 197-214.
 63. Staudt-Bickela, C. and W.J. Koros, *Improvement of CO₂/CH₄ separation characteristics of polyimides by chemical crosslinking*. Journal of Membrane Science, 1999. **155**: p. 145-154.

64. Wind, J.D., et al., *The Effects of Crosslinking Chemistry on CO₂ Plasticization of Polyimide Gas Separation Membranes*. Ind. Eng. Chem. Res., 2002. **41**: p. 6139-6148.
65. Hillock, A.M.W. and W.J. Koros, *Cross-Linkable Polyimide Membrane for Natural Gas Purification and Carbon Dioxide Plasticization Reduction*. Macromolecules, 2007. **40**: p. 583-587.
66. Wind, J.D., D.R. Paul, and W.J. Koros, *Natural gas permeation in polyimide membranes*. Journal of Membrane Science, 2004. **228**: p. 227–236.
67. Wind, J.D., *Improving Polyimide Membrane Resistance to Carbon Dioxide Plasticization in Natural Gas Separations*, in *Chemical Engineering*. 2002, The University of Texas at Austin: Austin, Texas. p. 215.
68. Hillock, A.M.W., *CROSSLINKABLE POLYIMIDE MIXED MATRIX MEMBRANES FOR NATURAL GAS PURIFICATION*, in *Chemical Engineering*. 2005, Georgia Institute of Technology: Atlanta, Georgia. p. 199.
69. Wallace, D.W., *Crosslinked Hollow Fiber Membranes for Natural Gas Purification and Their Manufacture from Novel Polymers*, in *Chemical Engineering*. 2004, The University of Texas at Austin: Austin, Texas. p. 202.
70. Wallace, D.W., C. Staudt-Bickel, and W.J. Koros, *Efficient development of effective hollow fiber membranes for gas separations from novel polymers*. Journal of Membrane Science, 2006. **278**: p. 92–104.
71. Wallace, D.W., et al., *Characterization of crosslinked hollow fiber membranes*. Polymer, 2006. **47**: p. 1207–1216.
72. Maeda, Y. and D.R. Paul, *Effect of antiplasticization on selectivity and productivity of gas separation membranes*. Journal of Membrane Science, 1987. **30**(1): p. 1-9.
73. Maeda, Y. and D.R. Paul, *Effect of Antiplasticization on Gas Sorption and Transport. II. Poly (phenylene Oxide)*. Journal of Polymer Science: Part B: Polymer Physics, 1987. **25**: p. 981-1003.

74. Vrentas, J.S., J.L. Duda, and H.C. Ling, *Antiplasticization and volumetric behavior in glassy polymers*. *Macromolecules*, 1988. **21**(5): p. 1470-1475.
75. Soong, S.Y., et al., *The effects of thermomechanical history and strain rate on antiplasticization of PVC*. *Polymer*, 2008. **49**(6): p. 1440-1443.
76. Garcia, A., et al., *Study of the relationship between transport properties and free volume based in polyamide blends*. *Journal of Membrane Science*, 2006. **284**(1-2): p. 173-179.
77. Duda, J.L., I. Hadj Romdhane, and R.P. Danner, *Diffusion in glassy polymers -- relaxation and antiplasticization*. *Journal of Non-Crystalline Solids*, 1994. **172-174**(Part 2): p. 715-720.
78. Won, Y.-g., et al., *Internal antiplasticization in copolymer and terpolymer networks based on diepoxides, diamines and monoamines*. *Polymer*, 1990. **31**(9): p. 1787-1792.
79. Mascia, L., *Antiplasticization of poly (vinyl chloride) in relation to thermal ageing and non-linear viscoelastic behaviour*. *Polymer*, 1978. **19**(3): p. 325-328.
80. Ranade, A., et al., *The solid state structure of polycarbonate blends with lead phthalocyanine*. *Polymer*, 2007. **48**(2): p. 624-631.
81. Slark, A.T., *The effect of intermolecular forces on the glass transition of solute-polymer blends*. *Polymer*, 1997. **38**(10): p. 2407-2414.
82. Al-Juaied, M. and W.J. Koros, *Performance of natural gas membranes in the presence of heavy hydrocarbons*. *Journal of Membrane Science*, 2006. **274**(1-2): p. 227-243.
83. Coleman, M.R. and W.J. Koros, *Conditioning of Fluorine-Containing Polyimides. 2. Effect of Conditioning Protocol at 8% Volume Dilution on Gas-Transport Properties*. *Macromolecules*, 1999. **32**(9): p. 3106 -3113.
84. Coleman, M.R. and W.J. Koros, *Conditioning of Fluorine Containing Polyimides. 1. Effect of Exposure to High Pressure Carbon Dioxide on Permeability*. *Macromolecules*, 1997. **30**(22): p. 6899 -6905.

85. Fleming, G.K. and W.J. Koros, *Carbon dioxide conditioning effects on sorption and volume dilation behavior for bisphenol A-polycarbonate*. *Macromolecules*, 1990. **23**(5): p. 1353-60.
86. Jordan, S.M., M.A. Henson, and W.J. Koros, *The effects of carbon dioxide conditioning on the permeation behavior of hollow fiber asymmetric membranes*. *J. Membr. Sci.*, 1990. **54**(1-2): p. 103-18.

CHAPTER 3

EXPERIMENTAL PROCEDURES AND MATERIALS

3.1 Introduction

This chapter contains a description of the experimental methods used in characterization of the membrane materials used in this work. Also contained is an outline of the steps undertaken in the development of a high molecular weight polymer for hollow fiber spinning.

3.2 Experimental Methods

3.2.1 Permeation

Permeation in this work was done on both dense film and asymmetric hollow fiber membranes.

3.2.1.1 Dense Film Preparation

Dense films were prepared by dissolving the polymer in tetrahydrofuran (THF) at ~ 5 to 10 wt% and extruding the solution through a 0.4 micron filter onto a Teflon[®] casting dish, on top of a level glass plate. The dish with the polymer solution is covered with an inverted glass funnel and capped with a Kimwipe[®] (Kimberly-Clark Corporation; Roswell, Georgia) plug to regulate the evaporation of THF from the nascent membrane.

The solid membrane is allowed to form overnight and then is dried in a vacuum oven at ~ 70 °C for 24 hrs. Subsequently, the membrane can be annealed at a desired temperature. Temperatures above 70 °C are not preferred for drying since the polymer used in this work is crosslinkable. Figure 3.1 below shows a schematic of the film formation process.

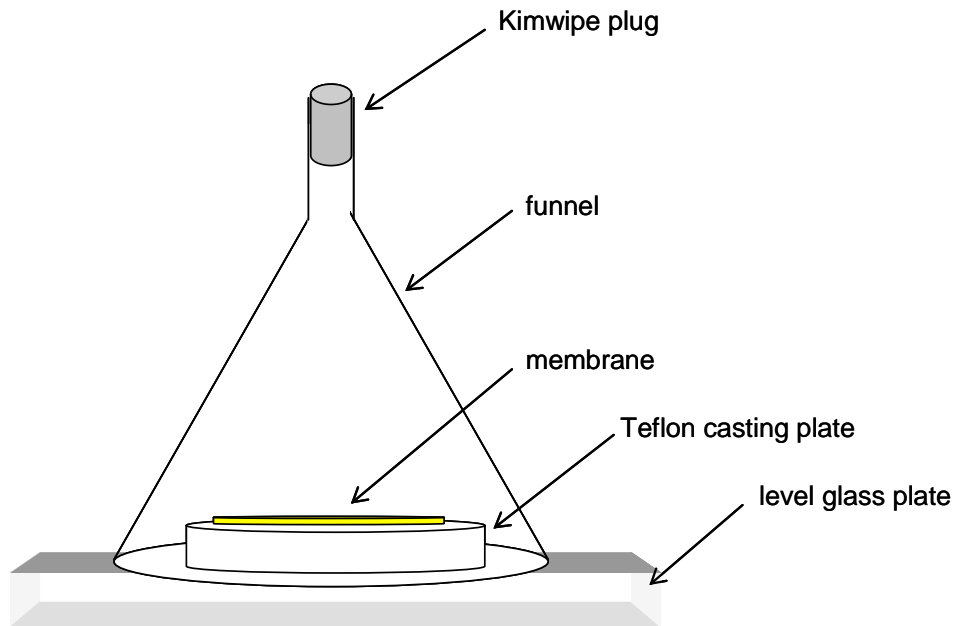


Figure 3.1: A schematic showing a dense film cast on a Teflon casting plate

3.2.1.2 Dense Film Permeation

Dense films, made as described in Section 3.2.1.1, were masked and fit into permeation cells according to the procedures described elsewhere [1]. A schematic depicting the assembly of the masked membrane and the cell is shown in Figure 3.2.

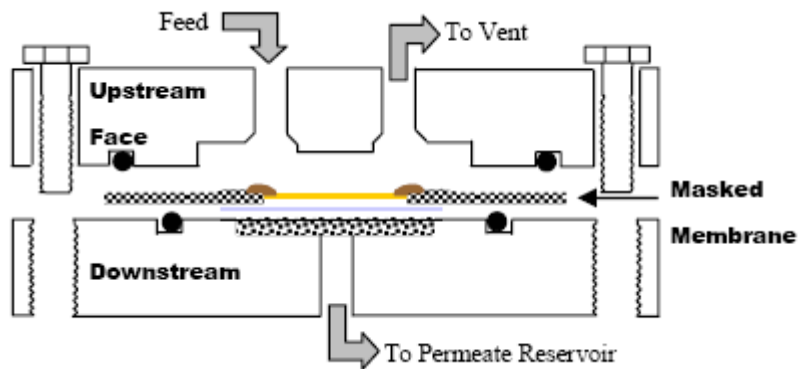


Figure 3.2: Schematic of a permeation cell. A cross section through the cell is shown with a “sandwich” type masked membrane. The membrane assembly is composed of: membrane, yellow; filter paper, light gray; epoxy, brown; adhesive backed aluminum, checkered. Bolts, shown at left and right, and o-rings, solid black circles, assure a leak tight seal [1].

After the cell is assembled it is connected to an isochoric permeation system, where intrinsic permeabilities can be obtained by monitoring the change in permeate pressure with time [2, 3]. The change in permeate pressure (dp/dt) at steady state is proportional to the flux, which when normalized by the membrane thickness and Δp , yields the permeability. A schematic showing the isochoric permeation system for dense film experiments is shown in Figure 3.3, where the cell in Figure 3.2 is represented as item 5.

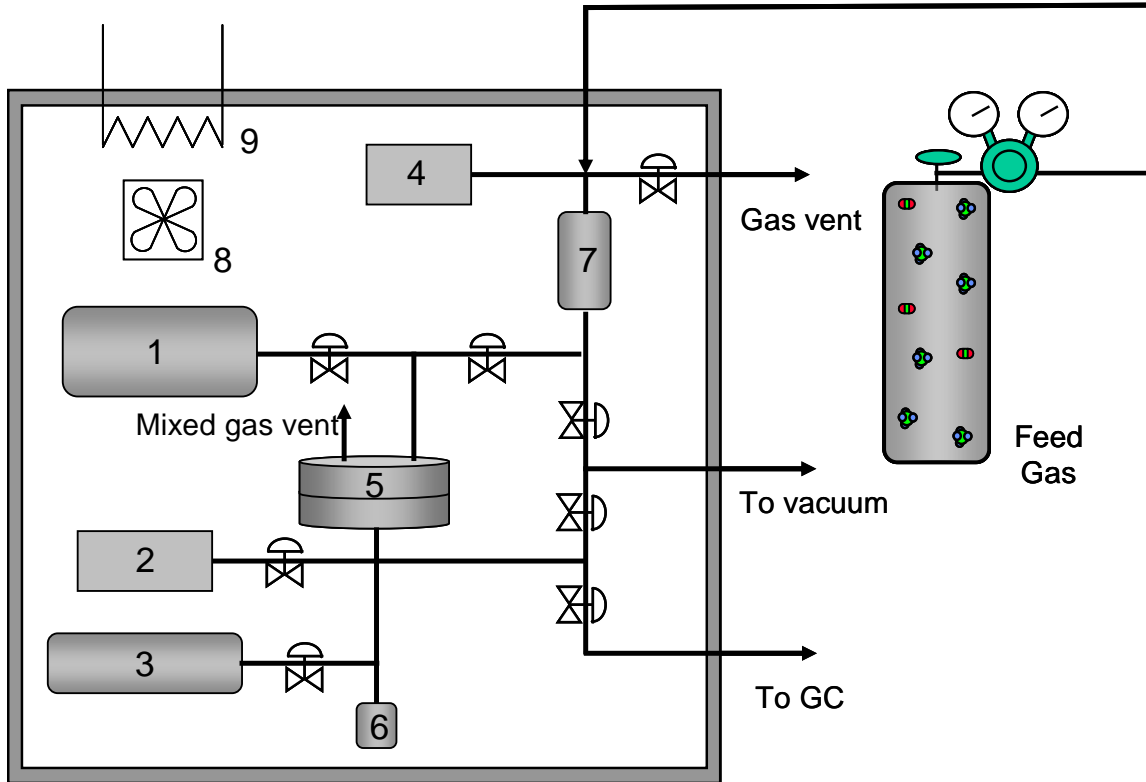


Figure 3.3: Isochoric (constant volume), variable pressure permeation system with dual upstream and downstream volumes. (1) Large (1000 cc) upstream reservoir; (2) Downstream pressure transducer; (3) Large (500 cc) downstream reservoir; (4) Upstream pressure gauge; (5) Permeation cell; (6) Small (10 cc) downstream reservoir; (7) Small (150 cc) upstream reservoir; (8) Fan; (9) Heat source (heat tape) with temperature control. Adapted from reference [4].

To obtain permeabilities from the constant volume, variable pressure permeation system, the following quantities can be used: slope of the permeate pressure vs. time (dp/dt) in torr/min; membrane thickness (l) in microns; downstream reservoir volume (V_R) in cm^3 ;

operating temperature (T) in Kelvin; and transmembrane pressure or fugacity difference (Δp or Δf) in psi, and can be plugged into equation 3.1 to obtain the permeability (P).

$$P = \frac{(1583 \times 10^3) \left(\frac{dp}{dt} \right) \cdot l \cdot V_R}{A \cdot T \cdot \Delta p} \quad (3.1)$$

In Equation 3.1, Permeability (P) is in the units of Barrer, defined below,

$$\text{Barrer} = 10^{-10} \frac{\text{cc(STP)} \cdot \text{cm}}{\text{cm}^2 \cdot \text{cmHg} \cdot \text{s}} \quad (3.2)$$

3.2.2 Asymmetric Hollow Fiber Permeation

3.2.2.1 Asymmetric Hollow Fiber Membrane Preparation: Spinning

An important criterion that must be met for industrial application of novel membrane materials is the ability to be formed into thin, low cost membranes that can be eventually packaged into high surface area modules [5]. Asymmetric hollow fibers are the preferred industrial standard for this because of the high surface area to volume ratios that are capable of being achieved, compared to other module configurations like the spiral wound and plate-in-frame types. Asymmetric hollow fiber membrane modules can have active surface area to volume ratios as high as 10,000 m²/m³ [6] and offer high productivities. This is due to the cylindrical geometry of the membrane and the ability to

reduce the actual separating layer to a thin “skin”, whereby the bulk of the membrane acts as the support. The support is a porous substructure that ideally has negligible resistance and lies underneath the outer skin layer, thereby providing the mechanical strength to the fiber. Figure 3.4 below shows the morphology of an ideal asymmetric hollow fiber membrane.

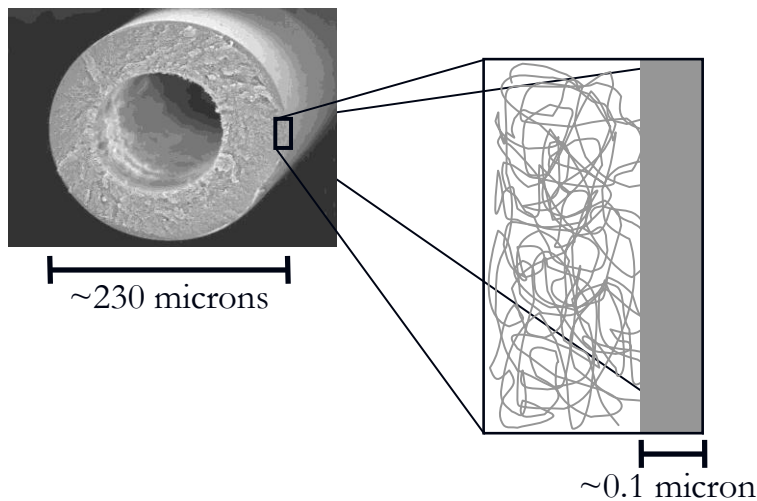


Figure 3.4: An asymmetric hollow fiber membrane with an outer selective skin layer on a porous support substructure

The process of making asymmetric hollow fiber membranes is called spinning. This occurs by co-extruding a polymer solution and a bore fluid through an annular die called a spinneret into an aqueous quench bath, where the polymer solution precipitates and is drawn up with a take-up device. The method of spinning used in this work is referred to as the dry jet/wet quench method [7-10] because the polymer solution passes

environmentally benign. Water and alcohols typically serve adequately for this requirement in most systems, because most of the polymers used for gas separations are hydrophobic. Aliphatic alcohols such as ethanol are commonly used as non-solvents, because they provide a greater window for use than water, which tends to be too strong a non-solvent. Additives such as lithium nitrate salts are sometimes used in dopes for various reasons such as viscosity enhancement, phase separation enhancement and pore formation [11, 12]. After a fiber is spun, it is usually dehydrated by exchanging with non-solvent fluids of decreasing surface tension before finally being dried. This fluid exchange is done to minimize capillary forces that would act on the fiber if dried directly from high surface tension fluids like water. These capillary forces may collapse the substructure of the fiber. More details on spinning will be addressed in Chapter 4 using the crosslinkable polymer used in this research.

3.2.2.2 Hollow Fiber Permeation

Hollow fibers used in this work were potted into modules according to the method described by Wallace [13], which is described in the Appendices. The modules contained fibers with active membrane lengths varying from ~ 10 cm to 20 cm, depending on the type of permeation experiment performed (pure or mixed gas). The number of fibers in a module was also chosen depending on the type of permeation to be performed. For instance, during pure gas permeation with the hollow fibers, as many as 40 fibers per module could be used; however, during mixed gas permeation the number of fibers is reduced to ~ 1 to 3 to reduce the membrane surface area for the experiments. A lower

surface area reduces the amount of gas that is vented off in the retentate stream since the stage cuts used are typically less than 1% during mixed gas permeation (see Section 3.1.3.2.3 for more information on mixed gas experimental set-up). The reasons for the low stage cuts are explained in Section 3.2.2.4. A figure showing a typical hollow fiber module is shown in Figure 3.6.

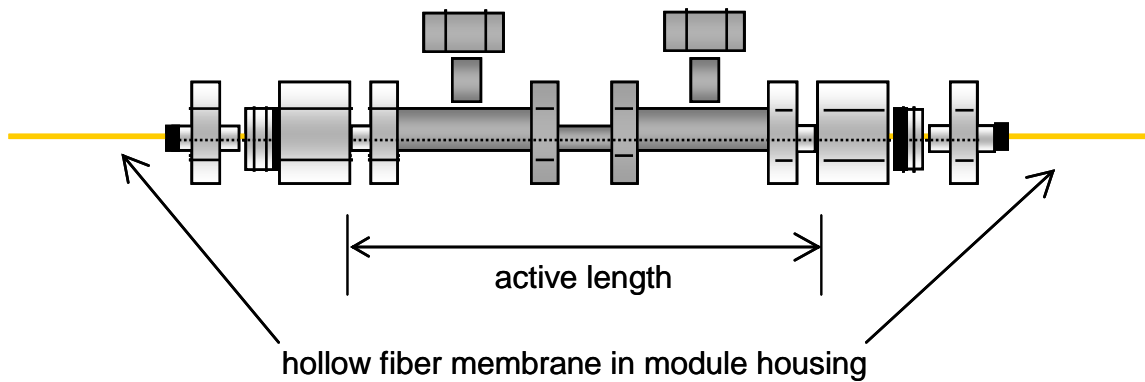


Figure 3.6: Schematic showing a hollow fiber membrane in a module housing, which interfaces the membrane with the permeation system.

3.2.2.2.1 Hollow Fiber Pure Gas Permeation

Pure gas permeation was carried out using a dead end, counter-current flow scheme with the feed on the bore side of the hollow fibers. Here, the entire feed stream permeates through the membrane and is collected only on the permeate side, the shell side, where the flow-rate can be measured using a bubble flow-meter. This configuration allows for multiple fiber modules to be tested head-on, with a common feed and under

the same test conditions. Thus, the permeance (P/l) can be obtained from multiple modules at the same time by measuring their individual volumetric flow-rates (v_p) in ml/sec; the operating temperature (T) in Kelvin; membrane area (A) in cm^2 ; the transmembrane pressure or fugacity difference (Δp or Δf) in psia, and using the following equation

$$\frac{P}{l} = 10^{-6} \cdot \frac{v_p \cdot 273.15}{5.17 \cdot A \cdot T \cdot \Delta p} \quad (3.3)$$

In Equation 3.3, permeance (P/l) is in the units of GPU, defined below,

$$GPU = 10^{-6} \frac{cc(STP)}{cm^2 \cdot cmHg \cdot s} \quad (3.4)$$

Figure 3.7 shows a schematic of the pure gas permeation set-up for asymmetric hollow fibers. In the figure, six modules are connected to the feed.

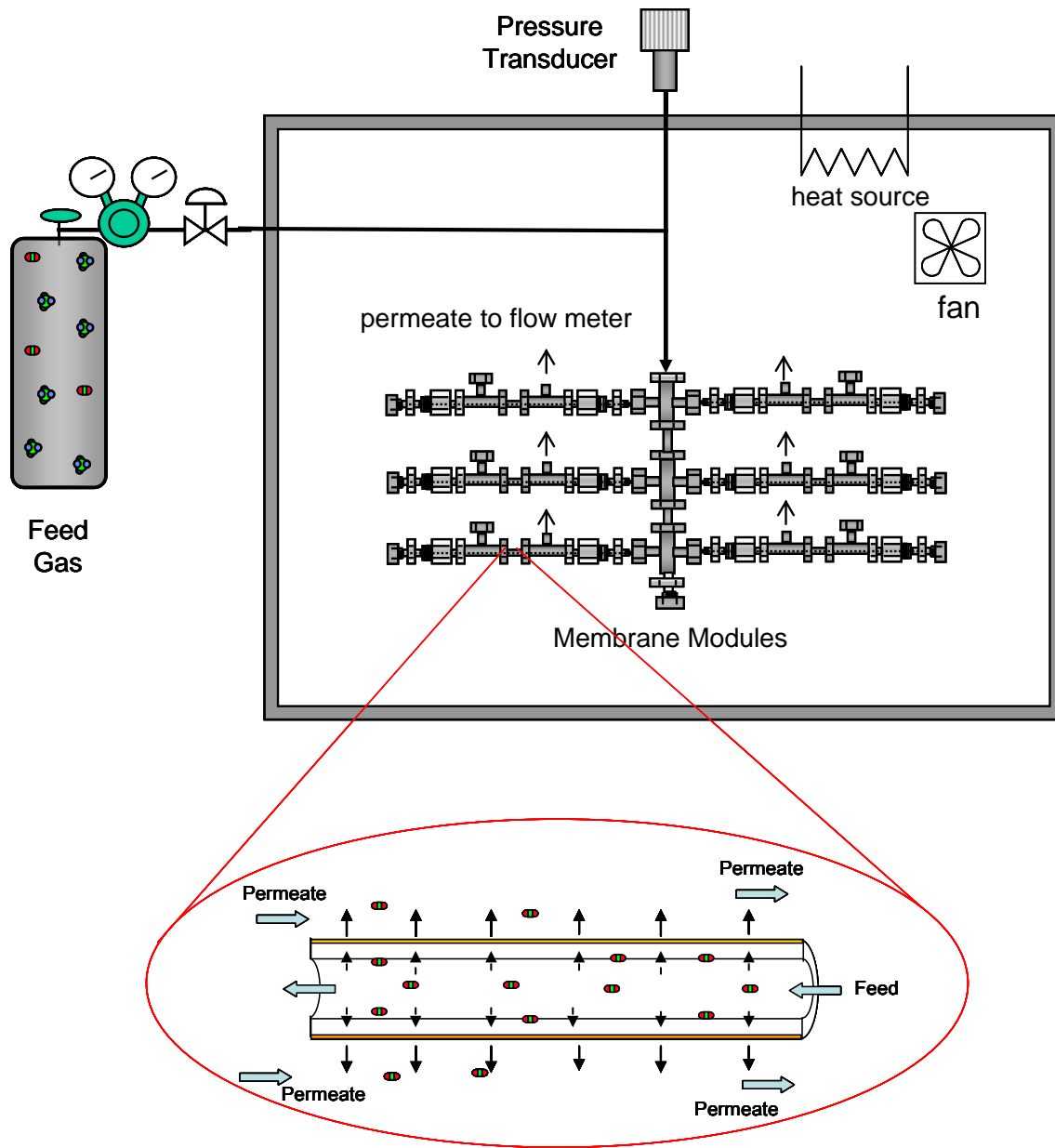


Figure 3.7: Schematic showing a variable volume system with the permeate stream at atmospheric pressure, set up for pure gas permeation experiments.

3.2.2.2.2 Hollow Fiber Mixed Gas Permeation

Mixed gas permeation experiments were carried out using a counter-current flow scheme with the feed on the shell side of the hollow fibers. In this case, the feed stream flows over the surface of the membrane and the permeate flux is controlled by a needle valve on the retentate side. The percentage of the feed that permeate through the membrane is called the stage cut. In determining intrinsic membrane properties, stage-cuts less than 1% were used to minimize concentration polarization (see Chapter 4) and to minimize feed composition variation, as the membrane selectively permeates the penetrants along the module. The permeate stream, collected on the bore side, is measured with a bubble flow-meter to determine the flux and can also be sent to a GC to analyze the compositions. The permeances can be obtained by measuring the following quantities: volumetric flow-rate of permeate (v_p) in ml/sec; mole fraction of component i in permeate (y_i); mole fraction of component i in the upstream (x_i), which is essentially equal to the mole fraction of i in the feed at low stage cuts; the operating temperature (T) in Kelvin; membrane active area (A) in cm^2 ; feed and permeate pressures (p_x) and (p_y) respectively, in psia; and fugacity coefficients of component i in the upstream and permeate streams (ϕ_{xi}) and (ϕ_{yi}) respectively; and using the following equation

$$\frac{P_i}{l} = 10^{-6} \cdot \frac{v_p \cdot y_i \cdot 273.15}{5.17 \cdot A \cdot T \cdot (\phi_y \cdot \phi_{xi} \cdot x_i - p_y \cdot \phi_{yi} \cdot y_i)} \quad (3.5)$$

In Equation 3.5, permeance (P/l) is in the units of GPU. A schematic showing the mixed gas permeation set-up used in this work is shown in Figure 3.8

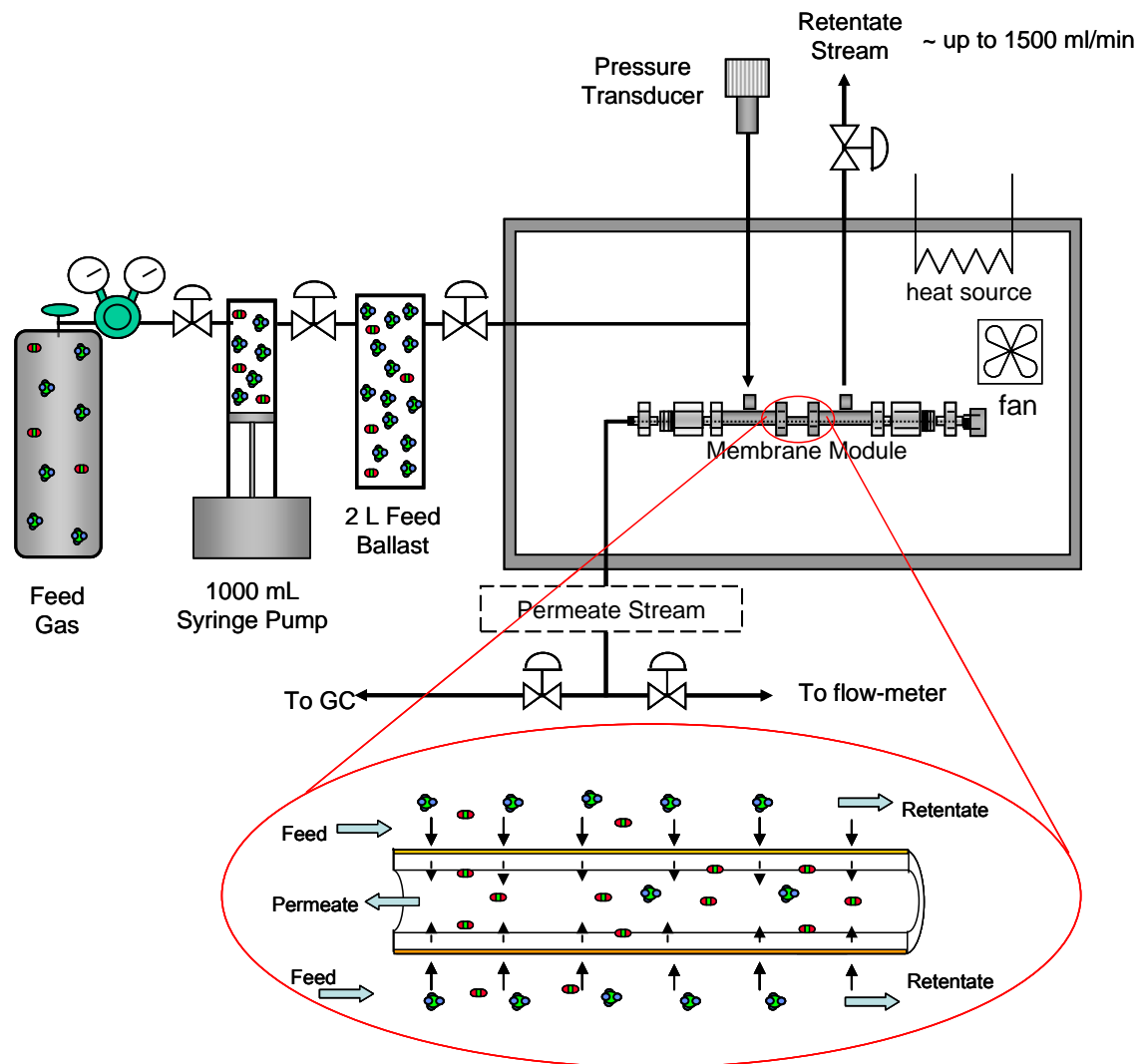


Figure 3.8: Schematic showing a variable volume system with the permeate stream at atmospheric pressure, set up for mixed gas permeation experiments. The syringe pump was used when the pressure in the feed gas cylinder was below the desired membrane feed pressure.

In Figure 3.8, the extra volume (2 L feed ballast) was used to facilitate setting and maintaining the feed pressure at a high value, especially for cases where the feed gas cylinders come at low starting pressures from the supplier. For instance, if a feed pressure

of 1000 psi was needed, the 2 L ballast will be pressurized to 1500 psi, so that as the piston is lowered to the bottom, the entire upstream would be at 1000 psi, with the piston completely lowered. The Isco® syringe pump can be set to maintain the upstream at a constant pressure. When the piston reaches the top of the syringe pump cylinder, the gas in the ballast is enough to maintain the upstream at a fairly constant pressure while the feed is recompressed.

3.2.3 Sorption

3.2.3.1 Pressure Decay Method

Gas sorption measurements were made using a pressure decay method, whereby the equilibrium sorbed concentration at a given pressure can be used to calculate the solubility coefficient. Before experiments, the system is evacuated for ~ 24 hrs. The method involves pressurizing a feed reservoir of known volume with a certain amount of gas and allowing the system to equilibrate thermally for ~24 hrs. The whole system is kept in a heated water bath with a circulator to maintain a constant temperature. A schematic depicting the system for the pressure decay is shown in Figure 3.9.

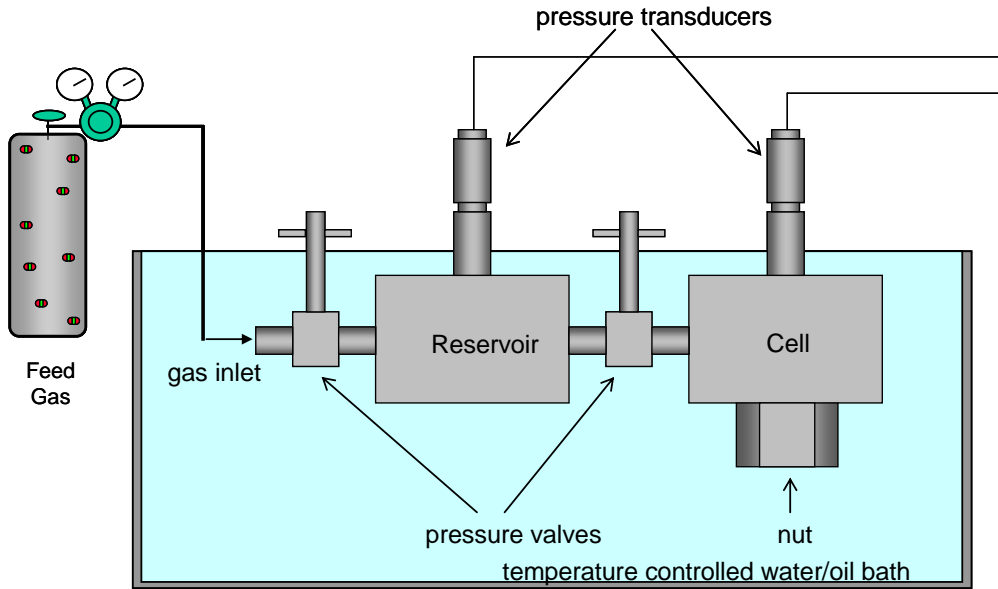


Figure 3.9: Pressure decay sorption apparatus used for gas sorption experiments.

The pressure valve between the feed reservoir and the cell (sample cell) is opened for a brief moment (~ 3 seconds) and then closed in order to introduce a dose of the feed gas into the cell. The pressure in both chambers is monitored via pressure transducers, attached to both chambers. The pressure in the cell will decay progressively indicating gas sorption into the sample in the cell. A mole balance can then be used to compute the amount of gas sorbed into the polymer at equilibrium, n_p , by obtaining the following quantities: system temperature, T ; ideal gas constant, R ; volume of sample cell, V_C ; volume of polymer sample, V_P ; volume of reservoir, V_R ; initial pressure of sample cell, $p_{C,I}$; final pressure of sample cell, $p_{C,F}$; initial pressure of reservoir, $p_{R,I}$; final pressure of

reservoir, $p_{R,F}$; compressibility factor for the gas at the pressures used, z . The mole balance is shown below in Equation 3.6.

$$n_P = \frac{1}{R \cdot T} \cdot \left[V_C - V_P \cdot \left(\frac{P_{C,I}}{z \phi_{C,I}} - \frac{P_{C,F}}{z \phi_{C,F}} \right) + V_R \cdot \left(\frac{P_{R,I}}{z \phi_{R,I}} - \frac{P_{R,F}}{z \phi_{R,F}} \right) \right] \quad (3.6)$$

The compressibility factors can be obtained from NISTL and are used to correct for gas phase non-idealities, which become important at higher pressures especially with the more condensable gases like CO₂.

3.2.3.2 Quartz-spring Sorption Method

Vapor sorption measurements can be made using a quartz-spring method, also known as a McBain balance. A schematic showing this system is shown in Figure 3.10.

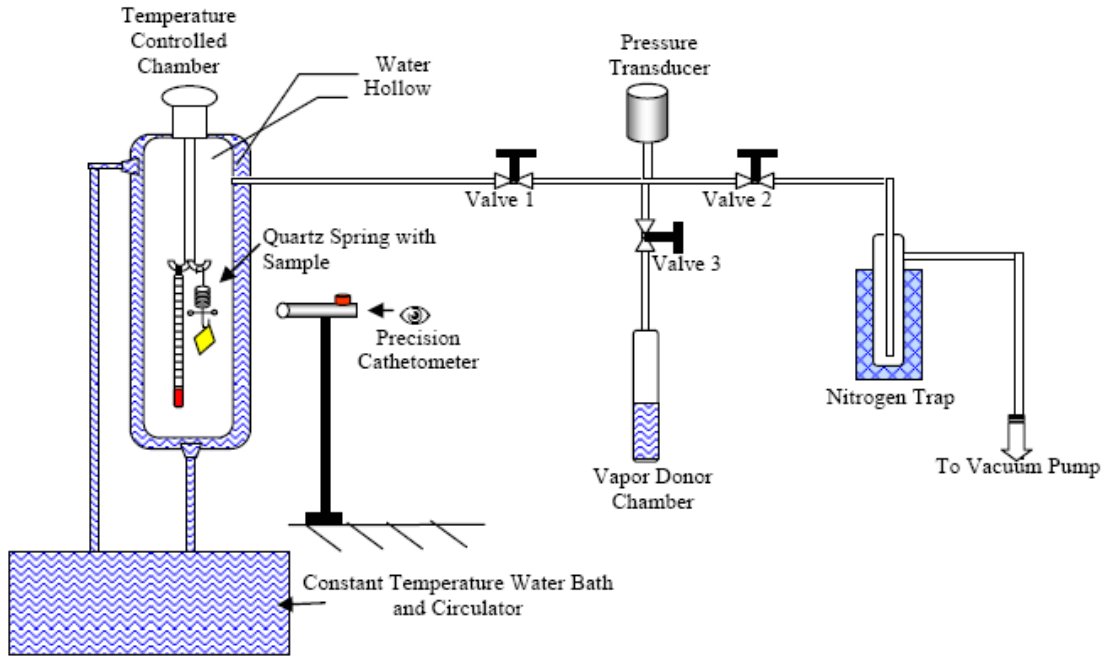


Figure 3.10: Quartz spring sorption apparatus used for vapor sorption experiments.

First the entire system is evacuated by pulling vacuum. The system leak rate can be determined by shutting valve 2 and monitoring the pressure rise with time. The sample chamber is isolated by shutting valve 1. The solvent can then be added to the donor chamber connected to a valve (valve 3). At this point, the head space of the vapor donor chamber is evacuated to remove air entrapped during the solvent addition. After this, the vapor donor chamber is isolated by closing valve 3 and the sample chamber is evacuated again, preparing the system for the vapor sorption experiment while thermal equilibrium is reached. To start the experiment, the vacuum valve (valve 2) is shut off, and the vapor can be introduced to the system by monitoring the system pressure as valve 3 is opened and closed. The amount of vapor sorbed at the equilibrium pressure is correlated, using Hooke's law, to the extension of the spring, which can be recorded using a cathetometer.

3.2.4 Scanning Electron Microscopy (SEM)

Scanning electron micrographs were obtained by first cryogenically fracturing the fibers in liquid nitrogen. Most times, fibers were soaked in hexane prior to fracturing in liquid nitrogen. This helped to freeze the fibers and ensure a smooth cut. The machine used in this work was a LEO 1530 thermally assisted field emission (TFE) scanning electron microscope.

3.2.5 Gel Permeation Chromatography (GPC)

Molecular weights of polymer batches were obtained by dissolving the polymer in solvents (mostly THF or DMF) at ~ 4wt%. The samples are usually filtered before analysis. Most times the molecular weights were determined by sending to the American

Polymer Standards Corporation, Mentor Ohio. The method used is described under ASTM D5296-05.

3.2.6 Fourier Transform Infra-red Spectroscopy (FTIR)

The FTIR in this work was done using a Bruker Tensor 27 FTIR spectrometer. Samples were analyzed using a Harrick MVP₂ micro ATR with at least 128 scans at a resolution of 2cm⁻¹.

3.2.7 Nuclear Magnetic Resonance Spectroscopy (NMR)

¹H NMR experiments were done in solution. The solution NMR studies were performed by dissolving samples in deuterated Dimethyl Sulfoxide (DMSO) at ~2.5wt%. The solutions were analyzed using a Varian Mercury Vx 300 spectrometer. ¹³C NMR experiments were done in solid state using a Bruker DSX 300 with the following specifications: 7 mm MAS rotor, 300 MHz ¹H, pulse sequence: CP-MAS with TOSS to suppress spinning side bands, spinning speed: 5 kHz, repetition delay of 4 s, contact time of 1 ms, 90 degree pulse length: 5 microseconds, number of scans: 10K.

3.3 Materials

The materials in this work were synthesized in the laboratory. Effects of the polymer on transport properties were important in the selection process and the synthesis conditions were modified to develop the material for spinning. The material of choice was PDMC (3:2), which stands for propane-diol monoesterified crosslinkable polyimide. Two variants of this polymer were made in this work. The first was based on the 6FDA-

DAM:DABA (3:2) backbone, following the dense film work done by Hillock et al. [14] and the other had a backbone consisting of 6FDA-mPDA:DABA (3:2), where the DAM monomer unit was replaced with mPDA. The structures of these two polyimides are shown in Figure 3.11 below.

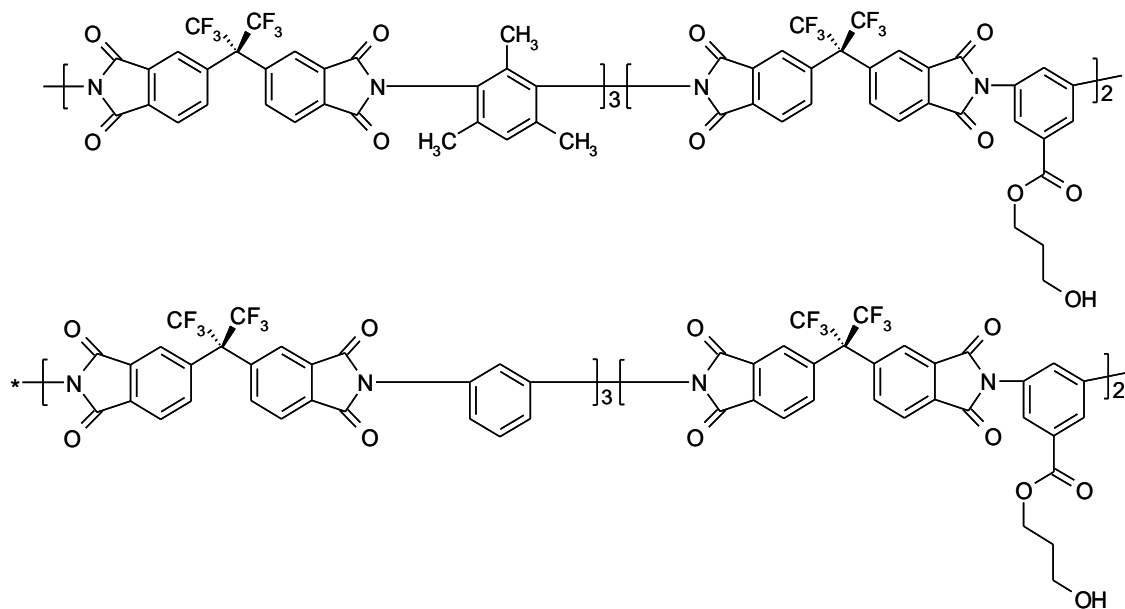


Figure 3.11: A schematic showing two PDMC (3:2) variants with two different backbone structures: 6FDA-DAM:DABA (3:2) (top) and 6FDA-mPDA:DABA (3:2)

The transport properties of the two PDMC (3:2) variants are not surprisingly very different. The DAM monomer is a more permeable monomer unit compared to the mPDA monomer, due to the disruption in chain packing from the bulky methyl groups. The productivity and separation capability of these two polymers are plotted on the famous Robeson's upper bound plot shown in Figure 3.12, which demonstrates the

tradeoff between permeability and selectivity for the CO₂/CH₄ pair using various polymers [15].

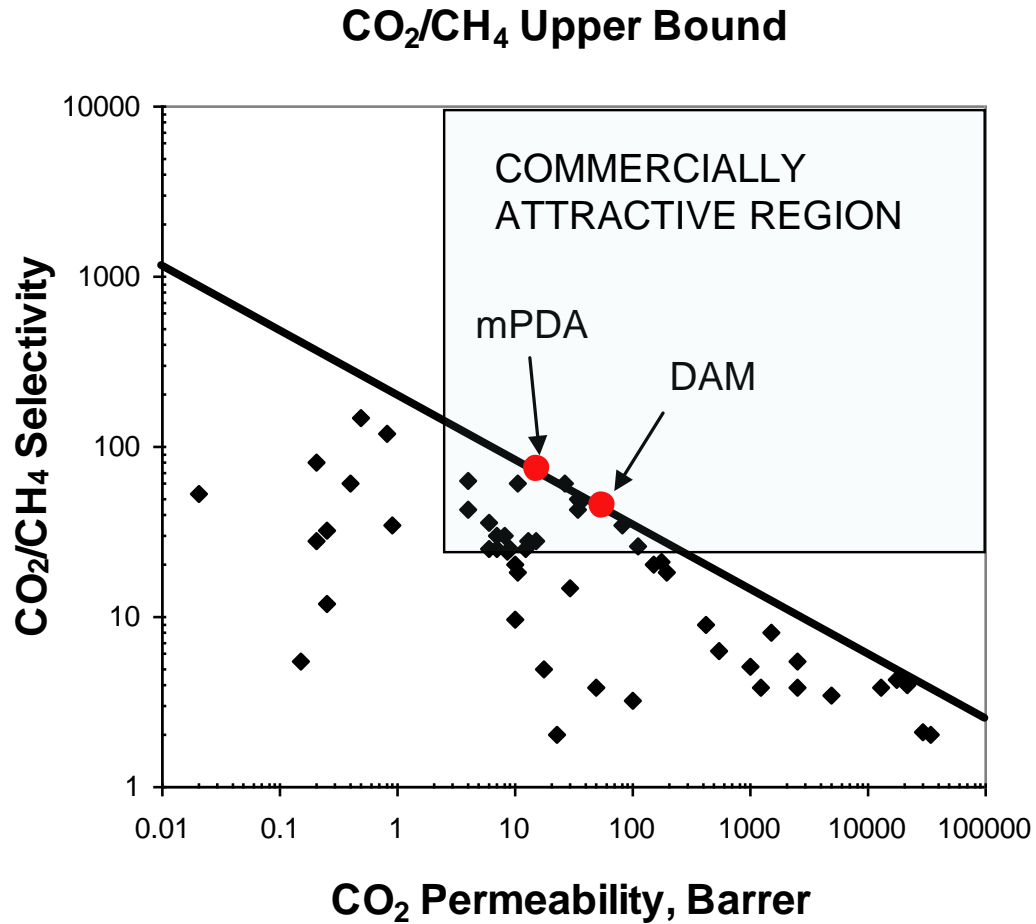


Figure 3.12: Robeson’s 1991 upper bound showing the tradeoff between permeability and selectivity using different polymers (black dots) [15], along with the permeability and selectivity values for the two PDMC (3:2) variants: using “DAM” prepared and measured by Hillock using a 10/90 CO₂/CH₄ feed at 65 psia, 35 °C [14], and using “mPDA” made and measured in this work and tested under the same conditions.

From Figure 3.12, it can be observed that there is a significant difference in the permeabilities (DAM: 58 Barrers and mPDA: 16 Barrers) and selectivities (DAM: 45 and mPDA: 72) of both polymers. Even though the permeability of the DAM variant is much higher, its selectivity is reduced. However, for practical application of these membranes for natural gas feeds, a permselectivity of 40 is considered high performance from a design perspective [16] and from the conversations with industrial collaborators. Translating these intrinsic polymer performance values into useful defect-free asymmetric membranes in highly productive hollow fiber forms is the foremost objective. Moreover, a more permeable material would be advantageous in increasing the productivity of smaller membrane modules, which are preferred especially in offshore applications where the size and weight of the membrane module are of great concern.

3.3.1 Polymer Synthesis

The crosslinkable polyimide synthesis starts with synthesizing the chosen polyimide backbone, namely 6FDA-DAM:DABA (3:2), via a polycondensation reaction by addition of the dianhydride, 4, 4'-(hexafluoroisopropylidene) diphthalic anhydride (6FDA), and diamines, 2,4,6-trimethyl-1,3-diaminobenzene (DAM) and 3,5-diaminobenzoic acid (DABA), in solution. The 6FDA and DAM monomers were purified by sublimation prior to use. The DAM monomer usually had more impurities extracted from it through the sublimation, but removal of the impurities was important for synthesis. In general, monomer sublimation enabled higher molecular weights and lower

polydispersities. Figure 3.13 below shows a picture of the sublimed monomers used in this work.

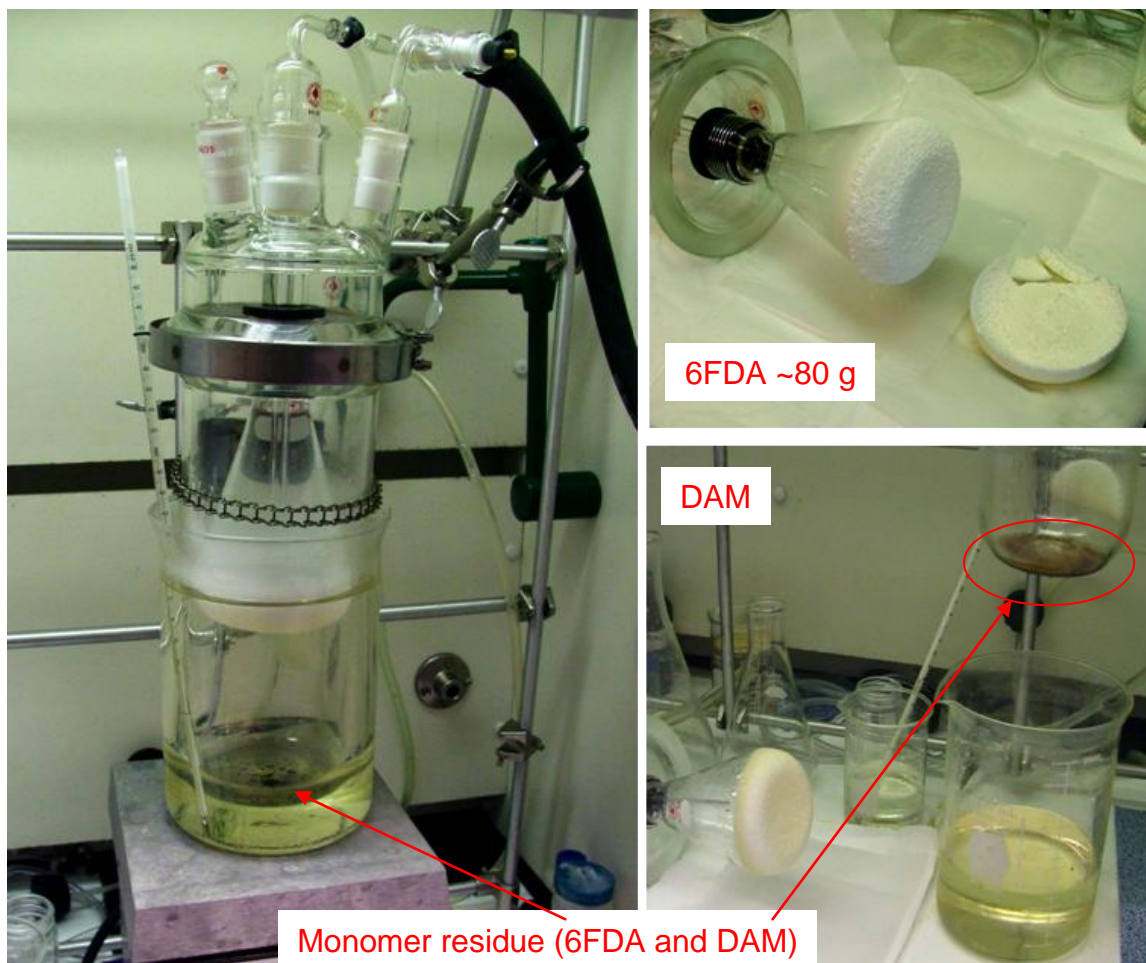


Figure 3.13: Pictures of the sublimation set-up and sublimed monomers used in this work.

The DABA monomer was used as received at 99.9% purity. The solvent used is n-methylpyrrolidone (NMP). In this study, the ratio of DAM to DABA is 3:2, which

translates to a 40% DABA content of the diamines. The reaction stoichiometry can be adjusted to change the DABA content and thus the crosslink density since the DABA monomer is the site for crosslinking, but doing so has subsequent effects on processing. For instance, higher DABA contents make the polymer more hydrophilic, thereby increasing the time for a solution made from the polymer to phase separate in an aqueous medium such as the quench bath during fiber spinning. The polycondensation reaction is very sensitive to water and care must be taken to ensure that there is minimal exposure to moisture. The solvent typically used is n-methylpyrrolidone (NMP). The solids concentration of the reactants in solution is about 20 wt% during the polymerization reaction. The reaction produces polyamic acid, the precursor to the polyimide and is characterized by the presence of amide and carboxylic acid groups on the chain.

3.3.2 Imidization

Imidization involves dehydration of the polyamic acid to form a cyclic polyimide. Studies showed that the polyamic acid could degrade over time if not imidized. In this study, this was noticed after ~2 days of leaving the polyamic acid unimidized, after which a drop in viscosity was noticed signifying a loss in molecular weight. Most commonly, imidization reactions are usually carried out chemically or thermally. Chemical imidization usually occurs at relatively lower temperatures and involves the use of an imidization catalyst and a chemical dehydrating agent since the temperatures are not high enough to effectively remove the water thermally. Common imidization catalysts used in this method are triethyl amine (TEA) and pyridine. A common dehydrating agent is acetic anhydride. The presence of a dehydrating agent helps reduce the possibility of

hydrolytic degradation that could decrease reactivity of the anhydride and thus lower the molecular weight; and at worst, may even cause chain scissioning. Also, although the chemical imidization technique offers the advantage of using lower temperatures, which is favorable for scale-up and prevention of unwanted thermally activated side reactions, it is prone to the formation of isoimides [17, 18]. However, these isoimides may eventually be converted to imides by heating the polymer at high temperatures but this undermines the advantage of using the low temperature imidization approach and adds an additional processing step. Furthermore, the chemical imidization approach is generally not preferred industrially due to issues associated with handling the reagents. It is also believed that complete imidization may not be achieved during chemical imidization since the reduced temperatures do not promote the chain mobility necessary for achieving complete imidization. However, this fact is hard to prove since the trace amic acid groups are hard to detect analytically at such low levels. It is preferred that almost complete imidization is achieved since the polyimide is subjected to a subsequent reaction during the synthesis of these crosslinkable polymers.

Thermal imidization occurs primarily by heating the reaction solution to a high temperature (~180 °C). The polymer used in this research are still soluble after imidization, thus the imidization is carried out in solution. This enables high levels of chain mobility and enhances imidization degrees when enough thermal energy is put in. However, there is the tendency to form crosslinks between the polymer or oligomer chains at high temperatures, which could affect solubility and processing. An advantage of this approach is that even though the water produced by the reaction is not chemically scavenged, the heating dehydrates the solution. A hydrolyzed anhydride would form less

reactive di-acids, but these may be recycled thermally and made more reactive. This makes this method a “brute force” approach. It has been observed that molecular weight build-up may occur even after 18 hrs of thermal imidization, where the molecular weight (M_w) rose from ~92,000 (at 18 hrs) to 103,000 (at 26 hrs). In this work, imidization temperatures between 180 °C and 200 °C are preferred. Figure 3.14 below shows the effects of temperature on the degree of imidization in a thermal imidization reaction.

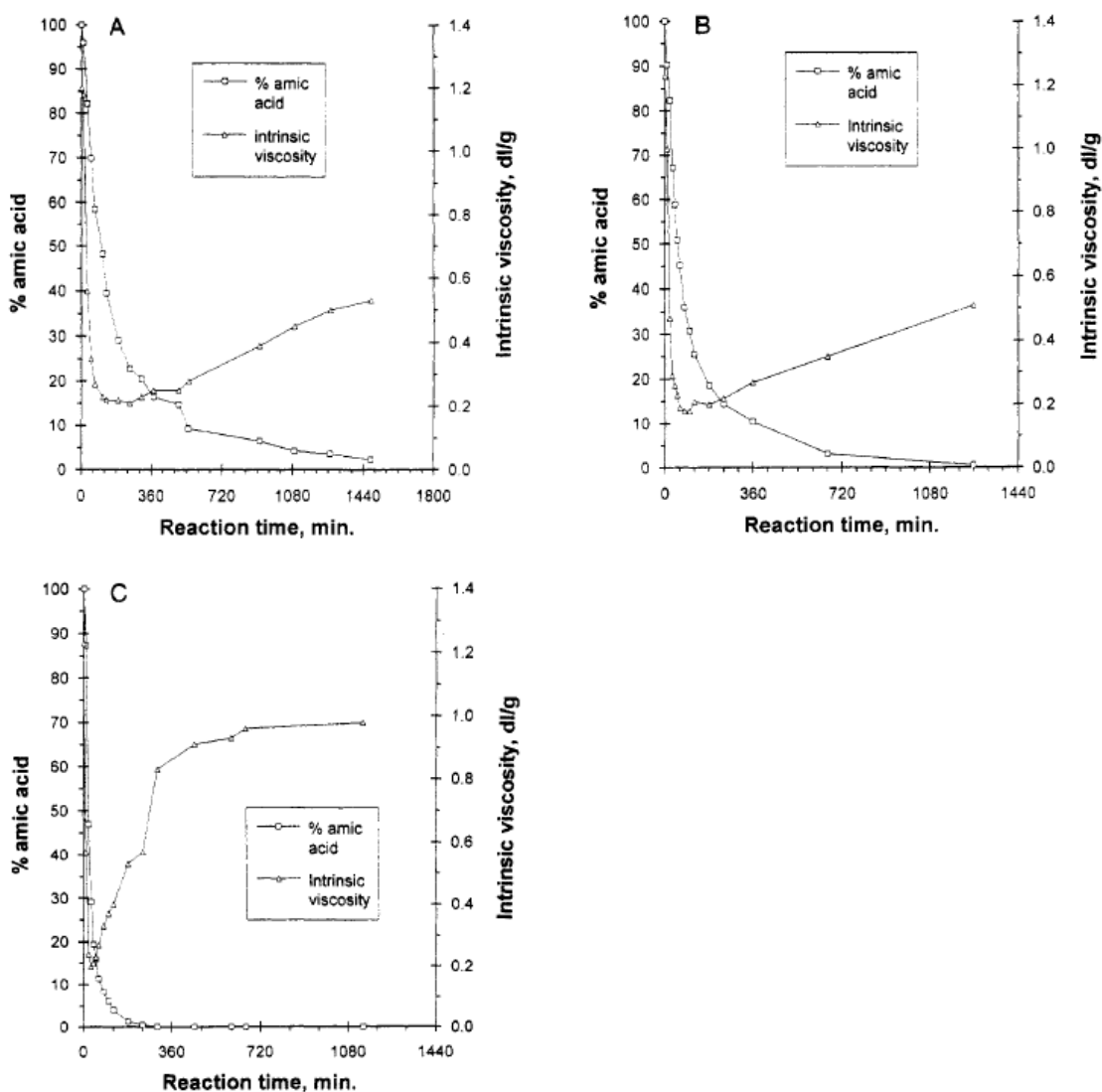


Figure 3.14: Effect of imidization temperature and time on intrinsic viscosity and residual % amic acid. Adapted from reference [19].

The polyimide is formed from the precursor polyamic acid by heating up the reaction solution to form the imide rings on the polyimide, essentially dehydrating the polyamic acid. An azeotropic drying agent such as ortho-dichlorobenzene (*o*-DCB) is used to aid in the removal of water formed from the reaction, thus driving the reaction forward. Here, ~2.5 ml *o*-DCB per gram of polymer was used for imidization. Typically, the polyimide is precipitated and dried at 100 to 120 °C under vacuum prior to further processing. However, as will be discussed in Section 3.3.5, precipitation here is not necessary. The solids concentration of the polymer in solution is about 13 wt% during imidization. The 6FDA, DAM and DABA monomers and the reaction sequence are shown in Figure 3.15.

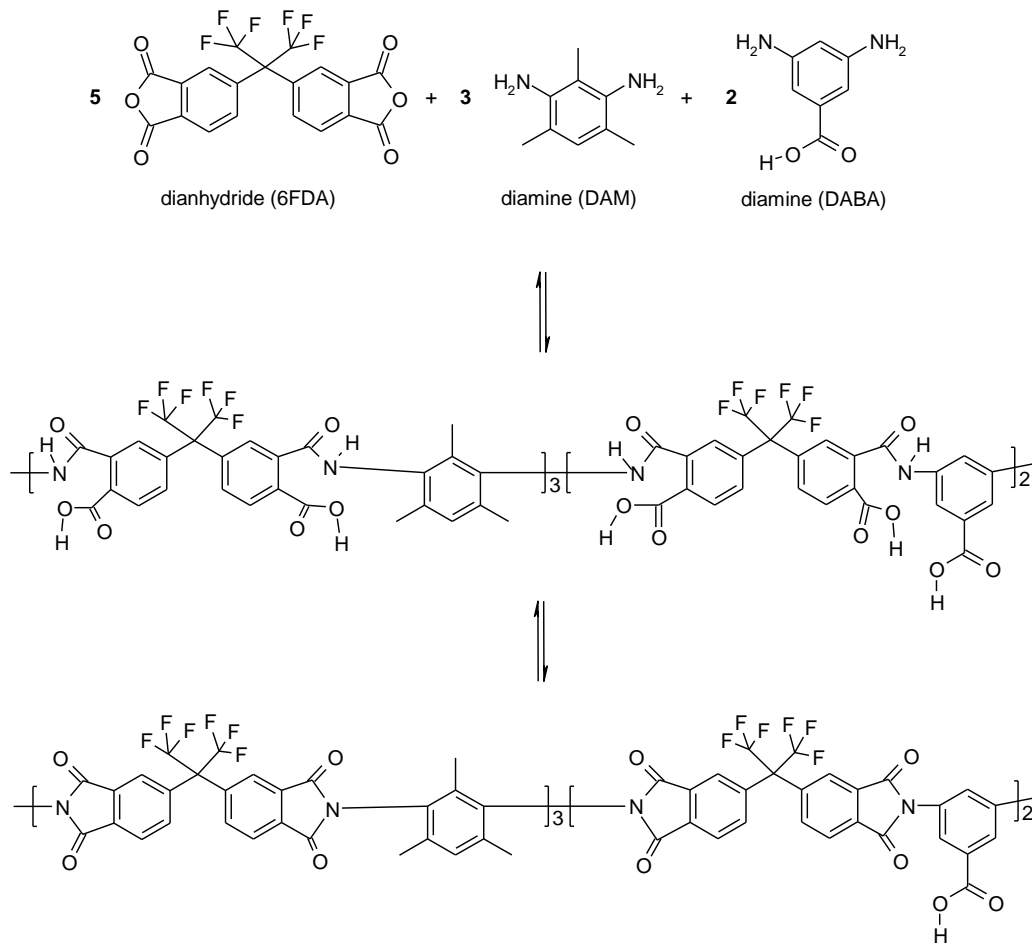


Figure 3.15: Synthesis steps for 6FDA-DAM:DABA (3:2) polyimide.

3.3.3 Crosslinking

The crosslinking method pursued here occurs in two steps: (1) the creation of a monoester “crosslinkable” polyimide, which can be processed in solution into a membrane form, and (2) transesterification/crosslinking, which occurs in the solid state

of the formed membrane. This eliminates the need to react the diol crosslinking agent with the polymer membrane in the solid state, which would require excessively swelling the membrane and may create defects in the membrane. This method also allows the process to be conveniently retrofitted into current membrane formation processes with a simple aqueous quench bath, with the crosslinking step taking place during final membrane drying.

3.3.3.1 Monoesterification

Once the polyimide is made, a monoesterification reaction is performed in solution, to form the crosslinkable polyimide. This is done by adding the crosslinking agent, 1,3-propanediol (40 – 70× stoichiometric amount), to the polyimide solution at about 140 °C for up to 18 to 24 hrs. The 1,3-propanediol molecules react with the pendant carboxylic acid group on the DABA moiety and give off water as the by-product. The water produced is about 0.8% of the reaction solution, and the diol used is 40 – 70 times the molar amount of water produced. This is done in order to enable high conversions of the DABA groups to esters without the need to apply excessive amounts of heat, which might crosslink the polymer and render it insoluble and unable to process. High ester yields are necessary for achieving high crosslinking degrees. Esterification reactions are acid catalyzed, [20] and the amount of catalyst added is a crucial factor as discussed in Section 3.3.4. 5 mg of para-toluenesulfonic acid (p-TSA) per gram of polymer has been used in earlier synthesis of these crosslinkable polyimides [13, 21-24]. As noted earlier, the final crosslinkable polyimide obtained from the reaction of 1,3-propanediol with the 6FDA-DAM:DABA (3:2) polyimide has been named “PDMC (3:2)”, which stands for

1,3-propanediol monoesterified crosslinkable polyimide (3:2). The monoesterification reaction can be monitored via the ester yields, which can be done using solution ^1H NMR as described elsewhere [21]. The monoesterification reaction is shown in Figure 3.16.

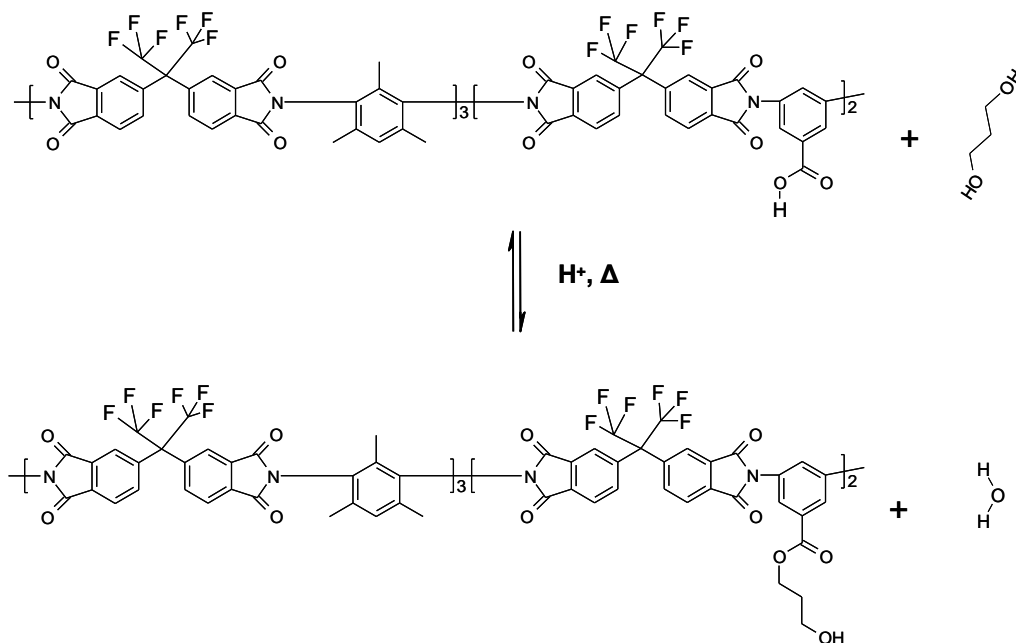


Figure 3.16: Monoesterification reaction for synthesizing 1,3-propanediol monoesterified crosslinkable (PDMC) polyimide (3:2).

The monoesterified polymer is usually precipitated by pouring the reaction solution slowly into a large bath containing equal volumes of methanol and water. The methanol/water bath should be large enough that the polymer synthesis solvents are mostly removed and the polymer is precipitated into fibrous solid. The fibrous solid can be homogenized into small particles using a blender to increase the surface area for

washing and drying of the polymer. The homogenized polymer powders can be washed continuously with the water/methanol bath and then filtered with an aspirator. During these washing steps, low molecular weight oligomers would be extracted forming an opaque filtrate. The polymer can then be air dried for ~ 24 hrs to remove the bulk of the water and then dried in a vacuum oven at 70 °C for ~ 24 hrs. The PDMC (3:2) polyimide can be subsequently made into the desired membrane form i.e. a dense film or hollow fiber membrane, since the material is still soluble in common solvents.

3.3.3.2 Transesterification

Once a membrane is made from the material, crosslinking is carried out by simply heating the membrane in the solid state at temperatures above ~150 °C under vacuum or an inert sweep gas to activate a transesterification reaction. Here, the pendant alcohol on one ester reacts with another ester to form a crosslink (see Figure 3.17 for a depiction of the transesterification/crosslinking between two polymer chain segments). Esterification reactions are reversible, and the reaction can be pushed to the formation of the crosslinks by pulling vacuum or by using an inert sweep gas to take off the reaction by-product, since there isn't an excess of reactants in this case as there are during monoesterification. In theory, one 1,3-propanediol molecule is evolved to form one crosslink, assuming the monoesterification reaction goes to completion. In the case that the monoesterification reaction does not go to completion, the unconverted DABA groups are still capable of reacting with the alcohol on a pendant ester of a converted DABA group, thus giving off a water molecule instead of the diol. This enables a high degree of crosslinking as long as reasonably high (>60%) ester yields are obtained and adequate activation energy for

crosslinking is reached. However, it is preferred that an ester yield of ~90% or above is obtained. Once crosslinking occurs, the material becomes insoluble and more resistant to swelling by feed components that undermine intrinsic selectivity.

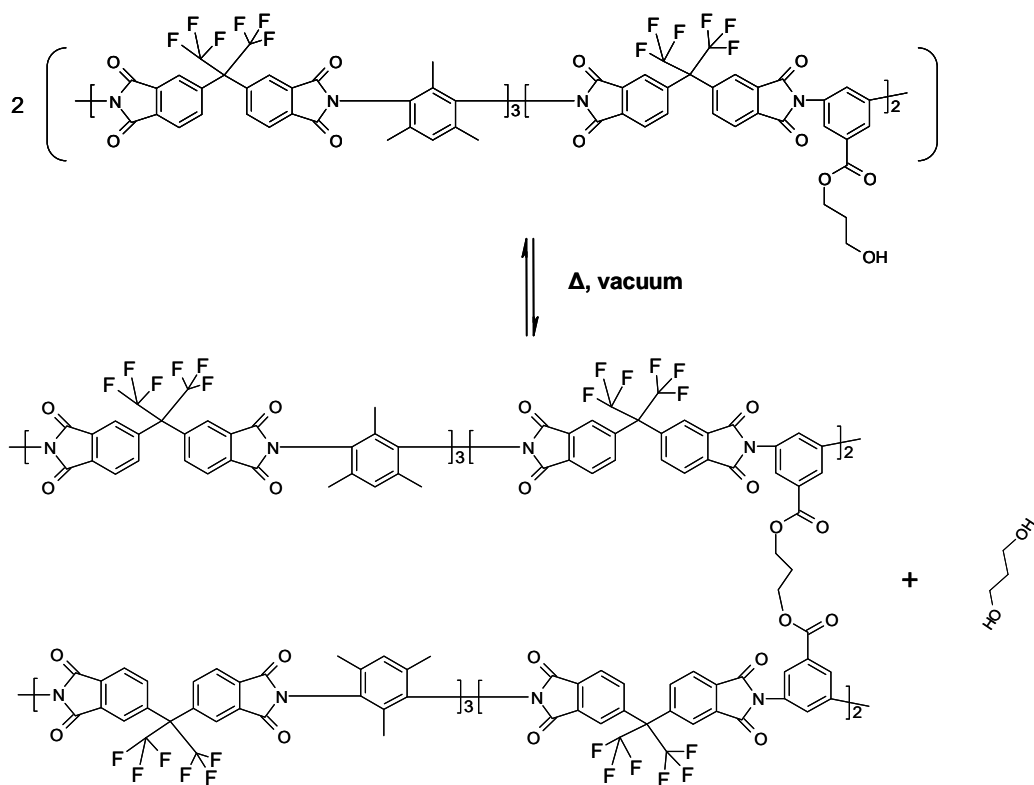


Figure 3.17: Crosslinking/transesterification reaction between two PDMC (3:2) polyimide chain segments.

3.3.4 Monoesterification effects on polymer

In conventional monoesterification reactions for making the crosslinkable monoester polyimide, the importance of extremely rigorous dehydration of the reaction

solution as the esters are formed was not stressed. This is partly because the monoesterification reaction occurs with an excess of the reactant diol, which drives the reaction forward to the formation of the ester product. Using conventional techniques, it was found that weight average molecular weights drop to as low as 30% of the original unesterified polyimide. The crosslinkable monoesters made from the conventional technique were typically about 20,000 to 40,000 (Mw) [13, 25]. This caused films made from the polymer to be very brittle before and even after crosslinking, presumably due to dangling uncrosslinked chain ends. These uncrosslinked chain ends are defects in the ultimate crosslinked network resulting from shorter chains in the lower molecular weight polymer. Figure 3.18 depicts a crosslinked network from a lower molecular weight polymer and a higher molecular weight polymer.

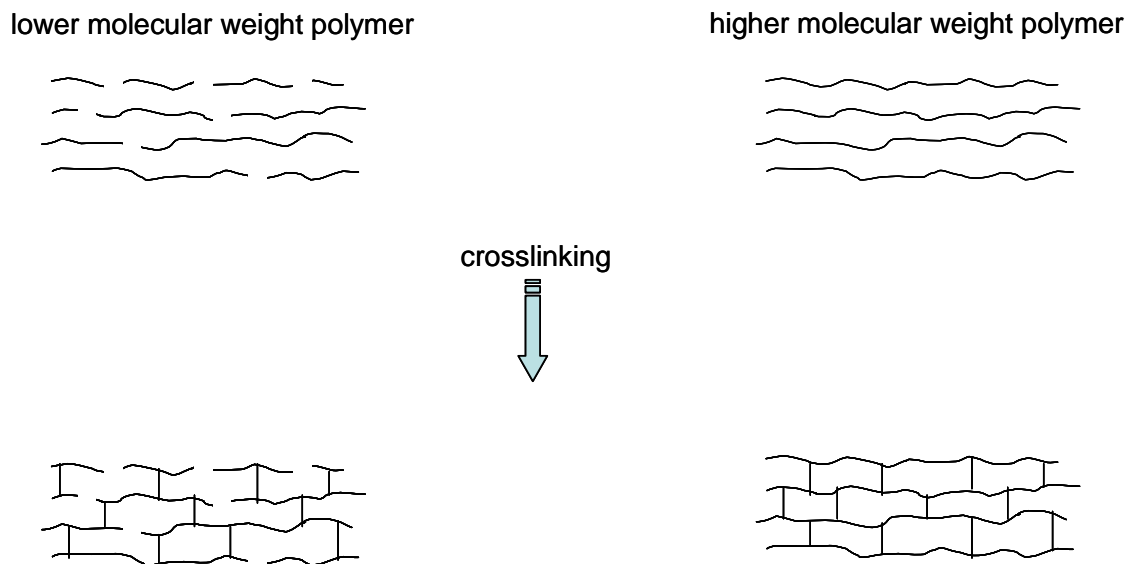


Figure 3.18: Schematic showing an irregular crosslinked network from a lower molecular weight backbone (left) and an improved network from a higher molecular weight backbone (right).

Moreover, solutions made from the lower molecular weight crosslinkable polyimide were relatively low in viscosity and hard to process into hollow fibers by solution spinning. Solution ^1H NMR was carried out on the low molecular weight crosslinkable monoester polyimides to characterize the ester yields by the method described by Wind et al. [21]. Typical “apparent ester yields” were close to 200%. The reason for the unusually high ester yields is explained in the next paragraph. A ^1H NMR spectrum from a low molecular weight monoester polyimide is shown in Figure 3.19, where the ester yield is about 160%.

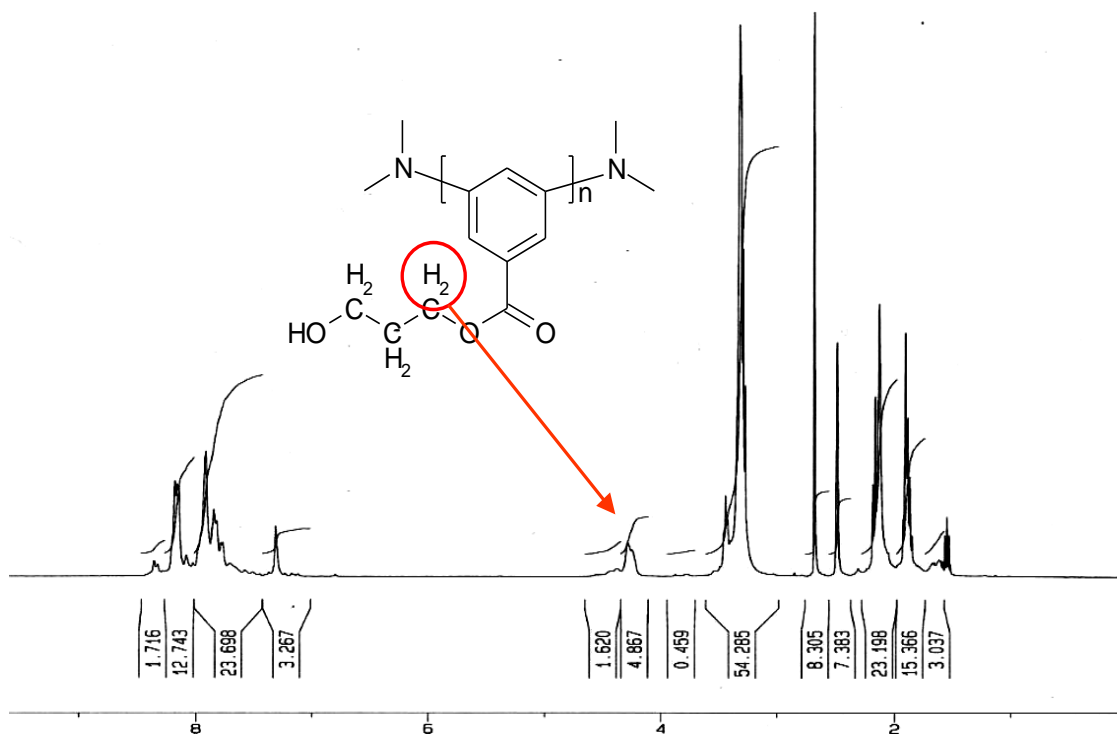


Figure 3.19: Solution ^1H NMR spectra of a PDMC (3:2) polyimide that experienced molecular weight loss.

From the unusually high ester yields and the huge drops in molecular weights, it was postulated that hydrolytic degradation was occurring at the imide rings as illustrated in the reaction sequence in Figure 3.20.

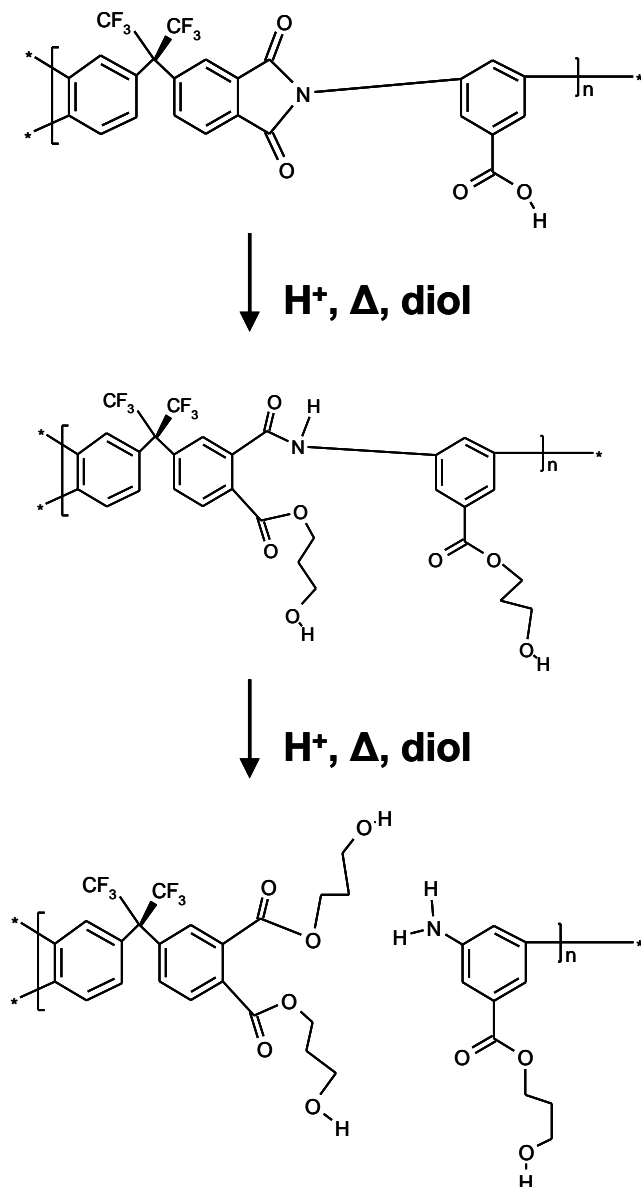


Figure 3.20: Reaction steps of a PDMC (3:2) chain segment undergoing chain scissioning on the imide ring.

Before the esterification reaction, imidization was confirmed by the reduction of the amide peaks from the polyamic acid precursor using IR and ^1H NMR until no change could be observed in the spectra. This corresponded to about 18 to 26 hrs of imidization at $\sim 190^\circ\text{C}$ during which the reaction distillate, which contains the water produced, was removed. These conditions complete the imidization reaction [26]. Amides can be seen at 1660 cm^{-1} and 1550 cm^{-1} on an IR spectrum, [27] which corresponds to the carbonyl (CONH) and C-NH groups respectively. It is believed that although the water produced from the monoesterification reaction makes up a small fraction of the total reaction solution, the elimination of this water helps in reducing subsequent molecular weight loss. A hydrolyzed imide can cleave and form its polyamic acid precursor, which contains amide groups and carboxylic acid groups. In this case, these carboxylic acid groups are capable of participating in the monoesterification reaction, thus increasing the observed apparent ester yields relative to the theoretical limit at 100% conversion if no imide cleavage had taken place. Furthermore, it was hypothesized that if the reaction continues at the same condition, the amides that hold the chain together may also cleave by hydrolysis, thereby further increasing more esters and ultimately in a loss of molecular weight. To check for imide cleavage, IR was carried out on the low molecular weight monoester polyimide. As shown in Figure 3.21, the presence of amides was observed on the IR spectrum, indicating that imide cleavage had indeed occurred.

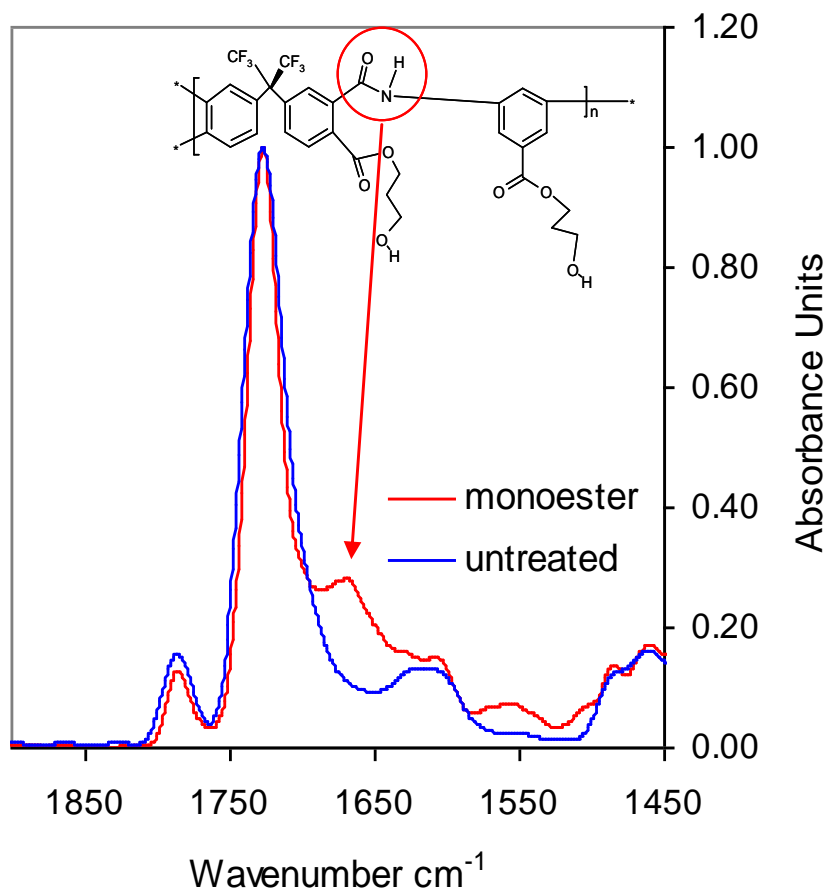


Figure 3.21: ATR-IR spectrum of a PDMC (3:2) polyimide that experienced molecular weight loss (red) and the precursor untreated/unesterified polyimide (blue).

To alleviate this situation, a Dean-Stark trap fitted to a condenser was utilized for the monoesterification reaction. A Dean-Stark trap is conventionally used for the imidization reaction to remove the water distilled from the reaction solution and the same idea was used for the monoesterification reaction. This helps in significantly reducing but not completely eliminating the water present, since water is intrinsically produced by the

reaction. Since this measure was not sufficient to completely eliminate the loss in molecular weight typically seen after monoesterification, a balance appears to exist between imide/amide chain scissioning and enabling high levels of the ester yield to be reached during monoesterification. The method chosen to approach this balance was to reduce the catalyst concentration during the reaction. Typically, 5 mg or more of para toluenesulfonic acid per gram polyimide is used to catalyze the reaction [13, 14, 21-24]. This amount was reduced to 2.5 mg para toluenesulfonic acid per gram polyimide. The reaction temperature was also lowered slightly from 140 °C to ~130 °C. The effects of this change in the reaction conditions were monitored over the course of the reaction and were positive. The molecular weights and ester yields were obtained by analyzing the precipitated reaction products over time intervals of 4 h, 8 h, 12 h, 16 h, 18 h, and 22 h. The conditions used for the NMR analysis of ester yields and the GPC analysis of molecular weights were held constant, to ensure consistency between the data. The plot in Figure 3.22 summarizes the results from this experiment.

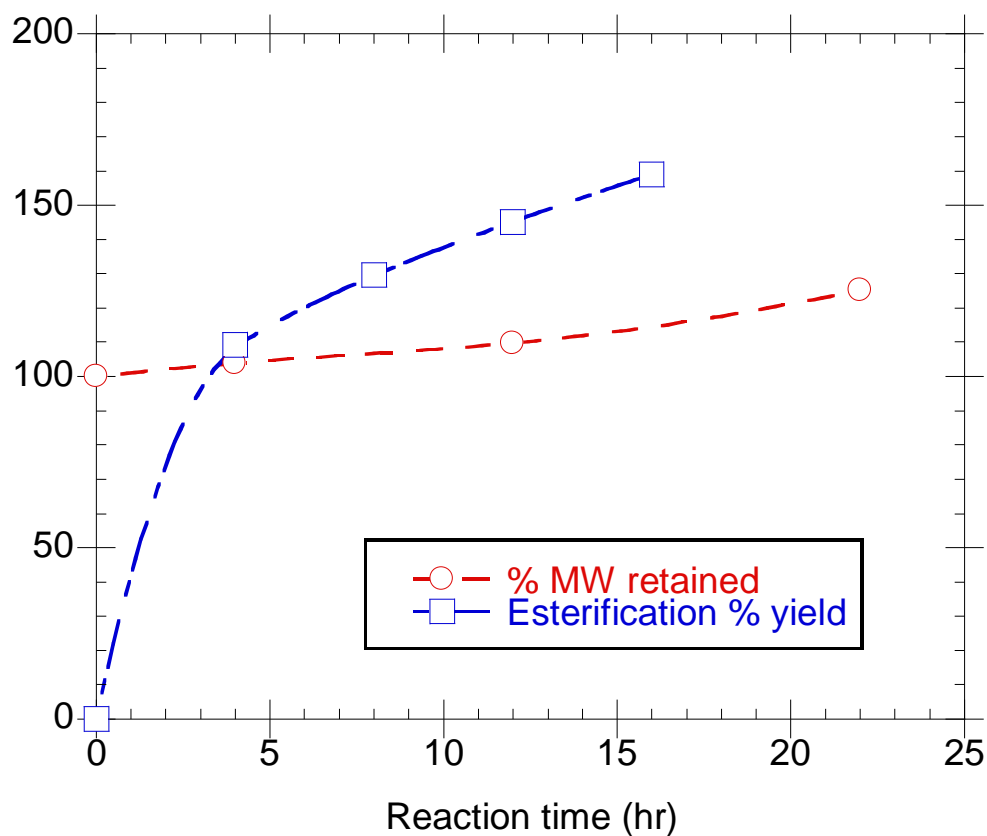


Figure 3.22: Monoesterification yield and weight average molecular weight trends of a PDMC (3:2) polyimide, showing no molecular weight loss and high ester yields. Increased molecular weights indicate the addition of the esters on the polymer chain from the diol crosslinking agent.

From Figure 3.22, it can be seen that there was no molecular weight loss from using the dehydration conditions stated previously and by using a reduced amount of catalyst. The molecular weight at 0 hr was 103,000 (Mw) with a polydispersity of 3. The preservation of the molecular weight was an important objective. The ester yields were found to still be greater than the theoretical yield at 100% conversion if no imide cleavage had occurred. IR was carried out on these higher molecular weight polyimide batches

obtained during the reaction to investigate the presence of amides. Figure 3.23 shows the spectra for this.

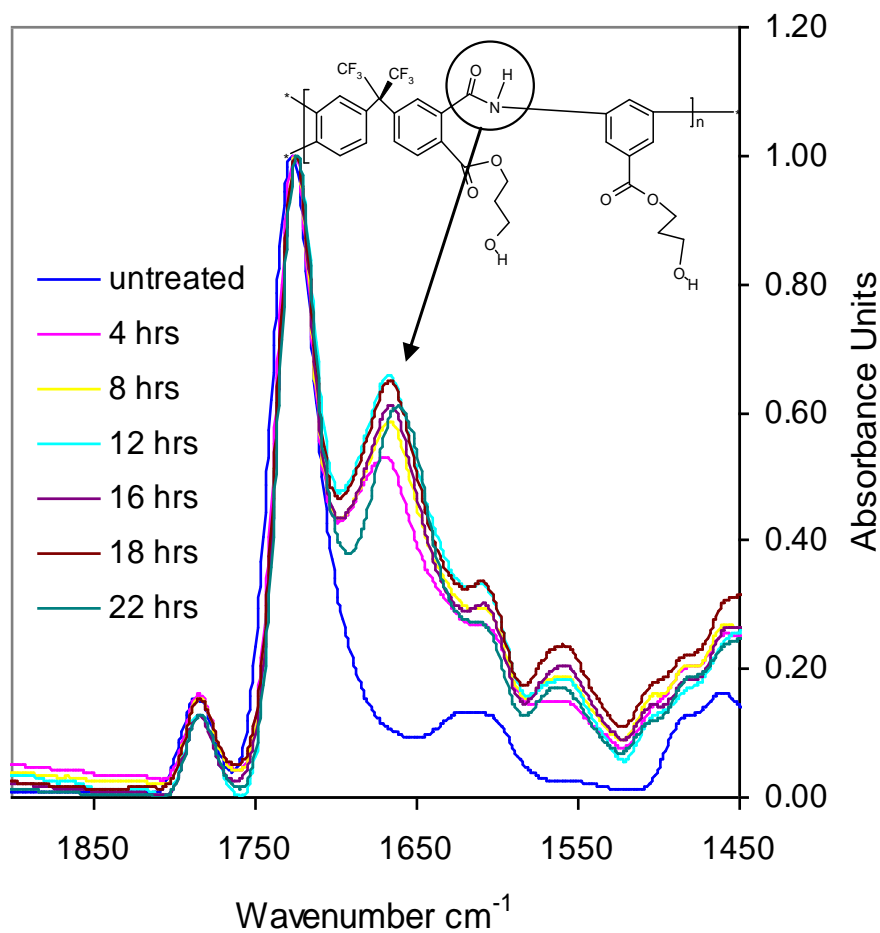


Figure 3.23: ATR-IR spectra of PDMC (3:2) polyimide samples that experienced no molecular weight loss, but show the resurgence of amide peaks (top) and the precursor untreated/unesterified polyimide (bottom/blue).

It can be seen from the spectra in Figure 3.23 that the amides had still appeared during the monoesterification reaction in the higher molecular weight crosslinkable monoester

polyimides as well. This resurgence appeared to an extent even higher than that for the batch that experienced molecular weight loss shown in Figure 3.21. This suggests that more amides were present, and may have been on the verge of leading to backbone scissioning if sufficiently activated or if excess moisture were present. However, even after 22 hrs of reaction under these modified monoesterification conditions, no molecular weight loss was observed.

Although ester yields were higher than normal, indicating imide ring opening, the molecular weight was preserved. Furthermore, IR analysis on the polyimide samples shows that the cleaved/ring-opened imides may be recycled by annealing at high temperatures, at which crosslinking occurs simultaneously. This can be seen in Figure 3.24, where the IR spectrum of an untreated/unesterified polyimide is plotted along with that for the esterified polyimide and its annealed version, where the temperature of annealing was ~245 °C. Figure 3.25 also shows that the crosslinking reaction also happens under the conditions shown in Figure 3.24, as the alcohol from the propane-diol disappears. However, the spectrum in Figure 3.25 indicates complete disappearance of the CH groups as well, which is unexpected. This is most likely a result of the ATR-IR sensitivity in these regions of the spectrum with high wave numbers. At higher wave numbers or lower wave length (λ), the penetration depth (d_p) of the IR beam is reduced according to Equation 3.7 below. More details on this can be found in the reference [28].

$$d_p = \frac{\lambda}{2 \cdot \pi \cdot n_1 \cdot \left(\sin^2 \theta - n_{21}^2 \right)^{1/2}} \quad (3.7)$$

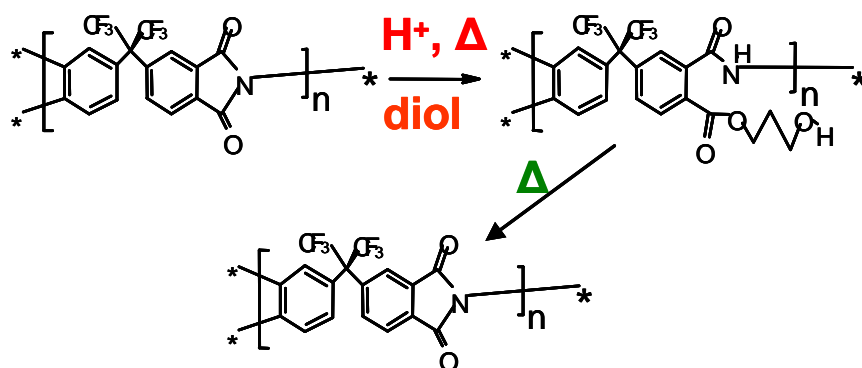
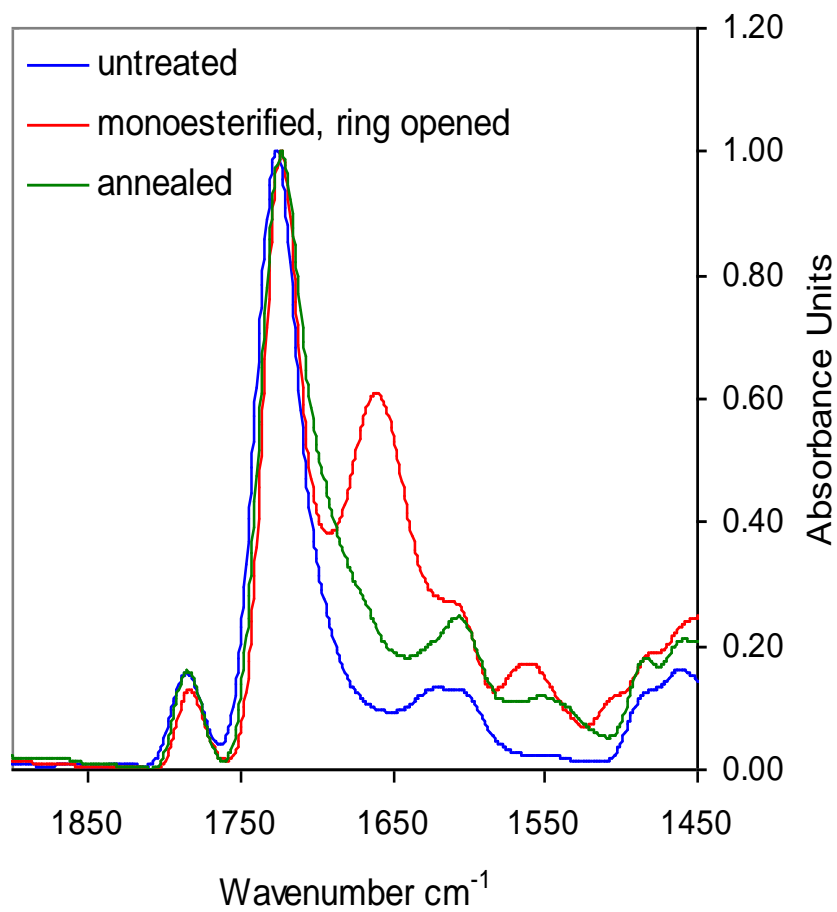


Figure 3.24: ATR-IR spectra of the precursor untreated/unesterified polyimide; a PDMC (3:2) polyimide (monoesterified) sample made from it that experienced no molecular weight loss, but shows the resurgence of amide peaks; and an annealed/crosslinked polyimide showing recyclization of the imide ring.

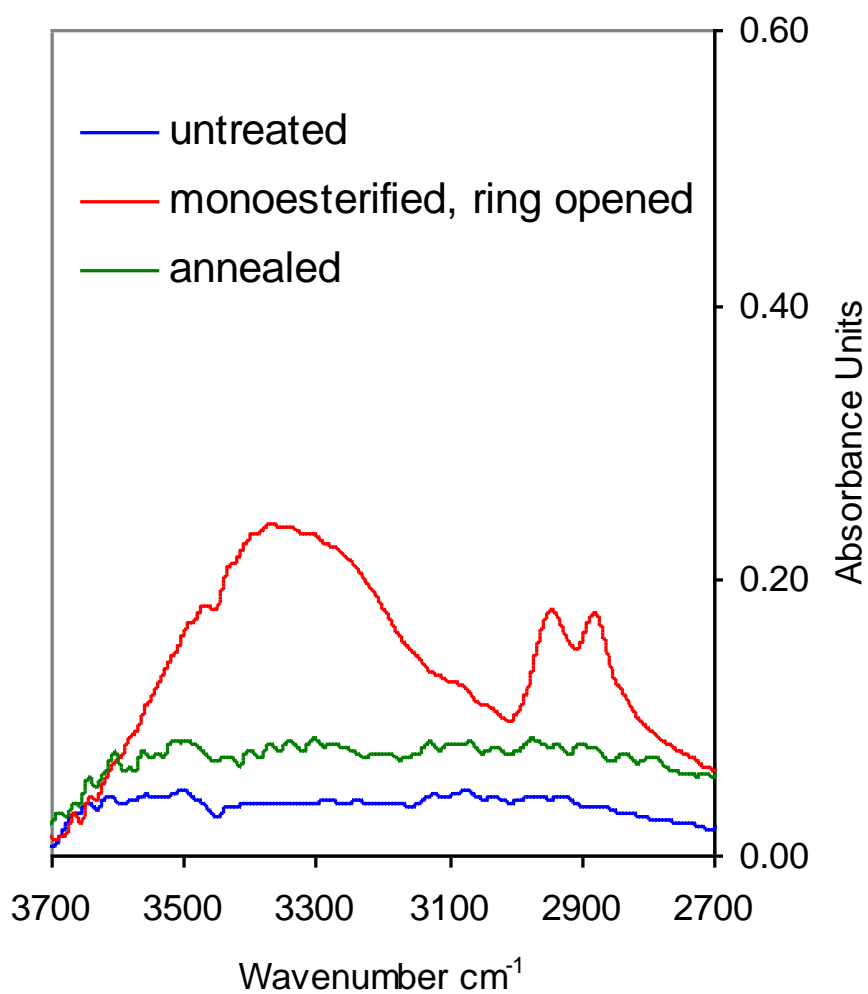


Figure 3.25: ATR-IR spectra of the precursor untreated/unesterified polyimide; a PDMC (3:2) polyimide (monoesterified) sample made from it that experienced no molecular weight loss, but shows the appearance of alcohols from propane-diol; and an annealed/crosslinked polyimide showing disappearance of the alcohol.

Low molecular weight monoesters were also experienced when the catalyst concentration using para toluenesulfonic acid was at 2.5 mg per gram polyimide but without the use of dehydration. This suggests that both the removal of water and the lowering of the catalyst concentration were important in preserving the molecular weight of the crosslinkable monoester polyimide, while still obtaining high monoester yields.

3.3.5 Reaction scale-up

To spin the crosslinkable polyimide in order to make hollow fibers for gas separations, the synthesis process was scaled up so that larger quantities (>100 g) of polymer could be made for hollow fiber production. The previous experiments were conducted in 100 – 500 ml reaction vessels used for making smaller quantities. In order to make such larger quantities of polymer, the reaction scale-up involved using a larger scale (~4 L) reactor. The surface area to volume ratio for the larger reactors are reduced compared to the smaller reactor vessels, and this reduces the efficiency for heating required for dehydrating the reaction solution. The reaction set-up is depicted in Figure 3.26 below.

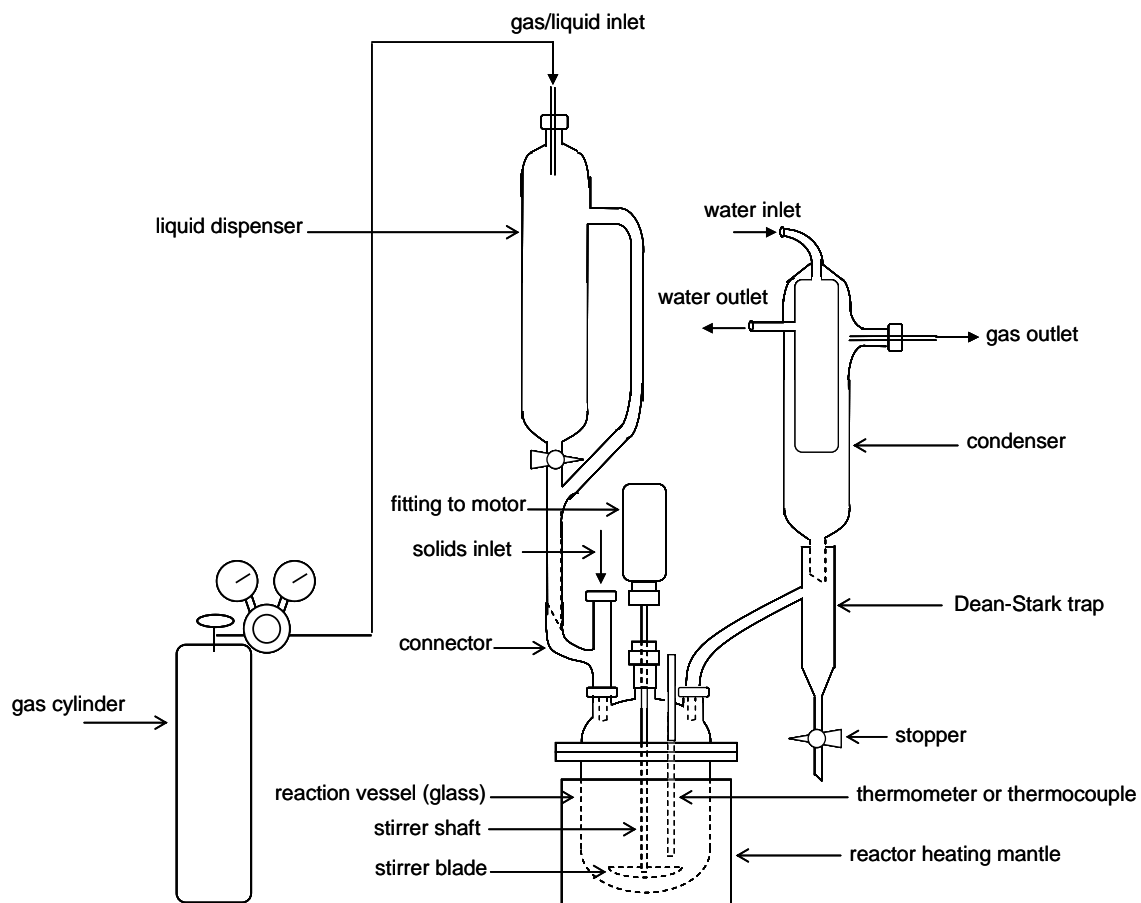


Figure 3.26: Schematic showing the set-up for polymer synthesis used in this work.

A one pot method was used for the monoesterification scale-up, where the *o*-DCB present in imidization, was present for esterification. This not only reduced the synthesis steps, labor, and solvent consumption, but was also geared to using the *o*-DCB

dehydrating agent present to facilitate the removal of water during monoesterification, while catalyst levels were still lowered. The ester yield on a batch made using this technique was ~90%, most likely because a smaller amount of catalyst was used here (~1.75 mg p-TSA per gram of polymer), and the weight average molecular weight was 105,000. During precipitation of this higher molecular weight monoester polyimide, the precipitate was a white fibrous solid as shown in Figure 3.27.



Figure 3.27: Picture showing precipitated PDMC polymer after large scale synthesis

This batch was used to demonstrate the effects of high molecular weight on spinning the crosslinkable polyimide (see Chapter 4). There is a plethora of literature on polyimide

synthesis [19, 29-41]; useful in making the untreated polyimide at a high starting molecular weight, but the focus here is on the preservation of that molecular weight during the monoesterification reaction by avoiding detrimental side reactions. Successive large batches have been made where using this technique enabled high molecular weights of the crosslinkable monoester, as high as 183,500, without molecular weight loss occurring on the precursor polyimide backbone.

3.4 Summary

In this chapter, it was found that the crosslinkable had to be synthesized using a newly developed protocol. The old method caused chain scissioning and made membranes less spinnable. The methods described here allowed the synthesis of higher molecular weight PDMC polymer batches, which were shown to be necessary for subsequent membrane formation processes as described in Chapter 4.

3.5 References

1. Moore, T.T., *EFFECTS OF MATERIALS, PROCESSING, AND OPERATING CONDITIONS ON THE MORPHOLOGY AND GAS TRANSPORT PROPERTIES OF MIXED MATRIX MEMBRANES*, in *Chemical Engineering*. 2004, The University of Texas at Austin: Austin, Texas. p. 283.
2. O'Brien, K.C., et al., *A new technique for the measurement of multicomponent gas transport through polymeric films*. *J. Membr. Sci.*, 1986. **29**(3): p. 229-38.
3. Pye, D.G., H.H. Hoehn, and M. Panar, *Measurement of gas permeability of polymers. I. Permeabilities in constant volume/variable pressure apparatus*. *J. Appl. Polym. Sci.*, 1976. **20**(7): p. 1921-31.
4. Adam, K., *THICKNESS DEPENDENT PHYSICAL AGING AND SUPERCRITICAL CARBON DIOXIDE CONDITIONING EFFECTS ON CROSSLINKABLE POLYIMIDE MEMBRANES FOR NATURAL GAS PURIFICATION*, in *Chemical & Biomolecular Engineering*. 2008, Georgia Institute of Technology: Atlanta. p. 200.
5. Baker, R.W., *Future Directions of Membrane Gas Separation Technology*. *Ind. Eng. Chem. Res.*, 2002. **41**: p. 1393-1411.
6. Kesting, R. E. and A.K. Fritzsche, *Polymeric Gas Separation Membranes*. 1993, New York: John Wiley and Sons Inc.
7. Pesek, S.C. and W.J. Koros, *Aqueous quenched asymmetric polysulfone membranes prepared by dry/wet phase separation*. *Journal of Membrane Science*, 1993. **81**: p. 71-88.
8. Pesek, S.C. and W.J. Koros, *Aqueous quenched asymmetric polysulfone hollow fibers prepared by dry/wet phase separation*. *Journal of Membrane Science*, 1994. **88**: p. 1-19.
9. McKelvey, S.A., D.T. Clausi, and W.J. Koros, *A guide to establishing hollow fiber macroscopic properties for membrane applications*. *Journal of Membrane Science*, 1997. **124**: p. 223-232.

10. Carruthers, S.B., G.L. Ramos, and W.J. Koros, *Morphology of Integral-Skin Layers in Hollow-Fiber Gas-Separation Membranes*. Journal of Applied Polymer Science, 2003. **90**: p. 399–411.
11. Kurdi, J. and A.Y. Tremblay, *The influence of casting solution structure on the microporosity of polyetherimide gas separation membranes prepared by the coagulation post-leaching method*. Journal of Membrane Science, 2001. **184**: p. 175–186.
12. Kurdi, J. and A.Y. Tremblay, *Preparation of Defect-Free Asymmetric Membranes for Gas Separations*. Journal of Applied Polymer Science, 1999. **73**: p. 1471–1482.
13. Wallace, D.W., *Crosslinked Hollow Fiber Membranes for Natural Gas Purification and Their Manufacture from Novel Polymers*, in *Chemical Engineering*. 2004, The University of Texas at Austin: Austin, Texas. p. 202.
14. Hillock, A.M.W. and W.J. Koros, *Cross-Linkable Polyimide Membrane for Natural Gas Purification and Carbon Dioxide Plasticization Reduction*. Macromolecules, 2007. **40**: p. 583-587.
15. Robeson, L.M., *Correlation of separation factor versus permeability for polymeric membranes*. J. Membr. Sci., 1991. **62**(2): p. 165-85.
16. Baker, R.W., *Future Directions of Membrane Gas Separation Technology*. Industrial & Engineering Chemistry Research, 2002. **41**(6): p. 1393-1411.
17. Kailani, M.H. and C.S.P. Sung, *Chemical Imidization Study by Spectroscopic Techniques. 1. Model Amic Acids*. Macromolecules, 1998. **31**(17): p. 5771-5778.
18. Kailani, M.H. and C.S.P. Sung, *Chemical Imidization Study by Spectroscopic Techniques. 2. Polyamic Acids*. Macromolecules, 1998. **31**(17): p. 5779-5784.
19. Kim, Y.J., et al., Macromolecules, 1993. **26**(6): p. 1344.
20. Bruce, P.Y., *Organic Chemistry*. 1995, New Jersey: Prentice-Hall: Englewood Cliffs.
21. Wind, J.D., et al., *Solid-State Covalent Cross-Linking of Polyimide Membranes for Carbon Dioxide Plasticization Reduction*. Macromolecules, 2003. **36**: p. 1882-1888.

22. Wind, J.D., et al., *Carbon Dioxide-Induced Plasticization of Polyimide Membranes: Pseudo-Equilibrium Relationships of Diffusion, Sorption, and Swelling*. *Macromolecules*, 2003. **36**: p. 6433-6441.
23. Kim, J.H., W.J. Koros, and D.R. Paul, *Effects of CO₂ exposure and physical aging on the gas permeability of thin 6FDA-based polyimide membranes: Part 2. with crosslinking*. *Journal of Membrane Science*, 2006. **282**(1-2): p. 32-43.
24. Wind, J.D., *Improving Polyimide Membrane Resistance to Carbon Dioxide Plasticization in Natural Gas Separations*, in *Chemical Engineering*. 2002, The University of Texas at Austin: Austin, Texas. p. 215.
25. Wallace, D.W., *PDMC polymer*, I. Omole, Editor. 2007: Atlanta.
26. Kim, Y.J., et al., *Kinetic and mechanistic investigations of the formation of polyimides under homogeneous conditions* *Macromolecules*, 1993. **26**: p. 1344–1358.
27. Dunson, D.L., *SYNTHESIS AND CHARACTERIZATION OF THERMOSETTING POLYIMIDE OLIGOMERS FOR MICROELECTRONICS PACKAGING*, in *Chemistry*. 2000, Virginia Polytechnic Institute and State University: Blacksburg, Virginia. p. 243.
28. Koenig, J.L., *Spectroscopy of Polymers*. Second ed. 1992, Washington DC: ACS Professional Reference.
29. SROOG, C.E., et al., *Aromatic Polypyromellitimides from Aromatic Polyamic Acide*. *JOURNAL OF POLYMER SCIENCE: PART A*, 1965. **3**: p. 1373-1390.
30. Bower, G.M. and L. Frost, *J. Polym. Sci.* . 1963. **A1**: p. 3135.
31. Kaas, R.L., *J. Polym. Sci.: Polym. Chem. Ed.*, 1981. **19**: p. 2255.
32. Dine-Hart, R.A. and W.W. Wright, *J. Appl. Polym. Sci.*, 1967. **II**: p. 609.
33. Frost, L.W. and I. Kesse, *J. Appl. Polym. Sci.* , 1964. **8**: p. 1039.
34. Yagci, H., C. Ostrowski, and L.J. Mathias, *J. Polym. Sci. Part A: Polym. Chem.*, 1999. **37**: p. 1189.
35. Ayala, D., et al., *J. Polym. Sci. Part A: Polym.Chem.*, 1999. **37**: p. 805.

36. Yang, C.-P. and S.-Y. Tang, *J. Polym. Sci. Part A: Polym. Chem.*, 1999. **37**: p. 455.
37. Brekner, M.J. and C. Feger, *J. Polym. Sci. Part A. Polym. Chem.*, 1987. **25**: p. 2005.
38. Husk, R.G., P.E. Cassidy, and K.L. Gerbert, *Macromolecules*, 1988. **21**: p. 1234.
39. Moy, T.M., C.D. DePorter, and J.E. McGrath, *Polymer*, 1993. **34**: p. 819.
40. Furukawa, N., M. Yuasa, and Y. Kimura, *J. Polym. Sci.: Part A: Polym. Chem.*, 1998. **36**: p. 2237.
41. Tan, B., et al., *J. Polym. Sci.: Part A: Polym. Chem.*, 1997. **35**: p. 2943.

CHAPTER 4

SPINNING A DEFECT-FREE CROSSLINKABLE POLYIMIDE: A STUDY ON PDMC (3:2)

4.1 Review

4.1.1 Defect-free asymmetric hollow fiber membranes

A considerable portion of this project focuses on translating the dense film work with the crosslinkable PDMC polymer to asymmetric hollow fibers, since this is an industrially preferred form of the membrane [1, 2]. Asymmetric hollow fibers provide high fluxes required for productive separations due to the ability to reduce the separating layer to a thin integral “skin” on the outer surface of the membrane. The high transmembrane pressure differences capable of being handled, and the high surface area to volume ratios and high packing densities achieved from such cylindrical morphologies make this type of membrane structure very favorable industrially. The productivity of a membrane can be characterized by the amount of penetrant that permeates through the membrane within a given time period and is inversely proportional to the thickness of the separating layer according to Equation 4.1.

$$productivity = \frac{P \cdot A \cdot \Delta p}{l} \quad (4.1)$$

In Equation 4.1, P is the intrinsic membrane permeability (a property of the material), A is the membrane surface area for permeation, Δp is the transmembrane pressure

difference driving force, and l is the membrane's effective thickness, which can be controlled morphologically. For this reason, it is clear that a thinner skin would allow use of smaller (lighter weight) modules and reduce capital costs for a given membrane, making the process exceptionally favorable for applications where space and weight are at a premium, such as in offshore natural gas treating. Asymmetric morphologies are desirable because the actual separating layer is reduced to a very small portion of the membrane, while the bulk of the membrane, *formed efficiently in the same fabrication process*, acts as a porous support with much less resistance to permeation. The pioneering work of Loeb and Sourirajan (around 1960) greatly advanced the field of membrane technology by their development of asymmetric membranes [3-7], which could be made by simply casting a solution of the membrane polymer in a certain way. Much of the success with asymmetric membranes was with cellulose acetate, greatly used in reverse osmosis applications and currently the "standard polymer" for use in commercial membranes for natural gas purification. The development of other types of polymers with high permeabilities and selectivities has been a rapidly growing area of membrane science, but so few of the materials have been used to make commercial membranes perhaps because they are unsuitable to be processed effectively into high flux membranes, which can be packed into high surface area modules [1]. Some work in the literature has focused on developing asymmetric hollow fibers from novel polymers [8-16], but this area of technology has proved to be challenging perhaps due to the small amount of publication in the open literature in this area [8].

Although thin skinned asymmetric membranes are preferred because of the increased productivities achievable, the tendency to create non-ideal morphologies that

undermine intrinsic membrane separation capability is increased (as the membrane thickness is decreased). One of such non-ideal morphologies is the occurrence of “pin-hole” defects that prevent gas molecules from selectively permeating through the membrane. The area of such a defect compared to the overall membrane area may be small (10^{-7} % surface porosity) [17], but its penetration through the selective skin permits a significant portion of the penetrant gas to flow through this “non-selective” region, thus reducing selectivity. If the areas of these defects are small enough, they may be “caulked” by coating the membrane with a very highly permeable polymer [17, 18]. One such polymer is silicone rubber, which is a rubbery polymer at room temperature, and has been shown to work well with many of the polymers used for gas separation. This coating layer reduces the non-selective contribution to the overall flux. The separation properties of a defective membrane may be upgraded by matching the membrane with the specific coating layer used. Analysis of the effects of such composite structures on the overall transport properties of membranes made from them can be treated using a resistance model, analogous to the famous series/parallel resistance concept in electric circuits [17]. Figure 4.1 shows a schematic representing this post-treatment process.

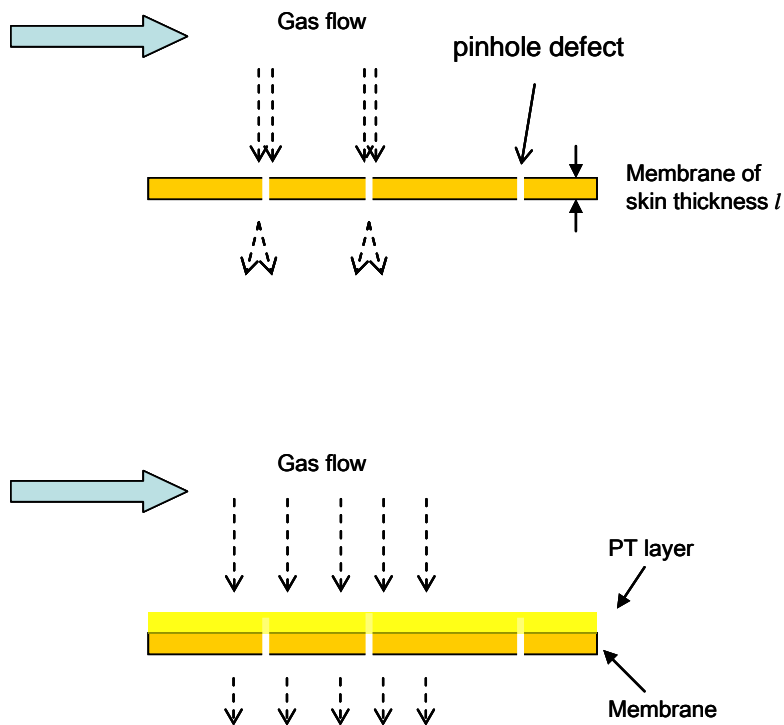


Figure 4.1: A membrane with pin-hole defects (top) and a composite membrane showing a post-treatment (PT) layer used to “heal” defects (bottom).

The ability to post-treat defective asymmetric membranes significantly enabled the application of membranes for many practical gas separations. Prior to this milestone by Henis and Tripodi of Monsanto, development of high flux asymmetric membranes was hampered by the inability to produce intrinsically defect-free, high flux membranes, due to the presence of pin-hole defects.

Currently, a significant number of polymers have been made into asymmetric hollow fibers that can be post-treated, offering intrinsic polymer separation capabilities and high fluxes. However, these huge developments have still been limited to gas separation applications with less aggressive feed mixtures where plasticization is not an

issue, probably since the post-treatment layer itself becomes less effective under high pressure plasticizing feeds [19]. Essentially all nitrogen from air applications using membranes now rely upon such “caulked” asymmetric hollow fiber membranes [20].

In such cases where both processing into defect-free asymmetric morphologies and plasticization is a challenge, such as in natural gas membrane applications, cellulose acetate membranes still remain the current standard but compromisingly offer selectivities for CO₂/CH₄ of less than 20 [20]. The advantage of the cellulose acetate polymers is its relative ease of processing into the desired asymmetric morphology that do not require caulking [21]. Nevertheless, slow progressions have been made in attempts to replace cellulose acetate membranes with more selective materials [1, 20]. For instance, work by Kosuri et al. demonstrated the ability to form defect-free asymmetric hollow fibers from Torlon[®], a polyamide-imide, which showed intrinsic selectivities for CO₂/CH₄ of over 50, and exceptional plasticization resistance to aggressive CO₂ rich streams at high pressures [11]; however, this polymer shows CO₂ permeabilities of less than 1 Barrer.

Wallace et al. [22, 23] first created asymmetric hollow fibers with the crosslinked PDMC polymer, but these fibers were defective and had to be post-treated to regain intrinsic polymer permselectivities. Figure 4.2 shows the work by Wallace et al., where a defective PDMC hollow fiber membrane was post-treated with a silicone rubber layer to heal the defects.

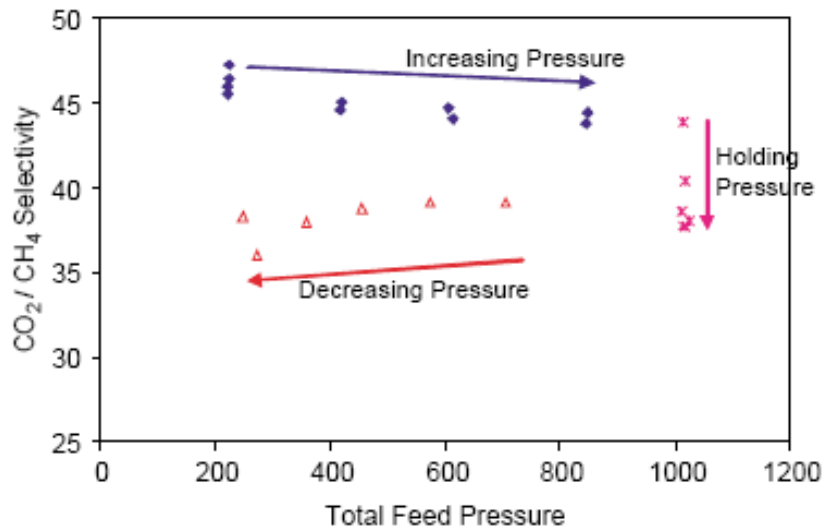


Figure 4.2: A post-treated PDMS hollow fiber membrane tested against high pressure feed containing 20% CO₂ in CH₄, showing the short-comings of the post-treatment process [22].

As can be seen from Figure 4.2, the advantage of the post-treatment diminishes as the feed conditions become more aggressive. Ultimately, the post-treated fiber lost the permselectivity gained from the caulking process in the presence of a relatively high pressure CO₂/CH₄ feed (up to 200 psi CO₂). Also, studies carried out with our industrial collaborators showed that post-treated fibers severely lost the performance enhancement from the post-treatment process once exposed to a feed containing toluene, a heavy hydrocarbon impurity. For this reason, the importance of a defect-free integral skin layer in achieving intrinsic crosslinked PDMS polymer separation properties within asymmetric hollow fiber membranes for aggressive feeds cannot be over emphasized, and is the primary focus of this chapter.

4.1.2 Other non-ideal morphologies

As previously stated, developing a thin skin layer in asymmetric membranes increases the risk of formation of non-ideal morphologies such as pin-hole defects. Other effects that may undermine intrinsic polymer separation capabilities in such non-ideal morphologies include external mass transfer resistance [24, 25] and substructure resistance [26].

4.1.2.1 External mass transfer resistance

In this scenario, if the flux of the membrane is high, by using a polymer with a high intrinsic permeability and/or by reducing the skin layer thickness, the resistance from external mass transfer zones may contribute significantly to the overall resistance of the membrane in operation. The observed separation performance of such a membrane in operation becomes dependent on the influence of this “boundary layer” region, where mass transfer effects external to the membrane occur. In this boundary layer region, the local concentrations of the penetrants are considerably different from their concentrations in the bulk region, and the resistance to transport of the molecules is dependent on their diffusivity in this region since the relative diffusivities are not significantly different in a gas phase, external resistance. The mass transfer resistance is a practical limitation, occurring as a result of the accumulation of the “slow gas” on the surface of the membrane as the “fast gas” selectively permeates through the membrane. Thus, the more selective the membrane or the higher the flux of a penetrant over the other, the more problematic these effects become. Figure 4.3 shows a depiction of this scenario.

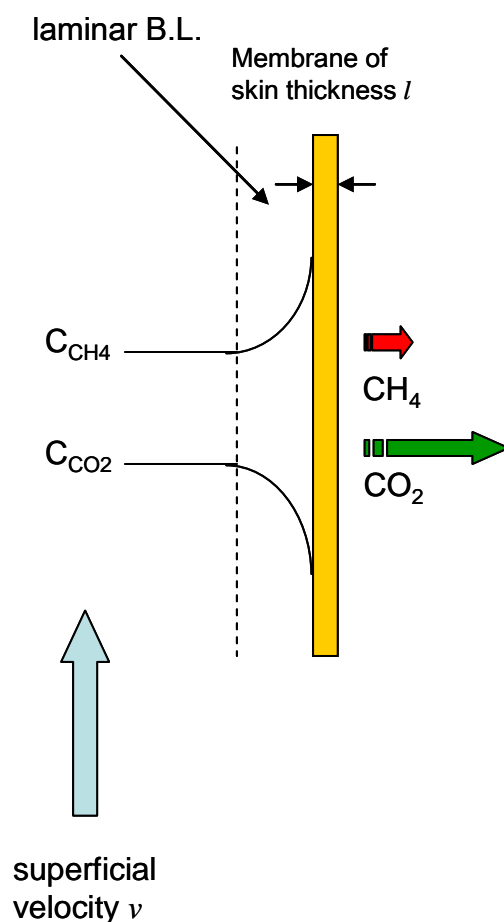


Figure 4.3: A membrane showing the boundary layer (BL) region during mixed gas permeation of CO₂ and CH₄.

The remedy for this situation, in general, depends on the operating conditions. The PDMC polymer, with an intrinsic permselectivity of ~45 and CO₂ permeability of ~58 Barrer (using a 10/90 CO₂/CH₄ feed at 65 psia, 35 °C) [27], can be considered a high performance polymer since its relatively high permeability and selectivity positions the polymer at the upper bound of Robeson's 1991 curve. Therefore, effects of mass transfer limitations are worthy of consideration in optimizing a membrane made from this

polymer. To check for potential external mass transfer effects on this polymer in thin skinned asymmetric hollow fibers, a simple resistance in series model was used. Here, the overall resistance is a contribution of the resistances from the membrane and the boundary layer, shown in Equation 4.2.

$$R_{overall} = R_m + R_{bl} \quad (4.2)$$

The resistance from the membrane and the boundary layer to component i are given as follows,

$$R_{m,i} = \left(\frac{l}{P} \right)_i \quad (4.3)$$

$$R_{bl,i} = \frac{1}{k_{bl,i} \cdot K_{bl,i}} \quad (4.4)$$

In Equation 4.3, l is the effective skin layer thickness of the membrane, P is the permeability of component i . In Equation 4.4, $k_{bl,i}$ is the mass transfer coefficient of component i , and $K_{bl,i}$ is the partitioning coefficient of component i to the boundary layer region, which is simply the inverse feed pressure. Using these expressions, estimates on the effects of external mass transfer on permeance and selectivity was enabled using the equations below

$$\left(\frac{P}{l}\right)_{overall,i} = \frac{1}{\left(\frac{l}{P}\right)_{m,i} + \frac{1}{k_{bl,i} + K_{bl,i}}} \quad (4.5)$$

$$\alpha_{i,j} = \frac{\left(\frac{l}{P}\right)_{m,j} + \frac{1}{k_{bl,j} \cdot K_{bl,j}}}{\left(\frac{l}{P}\right)_{m,i} + \frac{1}{k_{bl,i} \cdot K_{bl,i}}} \quad (4.6)$$

In the equations above, $k_{bl,i}$ can be obtained from empirical correlations under similar applications. Here, a mass transfer correlation developed by Cussler [28] for flow outside a capillary bed was used, where the rate of mass transfer was dependent on the diameter of the capillary (d), superficial velocity approaching bed (u), diffusion coefficient (D), viscosity (μ) and density (ρ) according to Equation 4.7, which was said to be sufficiently reliable when the capillaries are evenly spaced.

$$k_{bl,i} = \frac{D_i}{d} \cdot 0.8 \cdot \left(\frac{d \cdot u \cdot \rho_i}{\mu_i}\right)^{0.47} \cdot \left(\frac{\mu_i}{\rho_i \cdot D_i}\right)^{\frac{1}{3}} \quad (4.7)$$

From this analysis, it can be seen that there is a certain influence of the mass transfer coefficient on the separation performance, dependent on a few controllable variables. Since the permeability is intrinsic to the membrane material, the skin thickness is the main variable in controlling the membrane flux. Furthermore, the upstream velocity can be increased to induce turbulence, which can dramatically reduce the effects from the

boundary layer. The influence of these two variables, the skin thickness and the fluid velocity, on the separation performance of a membrane in operation is represented with this simple model for two membranes and shown in Figure 4.4. In Figure 4.4, one of the membranes has an intrinsic permeability of 50 Barrers (left) and the other 10 Barrers (right).

The permselectivity and permeances in Figure 4.4 are normalized by their intrinsic values, where external mass transfer effects are absent. From Figure 4.4, it can be observed that as the skin layer thickness is decreased, the permeances are compromised, especially for CO₂, the faster gas. Thus, the permselectivity is limited as the skin layer thickness is decreased. However, as can be seen from the analysis, if the velocity of the upstream is increased, the effects become diminished. In the laboratory, high velocities are maintained by limiting stage-cuts (molar flow ratio of permeate to feed) to less than 1%. However, to reach desired product purities in practical applications, much higher stage cuts are needed. Thus, these effects must be considered in the design of systems using this polymer.

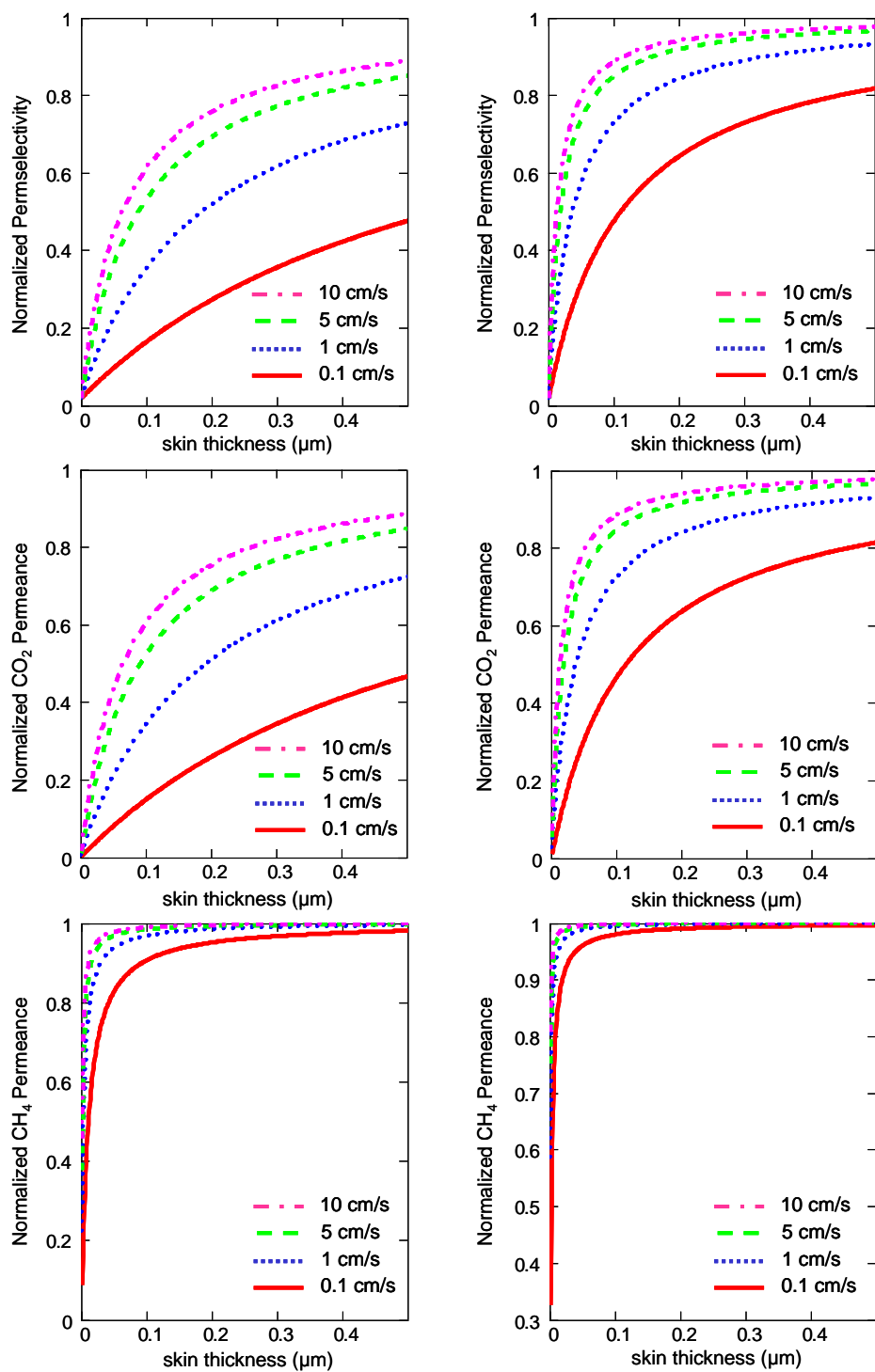


Figure 4.4: Effects of external mass transfer resistances on PDMC membrane performance. Parameters: 200 μm fiber OD, viscosity (μ) and density (ρ) at 1000 psi, 35 $^{\circ}\text{C}$, diffusion coefficient (D) using Fuller equation [29].

4.1.2.2 Substructure resistance

Another morphological effect of asymmetric membranes, sometimes neglected, is the resistance from the substructure. The substructure region can be considered to be any region beneath the dense skin layer, transitioning from a dense morphology to a micro porous network. A simplified schematic showing an asymmetric membrane with the three distinct transport layers: external boundary layer, dense skin layer, and substructure, is shown in Figure 4.5.

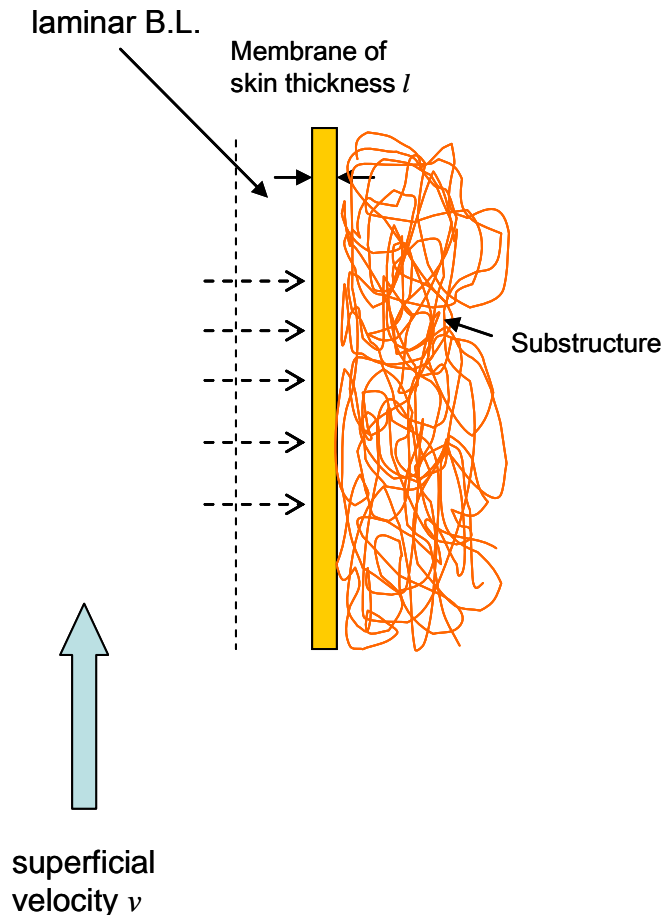


Figure 4.5: Schematic showing resistances from boundary layer, membrane, and substructure.

The effect of the substructure is much harder to determine because it may consist of several regimes of varying thicknesses, all of which their underlying transport mechanisms may be different. In transitioning from a dense layer to a porous region where viscous flow occurs, regimes exhibiting molecular sieving, surface diffusion, and/or Knudsen flow could conceptually be present. The degree to which any of these regimes contribute to the overall substructure is not easy to decouple; thus, the effect on the transport properties of the membrane from these regimes can be complex. A simple model assuming Knudsen flow in the substructure can be used to demonstrate the effects of such a non-selective transport mechanism on the overall performance of the membrane. Here, the resistance from the Knudsen regime is a function of the pore network structure (pore size, tortuosity, and porosity, and thickness of the region) represented by ϕ , the temperature (T) and the molecular weight (MW) of the penetrants according to the expression below

$$R_{substructure} = \frac{\phi \cdot \sqrt{MW_i}}{T} \quad (4.8)$$

Therefore, the overall resistance in the membrane can be expressed as the sum of the resistances from all the contributing regimes, i.e. the boundary layer, the membrane, and the substructure as follows,

$$R_{overall} = R_{bl} + R_m + R_{substructure} \quad (4.9)$$

Thus, the effect on the selectivity can be expressed using this resistance model as shown below, where the membrane CO₂ permeability used is 50 Barrer, permselectivity is 45, skin thickness is 0.2 μm, and the superficial velocity is 5 cm/s.

$$\alpha_{CO_2/CH_4} = \frac{\left(\frac{l}{P}\right)_{CH_4} + \frac{1}{k_{bl,CH_4} \cdot K_{bl,CH_4}} + \frac{\phi \cdot \sqrt{MW_{CH_4}}}{\sqrt{T}}}{\left(\frac{l}{P}\right)_{CO_2} + \frac{1}{k_{bl,CO_2} \cdot K_{bl,CO_2}} + \frac{\phi \cdot \sqrt{MW_{CO_2}}}{\sqrt{T}}} \quad (4.10)$$

A plot for the permselectivity as a function of the contribution of the structure factor ϕ , is shown below

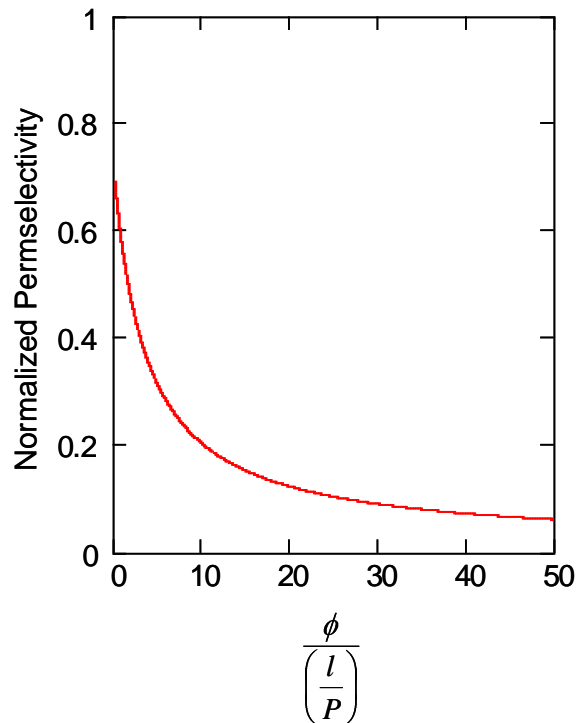


Figure 4.6: Analysis showing the effect of substructure resistance on permselectivity

Although the substructure factor may not be readily obtainable, the plot shown in Figure 4.6 shows a qualitative description indicating the permselectivity trends as Knudsen effects become significant. Eventually, the permselectivity approaches the Knudsen selectivity value for the gas pair.

A common (but similarly qualitative) method of indicating the presence of substructure resistance is by looking at the relative effects on the permeance of gases that are intrinsically considered to be fast and slow to the polymer, since Knudsen effects depress the flux of faster gases more. For instance, in a typical glassy polymer such as PDMC, helium is considered a fast gas, while oxygen and nitrogen are considered relatively slow gases. The intrinsic permselectivity for He/N₂ is usually over 40 and the O₂/N₂ permselectivity is usually about 4.5 – 5.5. However, the Knudsen selectivity for O₂/N₂ is ~0.9 and for He/N₂ ~2.7. This means that a degree of suppression in the He/N₂ selectivities more than that for O₂/N₂ would indicate substructure resistance. This method is frequently used since it is quick, and permeabilities for such probe gas molecules are usually readily available.

A more elegant method proposed by Clausi et al. [26] demonstrated that the effects in the substructure may be detected if the average pressure within the membrane is increased, so that viscous flow is forced within the substructure, while keeping the transmembrane pressure difference driving force constant. When viscous flow occurs in the substructure, there are no detrimental effects to the membrane's intrinsic properties. This method can be used in conjunction with the one described in the previous paragraph. More detail on this method can be found in the reference [26].

These analyses stress the fact that there is an “optimum” desired morphology in translating the PDMS polymer to a thin skinned asymmetric hollow fiber for practical application of these high performance polymers. It also shows that sub-optimal separation performance values in asymmetric hollow fibers may not just occur from pin-hole defects alone, but by the presence of other non-ideal morphologies for the membrane in operation. In the rest of this work, a permselectivity of 90% or greater of the intrinsic polymer pure gas permselectivity (i.e. O_2/N_2) would be considered defect-free. Pure gas permeation using more ideal gases like O_2 and N_2 eliminate concentration polarization; moreover, their similar molecular sizes reduce complications from substructure resistance on their permselectivity.

4.2 Hollow fiber spinning

Most of the events responsible for controlling the intricate morphology of a practical asymmetric hollow fiber membrane occur during the spinning process. As discussed in the previous section, practical asymmetric hollow fiber membrane morphologies would consist of an optimally thin skin layer, and a porous substructure. The fiber must also be of adequately small dimensions, circular, concentric, and with no macrovoids in the fiber wall, to withstand high pressures. However, apart from obtaining the desired macroscopic properties for membrane applications, the spinning process must occur in a fashion that can be scaled to produce large amounts of the hollow fiber membrane in a cost effective manner. Therefore, the spinnability of the material must

first be addressed in developing a hollow fiber membrane. Spinnability is the ability for the polymer to be processed or spun under a wide variation of conditions to allow adequate experimentation, without breakage occurring along the spin-line. The chart in Figure 4.7 gives a good depiction of the steps involved in translating a polymer into asymmetric hollow fiber membranes, concisely put into perspective by Carruthers et al. [30].

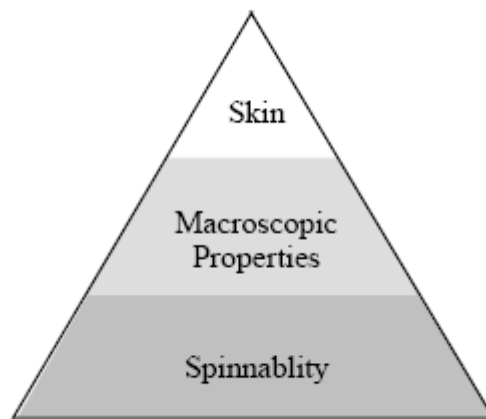


Figure 4.7: Schematic showing the steps involved in the development of a hollow fiber membrane, starting with spinnability: the ability to spin the fibers under realistic conditions; followed by macroscopic properties: including fiber size ($>300\ \mu\text{m}$), concentricity, and openness of substructure; and final skin integrity [30].

To achieve the economies of scale required to make the hollow fiber spinning process cost-effective, spinning speeds greater than about 50 m/min are preferred [2, 13]. In previous studies using these crosslinkable polymers, higher spinning speeds were not achieved due to low viscosity of the polymer solutions used in making the fibers [10]. There are ways that may alleviate this problem, such as with the use of viscosity enhancing salts e.g. lithium nitrate or by increasing polymer concentration in the dopes.

However, these methods have limitations and consequential negative effects on the transport properties of the final membrane if used extensively. Moreover, viscosity enhancing salts alone do not create the level of polymer chain entanglement in solution required to get adequate visco-elasticity for high tension spinning. A more direct approach by increasing the crosslinkable polymer molecular weight (see Chapter 3) to enhance solution visco-elasticity and spinnability is addressed in this thesis.

To form membranes into high pressure, high surface area/volume hollow fibers, fiber dimensions of about 300 microns or less are preferred [31, 32]. To achieve fibers with smaller radial dimensions, the fiber must withstand significant tension during drawing along the spin-line. The tension applied during spinning is related to the nominal draw ratio, defined as the ratio of take-up rate to the rate of extrusion from the spinneret. In previous studies using these crosslinkable polymers, nominal draw ratios could only go as high as 9 before spin line breakage was observed due to the lack of dope strength [10].

The reduced viscosities in previous studies reflected the relatively low polymer molecular weights, which were typically about 30,000 (M_w) [23, 33]. The work in Chapter 3 was done to develop the PDMC polymer for spinning into highly productive asymmetric hollow fibers at industrially relevant spinning speeds and to allow testing the resultant crosslinked fibers in realistic natural gas environments. The viability of using the improved molecular weight in achieving the intrinsic polymer separation capabilities in defect-free hollow fiber membranes will be discussed in Section 4.2.3.2.

4.2.1 Dope development

For a dope to be made from a polymer, the miscibility behavior needs to be mapped out. The dope must be a homogenous solution, therefore must contain a solvent for the polymer. Other additives are usually added in the dope for certain reasons that will be discussed; however, all the dope constituents can be broadly categorized to consist of the polymer (membrane phase), solvent, and non-solvent. Polymer miscibility may be described using equations which quantify the Gibbs free energy of mixing such as Equation 4.11 below, developed by Flory and Huggins [34].

$$\Delta G_m = R \cdot T \cdot (n_1 \cdot \ln \phi_1 + n_2 \cdot \ln \phi_2 + n_3 \cdot \ln \phi_3 + \chi_{12} \cdot n_1 \cdot \phi_2 + \chi_{13} \cdot n_1 \cdot \phi_3 + \chi_{23} \cdot n_2 \cdot \phi_3)$$

(4.11)

In Equation 4.11, the subscripts 1, 2, and 3 represent the non-solvent, solvent, and polymer respectively. R is the gas constant and T is the absolute temperature in Kelvin. The parameters n_i and ϕ_i represent the number of moles and the volume fraction of component i respectively. The parameter χ_{ij} is called the Flory-Huggins interaction parameter for components i and j and can be obtained from experiments [35]. Figure 4.8 below shows a ternary phase diagram that can, in principle, be obtained from data of the Gibbs free energy of mixing.

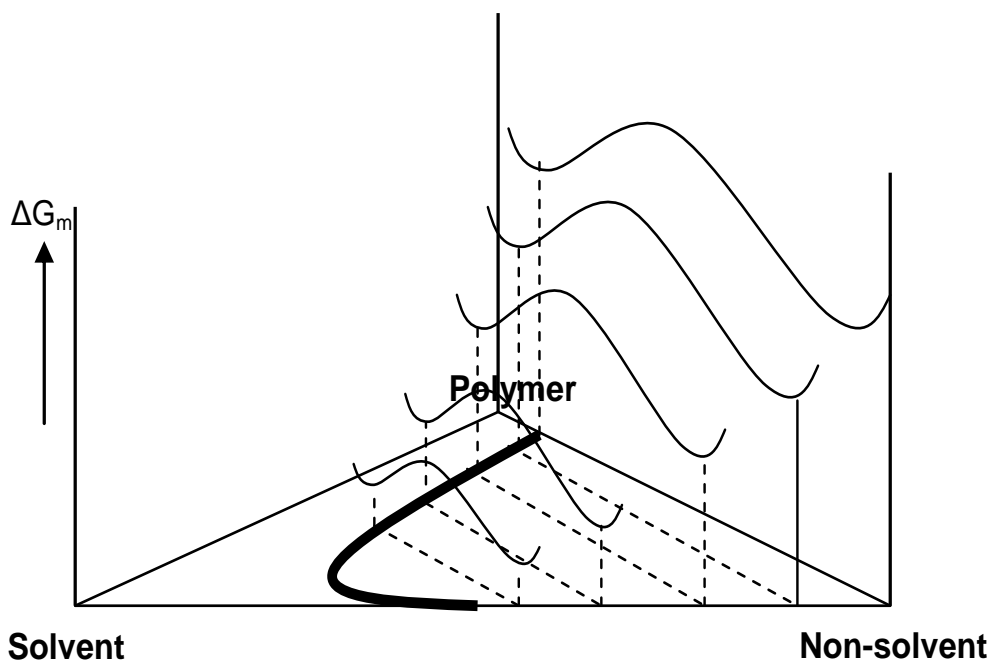


Figure 4.8: Ternary phase diagram showing the binodal (thick curve) that can be obtained from a Gibbs free energy of mixing equation [36].

Most often, it is adequate to simply estimate the miscibility boundary (binodal) of multi-component dopes, since most of the data required for the free energy equations are not readily available. Also, many times, more than one solvent and non-solvent may be present, or additives such as salts may be used, adding more complexity to the mathematical methods. For these reasons, cloud point experiments serve as a fast and accurate means of locating the binodal of the dopes. This method can be applied simply by making small solutions of the dope with the same polymer compositions and varying the compositions of the main solvent and non-solvent. The point at which phase separation occurs is monitored qualitatively by visual inspection. A two phase mixture is usually characterized by incomplete dissolution of the polymer or by apparent cloudiness

of the solution. Figure 4.9 below shows a ternary phase diagram depicting how the binodal can be determined from this technique, represented by the red dots in the ternary phase diagram. The final dope composition should be in the one phase region and preferably as close to the binodal as possible to ensure rapid phase separation once the dope is immersed in the quench bath. This helps prevent subsequent fiber collapse that could occur as the fiber traverses along the spin-line and encounters guide pins in the process. The quench bath is usually chosen to contain water (a non-solvent for most of the polymers used in these applications). This initial dope composition is represented as the star in Figure 4.9.

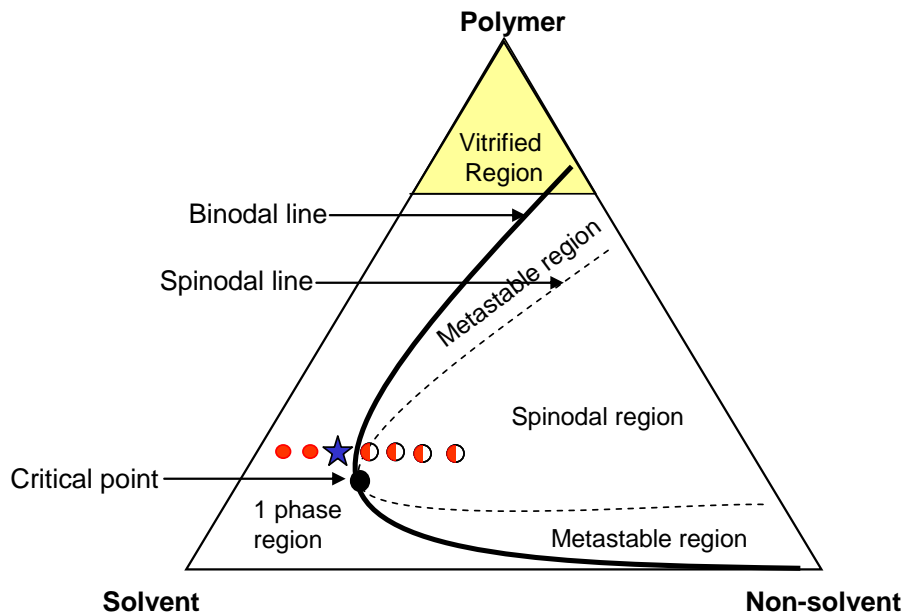


Figure 4.9: Ternary phase diagrams of polymer, solvent, and non-solvent for spinning hollow fibers demonstrating how to obtain the binodal. Filled (red) and unfilled (partially red) circles represent 1 and 2 phase compositions achieved at constant polymer concentration with increasing non-solvent addition.

4.2.2 Spinning parameters

4.2.2.1 Spin dope

Based on the preceding discussion, it is clear that formulating the right spin dope used for hollow fiber spinning is very important. The dope usually contains the polymer and various solvents, non-solvents, and additives. The polymer serves as the membrane solid phase and its composition in the dope influences the final membrane morphology greatly. Increasing the polymer concentration helps in skin formation, but can also increase unwanted resistance in the substructure. A good starting point for typical polymer compositions would usually range between 25–35 wt%. The molecular weight of the polymer is also important as it affects viscoelasticity required for drawing. It is preferred that molecular weights be above ~80,000 (M_w) based on past experience with the crosslinkable polymer.

The solvent serves to keep the solution homogeneously in one phase during extrusion from the spinneret. The choice of solvent is typically dependent on the polymer and on safety and environmental considerations. Higher boiling solvents like NMP, DMF, DMSO, and DMAc, are good candidates as they are all miscible with water, which allows use of an aqueous quench bath for coagulation. NMP has been used throughout this work due to its relatively less toxicity and its high boiling point. A fraction of the main solvent can be replaced with a more volatile solvent such as THF or acetone to induce evaporation in the air gap. The fraction of the volatile solvent can be adjusted to optimize the skin layer thickness.

The presence of non-solvent is case dependent and is discussed further in Section 4.2.3; however, the primary reason for using a non-solvent is to accelerate phase

separation as described in Section 4.2.1. Aliphatic alcohols are generally preferred because they allow a greater window of compositions than using stronger non-solvents like water. Ethanol, for example, is usually a good choice and is also beneficial for its volatility. Many times, salts like lithium nitrate can be used to accelerate phase separation as well. Lithium nitrate complexes with the solvent molecules mentioned above, and can be used as a viscosity modifier for this reason. When quenching occurs, the complex dissociates and phase separation is accelerated.

4.2.2.2 Bore fluid

The bore fluid is usually chosen to be a thermodynamically neutral fluid, which should ideally serve the purpose of maintaining an open bore during the spinning process. The choice of the bore fluid is dependent on the polymer system, but a generally convenient method of determining the bore fluid composition on a first spin is by extrapolation of the tangent line of the experimentally determined binodal towards the solvent/non-solvent axis on the ternary phase diagram [23] as shown in Figure 4.10.

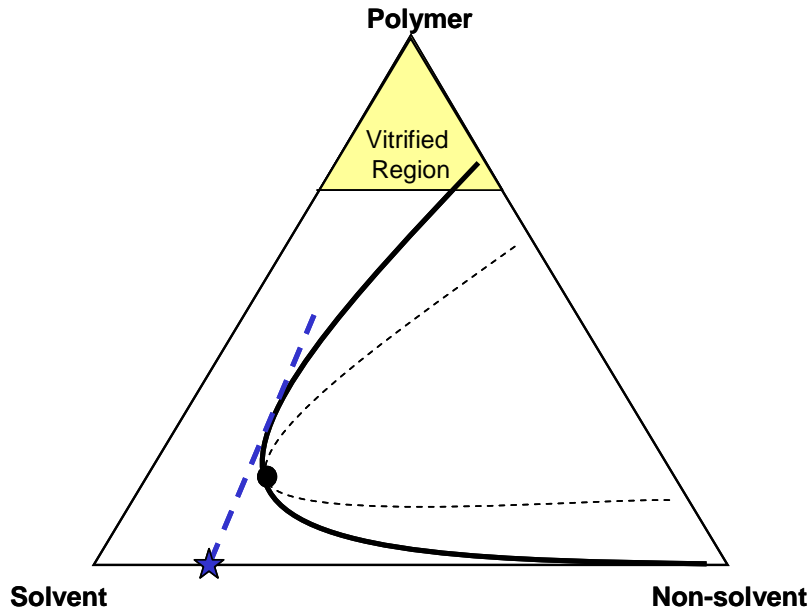


Figure 4.10: Determination of bore fluid composition by extrapolation of binodal towards solvent/non-solvent axis on ternary phase diagram. The bore fluid composition is indicated by the blue star.

4.2.2.3 Quench medium

The quench medium influences the phase separation process in forming the desired membrane morphology. The height of the bath is critical, as well as its temperature and composition. The compositions are generally chosen to accelerate phase inversion, which makes water a suitable choice since the polymers used are generally considered hydrophobic. Also, due to environmental constraints, water is always a safe choice. However, there can be solvents added for various reasons depending on the type of membrane formation approach used. Some of this is discussed in Section 4.2.3.1. The temperature of the water bath can also be elevated to speed up the diffusion process of solvents and non-solvents during coagulation. This can be advantageous since the crosslinkable polymers are less hydrophobic than other traditional polymers used and

their phase separation times, even in aqueous media, is much increased. The importance of accelerated phase separation comes from the need to fully vitrify the fiber before contacting the first guide roll, which could crush the fiber if not fully hardened. For these reasons, the bath height can also be adjusted to increase the critical distance before the fiber contacts the first guide roll. This is represented in Figure 4.11 below.

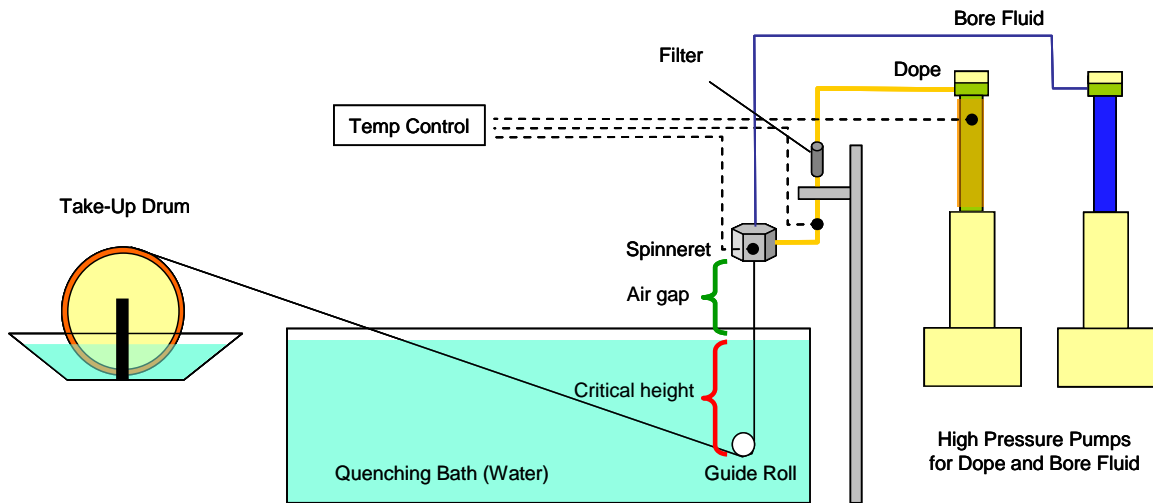


Figure 4.11: Schematic showing the spinning apparatus, with an air-gap and the critical quench bath height for phase separation.

4.2.2.4 Air gap

The air gap height mainly serves as a point for which evaporation occurs during dry-jet/wet quench spinning. This is discussed further in Section 4.2.3.1. The height in this region can be adjusted to increase the residence time during the dry jet step.

However, the maximum height achievable is limited by the visco-elastic characteristics of the dope. Therefore care must be taken in adjusting the air-gap height during spinning. Secondary variables that can be adjusted or recorded during the dry-jet step are the face velocity of the air stream surrounding the spin-line and the humidity. If spinning occurs in a fume hood, as done in this work, the face velocity of the hood can be adjusted to increase convection of the air. Alternatively, a convection chamber may be constructed for this purpose.

4.2.2.5 Spinneret temperature

The temperature of the spinneret is important especially when using the dry-jet/wet quench spinning method as discussed in Section 4.2.3.1. The evaporation of volatiles in the air-gap is increased with increasing the temperature during extrusion. However, a temperature too high will reduce dope viscosity and may cause spine-line instabilities. Temperatures between room temperature and ~80 °C are generally preferred.

4.2.2.6 Extrusion rate and draw ratio

The extrusion rate during spinning has an effect on the velocities achieved and the shear stresses during extrusion through the spinneret annulus. Shear forces at the outer region of the extruded fiber can influence the separation performance of the membrane since the skin layer is directly influenced in this region. There is some evidence that suggests that higher shear stresses may cause orientation of polymer chains in this region, leading to an increase in permselectivity [37-39]. The draw-ratio is defined as the ratio of the take-up to the extrusion rate. Thus, increasing the take-up speed of the fiber at a set

extrusion rate increases the draw ratio and ultimately reduces the radial dimensions of the hollow fiber. High draw ratios may also induce elongation stresses which cause chain orientation; however, such elongation stresses may negatively affect the skin formation process especially in dry-jet spinning.

4.2.2.7 Drying

The drying of an asymmetric hollow fiber membrane is an important process. The preservation of the delicate morphology after quenching during spinning can be achieved using a fluid exchange process. This is done to prevent capillary forces that act on the fiber when dried from a water wet state, which causes collapse of the substructure. The process involves a series of exchanges with fluids of lower surface tension, before final air drying. Table 4.1 shows a list of potential non-solvents for this purpose, assembled by Wallace [23], and listed by decreasing surface tensions. After solvent exchange and air drying, crosslinkable polymers are usually dried in a vacuum oven at ~ 70 °C to prevent premature crosslinking.

Table 4.1 Potential non-solvents for fluid exchanging before drying asymmetric hollow fibers [23, 40].

<i>Component</i>	<i>Surface tension (dynes/cm)</i>	<i>Normal boiling point (°C)</i>
Water	72.8	100
1-butanol	24.6	117.2
1-propanol	23.8	97.4
Acetone	23.7	56.2
Ethanol	22.8	78.5
Methanol	22.6	65
2-propanol	21.7	82.4
n-octane	21.8	125.7
n-hexane	18.4	69

4.2.3 Skin layer formation

4.2.3.1 Overview

Section 4.2.1 introduced information to guide dope development and the process of phase separation in forming the membrane, but no insight was given on skin formation or on what controls the asymmetric structure. Several mechanisms for skin layer formation in asymmetric membranes have been proposed by a number of researchers. Some of the studies were carried out by casting asymmetric films, which can be used as a first step in the transitioning process from a dense film to an asymmetric hollow fiber. However, there is no real substitute for the actual spinning process.

Loeb-Sourirajan asymmetric membranes were first developed around 1960, by a *wet phase inversion technique* to produce integrally skinned asymmetric membranes through a single process step. The casting dope contained a solvent for the polymer, and the solvent was miscible with the external coagulation medium. The coagulation medium was a non-solvent for the polymer, usually an aqueous quench bath. Once the polymer solution contacts the coagulation medium, or quench bath, phase inversion occurs by diffusion of solvent molecules out of the solution and non-solvent molecules into the solution, to create distinct polymer rich and poor phases. In other dope variants, a non-solvent is added to the polymer solution prior to quenching to accelerate phase inversion during the quenching step, similar to the process described in Section 4.2.1. In this wet phase inversion technique, the skin layer is formed, by definition, during the wet quenching step. The mechanism behind the skin layer formation via this process was hypothesized to result from a locally elevated polymer concentration on the outer-most region of the membrane due to either: solvent evaporation in the surrounding air prior to coagulation [41-43], or extremely fast solvent out flow compared to non-solvent inflow during the early moments of coagulation [44, 45]. Therefore, in this process, choice of solvent and non-solvents are most crucial. Most of the membranes produced by this technique had skin layers that were not completely defect-free, indicating that the process needed to be optimized. While the membranes were useful for reverse osmosis they were ineffective for gas separations without post-treatment.

Around the late 1980s, researchers at Permea Inc. developed a method to spin high flux asymmetric hollow fiber membranes using a phase inversion process from Lewis acid/base complex solvent systems. It was interestingly noted that high levels of

non-solvents (Lewis acids) could be incorporated into the solutions, via complexation with the solvent (Lewis base), compared to traditional polymer/solvent/non-solvent systems. It was believed that the concentration of the non-solvent present permits the manipulation of the effective layer thickness and structure of the skin. It was demonstrated that thinner skin layers could be achieved through this method, but the method produced skins that had defects and required post-treatment [15].

Other skin formation methods have been demonstrated by a few other researchers. van't Hof et al. showed, around 1992, that asymmetric membranes could be made using a dual bath method [46]. Here, the first bath consists of a non-solvent with reduced non-solvency power or reduced miscibility with solvent so that delayed de-mixing occurs (via increased solvent outflow compared to non-solvent inflow), to form a dense region on the outside. The second bath contains a strong non-solvent which promotes instantaneous de-mixing and complete phase separation. The success of this method relies on the careful choice of the dual bath constituents. Defect-free skins could be produced that did not require post-treatment. The draw-back here is that the skin thicknesses were relatively thick, resulting in reduced fluxes.

In the later 1990s and now more recently, Chung et al. [16, 47] have demonstrated the ability to form thin skinned asymmetric membranes using a binary dope (polymer and solvent), by manipulating rheological aspects of the spinning process. The implication of their success was in eliminating the requirement of a non-solvent in the dopes prior to quenching, as initially proposed by researchers at Permea. However, their earlier results produced fibers that had defects and had to be post-treated. Their most recent

development (2008) was shown to produce defect-free fibers using this method, but has only been shown on one polymer system currently [16].

In conjunction, during the beginning of the 1990s, researchers in the Koros group focused on manipulating a dry step in the fabrication process for flat sheet membranes, introducing a *dry/wet phase inversion* concept [41, 48-52]. In this method, the skin layer is formed by forced convective evaporation of dope components in the nascent membrane, prior to quenching in the aqueous bath. The evaporation during this step was believed to induce phase separation to form the nascent skin. The evaporation can be promoted by incorporating volatile solvents in the dopes and blowing an inert jet stream over the membrane. Most times, however, the velocity of the spin-line is sufficient to reduce external mass transfer resistances in a nascent skin and success can be achieved as long as the spinning process occurs at a sufficiently high temperature to enhance evaporation. This approach allowed production of thin skinned asymmetric hollow fiber membranes that were defect-free, requiring no post-treatment and was demonstrated on a number of systems, using commercially available polymers [11, 12, 52].

A common theme present in most of the skin formation mechanisms proposed is the increase in concentration of polymer in the outer layer by solvent removal either through a dry step or the wet step, which could cause phase separation in the nascent skin. The trajectory of the process can be represented on a ternary phase diagram as shown in Figure 4.12.

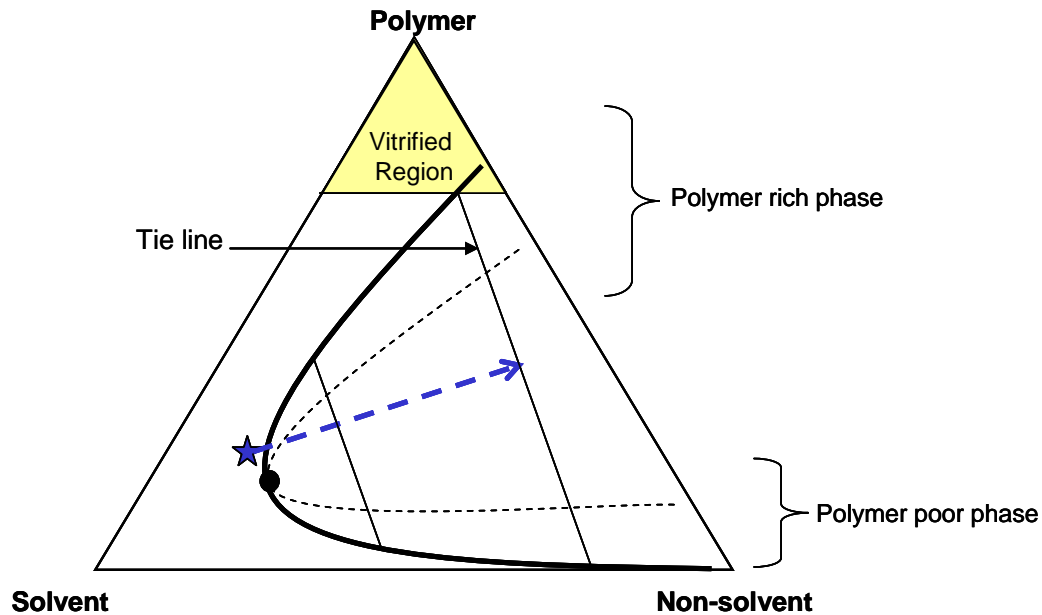


Figure 4.12: Ternary phase diagram showing the trajectory of the spinning dope as it undergoes phase separation to form polymer rich and poor phases.

The type of skin formed suggested by the phase separation mechanism shown in Figure 4.12, as indicated by the blue dashed line in the figure, would consist of a skin layer with polymer rich and poor phases. The amount of polymer rich phase present is dependent on mass transfer effects that allow how much solvent can be removed. Nevertheless, the presence of interstitial polymer poor phases after phase separation occurs would suggest that a defect-free fiber can only form if the polymer rich phases are consolidated after phase separation, as suggested by Pinnau et al. [41], which may occur through capillary forces acting on the spinodally decomposed network. Such post phase inversion coalescence of polymer rich phases seems dependent on the polymer system and on the level of plasticity in the wet polymer.

4.2.3.2 Current understanding

Depending on the dope composition, it is possible that vitrification of the skin layer may occur prior to phase separation, resulting from the evaporation of both solvent and non-solvent (if present) in the dope. This scenario is more preferable since further polymer chain rearrangements are not required in the formed skin after this dry step induced vitrification process. Clausi [12] and then Carruthers [32] proposed this idea, and found some success using Matrimid[®] polymer, a commercially available polyimide. Figure 4.13 shows a ternary phase diagram depicting this process. The blue dashed line represents the trajectory of the skin layer in the dry step and the red dashed line represents the trajectory of the substructure as it enters the unstable region of the ternary phase diagram.

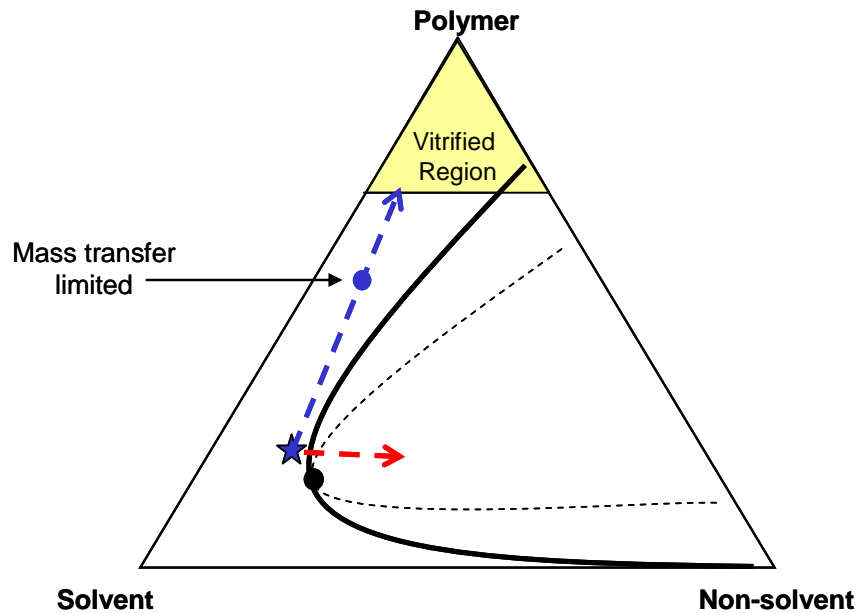


Figure 4.13: Ternary phase diagram showing the trajectory of the outer layer of a spinning dope as it undergoes vitrification to form a skin layer prior to quenching.

In this case, no consolidation is required in the outer region to form a dense defect-free layer. Then when quenching occurs, the underlying substructure phase separates to form a continuous network. This can be achieved by utilizing a volatile non-solvent as well as a volatile solvent in the dope. It may seem intuitive to add just a volatile solvent to the solution without a non-solvent, so that during evaporation, the polymer remains in the desired one phase region. However, the presence of the non-solvent is to accelerate phase separation and form a porous substructure during quenching, since the PDMC material is less hydrophobic than more traditional polymers used. Therefore, the volatility of the non-solvent is beneficial in keeping the solution in one phase and preventing the onset phase separation, which occurs when solvent is depleted and in the presence of a non-solvent. Such phase separation is preferred only for the substructure, and not the skin. However, external mass transfer effects that could affect vitrification during the dry step cannot be overlooked; especially since the time scale for the dry step is usually less than a second when operating under realistic spinning speeds (see Figure 4.13 for a depiction of this). For this reason, success was anticipated to be dependent on the temperature during spinning, the presence and composition of the volatile components, the air-gap height, and on the polymer characteristics (primarily molecular weight).

To increase polymer concentrations in the outermost layer to promote vitrification during this dry step, it seems intuitive to start with a dope with high polymer concentration; however, such high concentrations reduce the porosity of the substructure, adding undesired resistance to the membrane. Therefore, an increase in polymer molecular weight would be an alternative way to increase chain entanglement at the desired polymer concentration. Higher chain molecular weight also promotes vitrification

by reducing chain ends, which reduce the glass transition temperature of even a solvent free glassy polymer. Also, the maintenance of such a vitrified dense layer upon phase inversion during the wet quench step would be crucial and is believed to be enhanced by a higher degree of chain entanglement, since swelling effects during the phase inversion tends to degrade the selectivity of the skin.

In promoting the vitrification process, an increase in temperature is required for evaporation of the volatile components. Higher temperatures reduce the dope viscosity during extrusion, which may undermine spinnability and affect dense skin formation in a more complex way. Moreover, higher air-gap heights necessary for increasing residence times during the dry step also increases elongation stresses on the fibers. For these reasons, it is believed that a high molecular weight polymer material is of utmost importance in spinning fibers with defect-free skin layers using the PDMC material. Molecular weights used in previous attempts in spinning the PDMC polymer were about 30, 000 (M_w). It is not surprising that spinnability and the ability to form defect-free skin layers were problematic. Ultimately, of course, some limit must exist with regard to the molecular weight, since an infinitely high molecular weight material could not be dissolved.

4.3 Case studies on PDMC material

4.3.1 PDMC spinning – spinnability and macroscopic properties

Hollow fibers were spun from a high molecular weight batch of the crosslinkable monoester, PDMC (3:2), using a dope with compositions shown in Table 4.2. The

polymer molecular weight was 105,000 (M_w). The dope composition was determined using the method described in Section 4.2.1. To help accelerate phase separation during quenching, LiNO_3 was used in the dope. Also, the quench bath temperature was heated to 50–55 °C and the bath height was increased to 102 cm for this reason as well. The spinning conditions are shown in Table 4.3.

Table 4.2 Hollow fiber spinning dope compositions.

<i>Component</i>	<i>Wt %</i>
Polymer	35
NMP	42
LiNO_3	8
THF	15

Table 4.3 Hollow fiber spinning conditions.

<i>State #</i>	<i>Air-gap Height (cm)</i>	<i>Take-up Rate (m/min)</i>	<i>Dope Extrusion Rate (ml/hr)</i>	<i>Nominal Draw Ratio</i>	<i>Fiber O.D. (microns)</i>
1	10	50	180	15	~240
2	15	80	180	24	~200
3	15	122	180	37	~150
4	15	127	60	116	~80

Spinneret temperature: 46-48 °C; Aqueous quench bath temperature: 50-55 °C; Bore fluid composition: 80/20 wt.% NMP/ H_2O ; Bore fluid flow rate: 1/3 of dope extrusion rate.

As can be seen in Table 4.3, the increased molecular weight crosslinkable polyimide was able to be spun at nominal draw ratios as high as 116. This is an indication of the “spinnability” of the polymer. Previous attempts at spinning these crosslinkable polymers showed that draw-ratios were at a maximum at 9, using lower molecular weight versions. The highest take-up rate tested in this study was 127 m/min, which was the maximum testable with the apparatus used. This produced fibers with outer diameters of about 80 microns using a spinneret with a particularly large annulus. SEMs of state 2 and 4 from this experiment are shown in Figure 4.14.

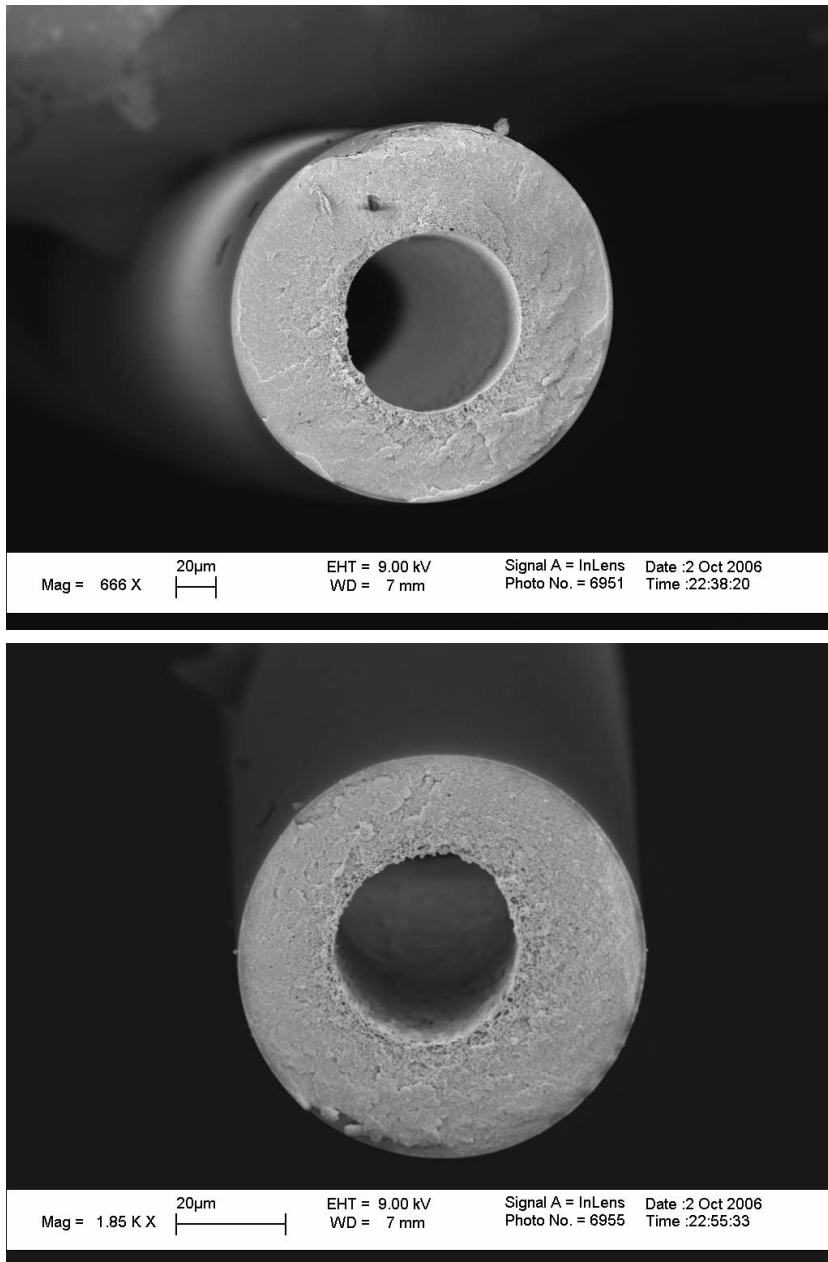


Figure 4.14: Scanning Electron Micrographs (SEM) of hollow fibers from states 2 (top) and 4 (bottom) of the PDMC (3:2) polyimide.

The nominal draw ratios do not take into account the die-swell that occurs as the polymer solution is extruded out of the spinneret. This is due to the fact that it is defined based on the ratio of the fiber take-up rate to extrusion rate. Nevertheless, the nominal draw ratios, as used here, do give a measure of the attenuation from fiber spinning. The permeation properties from state 2 of these fibers were measured and are shown in Table 4.4.

Table 4.4 Hollow fiber permeation properties.

<i>State #</i>	<i>He Perm.</i>	<i>O₂ Perm.</i>	α <i>O₂/N₂</i>	α <i>He/N₂</i>
2, Uncrosslinked (fiber)		28 GPU	4.4	
Uncrosslinked (dense film)	60.2 Barrer	7.1 Barrer	4.8	40

Conditions: feed pressure ~100 psia; temperature ~35 °C

From Table 4.4, it appears, from the permselectivities, that the fibers were defect-free. However, these fibers were subsequently tested for mixed gas CO₂/CH₄ separation and were shown to yield permselectivities of ~17 (versus ~35 for dense films) before and after crosslinking (using a 20/80 CO₂/CH₄ feed at 200 psia, 35 °C). While these fibers were viable for separating the CO₂/CH₄ pair at high pressure and were resistant to plasticization after crosslinking (see Chapter 5), their lower than intrinsic permselectivities indicate that the spinning conditions needed to be adjusted. However, to regain intrinsic permselectivity, the defective crosslinked fibers could be post-treated. This brought the CO₂/CH₄ permselectivity to 44 and the CO₂ permeance correspondingly dropped to 22 GPU from ~107 GPU, due to the added resistance of the silicone rubber

caulking layer. The minor defects suggest that the conditions for spinning these fibers were sub-optimal. While the fibers were shown to withstand the high tension spinning without spin-line breakage, the high orientation stresses occurring from excessively high draw ratios may aggravate the formation of defects in the skin layer. Moreover, typical draw-ratios used industrially are less than 10. The reason for using such high draw ratios was primarily to test the resilience of the fiber during spinning and to reduce the fiber dimensions to acceptable diameters (less than 300 μm) since the diameter of the spinneret annulus was $\sim 1270 \mu\text{m}$. The main objective of this experiment was to determine the spinnability and to achieve the desired macroscopic properties. Adequate phase separation occurred during quenching, evidenced by the circular (non-oval) fibers. Fibers were concentric and had no macrovoids and could withstand high pressures ($>1000 \text{ psi}$). The next step in the optimization process was taken by including a volatile non-solvent to the dope mixture as suggested by the analysis in Section 4.2.3.2 to aid in forming a defect-free skin layer. Also, the draw-ratios were lowered. Section 4.3.2 below shows the steps that were taken to improve the development of a defect-free fiber from the PDMC material.

4.3.2 PDMC spinning – skin integrity

4.3.2.1 First iteration spinning

A high molecular weight batch of the PDMC polymer was used for subsequent spinning as well. This time the molecular weight was 183,000 (M_w) with a polydispersity index of 3.8. A volatile non-solvent (ethanol) was added into the dope solution, and the

dope composition was determined by pre-setting the polymer, THF, and LiNO₃ concentrations and following the method described in Section 4.2.1, which was carried out at room temperature. The final dope formula is shown in Table 4.5 and was spun under the conditions shown in Table 4.6.

Table 4.5 Hollow fiber spinning dope compositions.

<i>Component</i>	<i>Wt %</i>
Polymer	35
NMP	33
LiNO ₃	6.5
THF	15
Ethanol	10.5

Table 4.6 Hollow fiber spinning conditions.

<i>State #</i>	<i>Air-gap Height (cm)</i>	<i>Take-up Rate (m/min)</i>	<i>Dope Extrusion Rate (ml/hr)</i>	<i>Nominal Draw Ratio</i>	<i>Fiber O.D. (microns)</i>
1	29	5.5	60	5	~480

Spinneret temperature: 55 °C; Aqueous quench bath temperature: 50 °C; Bore fluid composition: 80/20 wt.% NMP/H₂O; Bore fluid flow rate: 1/3 of dope extrusion rate.

The spinneret used was the same as that used previously, with an annulus size of 1270 μm . Due to this, the reduced draw ratios came with a trade-off, as the fibers produced were much larger ($\sim 480 \mu\text{m}$ vs. $\sim 200 \mu\text{m}$), which was above the desired limit ($< 300 \mu\text{m}$). The disadvantage here was that the larger fibers could not withstand pressures greater than ~ 700 psi. Figure 4.15 shows the magnitude of these differences in fiber sizes. Nevertheless, the permeation properties of the fibers made from this experiment were determined at lower pressures and can be seen in Table 4.7.

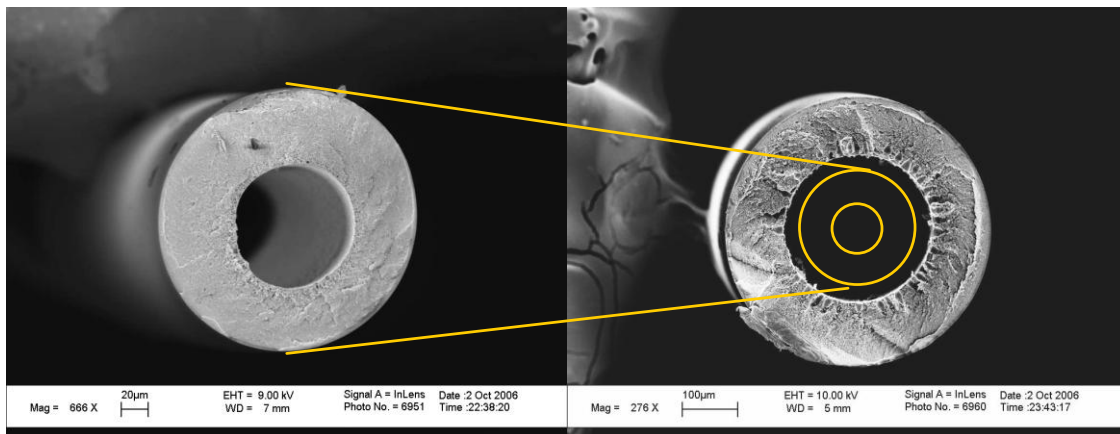


Figure 4.15: Schematic showing the differences in fiber sizes from using higher draw ratios (left) and lower draw ratios (right) as obtained from a spinneret with relatively large annulus ($\sim 1270 \mu\text{m}$)

Table 4.7 Hollow fiber permeation properties.

<i>State #</i>	<i>He Perm.</i>	<i>O₂ Perm.</i>	α	α
			<i>O₂/N₂</i>	<i>He/N₂</i>
1, Uncrosslinked (fiber)	130 GPU	19 GPU	4.8	31
Uncrosslinked (dense film)	60.2 Barrer	7.1 Barrer	4.8	40

Conditions: feed pressure ~100 psia; temperature ~35 °C

The gas permeation properties from this experiment indicate that the performance of the spun fibers had greatly improved. The O₂/N₂ permselectivity was at the intrinsic polymer value. The CO₂/CH₄ separation capability of these fibers increased about twice in comparison to the values obtained previously. The main differences were the addition of the volatile non-solvent (to keep the skin in one phase before vitrification), increasing the spinneret temperature from ~48 °C to 55 °C, and lowering the draw-ratios. However, as previously stated, the lower draw-ratios caused larger fiber diameters using the spinneret with a large annulus, and this limits the pressure handling capability of the fibers. The selectivity for He/N₂ also suggests the presence of significant substructure resistance, and is probably a consequence of the thick walled fibers.

4.3.2.2 High pressure defect-free fibers

To spin smaller diameter fibers at normal draw-ratios (< 10), a new spinneret was developed. The design of this spinneret was similar to that used previously (designed by Pesek [53]), but the annulus and bore needle sizes were reduced significantly. The outer

annulus was reduced from 1270 μm to 650 μm , while the bore needle OD was reduced from 671 μm to 320 μm .

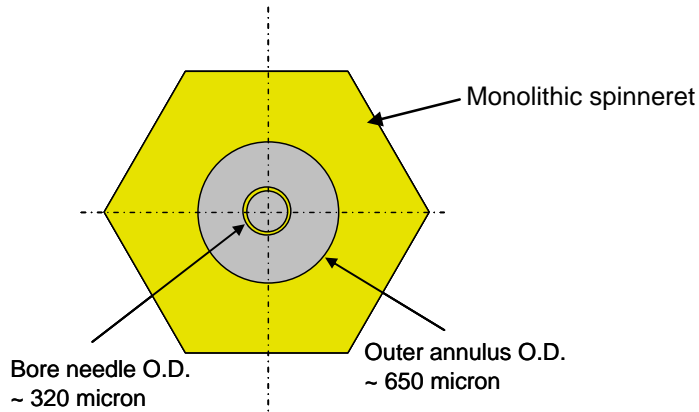


Figure 4.16: Schematic illustrating the sizes of the annulus and bore needle of the spinneret designed in this work for developing smaller OD fibers for high pressure applications.

Here, the same polymer with a molecular weight of 183,500 (M_w) was used and the dope composition was similar to that used previously. The minor change in the dope formulation was in the slightly reduced concentration of non-solvent (ethanol) and correspondingly increased solvent concentration. This brings the dope slightly further away from the binodal in the one phase region. This also prevents early phase separation of the nascent skin. The spinneret temperature this time was increased to 70 $^{\circ}\text{C}$ (from 55 $^{\circ}\text{C}$). The dope formula and spinning conditions can be seen in Tables 4.8 and 4.9 respectively. Two states were spun, with air gap heights as high as 33 cm.

Table 4.8 Hollow fiber spinning dope compositions.

<i>Component</i>	<i>Wt %</i>
Polymer	35
NMP	35
LiNO ₃	6.5
THF	15
Ethanol	8.5

Table 4.9 Hollow fiber spinning conditions.

<i>State #</i>	<i>Air-gap Height (cm)</i>	<i>Take-up Rate (m/min)</i>	<i>Dope Extrusion Rate (ml/hr)</i>	<i>Nominal Draw Ratio</i>	<i>Fiber O.D. (microns)</i>
1	33	50	120	6.3	~200
2	33	50	180	4.2	~230

Spinneret temperature: 70 °C; Aqueous quench bath temperature: 50 °C; Bore fluid composition: 80/20 wt.% NMP/H₂O; Bore fluid flow rate: 1/3 of dope extrusion rate.

The result of the experiment was that smaller diameter fibers could be obtained (for high pressure applications). More interestingly, a denser skin layer was formed, evidenced by the super high permselectivities as shown in Table 4.10. The permeation results from this experiment can be seen in Table 4.10.

Table 4.10 Hollow fiber permeation properties.

<i>State #</i>	<i>He Perm.</i>	<i>O₂ Perm.</i>	α	α
			<i>O₂/N₂</i>	<i>He/N₂</i>
1, uncrosslinked (fiber)	228 GPU	25 GPU	6.1	57
2, uncrosslinked (fiber)	273 GPU	31 GPU	6.2	55
2, uncrosslinked, aged ~300 days (fiber)	175 GPU	14 GPU	6.4	78
Uncrosslinked (dense film)	60.2 Barrer	7.1 Barrer	4.8	40

Conditions: feed pressure ~100 psia; temperature ~35 °C.

It can be seen from the permeation results that the fibers were superior to those obtained before. Here, due to the smaller spinneret annulus and high extrusion rates, shearing stresses were greater, which orients polymer chains on the outside, causing the permselectivity in the fiber to be greater than the permselectivity in dense films. This phenomenon has also been observed by other researchers [37-39]. The increase in diffusion selective resistance is reflected in the He/N₂ selectivity, as it shows a much higher increase from the dense film value than the case for O₂/N₂. The chain orientation effects were shown to still maintain the high selectivity after even 300 days as evidenced by the aged fiber. It can be seen that aging also caused further densification of the skin layer in the fibers (evidenced by further increase in permselectivity over time). This aging phenomenon occurs as the polymer chains in the skin layer relax to a more equilibrium

state and is a characteristic of glassy polymers. During this relaxation process, the fiber skin loses the excess free volume trapped during the vitrification and phase separation processes of spinning. Physical ageing leads to increases in selectivity and decreases in permeability. More discussion on physical ageing effects in these fibers can be seen in Chapter 5. When these fibers are annealed at 200 °C for 2 h, the O₂/N₂ selectivity drops to ~5.3 and the He/N₂ is about 71. This suggests that the chain orientation effects may reduce after crosslinking. However, the annealed (crosslinked) pure gas selectivity is still quite higher than the dense film crosslinked O₂/N₂ selectivity, which is about the same as the uncrosslinked selectivity for O₂/N₂.

The advantage of using the higher molecular weight crosslinkable polymers was apparent from being able to extrude the solution at higher spinneret temperatures, while maintaining significant polymer chain entanglement in the air-gap. The elevated spinneret temperature allows evaporation of volatiles (particularly THF) in the solution, which promotes vitrification on the outer skin layer of the nascent hollow fiber membrane as it passes through the air-gap. The evaporation of ethanol helps keep the skin in one phase until vitrification occurs. A polymer solution with a higher level of chain entanglement is believed to form a denser, defect-free skin layer once vitrification occurs as evidenced by the selectivities observed, which are at or greater than the dense film values. Figure 4.17 shows pictures of the cross-section of the skin layer and porous fiber wall.

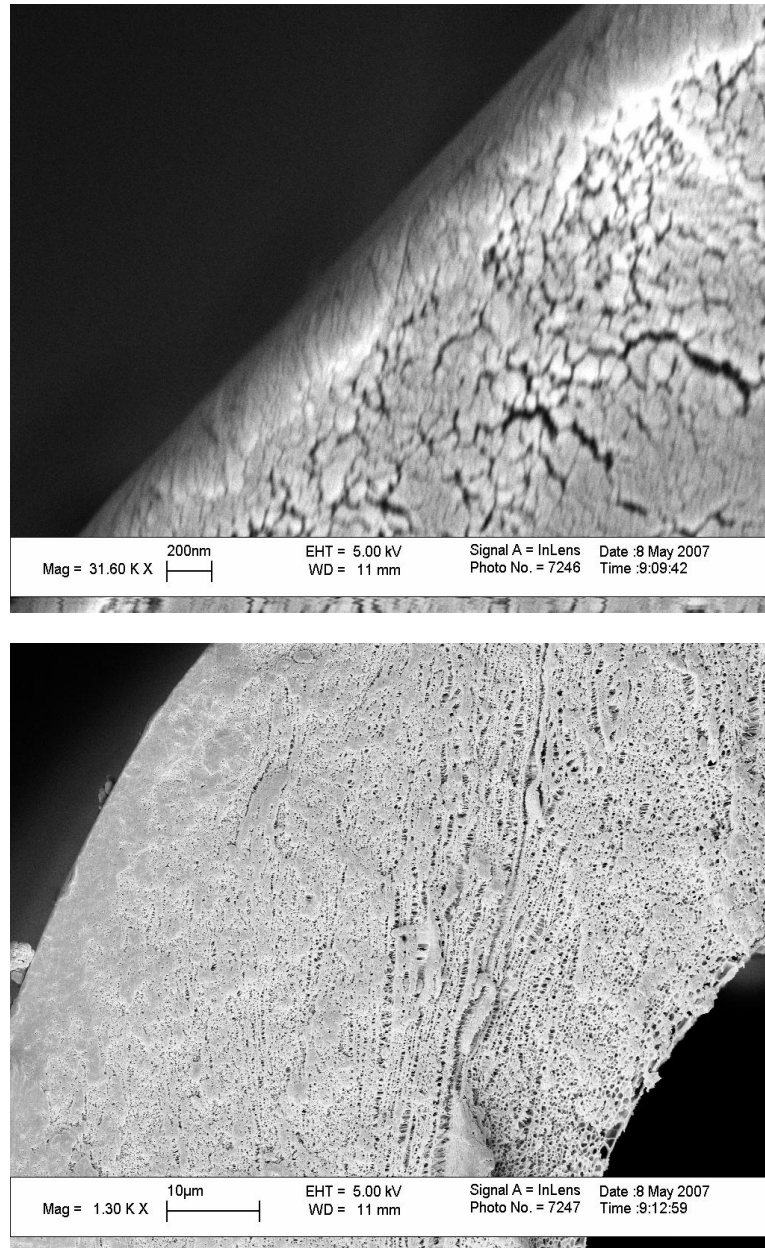


Figure 4.17: Scanning Electron Micrographs of a cross-section of the PDMC hollow fiber, showing the skin layer (top) and the porous fiber wall (bottom) that acts mostly as a support for the skin layer.

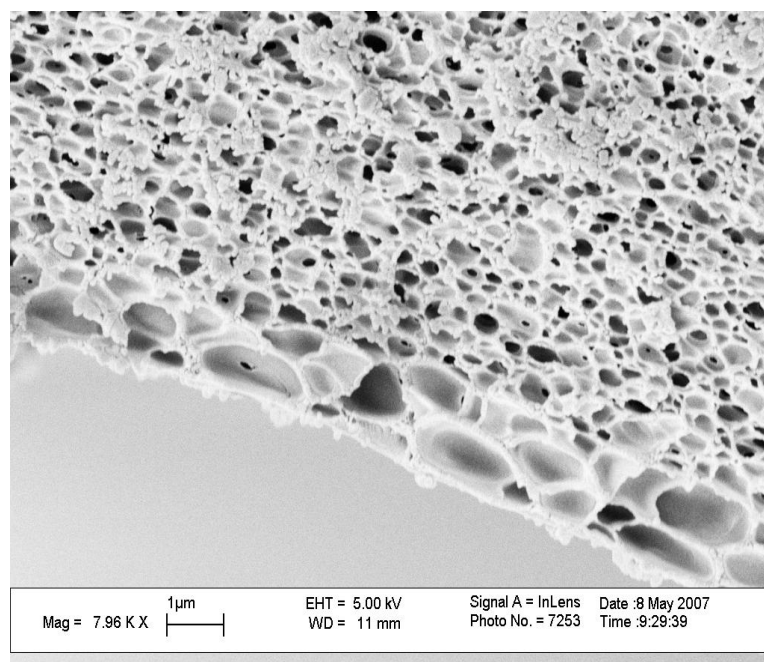


Figure 4.18: Scanning Electron Micrograph of a cross-section of the PDMC hollow fiber, showing the porosity of the substructure adjacent to the bore.

4.3.3 Preliminary characterization of defect-free fibers with a model natural gas feed and summary of Chapter 4

The higher molecular weight PDMC polymer was crosslinked by annealing the hollow fiber membrane under vacuum at 200 °C for 2 hrs. The crosslinked hollow fiber membranes were tested for their gas separation properties. Using a feed gas mixture consisting of 20/80 CO₂/CH₄ at 35 °C, the crosslinked hollow fibers were tested with the feed at 200 psi, and the CO₂ permeance was ~46 GPU while the CO₂/CH₄ permselectivity was recorded to be 43. The CO₂/CH₄ permselectivity at this pressure also

indicates the presence a defect-free skin layer in the hollow fiber membrane, thus requiring no further post-treatment. These defect-free PDMC hollow fibers made from the higher molecular weight polymer show permeances and selectivities higher than that for the lower molecular weight version, where the molecular weight was $\sim 29,000$ (M_w) [22, 33]. The lower molecular weight version of the PDMC hollow fiber membrane showed a CO_2 permeance of ~ 35 GPU and the CO_2/CH_4 permselectivity of 32 [22] after crosslinking and under similar test conditions. After crosslinking, the polymer chains theoretical attain “infinite” molecular weight. Thus, the enhancement in the performance of the transport properties and mechanical properties (non-brittleness) of the higher molecular weight polymer versus the lower molecular weight polymer after crosslinking suggests the presence of defects in the macromolecular crosslinked network (as illustrated in Chapter 3) that reduce the effect of the crosslinking on the lower molecular weight versions. More discussion on the effects of crosslinking and results on the effect of high pressure CO_2 on the defect-free fibers are shown in Chapter 5.

4.4 References

1. Baker, R.W., *Future Directions of Membrane Gas Separation Technology*. Industrial & Engineering Chemistry Research, 2002. **41**(6): p. 1393-1411.
2. Ekiner, O.M. and G. Vassilatos, *Polymeric membranes*. 1992, E. I. Du Pont de Nemours and Company: U.S.A.
3. Loeb, S. and S. Sourirajan, *Seawater Demineralization by Means of an Osmotic Membrane*. Adv. Chem. Ser., 1962. **38**: p. 117.
4. Lonsdale, H.K., *The evolution of ultrathin synthetic membranes*. Journal of Membrane Science, 1987. **33**(2): p. 121-136.
5. So, M.T., et al., *Preparation of asymmetric Loeb-Sourirajan membranes*. Journal of Polymer Science, Polymer Letters Edition, 1973. **11**(3): p. 201-5.
6. Stern, S.A., S.K. Sen, and A.K. Rao, *Permeation of gases through symmetric and asymmetric [Loeb type] cellulose acetate membranes*, in *J. Macromol. Sci., Phys.* 1974. p. 507-28.
7. Strathmann, H., P. Scheible, and R.W. Baker, *A Rationale for the Preparation of Loeb-Sourirajan-Type Cellulose Acetate Membranes*. J. Appl. Pol. Sci., 1971. **15**: p. 811-828.
8. Puri, P.S., *Fabrication of hollow fibre gas separation membranes*. Gas Separation & Purification, 1990. **4**(1): p. 29-36.
9. Ekiner, O.M. and G. Vassilatos, *Polyaramide hollow fibers for hydrogen/methane separation -- spinning and properties*. Journal of Membrane Science, 1990. **53**(3): p. 259-273.
10. Wallace, D.W., C. Staudt-Bickel, and W.J. Koros, *Efficient development of effective hollow fiber membranes for gas separations from novel polymers*. Journal of Membrane Science, 2006. **278**: p. 92-104.
11. Kosuri, M.R. and W.J. Koros, *Defect-free asymmetric hollow fiber membranes from Torlon®, a polyamide-imide polymer, for high-pressure CO₂ separations*. Journal of Membrane Science, 2008. **320**(1-2): p. 65-72.

12. Clausi, D.T. and W.J. Koros, *Formation of defect-free polyimide hollow fiber membranes for gas separations*. Journal of Membrane Science, 2000. **167**: p. 79–89.
13. McKelvey, S.A., D.T. Clausi, and W.J. Koros, *A guide to establishing hollow fiber macroscopic properties for membrane applications*. Journal of Membrane Science, 1997. **124**: p. 223-232.
14. Fritzsche, A.K., et al., *Polysulfone hollow-fiber membranes spun from Lewis acid:base complexes. II. The effect of Lewis acid-to-base ratio on membrane structure*. Journal of Applied Polymer Science, 1990. **39**(9): p. 1949-56.
15. Fritzsche, A.K., et al., *Characterization of asymmetric hollow fibre membranes with graded-density skins*. Gas Separation & Purification, 1989. **3**(3): p. 106-116.
16. Peng, N. and T.S. Chung, *The effects of spinneret dimension and hollow fiber dimension on gas separation performance of ultra-thin defect-free Torlon® hollow fiber membranes*. Journal of Membrane Science, 2008. **310**(1-2): p. 455-465.
17. Henis, J.M.S. and M.K. Tripodi, *Composite hollow fiber membranes for gas separation: the resistance model approach*. Journal of Membrane Science, 1981. **8**(3): p. 233-246.
18. Henis, J.M.S. and M.K. Tripodi, *Multicomponent Membranes for Gas Separations*. 1980, Monsanto Co.: United States.
19. Wallace, D.W., et al., *Characterization of crosslinked hollow fiber membranes*. Polymer, 2006. **47**(4): p. 1207-1216.
20. Baker, R.W. and K. Lokhandwala, *Natural Gas Processing with Membranes: An Overview*. Ind. Eng. Chem. Res., 2008. **47**: p. 2109-2121.
21. Peters, R., *Hollow fiber membrane materials: applications and limitations*, I. Omole, Editor. 2008: Houston, TX.
22. Wallace, D.W., et al., *Characterization of crosslinked hollow fiber membranes*. Polymer, 2006. **47**: p. 1207–1216.
23. Wallace, D.W., *Crosslinked Hollow Fiber Membranes for Natural Gas Purification and Their Manufacture from Novel Polymers*, in *Chemical Engineering*. 2004, The University of Texas at Austin: Austin, Texas. p. 202.

24. Bhattacharya, S. and S.-T. Hwang, *Concentration polarization, separation factor, and Peclet number in membrane processes*. Journal of Membrane Science, 1997. **132**(1): p. 73-90.
25. Wang, R., et al., *Characterization of hollow fiber membranes in a permeator using binary gas mixtures*. Chemical Engineering Science, 2002. **57**: p. 967 – 976.
26. Clausi, D.T., S.A. McKelvey, and W.J. Koros, *Characterization of substructure resistance in asymmetric gas separation membranes*. Journal of Membrane Science, 1999. **160**(1): p. 51-64.
27. Hillock, A.M.W. and W.J. Koros, *Cross-Linkable Polyimide Membrane for Natural Gas Purification and Carbon Dioxide Plasticization Reduction*. Macromolecules, 2007. **40**: p. 583-587.
28. Cussler, E.L., *Diffusion, Mass Transfer in Fluid Systems*. 2nd ed. 1997, Cambridge, UK: Cambridge University Press. 580.
29. Hines, A.L. and R.N. Maddox, *Mass Transfer: Fundamentals and Applications*. 1985, Englewood Cliffs: Prentice-Hall, Inc. 542.
30. Carruthers, S.B., *Integral-Skin Formation in Hollow Fiber Membranes for Gas Separations*, in *Chemical Engineering*. 2001, The University of Texas at Austin: Austin, Texas. p. 233.
31. Baker, R.W., *Membrane Technology and Applications*. 2nd ed. 2004: John Wiley & Sons, Ltd. 538 pp.
32. Carruthers, S.B., G.L. Ramos, and W.J. Koros, *Morphology of Integral-Skin Layers in Hollow-Fiber Gas-Separation Membranes*. Journal of Applied Polymer Science, 2003. **90**: p. 399–411.
33. Wallace, D.W., *PDMC polymer*, I. Omole, Editor. 2007: Atlanta.
34. Flory, P.J., *Principles of Polymer Chemistry*. 1953, Ithaca: Cornell University Press.
35. Mulder, M., *Basic Principles of Membrane Technology*. 1996: Kluwer Academic Publishers: Dordrecht.
36. Mulder, M. and Editor, *Basic Principles of Membrane Technology, Second Edition*. 1996. 564 pp.

37. Ismail, A.F., et al., *Direct measurement of rheologically induced molecular orientation in gas separation hollow fibre membranes and effects on selectivity*. Journal of Membrane Science, 1997. **126**(1): p. 133-137.
38. Ismail, A.F., et al., *Production of super selective polysulfone hollow fiber membranes for gas separation*. Polymer, 1999. **40**(23): p. 6499-6506.
39. Sharpe, I.D., A.F. Ismail, and S.J. Shilton, *A study of extrusion shear and forced convection residence time in the spinning of polysulfone hollow fiber membranes for gas separation*. Separation and Purification Technology, 1999. **17**(2): p. 101-109.
40. *CRC Handbook of Chemistry and Physics*. 70 ed, ed. R.C. Weast. 1989, Boca Raton, FL: CRC Press Inc.
41. Pinnau, I. and W.J. Koros, *A Qualitative Skin Layer Formation Mechanism for Membranes Made by Dry/ Wet Phase Inversion*. Journal of Polymer Science: Part B Polymer Physics, 1993. **31**: p. 419-427.
42. Castellari, C. and S. Ottani, *Preparation of reverse osmosis membranes. A numerical analysis of asymmetric membrane formation by solvent evaporation from cellulose acetate casting solutions*. Journal of Membrane Science, 1981. **9**(1-2): p. 29-41.
43. Krantz, W.B., et al., *Theoretical study of the transport processes occurring during the evaporation step in asymmetric membrane casting*. Journal of Membrane Science, 1986. **29**(1): p. 11-36.
44. Pinnau, I. and W.J. Koros, *A qualitative skin-layer formation mechanism for membranes made by dry/wet phase inversion*. Journal of Polymer Science, Part B: Polymer Physics, 1993. **31**(4): p. 419-27.
45. Yilmaz, L. and A.J. McHugh, *Modelling of asymmetric membrane formation. I. Critique of evaporation models and development of a diffusion equation formalism for the quench period*. Journal of Membrane Science, 1986. **28**(3): p. 287-310.
46. van't Hof, J.A., et al., *Preparation of asymmetric gas separation membranes with high selectivity by a dual-bath coagulation method*. Journal of Membrane Science, 1992. **70**(1): p. 17-30.

47. Chung, T.S., S.K. Teoh, and X. Hu, *Formation of ultrathin high-performance polyethersulfone hollow-fiber membranes*. Journal of Membrane Science, 1997. **133**(2): p. 161-175.
48. Pinnau, I. and W.J. Koros, *Defect-free ultrahigh flux asymmetric membranes*, in U.S. 1990, (University of Texas System, USA). Us. p. 15 pp.
49. Ingo Pinnau, W.J.K., *Structures and gas separation properties of asymmetric polysulfone membranes made by dry, wet, and dry/wet phase inversion*. Journal of Applied Polymer Science, 1991. **43**(8): p. 1491-1502.
50. Pinnau, I. and W.J. Koros, *Influence of quench medium on the structures and gas permeation properties of polysulfone membranes made by wet and dry/wet phase inversion*. Journal of Membrane Science, 1992. **71**(1-2): p. 81-96.
51. Pesek, S.C. and W.J. Koros, *Aqueous quenched asymmetric polysulfone membranes prepared by dry/wet phase separation*. Journal of Membrane Science, 1993. **81**: p. 71-88.
52. Pesek, S.C. and W.J. Koros, *Aqueous quenched asymmetric polysulfone hollow fibers prepared by dry/wet phase separation*. Journal of Membrane Science, 1994. **88**: p. 1-19.
53. Pesek, S.C., *Aqueous quenched asymmetric polysulfone flat sheet and hollow fiber membranes prepared by dry/wet phase separation*. 1993. p. 260 pp.

CHAPTER 5

CROSSLINKABLE ASYMMETRIC HOLLOW FIBER MEMBRANES FOR NATURAL GAS (CO₂/CH₄) SEPARATIONS AND PLASTICIZATION RESISTANCE

5.1 Introduction

This chapter contains the experimental characterization results for the PDMC hollow fiber membranes made in Chapter 4. The results demonstrate the efficacy of the crosslinking approach in stabilizing the membranes. The stability is illustrated using aggressive feed conditions (higher pressures) with pure CO₂ and binary mixed gas CO₂/CH₄ feeds. All calculations are based on fugacity driving force as opposed to pressure. The reason for this is discussed in this chapter. The performance stability against high pressure CO₂ feeds, and the effects of crosslinking, CO₂ concentration and pressure, fiber ageing, and test temperature were also investigated in the next sections. The experimental uncertainty in the permeation data is within ~5% based on multiple permeation readings.

5.2 Natural gas permeation and stability for high CO₂ content feeds

5.2.1 Effect of crosslinking temperature on separation performance of *defect-free* membranes

In characterizing the defect-free fibers from Section 4.3.2.2 of Chapter 4, the behavior of the dense film analogues were studied. It is observed that after crosslinking the dense films, both CO₂/CH₄ permselectivity and CO₂ permeability increase. The latter observation is contrary to conventional wisdom, which suggests that crosslinking causes densification of the matrix and leads to reduction in permeability. The materials studied here are unique in the sense that the transport effects are dependent on the crosslinking agents, which may vary in size and reactivity. Tables 5.1 shows the dense film results for the PDMC polymer from Hillock et al. [1].

Table 5.1: Pure gas permeation properties due to crosslinking the PDMC films from Hillock's work [1]. Test temperature 35 °C, pressure 65 psia.

<i>Membrane form</i>	<i>CO₂ Perm. (Barrer)</i>	α <i>CO₂/CH₄</i>
Uncrosslinked	17.1	34.0
Crosslinked (220 °C)	57.5	37.1
Crosslinked (295 °C)	77.3	39.9

The increase in permeability in dense films due to crosslinking is presumably due to the creation of free volume in the polymer matrix. This may occur due to the crosslinking agent “propping” the polymer chain segments apart, and/or the elimination of one of the monoesterification crosslinking agent during the transesterification reaction at each point

of crosslinking. The increase in permselectivity is presumably reflective of the reduced chain mobility from the crosslinking, which makes the polymer more diffusion selective; however, an increase in free volume may also make the polymer more sorption selective for the more condensable CO₂. This hypothesis is supported by sorption measurements carried out on crosslinked dense films [2]. The long chain aliphatic diol crosslinking agents tend to be more reactive than shorter chain or non-aliphatic ones, and this may also translate to a high crosslinking degree at a given final annealing/crosslinking temperature and higher permeability [2]. For instance, a butylene glycol crosslinking agent (4-carbon chain diol) was shown to be more reactive than a 1,4-cyclohexanedimethanol, ethylene glycol, and 1,4-benzenedimethanol crosslinking agent [3]. The effects on permeability are shown in Figure 5.1.

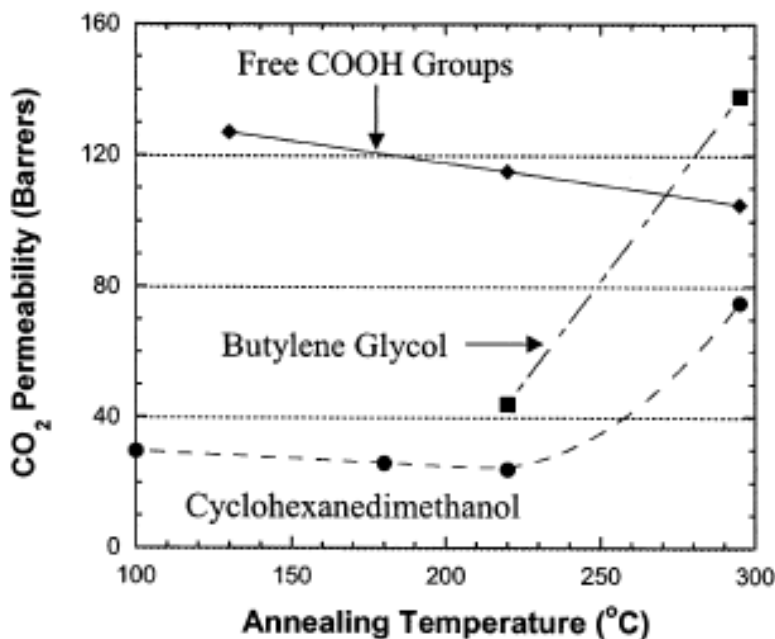


Figure 5.1: Effect of crosslinking agent and crosslinking temperature on permeability in dense film membranes [2]. Note that these polymers have different backbone structures from the ones used in this work so their absolute permeability values are not directly comparable.

It can be observed from Figure 5.1 that the permeability can increase with the polymers with crosslinking agents (versus free COOH), more so with the more reactive butylene glycol. However, with the free acid groups, the permeability decreases with annealing temperature.

A study to determine the effects of crosslinking temperatures was performed on the PDMC (3:2) hollow fibers. Permeation in these hollow fibers were performed using less than 1% stage cuts. Also, the permeation was allowed to reach steady state over time, during which data was recorded approximately after every hour and did not deviate more than ~5% within the first 2 h. Note that diffusional steady state should have occurred in a matter of seconds for these very thin selective layers on the fibers, so the 2 h is felt to be quite conservative. Therefore 2 h of permeation was chosen for consistency between data sets. Moreover, this helped in conserving gas since the stage cuts were less than 1% and the retentate stream is vented to the atmosphere. *Decreases in permeances* and increases in permselectivity were observed in hollow fibers. Table 5.2 shows the performance of an annealed PDMC hollow fiber.

Table 5.2: Mixed gas permeation properties due to crosslinking the PDMC fibers used in this work. Feed: 20/80 CO₂/CH₄ gas at 200 psia, 35 °C.

<i>Membrane form</i>	<i>CO₂ Perm. (GPU)</i>	<i>α CO₂/CH₄</i>
Uncrosslinked	206	30
Crosslinked (200 °C, 2h)	57	41

From the data in Table 5.2, it can be inferred that the heating both causes crosslinking and also anneals the fiber, thereby accelerating the ageing process of the fiber, since chain mobility is increased during heating. More discussion on the effects of ageing can be seen in Section 5.2.5. Both crosslinking and ageing cause an increase in permselectivity; however, there is a varied effect on the permeance. Usually, declines in permeances occur due to declines in permeability as seen in ageing dense films [4-8]. Therefore, since the decline in permeability does not occur in thick dense films after crosslinking, the decline in permeance seen with the asymmetric hollow fibers can probably be attributed to a densification of the skin layer. This is further inferred since the added resistance is selective to the gas molecules, evidenced by the increase in permselectivity.

Other crosslinking temperatures were investigated to determine the effect of annealing temperature on stability of the fibers against high pressure CO₂. A model natural gas mixture with 50% CO₂ at high pressures was used for this experiment. Figures 5.2–5.5 below show the plots for the permselectivity, separation factor, and permeances for CO₂ and CH₄ for fibers crosslinked at different crosslinking temperatures.

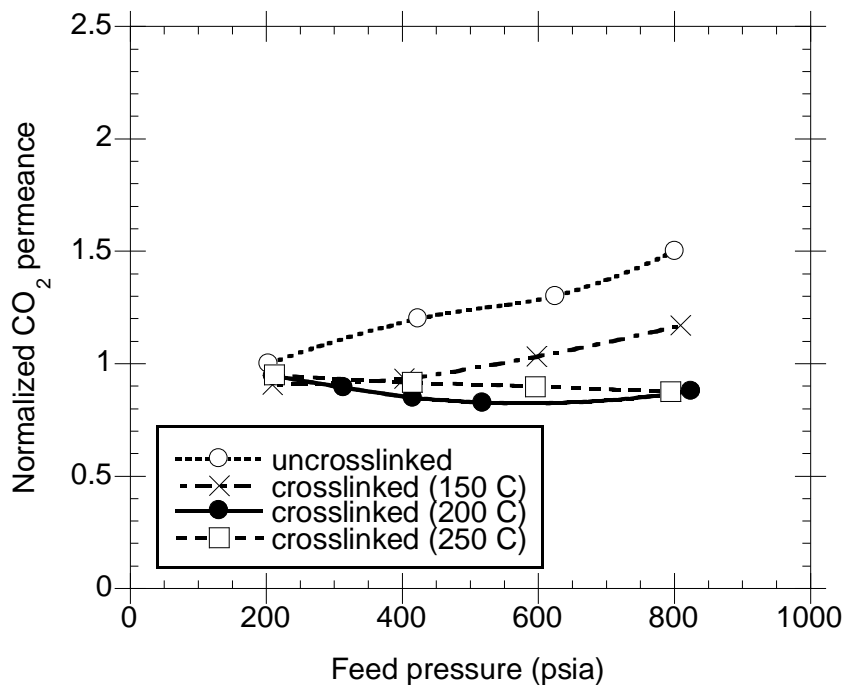


Figure 5.2: Effect of crosslinking temperature on CO₂ permeance using a mixed gas feed with 50% CO₂. Test temperature was 35 °C.

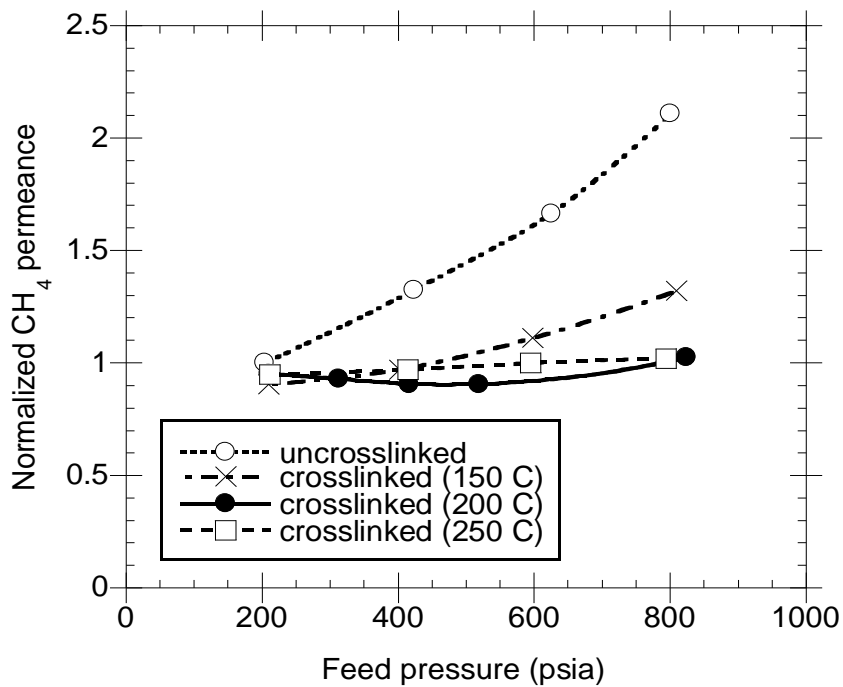


Figure 5.3: Effect of crosslinking temperature on CH₄ permeance using a mixed gas feed with 50% CO₂. Test temperature was 35 °C.

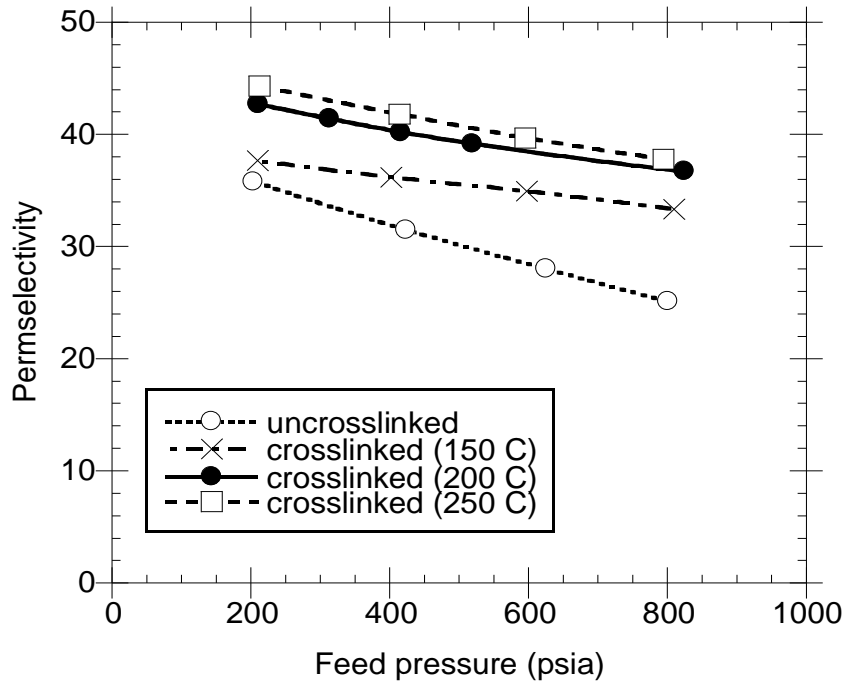


Figure 5.4: Effect of crosslinking temperature on permeability for CO₂/CH₄ mixed gas with 50% CO₂. Test temperature was 35 °C.

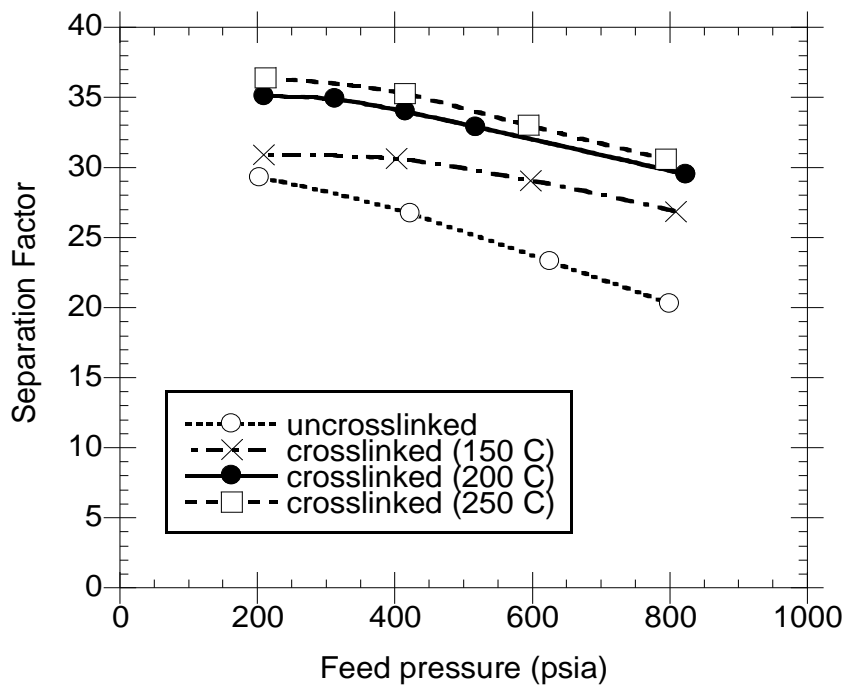


Figure 5.5: Effect of crosslinking temperature on separation factor for CO₂/CH₄ mixed gas with 50% CO₂. Test temperature was 35 °C.

From the plots above, it can be seen that the uncrosslinked fibers are clearly unstable in the presence of high CO₂ partial pressures as evidenced by the lower permselectivities and the upswing in both the CO₂ and CH₄ permeance isotherms. Due to the absence of crosslinking in these fibers, the CH₄ permeance increases more than the CO₂ permeance, which causes a significant drop in permselectivity over the pressure range tested. With the absence of crosslinking, an increase in the CO₂ partial pressure causes the membrane to swell and a loss in the CH₄ product is observed, which is evidenced by the huge upswing in its permeance compared to that for CO₂. The fiber crosslinked at 150 °C shows a slightly different trend. The selectivities are higher than the uncrosslinked version, indicating that a higher crosslinking degree was achieved; however, the selectivities were lower than those for the higher temperature crosslinked fibers, which suggest that the fiber didn't crosslink to the extent as did the 200 °C and 250 °C fibers. Additionally, for the 150 °C crosslinked case, there is an upswing in the permeances of both CO₂ and CH₄, indicative of significant swelling occurring. However, the degree at which the CH₄ permeance isotherm increases relative to that for CO₂ is reduced here compared with the uncrosslinked case. This suggests that the fiber is crosslinked somewhat and enough to prevent excessive losses of the CH₄ product due to plasticization. However, a higher crosslinking degree is recommended since both of the lower temperature annealing samples show upturns, which indicate signs of potential instabilities that would cause loss of more of the CH₄ product.

The 200 °C and 250 °C crosslinked fibers both show higher selectivities than the uncrosslinked and 150 °C crosslinked versions, and their permeance isotherms show no

drastic upturns for both CO₂ and CH₄. This indicates that the degree of crosslinking at these temperatures is sufficient to stabilize the fibers. Also, solid state ¹³C NMR, as shown in Figure 5.6, suggests that at 200 °C, ~90 % crosslinking occurs. This was estimated based on calculations from the peak areas in the NMR spectrum. The peak under the green arrow in Figure 5.6 represents the middle aliphatic carbon from the propane diol crosslinking agent. From two monoester groups with each a pendant alcohol, it takes only one to crosslink. Therefore, 50% of the alcohols should evolve when all the monoesters are fully crosslinked. In Figure 5.6, the NMR spectra suggest that 45% of the alcohols had evolved, which translates to ~90% crosslinking at 200 °C. However, analysis of these results from the peak areas must be evaluated cautiously as resolution from solid state spectra is not clear-cut as indicated by the broad peaks. Nevertheless, due to scale-up considerations using lower cost conventional ovens, lower temperatures are preferred commercially. This suggests that, without the intervention of catalysts (as discussed in Chapter 7), the 200 °C crosslinking temperature seems optimal.

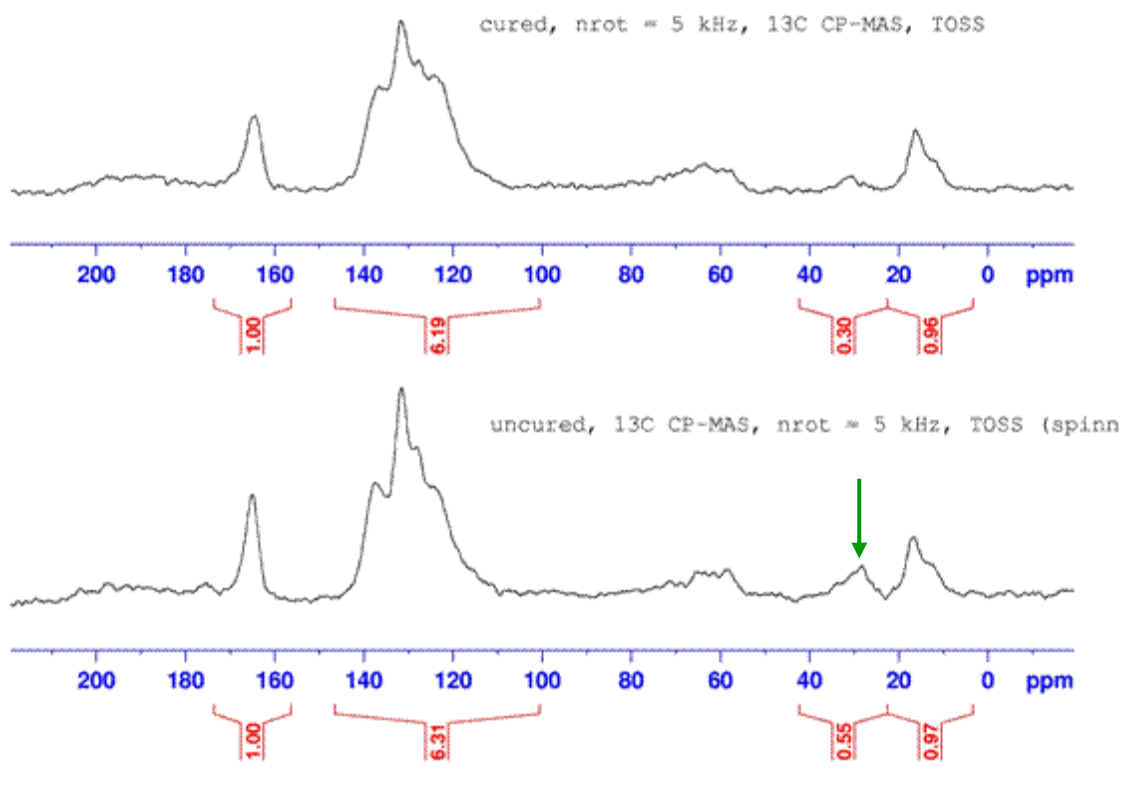


Figure 5.6: Solid state ^{13}C NMR spectrum of an uncrosslinked PDMC polymer (lower) and a 200 °C crosslinked PDMC polymer (above). The green arrow indicates the middle aliphatic carbon from the propane diol crosslinking agent.

5.2.2 Effect of CO_2 concentration in feed

5.2.2.1 Permeation experiments on defect-free crosslinked PDMC

The permeation properties of the 200 °C crosslinked fibers were investigated with a reduced percentage of CO_2 to determine the characteristics of the membrane with less aggressive feeds. Figures 5.7–5.10 show the results from this experiment.

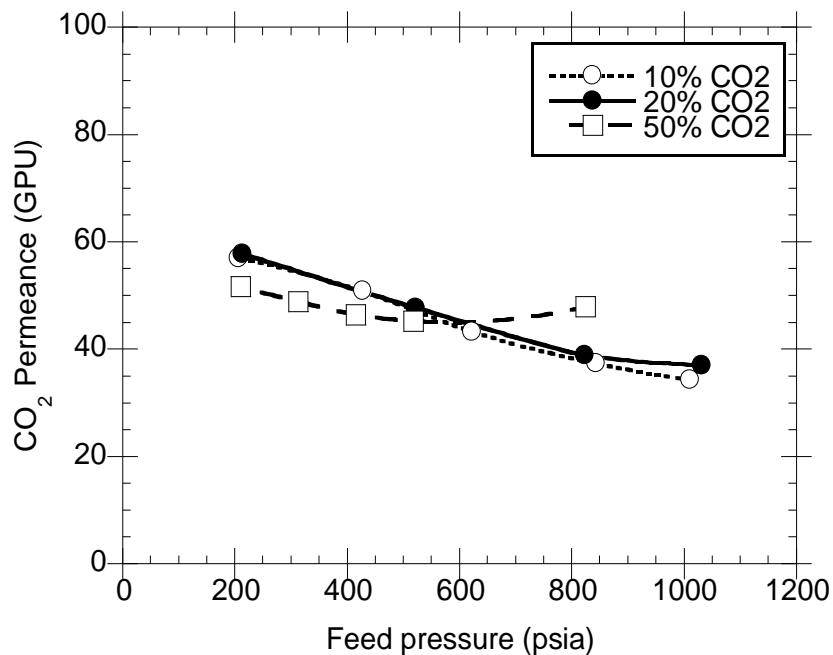


Figure 5.7: Carbon dioxide permeance versus feed pressure for 200 °C crosslinked PDMC hollow fibers tested using different feed concentrations of CO₂ at 35 °C.

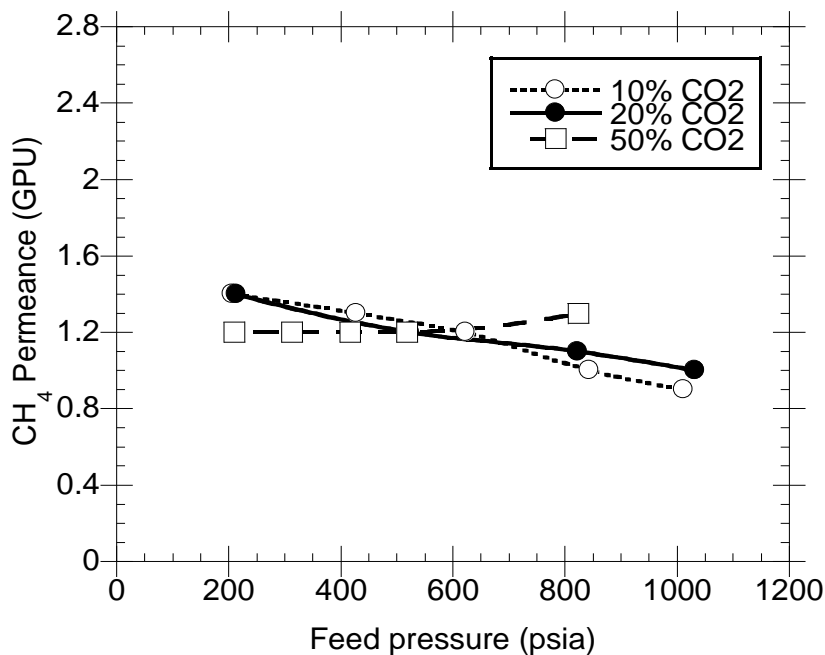


Figure 5.8: Methane permeance versus feed pressure for 200 °C crosslinked PDMC hollow fibers tested using different feed concentrations of CO₂ at 35 °C.

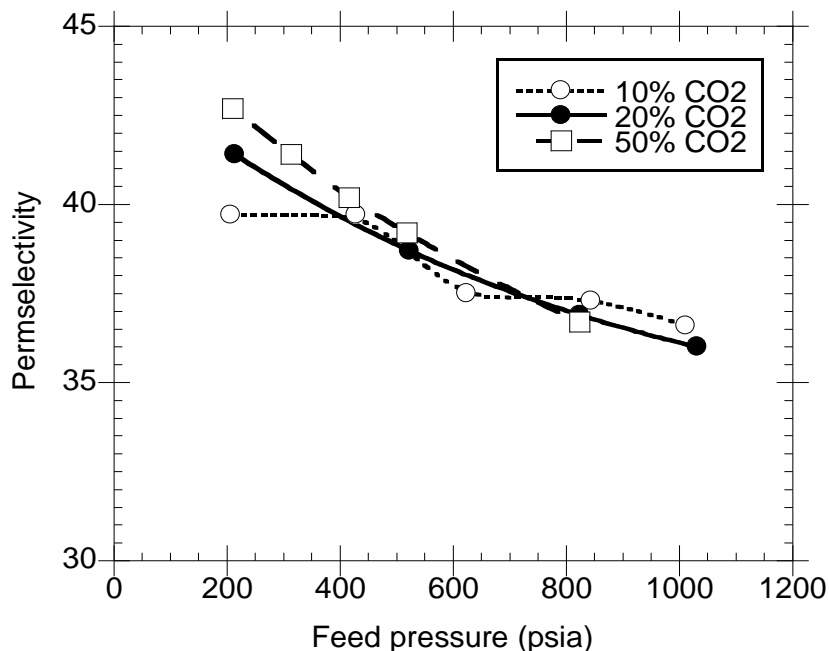


Figure 5.9: CO₂/CH₄ permselectivity versus feed pressure for 200 °C crosslinked PDMC hollow fibers tested using different feed concentrations of CO₂ at 35 °C.

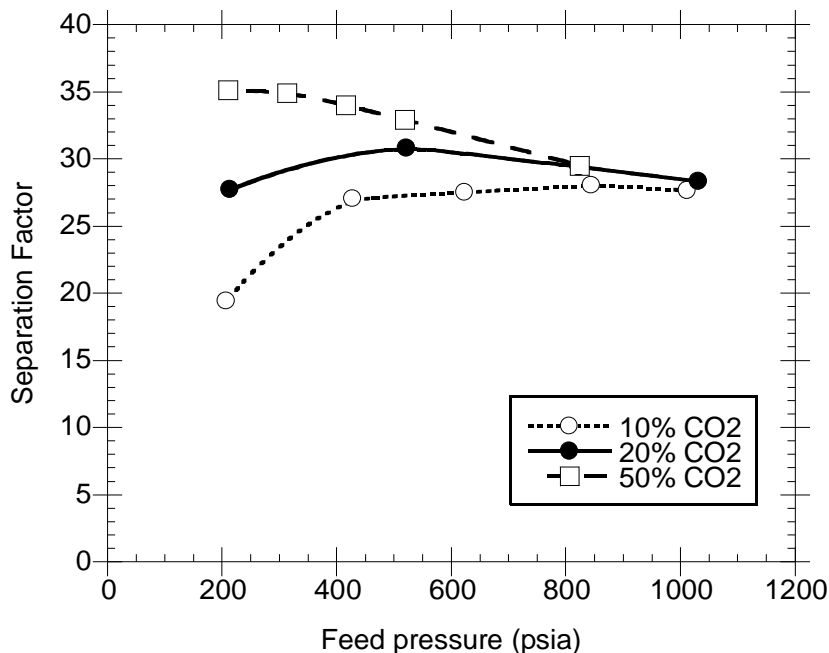


Figure 5.10: CO₂/CH₄ separation factor versus feed pressure for 200 °C crosslinked PDMC hollow fibers tested using different feed concentrations of CO₂ at 35 °C.

The CO₂ molecules have more of an advantage for sorption over CH₄, since CO₂ is more condensable. As the pressure is increased and the unrelaxed volume becomes saturated, the sorption advantage of CO₂ is reduced, thus its relative permeance and permselectivity over CH₄ is decreased as the pressure is increased. Section 5.2.2.2 below explains these effects further.

5.2.2.2 Sorption analysis on crosslinked PDMC

From the permeation results shown in Figure 5.9, it can be observed that there are slight declines in the permselectivity as the feed pressure is increased. This is typically seen in glassy polymers in the absence of plasticization, even in the dense film form [9, 10]. Competition for sorption sites between gas or vapor molecules could result in a decline in permeance. When both gases are simultaneously introduced to a glassy polymer membrane at low enough pressures, carbon dioxide will displace the less condensable methane molecules. This is why the mixed gas selectivity (~45) tends to be higher than the pure gas selectivity (~35–37) for separating carbon dioxide from methane at the same total feed pressure and in the absence of plasticization [1]. However, an increase in the feed pressure causes both gases to saturate the Langmuir sites, thereby reducing the CO₂ sorption advantage. This can be shown mathematically using Equation 5.1, as the terms in the denominator on the right hand side of the equation increase, the sorption of CO₂ decreases.

$$S_{CO_2} = \frac{C_{CO_2}}{f_{CO_2}} = k_{D,CO_2} + \frac{C'_{H,CO_2} \cdot b_{CO_2}}{1 + b_{CO_2} \cdot f_{CO_2} + b_{CH_4} \cdot f_{CH_4}} \quad (5.1)$$

Depending on the pressure and compositions of the permeate, this can become apparent as a decrease in the CO₂ permeance and a corresponding decrease in the CO₂/CH₄ permselectivity, since the sorption selectivity is decreased as the binary feed pressure is increased. This is described using Equations 5.2 and 5.3 below. A description of the terms in these equations can be found in Chapter 2.

$$\frac{P_{CO_2}}{l} = \frac{D_{D,CO_2} \cdot k_{D,CO_2}}{l} \cdot \left(1 + \frac{F_{CO_2} \cdot K_{CO_2} \cdot \frac{f_{CO_2,up}}{f_{CO_2,up} - f_{CO_2,d}}}{1 + b_{CO_2} \cdot f_{CO_2,up} + b_{CH_4} \cdot f_{CH_4,up}} - \frac{F_{CO_2} \cdot K_{CO_2} \cdot \frac{f_{CO_2,d}}{f_{CO_2,up} - f_{CO_2,d}}}{1 + b_{CO_2} \cdot f_{CO_2,d} + b_{CH_4} \cdot f_{CH_4,d}} \right) \quad (5.2)$$

$$\alpha_{CO_2/CH_4} = \frac{P_{CO_2}}{P_{CH_4}} = \frac{D_{D,CO_2} \cdot k_{D,CO_2}}{D_{D,CH_4} \cdot k_{D,CH_4}} \cdot \frac{\left(1 + \frac{F_{CO_2} \cdot K_{CO_2} \cdot \frac{f_{CO_2,up}}{f_{CO_2,up} - f_{CO_2,d}}}{1 + b_{CO_2} \cdot f_{CO_2,up} + b_{CH_4} \cdot f_{CH_4,up}} - \frac{F_{CO_2} \cdot K_{CO_2} \cdot \frac{f_{CO_2,d}}{f_{CO_2,up} - f_{CO_2,d}}}{1 + b_{CO_2} \cdot f_{CO_2,d} + b_{CH_4} \cdot f_{CH_4,d}} \right)}{\left(1 + \frac{F_{CH_4} \cdot K_{CH_4} \cdot \frac{f_{CH_4,up}}{f_{CH_4,up} - f_{CH_4,d}}}{1 + b_{CH_4} \cdot f_{CH_4,up} + b_{CO_2} \cdot f_{CO_2,up}} - \frac{F_{CH_4} \cdot K_{CH_4} \cdot \frac{f_{CH_4,d}}{f_{CH_4,up} - f_{CH_4,d}}}{1 + b_{CH_4} \cdot f_{CH_4,d} + b_{CO_2} \cdot f_{CO_2,d}} \right)} \quad (5.3)$$

Therefore, to further understand the permeation behavior, sorption experiments were carried out on the PDMC polymer fibers. Figure 5.11 shows the sorption experiments performed on the PDMC hollow fibers crosslinked at 200 °C using CO₂ and CH₄ gases.

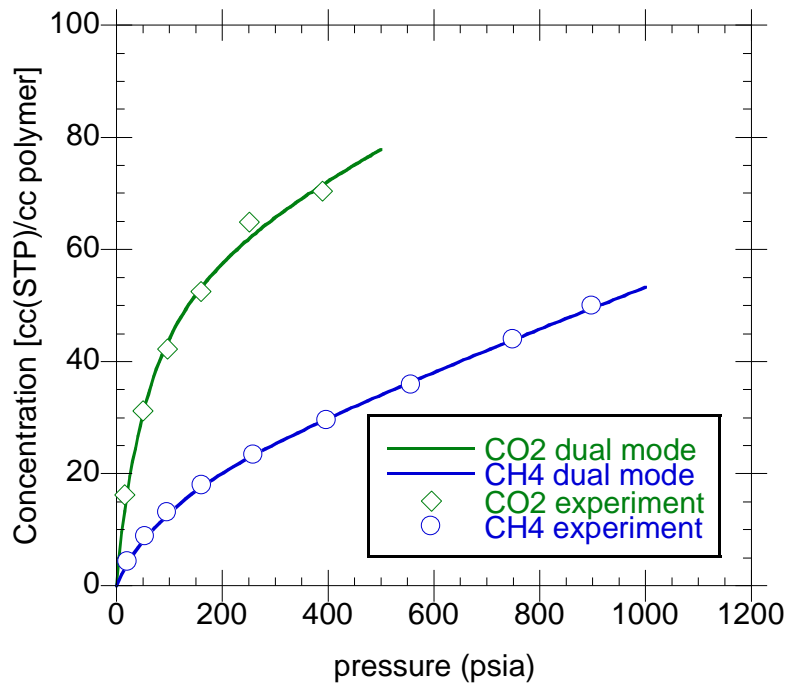


Figure 5.11: Carbon dioxide and methane sorption isotherms for 200 °C crosslinked PDMC hollow fibers tested at 35 °C. Solid lines are dual mode fit.

The sorption data obtained from the crosslinked PDMC fibers can be fit to the dual-mode model [11, 12], and the sorption parameters can be obtained and analyzed. The dual-mode sorption parameters are shown in Table 5.3.

Table 5.3 Dual mode sorption parameters for CO₂ and CH₄ at 35 °C.

<i>Gas</i>	k_D [cc(STP)/cc polymer·psi]	C_H' [cc(STP)/cc polymer]	b [1/psi]
CO ₂	0.043	62.6	0.018
CH ₄	0.035	19.6	0.010

From the sorption parameters obtained from the pure gas sorption data, the sorption coefficients and sorption selectivities can be estimated for binary gas mixtures. Figure 5.12 and 5.13 show the sorption coefficient for CO₂ and sorption selectivity for CO₂/CH₄ respectively, using different feed concentrations of CO₂ and increasing pressure.

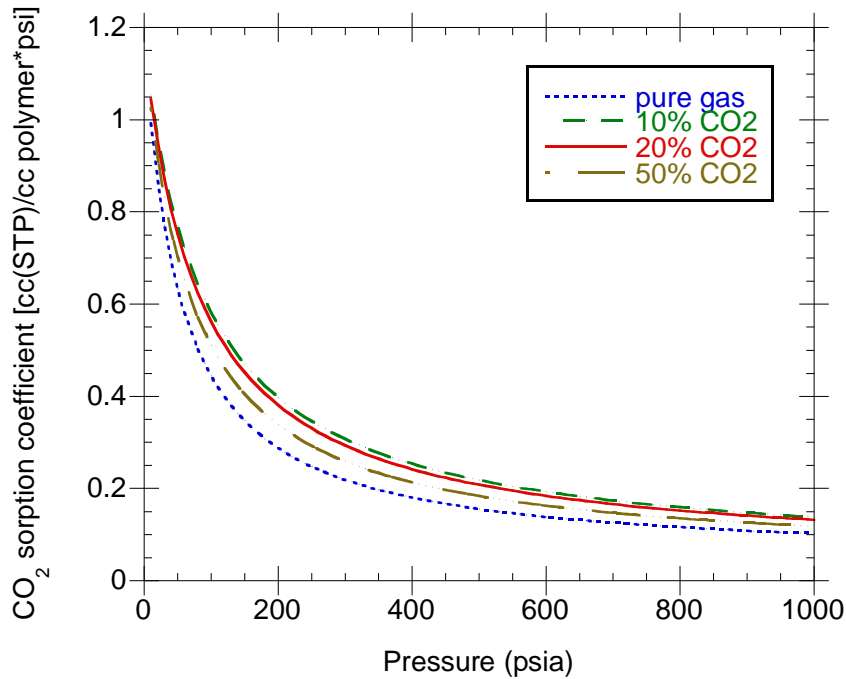


Figure 5.12: Carbon dioxide sorption coefficients calculated using dual mode model at different CO₂ concentrations in the feed.

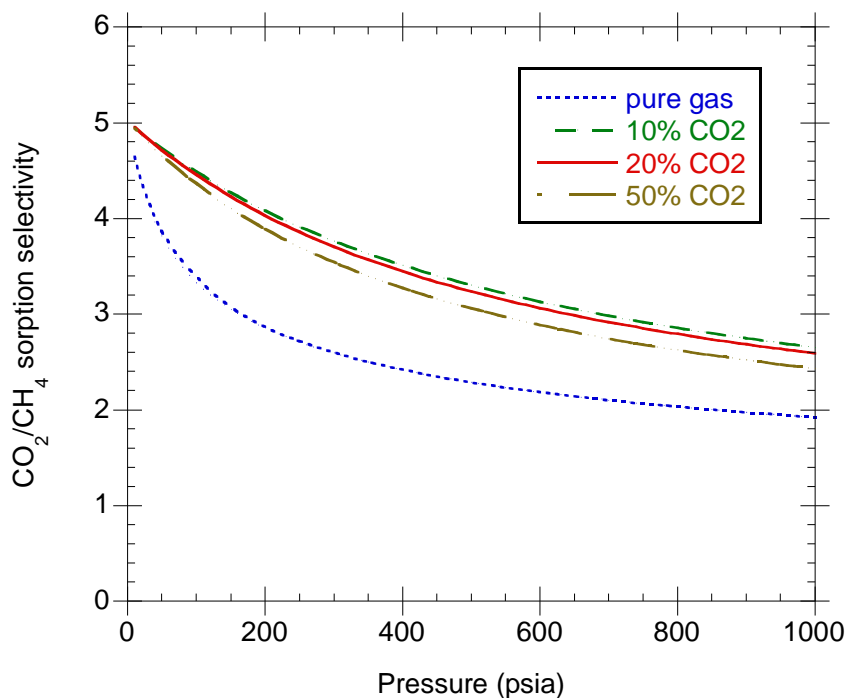


Figure 5.13: CO₂/CH₄ sorption selectivities calculated using dual mode model at different CO₂ concentrations in the feed.

From the sorption plots, it can be seen that the model predicts a higher sorption coefficient for CO₂ in the mixed gases than in the pure gas. Also, the mixed gas sorption selectivities are estimated to be higher than the pure gas sorption selectivity at the same total feed pressure. This explains why the mixed gas permselectivity is observed to be higher than the pure gas permselectivity, as observed in dense films and hollow fibers in this work. As also seen in the plots, as the pressure is increased, the sorption effects cause declines in the sorption coefficient and sorption selectivity; therefore, it is expected that these trends also transpire during permeation as reductions in permeance and permselectivities are also observed even in the absence of plasticization. Also, as the

feed pressure is increased or as the CO₂ levels are increased, the dual mode model predicts increases in the effective diffusion coefficients. However, it is expected that the diffusion coefficients may also increase as a result of swelling in more aggressive feeds with high CO₂ partial pressures.

Some noteworthy trends can be observed from the experimental data. As shown in Figure 5.9, the permselectivities using the mixed gas feeds are higher than that for the pure gas feed, as predicted by the dual mode sorption. Furthermore, as the mixed gas CO₂ content is increased from 10% to 50%, the permselectivity is still increased in the low pressure regions. This is not due to sorption effects alone but due to dual mode permeation effects according to Equation 5.3.

However, in Figure 5.9, it can be seen that as the feed pressure is increased, the beneficial effects of the higher CO₂ content diminish as swelling increases since the permselectivity decreases beyond the values observed with the lower CO₂ content. This observation suggests that there is a critical level of free volume with which the permeation of CO₂ is favored. Beyond this level, swelling effects may start to cause undesired methane loss. This is seen at about 300 psi partial pressure of CO₂ in the binary feed. This swelling level may be due to plasticization or bulk flow. However, the advantage of crosslinking comes from being able to reduce the level of swelling significantly compared to what would be seen in an uncrosslinked polymer, thereby preserving the permselectivity of the membrane.

The transport properties of polymer membranes can be modeled more quantitatively using the dual-mode transport theory as well, in the absence of plasticization or swelling or swelling induced bulk flow effects [12]. Using this model,

the diffusion coefficients in the Henry's law regime and the Langmuir (hole filling) regime can be obtained respectively through curve fitting of permeation data. In this case, the pure gas sorption and permeation experiments can be used to predict mixed gas effects. Also, using the model on existing mixed gas permeation data enables the determination of diffusion coefficients, which describe events occurring during mixed gas permeation. For the models, CO₂ transport parameters were obtained from fitting pure gas CO₂ data from Hillock as shown in Figure 5.14 by fitting to Equation 5.2, without any second component term and for and down stream pressure that applied to her studies. An effective skin thickness for the crosslinked fiber was estimated to be ~1 μm based on permeation on crosslinked PDMC fibers and films. The CH₄ transport parameters were obtained from the gas mixture with 90% CH₄ (10% CO₂) used as shown in Figure 5.8, since there was no evidence of plasticization with the low CO₂ content. The transport model parameters obtained can be seen in Table 5.4 below.

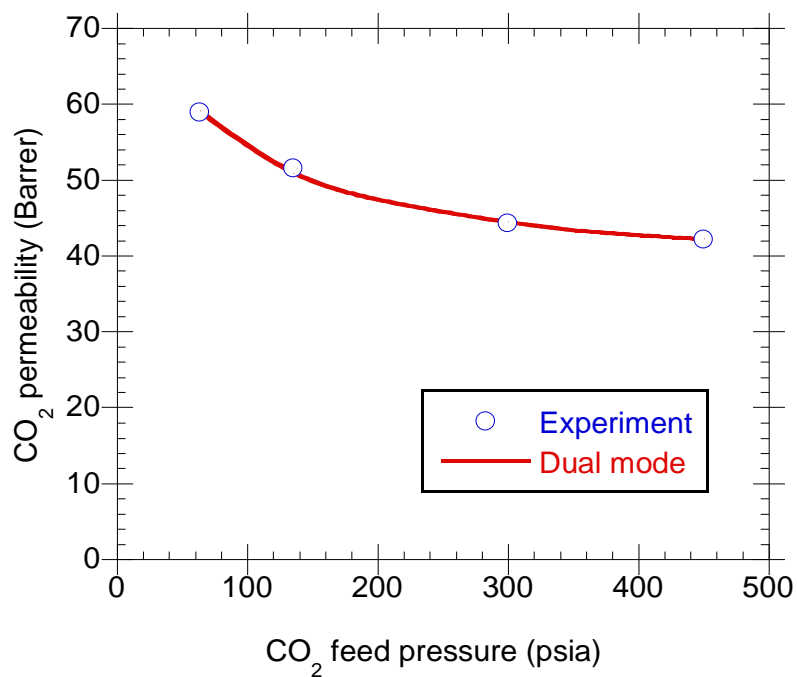


Figure 5.14: Pure gas CO₂ permeation isotherm used to obtain model parameters from a dense film crosslinked PDMC.

Table 5.4: Transport model parameters for crosslinked PDMC.

<i>Gas</i>	D_D/l ($\times 10^{-4}$) <i>cm/s</i>	D_H/l ($\times 10^{-4}$) <i>cm/s</i>	F D_H/D_D
CO ₂	44.3	2.17	0.049
CH ₄	1.16	0.602	0.519

Frame of reference effects were also considered [13]. As the CO₂ content increases in the membrane, bulk flow losses of CH₄ can occur. This can be accounted for by including the frame of reference term in the flux equations. Thus, the dual mode model and the frame of reference model were used to predict the expected behavior of the PDMC membrane in the presence of the aggressive feed containing 50% CO₂. The dual mode model for permeation can be seen in Equation 5.2. For the frame of reference model, Equations 5.4–7 are used and solved iteratively for each pressure point.

$$n_i = \frac{\rho \cdot D_{D,i}}{l} \cdot \frac{\ln \left[\frac{1 - \omega_{i,d} \cdot \left(1 + \frac{1}{r}\right)}{1 - \omega_{i,up} \cdot \left(1 + \frac{1}{r}\right)} \right]}{\left(1 + \frac{1}{r}\right)} \quad (5.4)$$

$$n_j = \frac{\rho \cdot D_{D,j}}{l} \cdot \frac{\ln \left[\frac{1 - \omega_{j,d} \cdot (+r)}{1 - \omega_{j,up} \cdot (+r)} \right]}{(+r)} \quad (5.5)$$

$$r = \frac{n_i}{n_j} \quad (5.6)$$

$$\frac{P_A}{l} = \frac{22400 \cdot n_A}{M_A \cdot \Delta f_A} \quad (5.7)$$

The mass fractions (ω) were calculated from sorption data (see Chapter 2 for further details). The model predictions are shown below.

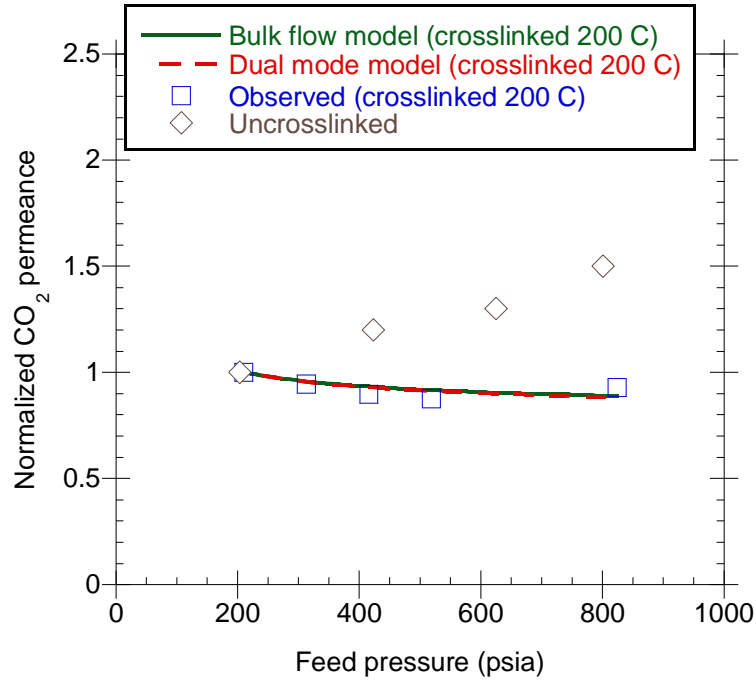


Figure 5.15: Bulk flow and dual mode model predictions of CO₂ permeance isotherm using a 50/50 CO₂/CH₄ mixture at 35 °C in a crosslinked PDMC hollow fiber.

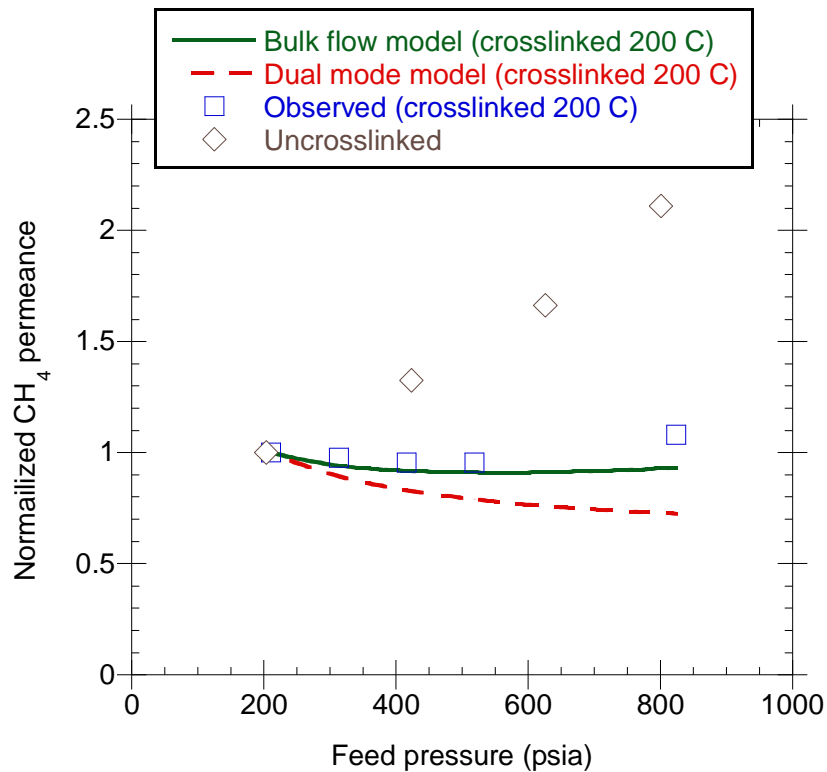


Figure 5.16: Bulk flow and dual mode model predictions of CH₄ permeance isotherm using a 50/50 CO₂/CH₄ mixture at 35 °C in a crosslinked PDMC hollow fiber.

As can be seen from the model predictions, the dual mode model and the frame of reference model both describe the CO₂ permeance behavior fairly well even till the feed pressure reaches 800 psia (about 400 psia CO₂). The CH₄ permeance isotherm however deviates from the dual mode model predictions and follows the bulk flow model from the start, up till somewhere between 600 and 800 psia feed pressure. This suggests that a significant portion of the flux of CH₄ is contributed by the bulk coupling effects between the transport of CO₂ and CH₄ through the membrane. Essentially, CO₂ “drags” along the

CH₄ molecules due to the high sorbed concentrations in the membrane. As the pressure increases to about 800 psia (400 psia of CO₂), the CH₄ permeance seems to diverge from the predicted values, even when the frame of reference is accounted for in the bulk flow model. This suggests that some swelling effects and resultant plasticization were indeed occurring in the asymmetric hollow fibers under these aggressive conditions. However, the crosslinking mitigates the extent to which swelling occurs; thus the permselectivity is not adversely affected as evidenced when compared with the uncrosslinked version.

5.2.2.3 Practical considerations in separation

The permeance (or permeability) gives fundamental insight as to events occurring in the membrane as penetrants permeate through, and as mentioned previously, the ratio of the permeances is called the permselectivity. However, this permselectivity is ideal relative to the actual separation performance, which is represented by the separation factor. As the membrane's permeate pressure increases from idealistic vacuum conditions, the separation factor deviates from the permselectivity even though the membrane material itself may not be affected significantly. Most of the work reported in the literature is done under vacuum permeate conditions; but in this work, permeate pressures are at ambient conditions, thus permselectivities and separation factors are both reported to reflect practical separation performance values. If the permeation behavior of the membrane is adequately modeled to account for competition and plasticization effects, the separation factor can be derived from the operating pressures and feed compositions using mass balance equations. The expression for the separation factor at a negligible stage cut is given by Equation 5.8 [14] and Equation 5.9.

$$y_{CO_2} = \frac{\phi}{2} \cdot \left[x_{CO_2} + \frac{1}{\phi} + \frac{1}{\alpha - 1} - \sqrt{\left(x_{CO_2} + \frac{1}{\phi} + \frac{1}{\alpha - 1} \right)^2 - \frac{4 \cdot \alpha \cdot x_{CO_2}}{(\alpha - 1) \cdot \phi}} \right] \quad (5.8)$$

$$SF = \frac{y_{CO_2} / x_{CO_2}}{y_{CH_4} / x_{CH_4}} \quad (5.9)$$

In Equations 5.8 and 5.9, y_{CO_2} and y_{CH_4} are the permeate mole fractions for CO₂ and CH₄ respectively; x_{CO_2} and x_{CH_4} are the feed mole fractions for CO₂ and CH₄ respectively; ϕ is the pressure ratio (feed pressure/permeate pressure); and α is the membrane permselectivity (P_{CO_2}/P_{CH_4}).

From Equations 5.8 and 5.9, a plot of the separation factor versus feed pressure at different feed compositions and various permeate pressures can be determined and is shown in Figures 5.17–5.19. For simplicity in illustrating these effects on the separation factor, the permselectivities used for these equations were obtained by fitting of the permselectivity versus feed pressure data in Figure 5.9, using a linear expression shown in Equation 5.10 with the coefficients in Table 5.5.

$$\alpha = \alpha_o - m \cdot P_{up} \quad (5.10)$$

Table 5.5: Linear correlation coefficients for permselectivity data from Figure 5.9.

CO_2/CH_4 <i>mix</i>	α_o	m	R^2
10/90	38.7	0.0078	0.967
20/80	41.2	0.0111	0.995
50/50	43.4	0.0160	0.992

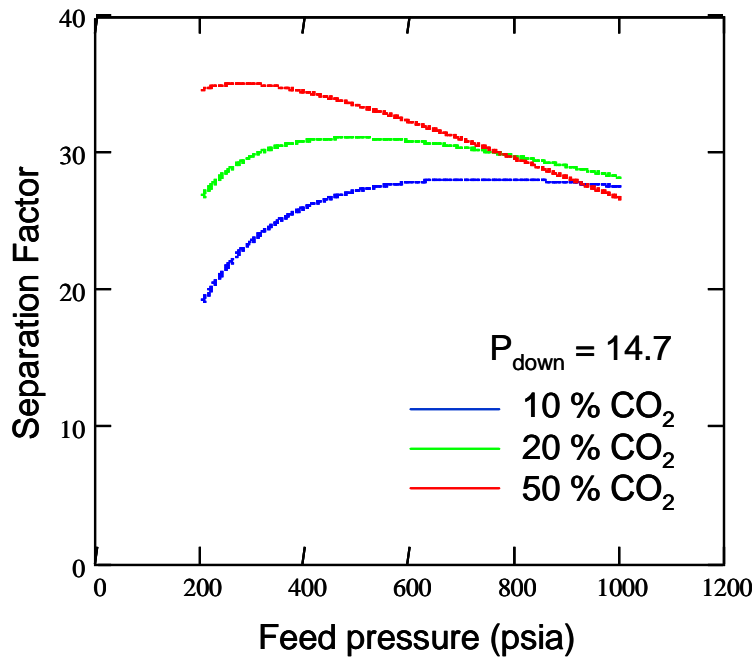


Figure 5.17: CO_2/CH_4 separation factors calculated using Equation 5.8–10 at a 14.7 psia permeate pressure using different CO_2 concentrations in the feed.

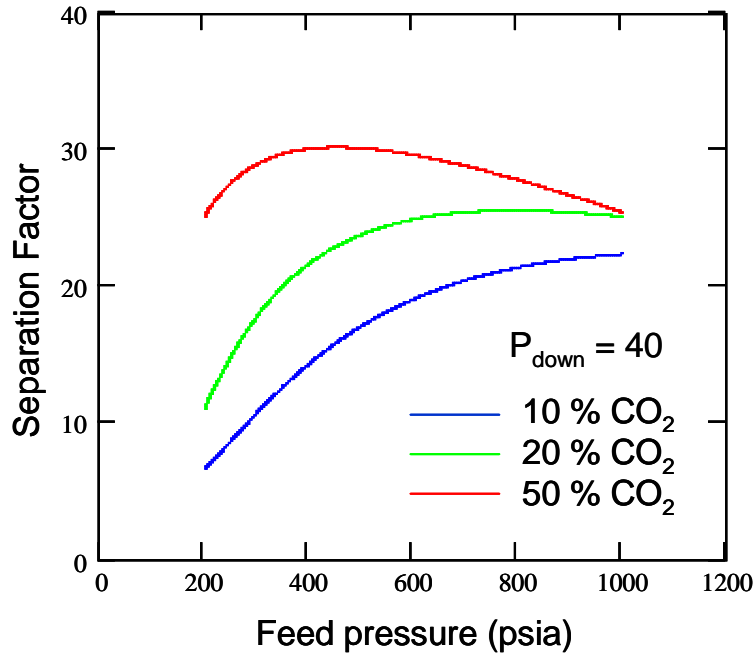


Figure 5.18: CO₂/CH₄ separation factors calculated using Equation 5.8–10 at a 40 psia permeate pressure using different CO₂ concentrations in the feed.

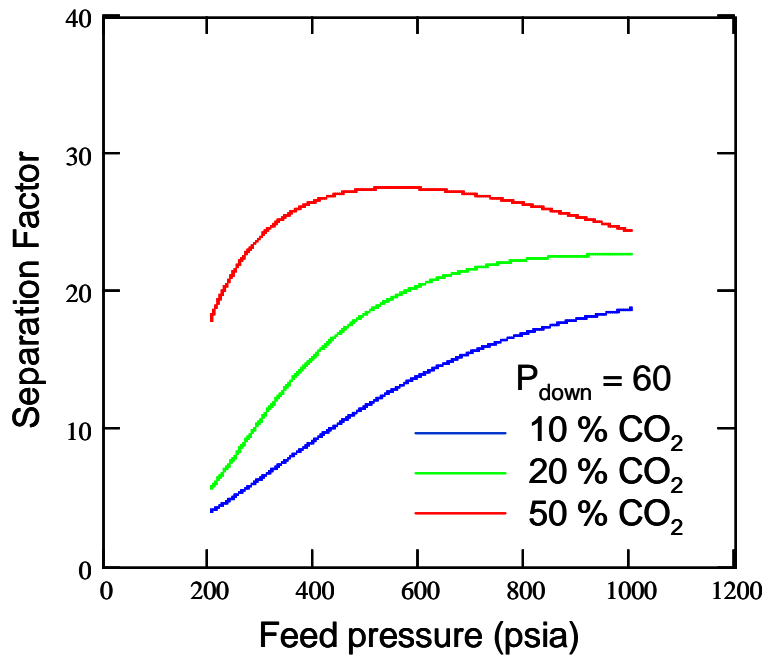


Figure 5.19: CO₂/CH₄ separation factors calculated using Equation 5.8–10 at a 60 psia permeate pressure using different CO₂ concentrations in the feed.

Under vacuum permeate conditions the separation factor equals the permselectivity. From Figure 5.17, it can be observed that there is an effect of the permeate pressure on the separation factor. When the permeate pressure is at 14.7 psia, as shown in Figure 5.17, the separation factor is reduced because the pressure ratio is significantly reduced. At lower feed pressures, the separation factor is much higher using the higher CO₂ content feeds because the partial pressure difference driving force is higher. In this lower feed pressure region, the separation is pressure ratio limited. As the feed pressure is increased, the pressure ratio increases and the separation factor approaches a maximum, after which effects more relevant to the membrane material itself become apparent as seen by the corresponding declines in permselectivity. The plots in Figure 5.17 correspond well with what is seen in experimentally in Figure 5.10. From Figures 5.18 and 5.19, the effects of increased permeate pressure to 40 psia and 60 psia are shown and indicate that there are further declines in the separation factor, especially at lower feed pressures. Typical pressure ratios encountered industrially can range from about 10–15 [15], which corresponds to a permeate pressure between 60 and 100 psia using a feed at 1000 psia. The plots in Figures 5.18 and 5.19 show that there is a maximum separation achievable at a given feed pressure (or permeate pressure) using various feed mixtures, and suggests that practical considerations aimed at reducing the permeate pressure may be beneficial. Moreover, the estimations used in the plots in Figures 5.18 and 5.19 assume that the increased permeate pressures do not change the membrane material's intrinsic permselectivity. In reality the increased permeate pressure may reduce permselectivity due to swelling since the average concentration in the membrane would

be increased. However, the crosslinking should mitigate this effect from swelling caused by increased permeate pressures.

5.2.3 Hollow fiber performance stability over time

Some further testing was done on the fibers to study their resistance to plasticization in the presence of the high CO₂ partial pressures over long time periods. This was done by using a 20/80 CO₂/CH₄ feed at the maximum test pressure of 1000 psi, which corresponds to a CO₂ partial pressure of 200 psi. The permeation results for this can be seen below in Figure 5.20 and 5.21.

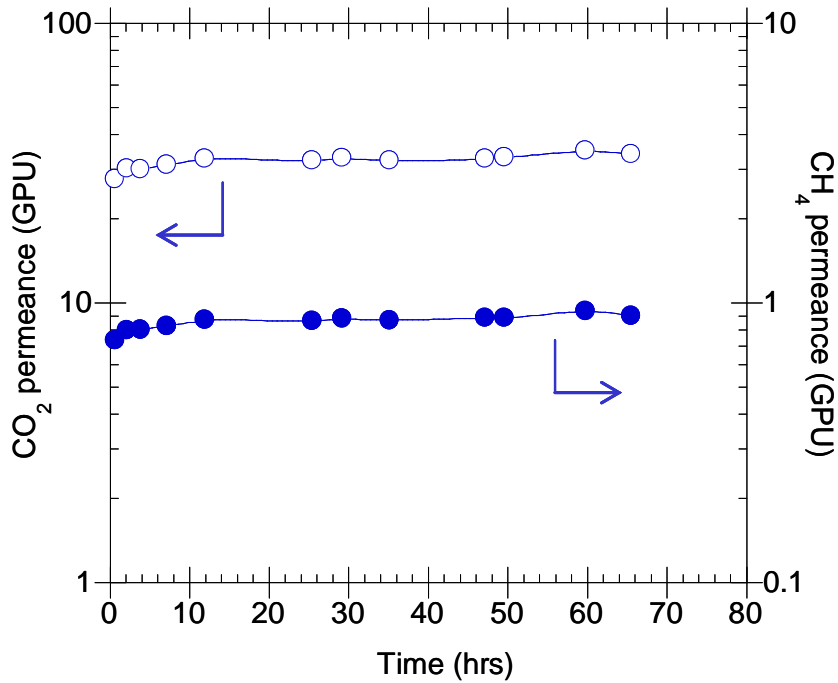


Figure 5.20: Stability over time of the CO₂ and CH₄ permeances using 200 °C crosslinked PDMC hollow fibers in a feed with 20% CO₂.

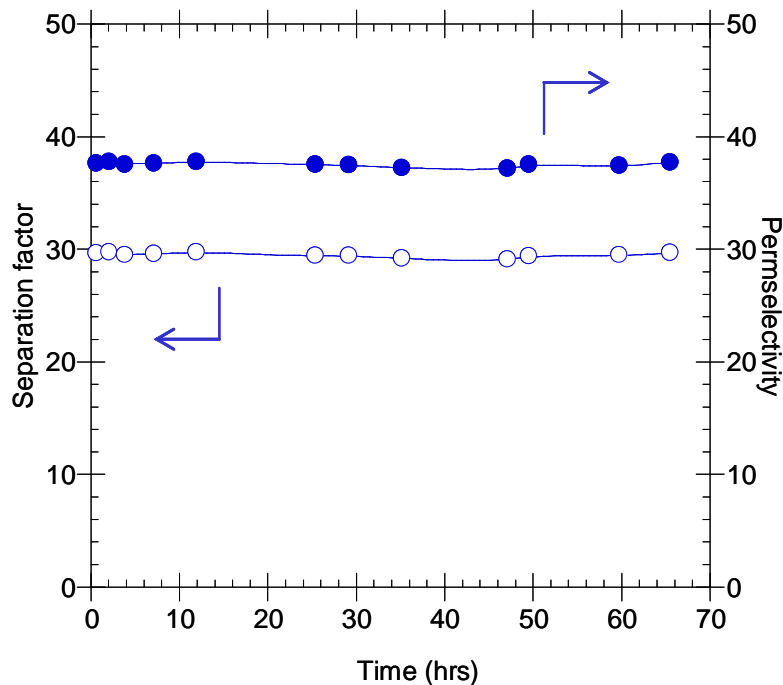


Figure 5.21: Stability over time of the CO₂/CH₄ permselectivity and separation factor using 200 °C crosslinked PDMC hollow fibers in a feed with 20% CO₂.

The results above show that the crosslinked fibers perform well and maintain performance with 200 psi CO₂ in the feed. Subsequently, the crosslinked fibers were tested with the 50/50 CO₂/CH₄ feed at a total pressure of 800 psi, which corresponds to a CO₂ partial pressure of 400 psi (twice the amount of CO₂ used previously). In terms of the CO₂ content in the feed, this corresponds to a total feed pressure of 2000 psi using the 20/80 CO₂/CH₄ feed mix. The permeation results for this can be seen below in Figure 5.22 and 5.23.

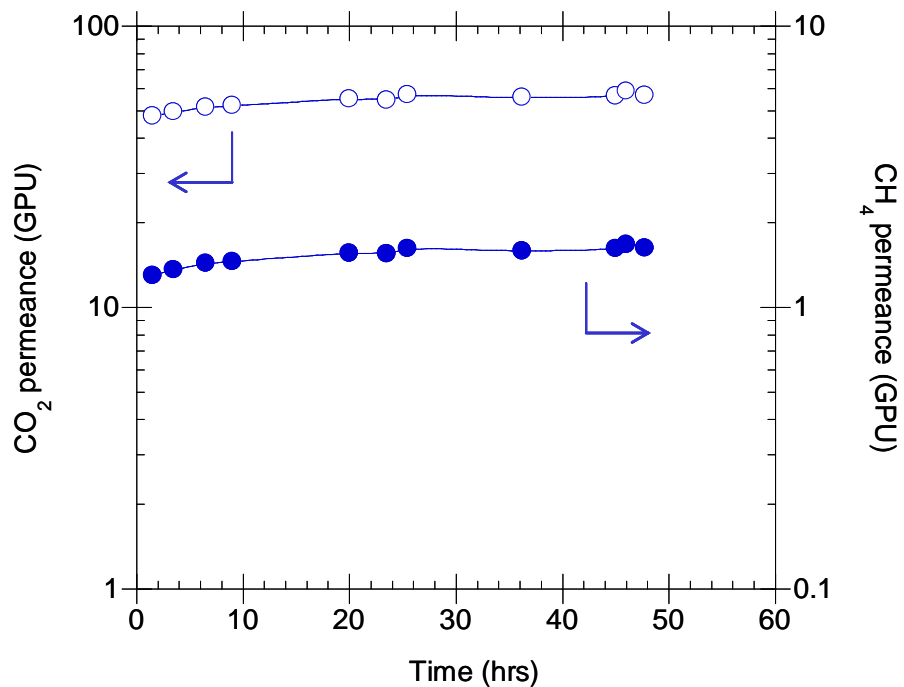


Figure 5.22: Stability over time of the CO₂ and CH₄ permeances using 200 °C crosslinked PDMC hollow fibers in a feed with 50% CO₂.

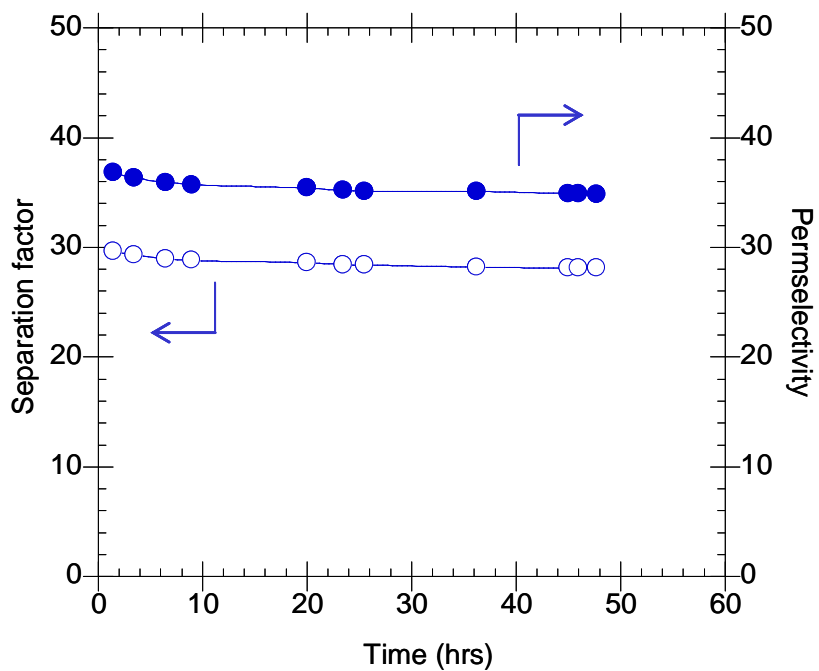


Figure 5.23: Stability over time of the CO₂/CH₄ permselectivity and separation factor using 200 °C crosslinked PDMC hollow fibers in a feed with 50% CO₂.

The results above show that the crosslinked fiber retains good permeance and permselectivity under these conditions but shows slight permselectivity loss initially (first 10 hrs). Notwithstanding this fact, the membrane stabilizes after the next 40 h of testing. This suggests there is some dilation occurring from this high CO₂ content when the membrane is initially exposed, but the extent of the dilation is controlled by the crosslinking. The uncrosslinked version, on the other hand, began to swell excessively at CO₂ partial pressures as low as 100 psi (the lowest CO₂ partial pressure tested).

5.2.4 Effect of gas phase non-idealities (fugacity)

In analyzing membrane performance at high pressures, pressure based calculations do not account for the gas phase non-idealities that occur. At higher pressures, carbon dioxide deviates from non-ideality much more so than methane as shown in Figure 5.24. The real driving force for the separation is the fugacity, which accounts for this non-ideality. The calculations in all prior plots have been corrected using fugacity coefficients obtained using the virial equation of state. The effect of the fugacity correction is even more evident as the feed pressure is increased.

Although the abscissas on the plots in the Figure 5.9 show pressure units (experimental set point), as in all the figures, the permselectivities calculated are based on fugacity corrections in the permeances. The effect of this correction is shown in Table 5.6.

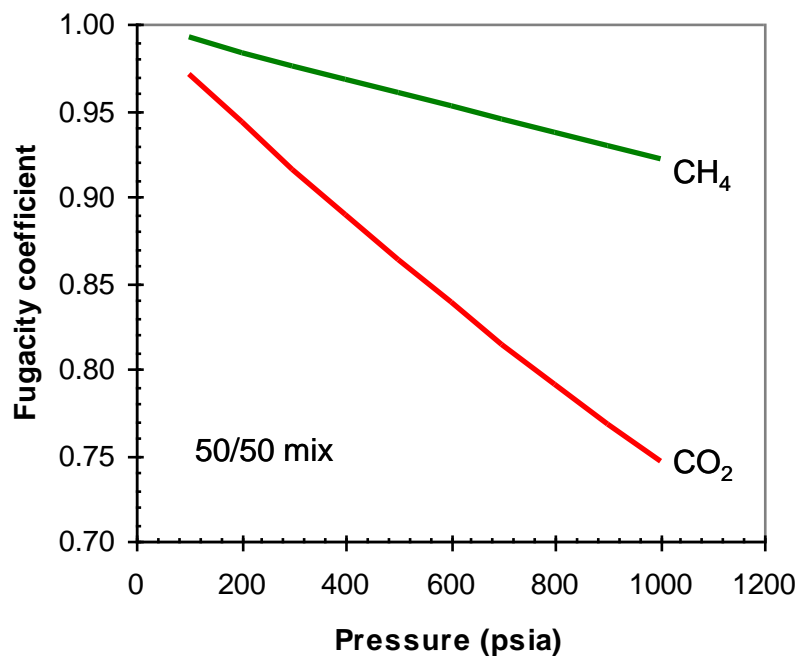


Figure 5.24: Carbon dioxide and methane fugacity coefficients as a function of feed pressure from the virial equation of state using a binary mixture with 50% CO₂ at 35 °C.

Table 5.6 Fugacity effects on performance.

<i>Condition</i>	<i>CO₂/CH₄ mix</i>	<i>% α retained from 200 – 800 psi</i>	
		Pressure based	Fugacity based
Crosslinked (200 °C)	20/80	82	89
Crosslinked (200 °C)	50/50	75	86
Uncrosslinked	50/50	62	70

The preceding figures show that the crosslinked fiber can be used effectively at high pressures even with high CO₂ content in the feed. The data also shows why crosslinking

is important. Testing with the 50/50 CO₂/CH₄ mix on the uncrosslinked fiber and comparing with the crosslinked version shows that crosslinking really does help stabilize the fiber in mixed gas feeds. The uncrosslinked fiber shows plasticization effects as the CO₂ and CH₄ permeances concomitantly increase. Here, the data in Table 5.6 also shows why analysis based on fugacity is important. Table 5.6 shows that using pressure based calculations, the retained permselectivities for the *crosslinked* fibers are 82% and 75% for the 20/80 and 50/50 mixtures respectively, within the pressure range tested in Figure 9. One may be deceived to think that the extra losses with the 50/50 mix might be associated with changes in the material (i.e. plasticization or frame of reference effects). This turns out not to be the case, as correcting for fugacity shows that the retained permselectivities for the fibers were actually 89% and 86% for the respective gas mixtures.

The effects of crosslinking on stabilizing the membrane against plasticization may, therefore, also be underestimated when fugacity corrections are neglected. Comparing the data for the crosslinked and uncrosslinked fiber shown in Table 5.6 reveals that the retained permselectivity of the uncrosslinked version is 70% and not 62%. Crosslinking helps eliminate ~16% (86%-70%) of the loss associated with plasticization when fugacity is used. If pressure based calculations were used (instead of fugacity), it would indicate that the crosslinking eliminates 13% (75%-62%) of the loss associated with plasticization, which is an underestimation.

5.2.5 Effect of ageing on separation performance

5.2.5.1 Effect of ageing on absolute separation performance values

It was found that the performance of the PDMC hollow fibers is highly dependent on the age of the fiber. Pure and mixed gas permeation was carried out on the fibers at different ages. The results from this experiment on the uncrosslinked fiber can be seen in Figure 5.25 and Table 5.7.

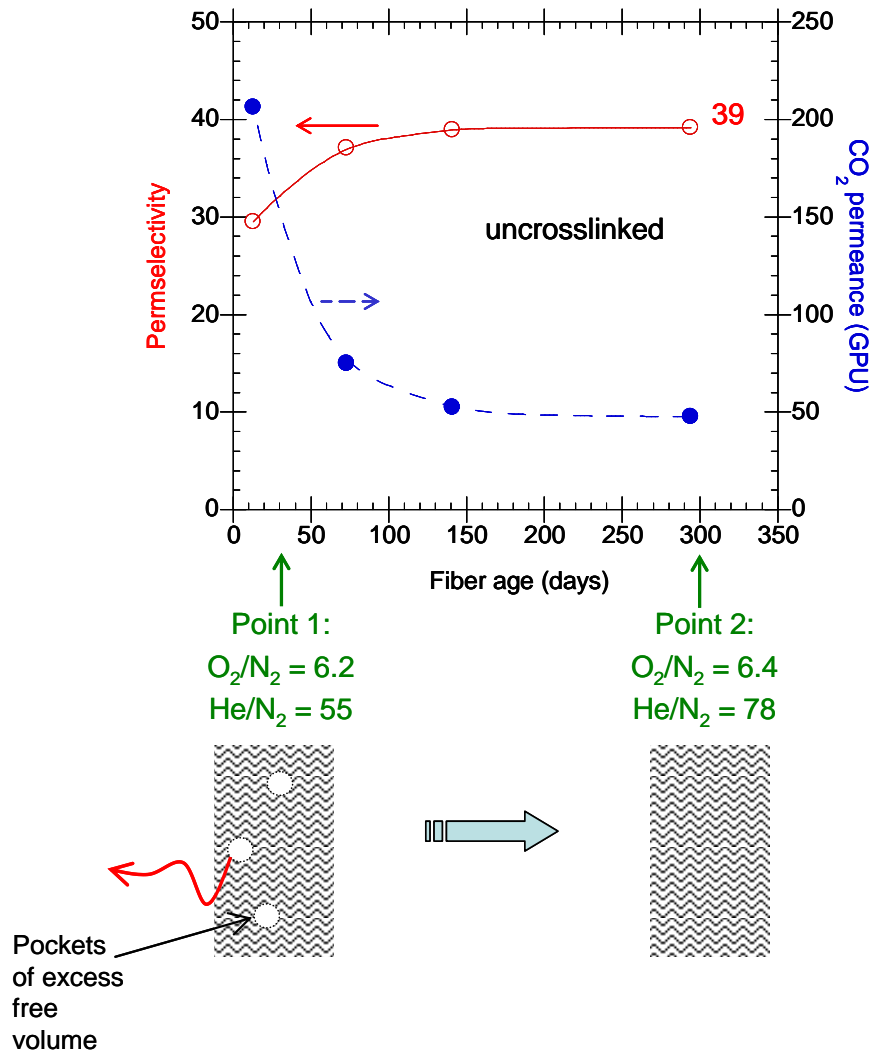


Figure 5.25: Ageing effects on separation performance using an uncrosslinked PDMC hollow fiber. CO₂/CH₄ permeation using mixed gas at 200 psia with 20% CO₂ at 35 °C. O₂, N₂, He tests using pure gases at 100 psia, 35 °C.

Table 5.7 Ageing effects on performance.

<i>Gas</i>	<i>He</i>	<i>O₂</i>	<i>N₂</i>	<i>CO₂</i>	<i>CH₄</i>
Decrease in permeance from 1 to 2 from ageing	35 %	53 %	55 %	~69 %	~75 %
Increase in permselectivity from 1 to 2 from ageing	42 % (N ₂)	3.2 % (N ₂)		~23 % (CH ₄)	
Kinetic diameter (Å)	2.6	3.46	3.64	3.3	3.8
Critical temperature (K)	5.2	154.4	126.1	304.2	190.7

The trends above show that there is a significant drop in the permeance of the fibers after ageing for several months. It must be noted that during the ageing process, in between times of testing, the membranes were dormant. The performance seen here is expected to be different if the fiber is continuously exposed to the feed gas during the ageing period. The greater part of the decline occurs in the early stage of the ageing process, just after the fiber is spun. This can be attributed to the trapping of high amounts of excess free volume due to the rapid quenching during spinning or due to the residual solvent that remained in the fiber, which may act as a plasticizer. In transforming from a polymer solution to a vitrified membrane, there may exist unrelaxed volume or local micro-void packing defects in the polymer skin. These defects are packing disruptions in the rigid polymer's segmental conformation, which eventually disappear as the polymer chains relax to a more equilibrium state. The timescales to reach equilibrium chain packing

conformations is extremely long, but as observed experimentally, the polymer approaches this limit asymptotically. Such ageing trends were also observed by Kratochvil in dense films [4].

The CO₂ permeance drops from ~ 200 GPU, just after the fiber was spun, down to about 50 GPU (at point 2 in Figure 5.25). Correspondingly, the CO₂/CH₄ permselectivity increases significantly from ~ 30 to 39. These are typical signs of ageing in the polymer matrix. The aged fibers were heated in an oven at 70 °C for ~ 24 hrs. These are the same drying conditions that were done before the fibers were tested at all (i.e. at age 0). The re-dried fibers were retested and the CO₂/CH₄ selectivity went up slightly from 39 to 40, while the CO₂ permeance went up from ~ 37 to 39 GPUs. This indicates that adsorbed moisture was not the cause of the decline in permeance, since the original permeance was not regained. However, the drying did show some benefit.

Pure gas permeation tests were performed at two time periods, point 1 and 2, shown in Figure 5.25 above. The data in Table 5.7 above shows trends that indicate that the fiber is becoming denser by diffusion of free volume out of the skin layer and/or by a contraction of the lattice, induced by the polymer chain relaxations within the fiber. The rapid ageing process shown in these thin skinned hollow fibers suggest that diffusion of free volume is the dominant cause of the ageing process, since the exposed surface area to volume ratio of the thin skins are large and the surface acts as a sink for the diffusion process. This can be further investigated by observing the free volume distributions within the skin layer as the fiber ages. However, this was beyond the scope of this work.

From a kinetic perspective, looking at the trends in Table 5.7, it is observed that there is a decrease in the permeance of the slower gases (O₂ and N₂) more than that for

the faster gas (He); which suggests an increase in selective resistance. In other words, the pure gas data shows that the He/N₂ selectivity increases much more than the O₂/N₂ selectivity. Helium serves as a good probe gas molecule among the pure gases used because its kinetic diameter is much smaller compared to the rest (2.6 Å vs. 3.46 Å and 3.64 Å for O₂ and N₂ respectively). Therefore, its flux through the selective skin layer should be less affected - as was noticed experimentally. The pure gases (O₂, N₂, and He) are sufficient for analyzing these kinetic effects in the hollow fiber membrane. Moreover, from a thermodynamic perspective, it is noticed that there is a decrease in the permeance of the condensables (CO₂ and CH₄) more than that for the less condensable gases (He, O₂, and N₂), which suggests a reduction in unrelaxed free volume into which favorable sorption can occur. The condensability of a gas can be reflected by its critical temperature, wherein the more condensable gases have higher critical temperatures. Here, we see that the permeance drop for both CO₂ and CH₄ is much more than that for O₂, N₂, or He. This observation is striking for the case of CO₂ because its kinetic diameter is smaller than that of O₂ and N₂. This can be explained by reasoning that the more condensable gases are energetically more favorable to condense into the pockets of free volume within the polymer matrix due to enthalpic effects of sorption. Thus, as the fiber ages and the free volume pockets diffuse out of the matrix, these pockets are reduced, resulting in a greater loss in the permeance of the condensables than that of the less condensable gases.

The performance of a fiber crosslinked at 200 °C was also analyzed to observe the effects of ageing. Figure 5.26 below shows the performance of this fiber while ageing, after it was crosslinked at 200 °C (2 h).

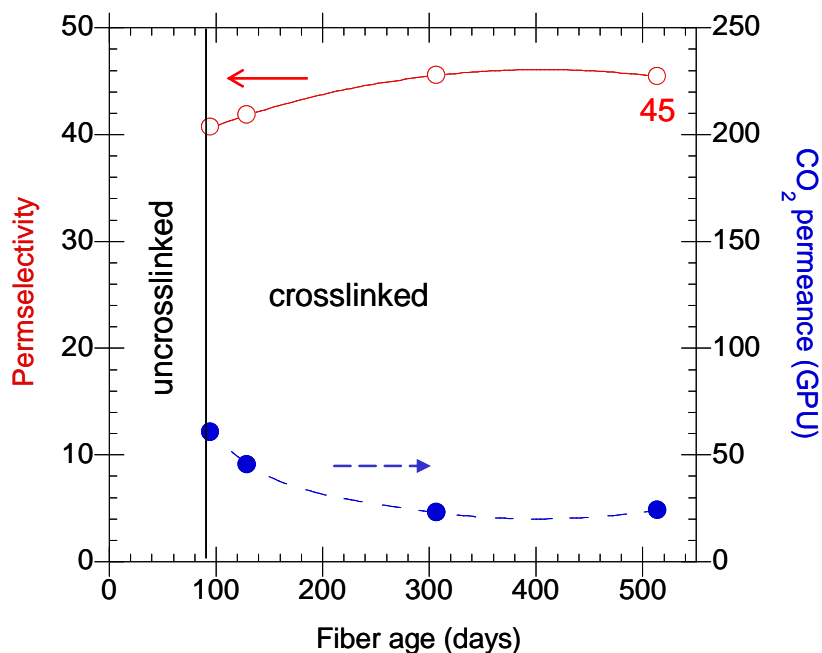


Figure 5.26: Ageing effects on separation performance using a crosslinked PDMC hollow fiber. CO₂/CH₄ permeation using mixed gas at 200 psia with 20% CO₂ at 35 °C.

From the figure above it can be seen that the crosslinked fibers also age, with a decrease in the permeance and an increase in permselectivity. It is believed that the heat treatment used to crosslink the fiber also accelerates the ageing process, especially in asymmetric hollow fibers. This difference between the fiber and dense film trend arises due to the thin skins in the fibers, which are vitrified during the rapid spinning process as opposed to the slow solvent evaporation process used in dense films. The use of catalysts to enhance crosslinking degrees at lower temperatures might alleviate effects from excessive annealing in asymmetric hollow fibers (as long as the catalysts themselves do not reduce the permeance), since lower annealing temperature should reduce possible

transition layer compaction issues. To ideally study the effects of ageing, the effects of time, storage temperature, and sample thickness need to be decoupled and this work is more suited for dense film studies. Further information on effects of ageing in glassy polymers can be found in the literature [4-8].

5.2.5.2 Effect of ageing on pressure dependence of separation performance

In this study, an increase in feed pressure was carried out on the aged, crosslinked fiber at 35 °C using a 20/80 CO₂/CH₄ feed. The aged fiber was stored at ambient pressure under air at ~35 °C. If the free volume had been reduced in the fiber, the pressure dependence of the fiber would reduce according to the dual mode theory of transport. The data from this experiment was compared with that for a less aged fiber at the same test temperature, since that data was available from previous studies. Figures 5.27–30 below show the performance for these two fibers at different degrees of ageing.

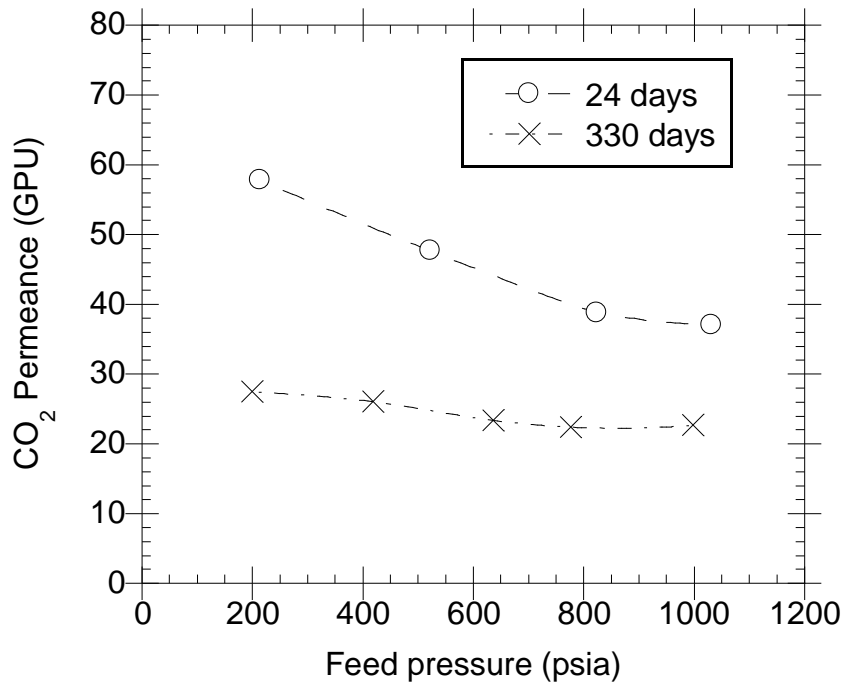


Figure 5.27: Effect of fiber age on CO₂ permeance versus feed pressure.

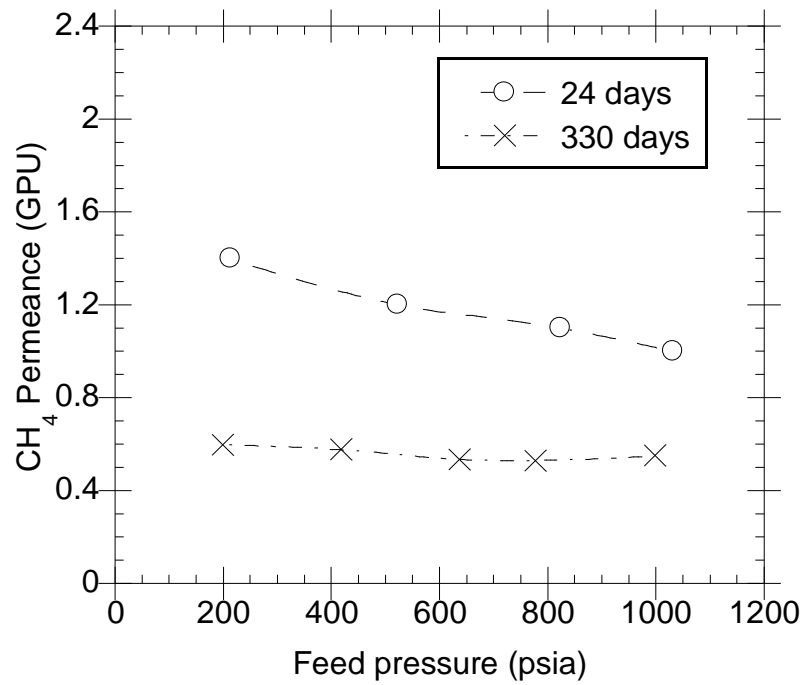


Figure 5.28: Effect of fiber age on CH₄ permeance versus feed pressure.

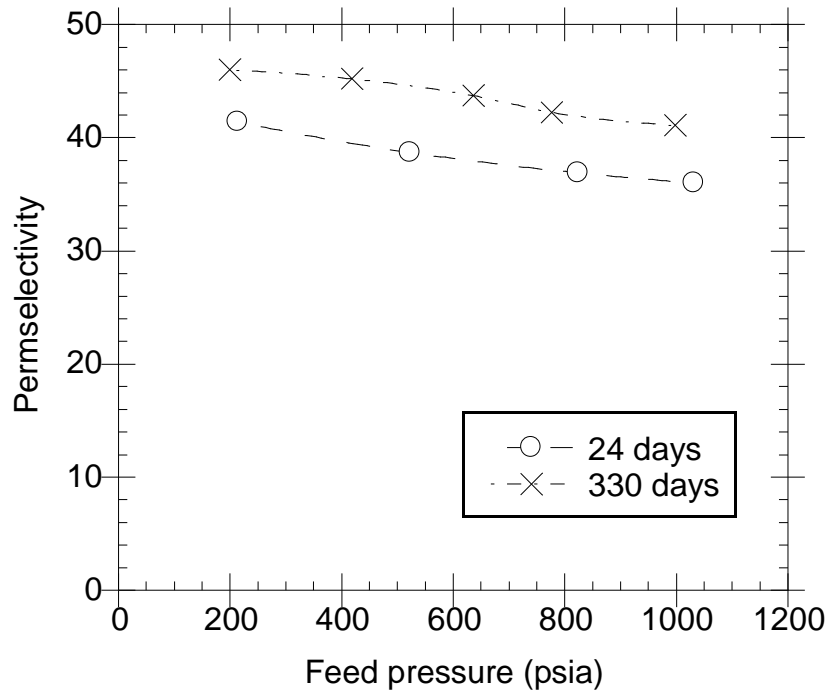


Figure 5.29: Effect of fiber age on CO₂/CH₄ permselectivity versus feed pressure.

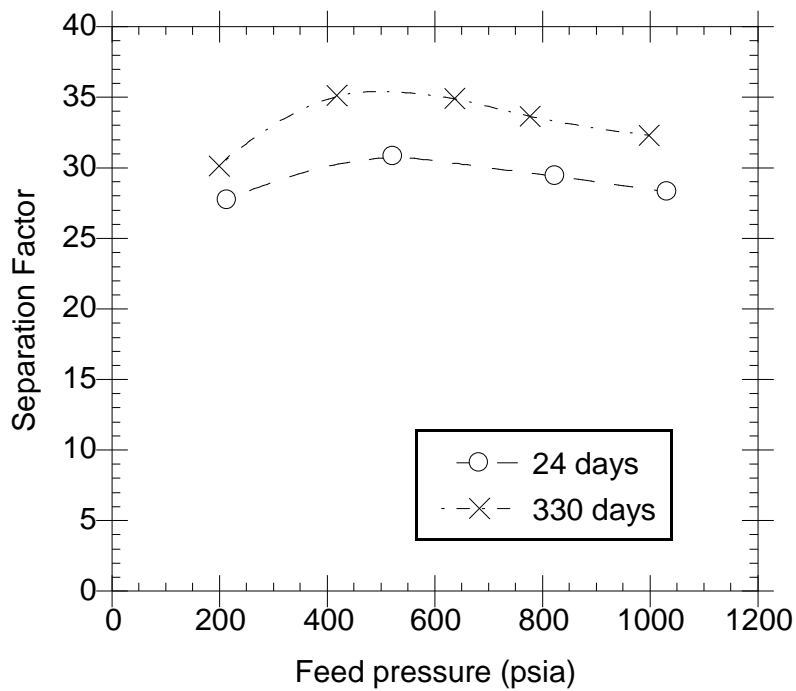


Figure 5.30: Effect of fiber age on CO₂/CH₄ separation factor versus feed pressure.

From the results above, it can be seen that the two fibers perform differently. In accordance to the observations shown in the previous section, the selectivity increases and the permeance decreases as the fiber ages. Moreover, the effect of ageing on the permeance as a function of feed pressure on both fibers is different as shown in Figure 5.27 and 5.28 above. The less aged (24 days) fiber shows more of a dual-mode effect (decrease in permeance as pressure is increased), suggesting the presence of more Langmuir sites or free volume pockets. This observation, again, supports the argument that the ageing is occurring as a result of free volume reduction in the membrane skin layer since the Langmuir capacity constant is proportional to the amount of excess free volume in the polymer according to Equation 5.11.

$$C_H \propto \frac{V_g - V_l}{V_l} \quad (5.11)$$

In the isotherms in Figures 5.27 and 5.28, the aged (330 days) fiber shows less of a decrease in permeance with increasing feed pressure, indicating less free volume or a denser skin layer. Thus, the extent of pressure dependence of the permeance may be more appropriate than the absolute permeance per se in identifying what extent a fiber has aged versus another fiber, since the absolute value of the permeance also depends on the actual skin thickness of each fiber, which is not readily obtainable. This fact is based on the definition of permeance,

$$\frac{Flux_i}{\Delta p_i} = \frac{P_i}{l} \quad (5.12)$$

In the permeance expression above, Δp_i is the transmembrane partial pressure difference, P_i is the permeability, and l is the membrane thickness.

5.2.6 Effect of temperature on separation performance

The aged crosslinked fiber (~330 days old) was further tested at elevated temperatures. The test temperature was increased to 50 °C and 80 °C to simulate the fiber performance under typical field operating conditions. The results from this experiment can be seen in Figures 5.31–34 below.

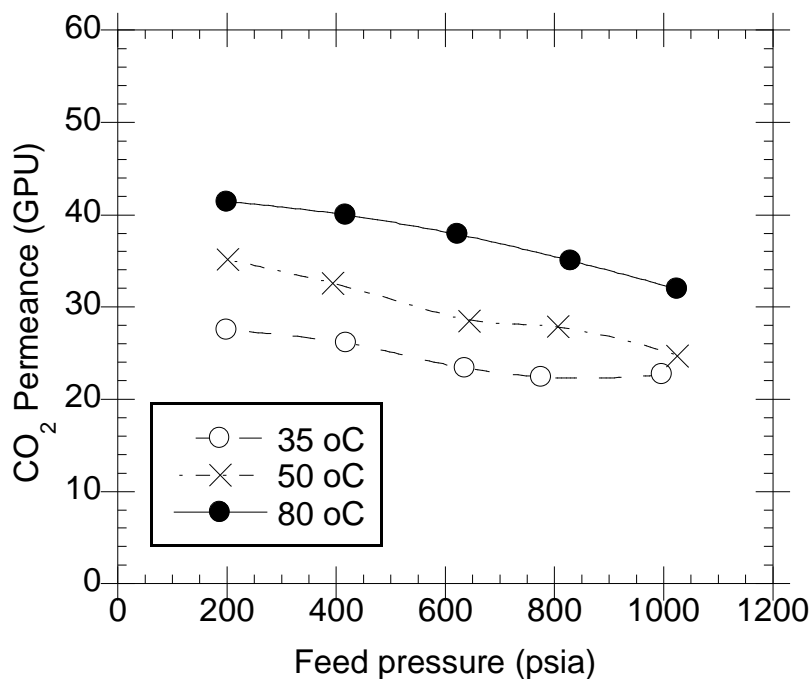


Figure 5.31: Permeances for CO₂ for a crosslinked PDMC fiber using a 20/80 CO₂/CH₄ feed at 35 °C, 50 °C, and 80 °C.

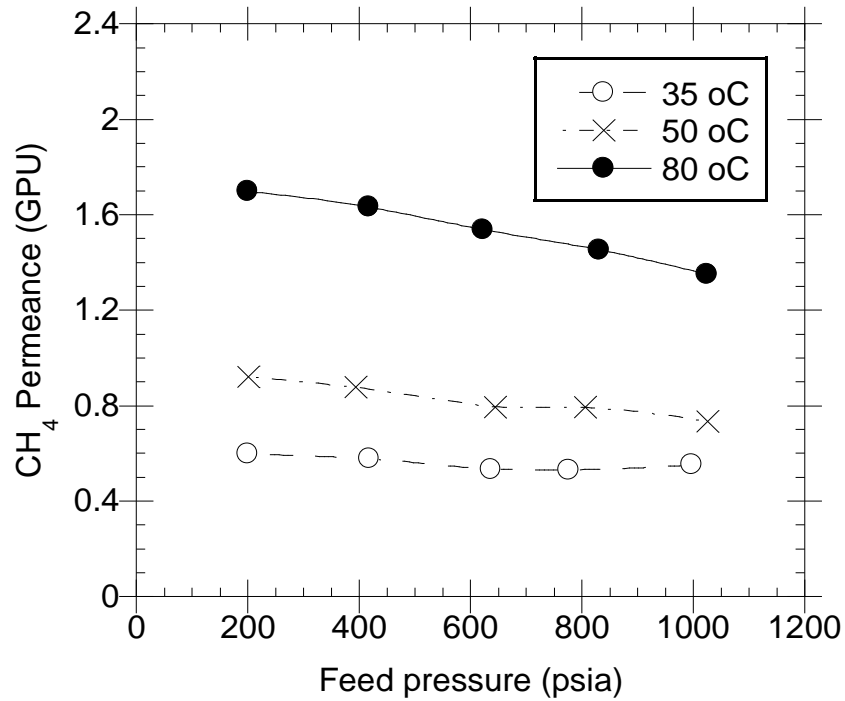


Figure 5.32: Permeances for CH₄ for a PDMC fiber using a 20/80 CO₂/CH₄ feed at 35 °C, 50 °C, and 80 °C.

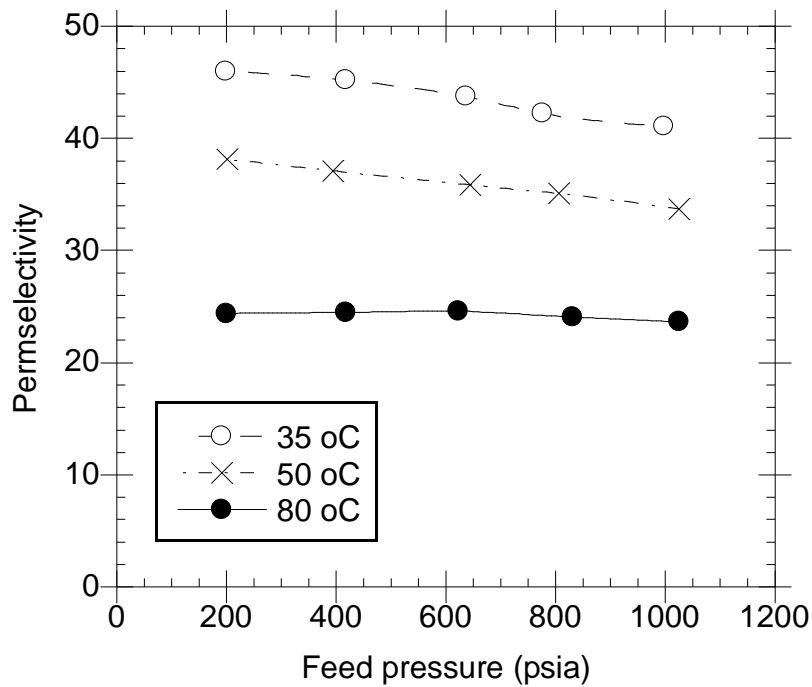


Figure 5.33: Permeability for a PDMC fiber using a 20/80 CO₂/CH₄ feed at 35 °C, 50 °C, and 80 °C.

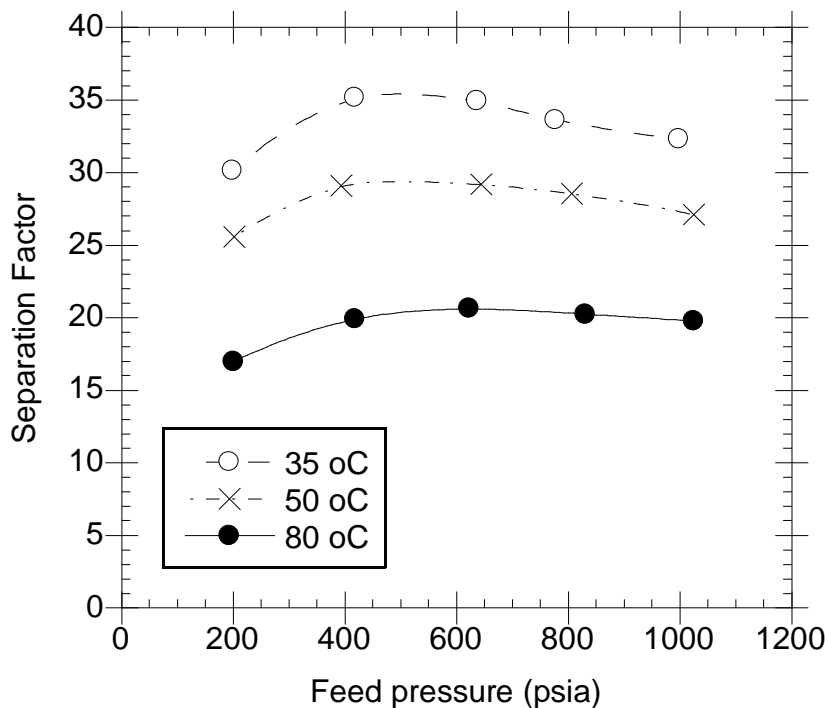


Figure 5.34: Separation factor for a PDMC fiber using a 20/80 CO₂/CH₄ feed at 35 °C, 50 °C, and 80 °C.

From the data above, it is observed that as the test temperature is increased, the permselectivity decreases and the permeances increase for both gases. The increase in CH₄ permeance is more than that for CO₂ and this becomes even more pronounced as the temperature is increased from 50 °C to 80 °C. The cause of this is likely due to the reduction in sorption of the gases on the polymer and an increase in the diffusion. A reduction in the sorption coefficient would have an effect of reducing the permeability of both gases and would affect CO₂ more, since it sorbs greater than CH₄. However, as shown in the figures, the permeances actually increase. This is due to the increase in the diffusion coefficients for the gases as the chain mobility of the polymer increases due to

the temperature increase. Since the permeability is a product of sorption and diffusion, and if the effect of increasing the diffusion coefficient is greater than the effect on decreasing sorption, the net effect is an increase in permeability or permeance. This is illustrated by Equation 5.13 below. The heat of sorption is usually negative and the energy for activation for diffusion is usually positive.

$$P_i = D_{o,i} \cdot S_{o,i} \cdot \exp\left(\frac{-E_d + \Delta H_s}{R \cdot T}\right) \quad (5.13)$$

The increase in E_{d,CH_4} ultimately causes a reduction in permselectivity (as observed), and a loss of the valuable CH_4 product at these elevated temperatures. Activation energies were computed from the permeation data at elevated temperatures. At 800 psia, with the 10/90 CO_2/CH_4 feed, the activation energy for CO_2 is ~8.77 KJ/mol, and for CH_4 is ~20.2 KJ/mol. This again suggests that there is more of a temperature dependence of CH_4 than CO_2 , explainable since the activation energy for permeation is a sum of the activation energy for diffusion and the enthalpy of sorption. Therefore, since CO_2 is more condensable and has more of an affinity with the polymer, its enthalpy of sorption is more negative than that for CH_4 . Also, since this effect is still pronounced even at high pressures where the sorption advantage of the condensable CO_2 is reduced, it is believed that the extent of CH_4 increase in diffusivity is much more than that for CO_2 , and is the main reason for the loss of selectivity. The increased temperature tests were done to simulate the membrane performance under typical field conditions. The results above suggest that the membrane performs better at lower temperatures, due to the greater temperature dependence of CH_4 . This probably means that the feed may not need to be

preheated to higher temperatures during operation. It is understood that the feeds are usually preheated to prevent condensation of the natural gas liquids on the membrane. This is done because the membrane cools as the gas permeates from high pressure to low pressures as a result of a Joule-Thomson expansion of the gas, and there is an increase in partial pressure of the condensables due to the removal of CO₂.

5.2.7 Permeation characterization of non-defect-free PDMC fibers

The hollow fibers from Section 4.3.1 of Chapter 4 were tested to determine the gas separation properties of the membrane. Before testing with the CO₂ containing feeds, the hollow fiber was crosslinked by heating at 200 °C in a vacuum oven for 1 h. This procedure activated the transesterification reaction required to stabilize the membrane in the presence of high pressure CO₂ feeds. Figure 5.35 shows the performance of a fiber used in this work, and crosslinked at 200 °C for 1 h as compared with a fiber used by Wallace [16] crosslinked at 200 °C for 24 h. As can be seen, the stability of both fibers is very similar, suggesting that 1 h crosslinking at 200 °C is sufficient. Moreover, TGA-IR analysis suggests that at 200 °C, the crosslinking reaction occurs quickly, and is mostly complete within 1 h [17]. Lower annealing temperatures and times are preferred to preserve the morphology of the fiber.

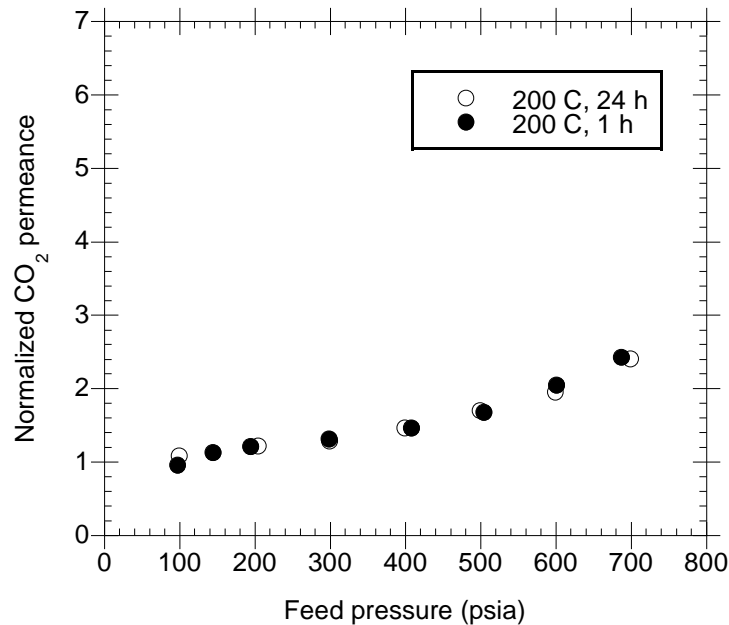


Figure 5.35: PDMC hollow fiber stability against a high pressure CO₂ feed, using 200 °C crosslinking for 24 h [16] and 1 h. Normalized permeance is the permeance at each pressure versus permeance at 100 psia.

Subsequently, the crosslinked fibers were tested by pressurizing the membrane with a model natural gas mixture, a CO₂/CH₄ feed with 20% CO₂ at 35 °C. For these permeation experiments, the membrane was exposed to the feed for ~1 h to allow sufficient time for steady state measurements to be recorded. Figures 5.36 and 5.37 show the permeation results from testing the membrane using this model natural gas mixture on the 200 micron O.D. fiber shown in Figure 4.14 in Section 4.3.1 of Chapter 4.

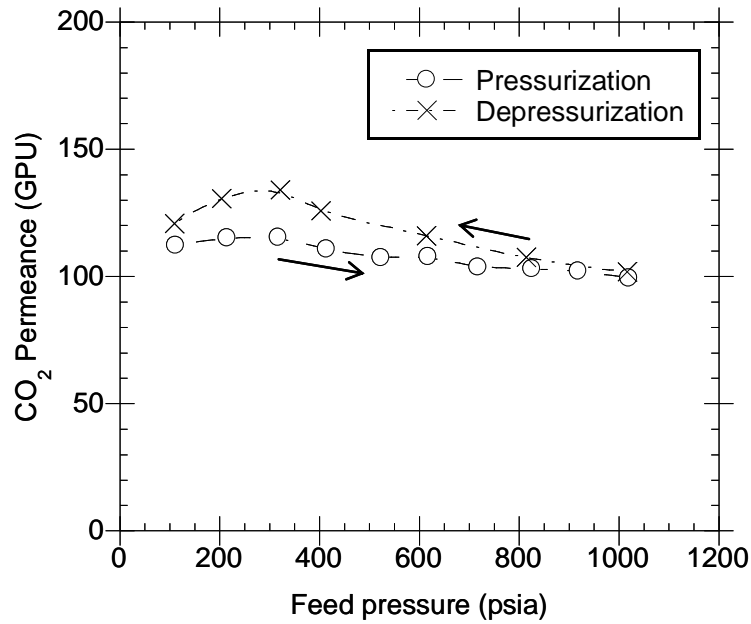


Figure 5.36: Mixed gas permeation using a 20/80 CO₂/CH₄ feed at 35 °C demonstrating the CO₂ permeance of a crosslinked PDMS (3:2) hollow fiber membrane at elevated feed pressures.

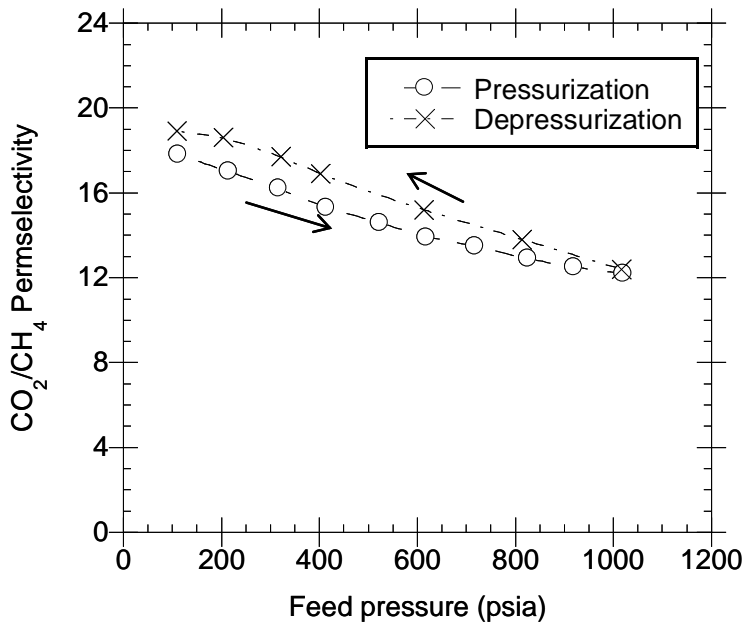


Figure 5.37: Mixed gas permeation using a 20/80 CO₂/CH₄ feed at 35 °C demonstrating the permselectivity of a crosslinked PDMS (3:2) hollow fiber membrane at elevated feed pressures.

The high pressure permeation data in Figure 5.36 shows a CO₂ permeance ≥ 100 GPU as the membrane was pressurized to about 1000 psia, which translates to a CO₂ partial pressure of 200 psia, and then depressurized. During pressurization, there is no increase in the permeances, indicating no plasticization. Instead, there is a decrease in the permeance of CO₂ and in the CO₂/CH₄ permselectivity, indicative of dual mode sorption competition effects. During the depressurization, a moderate hysteresis was observed, which indicates that some swelling was occurring due to CO₂ conditioning of the membrane to a higher free volume state when it sorbed onto the polymer [18]. However, the swelling did not cause detrimental effects on the separation capability of the membrane, presumably due to the crosslinking, which stabilizes the matrix. This is evidenced by observing the permselectivities in Figure 5.37, which shows no loss in selectively permeating the gas molecules even as the membrane was conditioned during the depressurization process. In fact, the CO₂/CH₄ permselectivity increased as a result of the slight conditioning. This is an unusual trend in polymer membrane science, because there is usually a trade off between a membrane's selectivity and permeability [19]. Presumably, CO₂ was able to compete successfully for the added free volume introduced by the conditioning process. This may be envisioned by analyzing Equation 5.14, adapted from the reference [20, 21].

$$\Delta \left[\frac{V_g - V_l}{V_l} \right] = \frac{\Delta C_H'}{\rho^*} \quad (5.14)$$

As excess free volume is created during permeation, the change in the excess free volume can be represented by the change in Langmuir capacity constants and the liquid-like molar sorbed density (ρ^*) of the penetrants in the Langmuir region. The selectivity of the penetrants for this extra free volume may then be represented by the ratio of the penetrant capacity constants, which then relates to their sorbed densities as seen in Equation 5.15.

$$\frac{\Delta C'_{H,CO_2}}{\Delta C'_{H,CH_4}} \approx \frac{\rho^*_{CO_2}}{\rho^*_{CH_4}} \quad (5.15)$$

Since the sorbed density of CO₂ would be larger than that for CH₄, it makes sense that CO₂ would “claim” the extra volume.

The crosslinked hollow fiber membrane was compared for its resistance to plasticization with pure CO₂ gas feeds at 35 °C and at elevated pressures with the uncrosslinked version. The isotherms in Figure 5.38 show the results from this experiment and it can be seen that the uncrosslinked fibers are unstable, evident by the huge increase in the CO₂ permeance. On the other hand, the crosslinked fiber shows reasonably good stability even up to 700 psia of CO₂, although there is some creep in the isotherm as the pressure is increased. This illustrates the importance of crosslinking in stabilizing the hollow fiber membrane in the presence of plasticizing feeds.

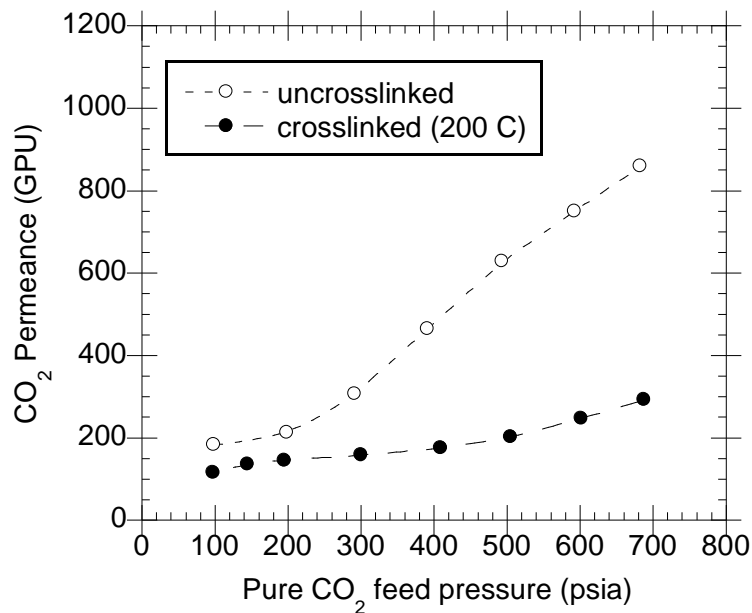


Figure 5.38: Plasticization curves for a crosslinked and uncrosslinked PDMC (3:2) polyimide. Test temperature was 35 °C.

As mentioned in Chapter 4, these fibers showed viability for separating the CO₂/CH₄ gas pair at high pressures, but the permselectivities shown in Figure 5.37 fall short of the intrinsic polymer permselectivity, which is about 45 at 65 psia and 35 °C [1]. This is why the defect-free fibers from Chapter 4 were thus used for the previous permeation characterization presented in the earlier part of this chapter.

5.3 Summary

In this chapter, the characteristics of the crosslinked and uncrosslinked PDMC polymer membranes were explored to demonstrate their performance up to CO₂ partial pressures of 400 psia. The crosslinked membranes were shown to be much more resistant

to swelling induced losses of CH₄, which occur from the high partial pressures of CO₂. The performance of the fibers was shown to be very dependent on their age. The ageing process increases permselectivity and reduces permeances as the excess free volume is removed from the fiber. The high performance of the PDMC membrane was also found to be very dependent on the temperature, and there appeared to be much higher temperature dependence for CH₄ than for CO₂.

5.4 References

1. Hillock, A.M.W. and W.J. Koros, *Cross-Linkable Polyimide Membrane for Natural Gas Purification and Carbon Dioxide Plasticization Reduction*. *Macromolecules*, 2007. **40**: p. 583-587.
2. Wind, J.D., et al., *Solid-State Covalent Cross-Linking of Polyimide Membranes for Carbon Dioxide Plasticization Reduction*. *Macromolecules*, 2003. **36**: p. 1882-1888.
3. Wind, J.D., *Improving Polyimide Membrane Resistance to Carbon Dioxide Plasticization in Natural Gas Separations*, in *Chemical Engineering*. 2002, The University of Texas at Austin: Austin, Texas. p. 215.
4. Adam, K., *THICKNESS DEPENDENT PHYSICAL AGING AND SUPERCRITICAL CARBON DIOXIDE CONDITIONING EFFECTS ON CROSSLINKABLE POLYIMIDE MEMBRANES FOR NATURAL GAS PURIFICATION*, in *Chemical & Biomolecular Engineering*. 2008, Georgia Institute of Technology: Atlanta. p. 200.
5. Kim, J.H., W.J. Koros, and D.R. Paul, *Physical aging of thin 6FDA-based polyimide membranes containing carboxyl acid groups. Part I. Transport properties*. *Polymer*, 2006. **47**(9): p. 3094-3103.
6. Kim, J.H., W.J. Koros, and D.R. Paul, *Physical aging of thin 6FDA-based polyimide membranes containing carboxyl acid groups. Part II. Optical properties*. *Polymer*, 2006. **47**(9): p. 3104-3111.
7. Kim, J.H., W.J. Koros, and D.R. Paul, *Effects of CO₂ exposure and physical aging on the gas permeability of thin 6FDA-based polyimide membranes: Part I. Without crosslinking*. *Journal of Membrane Science*, 2006. **282**(1-2): p. 21-31.
8. Kim, J.H., W.J. Koros, and D.R. Paul, *Effects of CO₂ exposure and physical aging on the gas permeability of thin 6FDA-based polyimide membranes: Part 2. with crosslinking*. *Journal of Membrane Science*, 2006. **282**(1-2): p. 32-43.
9. Wind, J.D., et al., *The Effects of Crosslinking Chemistry on CO₂ Plasticization of Polyimide Gas Separation Membranes*. *Ind. Eng. Chem. Res.*, 2002. **41**: p. 6139-6148.

10. Wind, J.D., D.R. Paul, and W.J. Koros, *Natural gas permeation in polyimide membranes*. Journal of Membrane Science, 2004. **228**: p. 227–236.
11. Koros, W.J., *Model For Sorption of Mixed Gases in Glassy Polymers*. Journal of Polymer Science, Polymer Physics Edition, 1980. **18**(5): p. 981-992.
12. Koros, W.J., et al., *Model For Permeation of Mixed Gases and Vapors in Glassy Polymers*. Journal of Polymer Science, Polymer Physics Edition, 1981. **19**(10): p. 1513-1530.
13. Kamaruddin, H.D. and W.J. Koros, *Some observations about the application of Fick's first law for membrane separation of multicomponent mixtures*. Journal of Membrane Science, 1997. **135**: p. 147-159.
14. Baker, R.W., *Membrane Technology and Applications*. 2nd ed. 2004: John Wiley & Sons, Ltd. 538 pp.
15. Baker, R., *Designing Membranes for Future Membrane Gas Separation Applications*, in *International Congress on Membranes and Membrane Processes (ICOM) 2008*. 2008: Honolulu, Hawaii.
16. Wallace, D.W., *Crosslinked Hollow Fiber Membranes for Natural Gas Purification and Their Manufacture from Novel Polymers*, in *Chemical Engineering*. 2004, The University of Texas at Austin: Austin, Texas. p. 202.
17. Wallace, D.W., et al., *Characterization of crosslinked hollow fiber membranes*. Polymer, 2006. **47**: p. 1207–1216.
18. Al-Juaied, M. and W.J. Koros, *Performance of natural gas membranes in the presence of heavy hydrocarbons*. Journal of Membrane Science, 2006. **274**(1-2): p. 227-243.
19. Robeson, L.M., *Correlation of separation factor versus permeability for polymeric membranes*. Journal of Membrane Science, 1991. **62**: p. 165-185.
20. Koros, W.J. and D.R. Paul, *Carbon dioxide sorption in poly(ethylene terephthalate) above and below the glass transition*. J. Polym. Sci., Polym. Phys. Ed., 1978. **16**(11): p. 1947-63.

21. Koros, W.J. and D.R. Paul, *Transient and steady-state permeation in poly(ethylene terephthalate) above and below the glass transition*. J. Polym. Sci., Polym. Phys. Ed., 1978. **16**(12): p. 2171-87.

CHAPTER 6

PERFORMANCE OF CROSSLINKABLE HOLLOW FIBER MEMBRANES IN THE PRESENCE OF TOLUENE CONTAMINANT

6.1 Introduction

This chapter contains experiments that characterize the permeation properties of the PDMC hollow fibers (crosslinked at 200 °C) in the presence of toluene, a highly sorbing contaminant. Typical feeds streams in natural gas sweetening applications are pre-treated so that the level of hydrocarbon impurities is reduced substantially as shown in Figure 6.1.

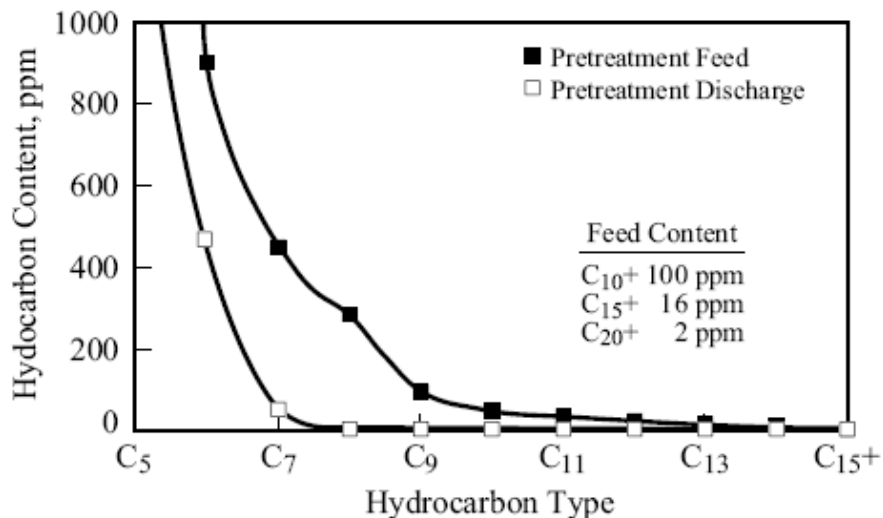


Figure 6.1: Graph illustrating the extent to which a natural gas feed may be pretreated before being fed to a membrane [1].

Despite pretreatment, there still remains a significant amount of impurities in the feed, and upsets can occur, so it necessary to determine the performance of a membrane in the presence of a range of contaminant concentrations. The effects of the presence of heavy hydrocarbons on membrane performance can be deleterious to membrane in operation [2-4]. The effect of the impurity is dependent on the membrane structure, contaminant type and concentration of impurity. Toluene, a C7 aromatic, was chosen as the model contaminant for the studies in this chapter. Firstly, the sorption of toluene in the crosslinked PDMC polymer is shown, and then permeation data are presented to represent events occurring in the presence of feed stream contamination. For the permeation studies with the toluene contaminant, initial experiments were performed using an available gas cylinder at the time of testing. This is shown in Section 6.3.1. Subsequently, a more complete characterization was performed and results from these are presented in Section 6.3.2.

6.2 Sorption with toluene vapors

A sorption experiment was performed on the PDMC hollow fibers to determine the mass uptake of toluene at high activities (from 0 to >0.8) at 35 °C. The results of this experiment can be seen in Figure 6.2.

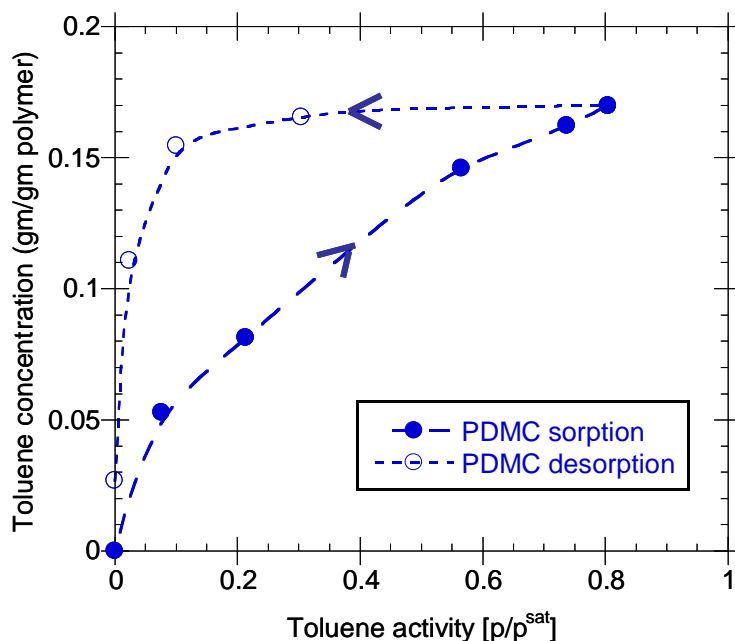


Figure 6.2: Toluene sorption and desorption isotherms in 200 °C crosslinked PDMC hollow fibers tested at 35 °C. For each point, measurements were made after ~24 h.

From the sorption isotherm shown in Figure 6.2, it is observed that there is a significant mass uptake (between 15–20 wt%) of the toluene vapors as the activity is increased. A desorption experiment was also carried out on the fiber samples and indicated that a certain amount of toluene remains in the fiber after the feed is removed, as evidenced by the hysteresis. As the toluene is evacuated from the sorption chamber by pulling vacuum for 48 h, it is noticed that there still remains ~2.5 wt% toluene residual in the fiber. Undoubtedly, this level would eventually fall to zero; however, the time for complete removal may be extremely long at 35 °C. Dual mode sorption parameters were obtained

from the sorption data by fitting the dual mode model with the sorption isotherm as shown in Figure 6.3 and Table 6.1. The dual mode sorption parameters for CO₂ and CH₄ are also shown in Table 6.1 for comparison.

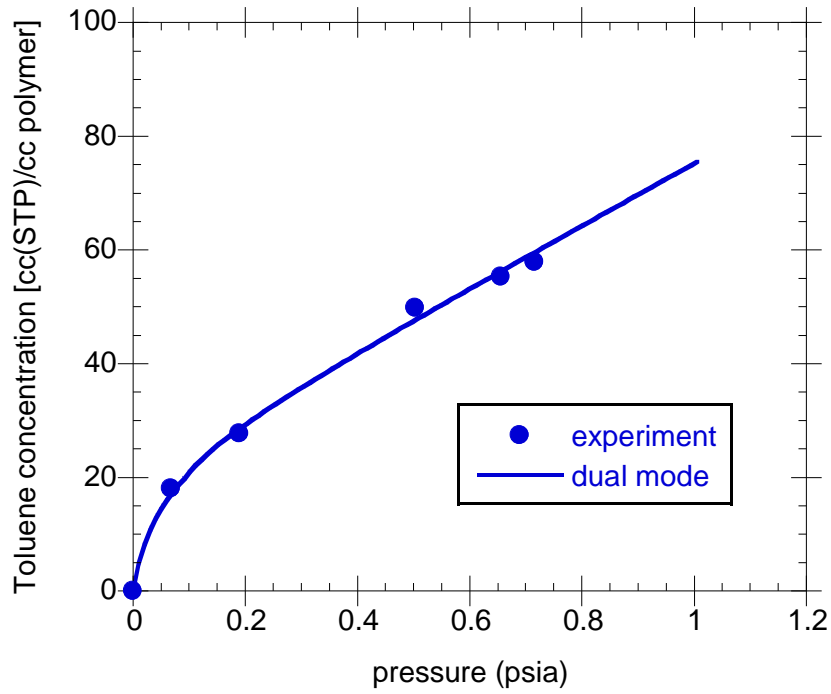


Figure 6.3: Sorption isotherm for toluene in PDMC hollow fiber membranes crosslinked at 200 °C.

Table 6.1 Dual mode sorption parameters for CO₂, CH₄, and toluene at 35 °C in PDMC hollow fibers crosslinked at 200 °C.

<i>Gas</i>	k_D [cc(STP)/cc polymer·psi]	C_H' [cc(STP)/cc polymer]	b [1/psi]
Toluene	57	20	29
CO ₂	0.043	62.6	0.018
CH ₄	0.035	19.6	0.01

The sorption characteristics of the PDMC polymer in the presence of toluene helps explain the observations made during permeation. The permeation results are presented in the following sections.

6.3 Stability against natural gas feeds with toluene impurity

6.3.1 Preliminary studies

The performance of the crosslinked PDMC hollow fiber membranes was evaluated with an available gas mixture with the toluene contaminant. These studies were performed by exposing the same membrane to a toluene containing feed twice.

6.3.1.1 First exposure

The crosslinked hollow fiber membrane was first exposed to a toluene containing feed through a sequence of steps described below in Figure 6.4 and Table 6.2.

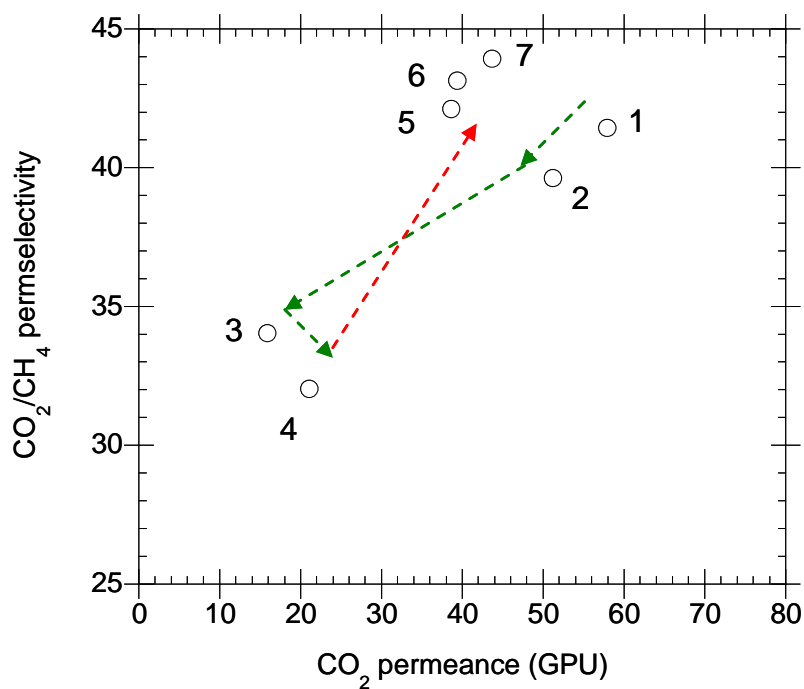


Figure 6.4: Performance of crosslinked fibers tested under various conditions with and without impurities. The numbers beside each point indicate a test condition as described in Table 6.2. The red arrow between points 4 and 5 represents a 2 week interval.

Table 6.2: Description of numbered points in Figure 6.4.

#	<i>description</i>
1	200 psia; no toluene; 35 °C
2	400 psia; no toluene; 35 °C
3	400 psia; toluene activity ~0.13; 35 °C
4	400 psia; toluene activity ~0.13; 50 °C (~2 weeks)
5	400 psia; no toluene; 35 °C (70 °C vacuum dried for 96 h)
6	400 psia; no toluene; 35 °C
7	200 psia; no toluene; 35 °C

The points in Figure 6.4 above show serially numbered points in chronological order, representing different testing conditions. Point 1 is the fiber tested using a clean binary feed at 200 psia. The CO₂ permeance here is ~58 GPU and the selectivity is ~41. An increase in pressure from 200 psia to 400 psia would result in a slight decrease in permeance and selectivity as expected from the binary CO₂/CH₄ feed analysis presented in Chapter 5. This is illustrated in Point 2, and makes the test pressure comparable to that which was used when toluene was first introduced to the feed. Subsequently, using a CO₂/CH₄ feed with 293 ppm toluene at 400 psia (toluene activity of ~0.13), the hollow

fiber permeance and selectivity of CO₂/CH₄ decreased. The critical temperature of toluene is ~594 K [5] and therefore it is expected that toluene is more condensable than CO₂ and CH₄. This is confirmed by the sorption data in Table 6.1, which shows a high affinity constant for toluene compared with CO₂ and CH₄ using the crosslinked PDMC polymer. This causes the excess free volume in the polymer to be occupied by toluene molecules, which also do not diffuse as fast through the membrane as CO₂ or CH₄. The occupation of these Langmuir regions is illustrated in Figure 6.4.

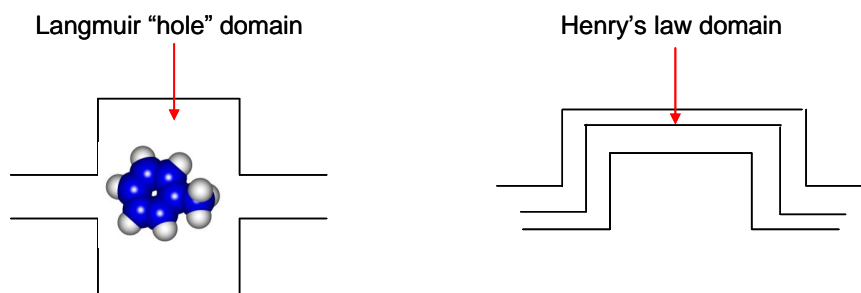


Figure 6.5: Schematic illustrating the occupation of a chain packing defect or excess free volume (or Langmuir domain) by the toluene molecule, which may causes declines in permeance of CO₂ and CH₄ even at low feed pressures and low toluene concentrations.

This decrease in permeance and selectivity reduces any benefits of the excess free volume, since the CO₂ permeance is decreased to a much more extent than the CH₄ permeance and CO₂ is the desired permeate. The membrane was exposed to the toluene feed for at least 24 h and this is illustrated as Point 3 in the figure. The temperature was then increased to ~50 °C, and the performance was evaluated during exposure. As can be seen from Point 4, this did increase the permeances somewhat, but there was a corresponding drop in the selectivity. Since toluene already sorbs more than both CO₂ and CH₄, the further drop in selectivity suggests that the increase in diffusion coefficients

causes the selectivity decline, since the diffusion coefficient of CH₄ was increased more than that for CO₂. This corresponds with the temperature studies carried out in Chapter 5 with the binary feed. The toluene feed was subsequently removed from the membrane. After about 2 weeks, the membrane was retested using a clean binary feed at 400 psia again. This is indicated as Point 5. It was observed that the removal of the toluene feed and purging with a clean binary feed almost regenerates the fiber's performance values to that observed prior to contamination. It did not appear that the membrane was irreversibly damaged by the toluene impurity, which was fed to the membrane continuously for over 48 h.

It appears that the new state of the fiber was denser than the original state as evidenced by the increase in permselectivity and reduction in permeance after exposure and removal of the contaminant. It is believed that this new state may be caused by the residual amount of toluene in the membrane, which can act as an antiplasticizer. This corresponds with Maeda and Paul's work, which showed that certain low molecular weight compounds mixed into to a polymer matrix at low concentrations may retard the segmental motions of the polymer matrix [6]. Paul and Maeda found that at the lower end of the concentration range, the additive caused declines in permeance and increase in selectivity, while at the higher end of the additive's concentration range a decrease in permeance and decrease in selectivity were observed.

To investigate the presence of possible excess toluene in the membrane, the fiber module was placed in a vacuum oven at 70 °C for ~4 days to remove the toluene without significantly changing the intrinsic fiber performance from any heating effects. The performance of the membrane after retesting can be seen at Point 6. The effect of the

extra vacuum treating did not cause any appreciable improvement, indicating that the in-situ purging after 2 weeks of dormancy was sufficient to practically regenerate the fiber to appreciable separation performance values. The pressure was finally lowered to 200 psia, bringing the test conditions to the same as that used at Point 1. The performance after reducing the pressure is shown at Point 7, which shows a higher selectivity and lower permeance than the original value, suggesting that the polymer is in a more tightly packed state.

6.3.1.2 Second exposure

The same fiber module that was exposed to toluene in Section 6.2.1.1 was retested by re-introducing the toluene feed in a sequence of conditions. A feed pressure of 400 psia was chosen for the tests to compare with the data in Figure 6.4. The re-exposure experiments are shown in Figure 6.6 and Table 6.3.

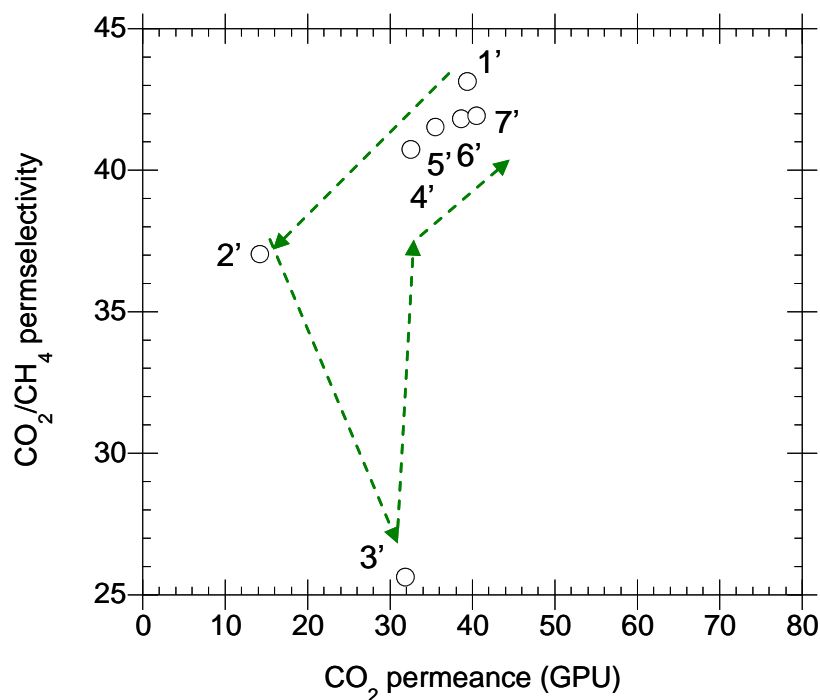


Figure 6.6: Performance of crosslinked fibers tested under various conditions with and without impurities after first exposure shown in Figure 6.4 and Table 6.2. The numbers beside each point indicate a test condition as described in Table 6.3.

Table 6.3: Description of numbered points in Figure 6.5.

#	<i>description</i>
1'	400 psia; no toluene; 35 °C
2'	400 psia; toluene activity ~0.13; 35 °C
3'	400 psia; toluene activity ~0.13; 80 °C
4'	400 psia; no toluene; 35 °C (in-situ purged ~2 h)
5'	400 psia; no toluene; 35 °C (in-situ purged ~6 h)
6'	400 psia; no toluene; 35 °C (in-situ purged ~16 h)

Point 1' in Figure 6.6 above represents Point 6 in Figure 6.4, which is the last point at 400 psia after the fiber was regenerated. The fiber was subsequently re-exposed to the toluene feed as done previously. The membrane performance was lowered again to a similar permeance as was observed before, due to the presence of the toluene, indicated by Point 2'. Subsequently, a more elevated test temperature of 80 °C was used to determine how much permeance could be recovered by increasing the temperature from 35 °C. This is represented as Point 3'. Point 3' shows that at 80 °C, there is the usual trade-off. There is a substantial increase in the permeance at 80 °C but the selectivity dropped as the permeance increased. As opposed to the previous experiment, after removing the toluene in the feed, here the membrane was immediately tested with a clean binary feed. The Points 4', 5', and 6' represent the in-situ purged membrane at different times after the toluene was removed. It was observed that the fiber membrane regains ~100% of its performance values in about 16 h of testing. The new selectivity at Point 6' was 42 while the CO₂ permeance was ~ 39 GPU at 400 psia, 35 °C. These experiments indicate that the crosslinked fiber is quite robust with the toluene impurity, although there were declines in the separation performance in the presence of the toluene impurity.

6.3.2 More aggressive feeds

6.3.2.1 Effects of increasing concentration of toluene on crosslinked PDMC fibers

To further explore the range of compositions of toluene the PDMC hollow fiber membrane could withstand, more characterization experiments were performed on the

membrane using higher toluene levels. These experiments help understand if sorption alone can be used to describe the events occurring during exposure or if higher toluene levels will cause plasticization or antiplasticization. The 200 °C crosslinked PDMC hollow fiber membrane was tested with toluene-containing natural gas feeds (~10% CO₂ and balance CH₄) at different concentrations of toluene: 30 ppm, 100 ppm, 200 ppm, 500 ppm, and 1000 ppm. Each level of feed contamination was introduced to the membrane at pressures up to 1000 psia to demonstrate the efficacy of the hollow fiber in maintaining good separation between the CO₂ and CH₄ molecules at increasingly high concentrations of the toluene impurity. These experiments are shown in Figures 6.7–10.

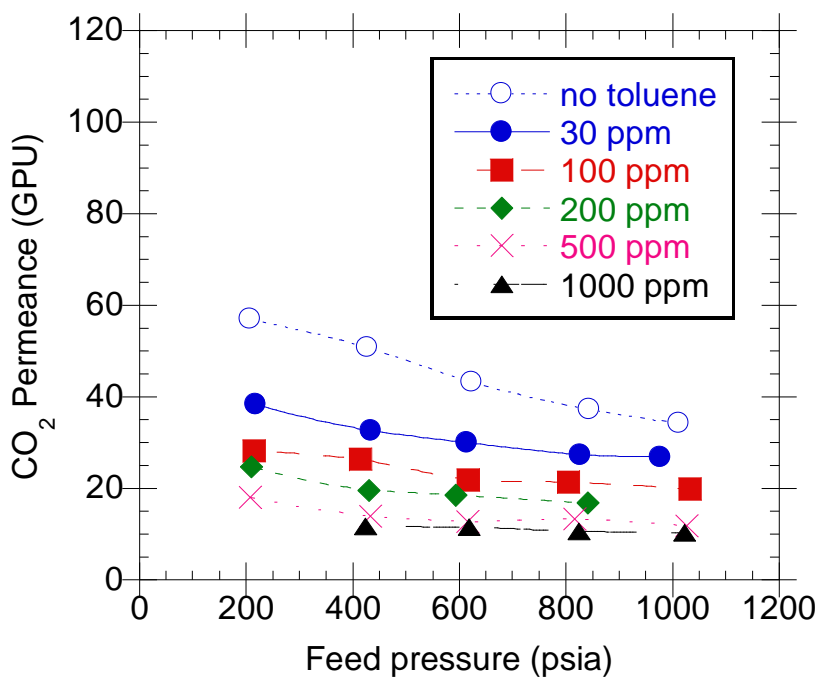


Figure 6.7: Effect of toluene at different feed pressures on the CO₂ permeance using a 200 °C crosslinked PDMC hollow fiber membrane. Test temperature: 35 °C.

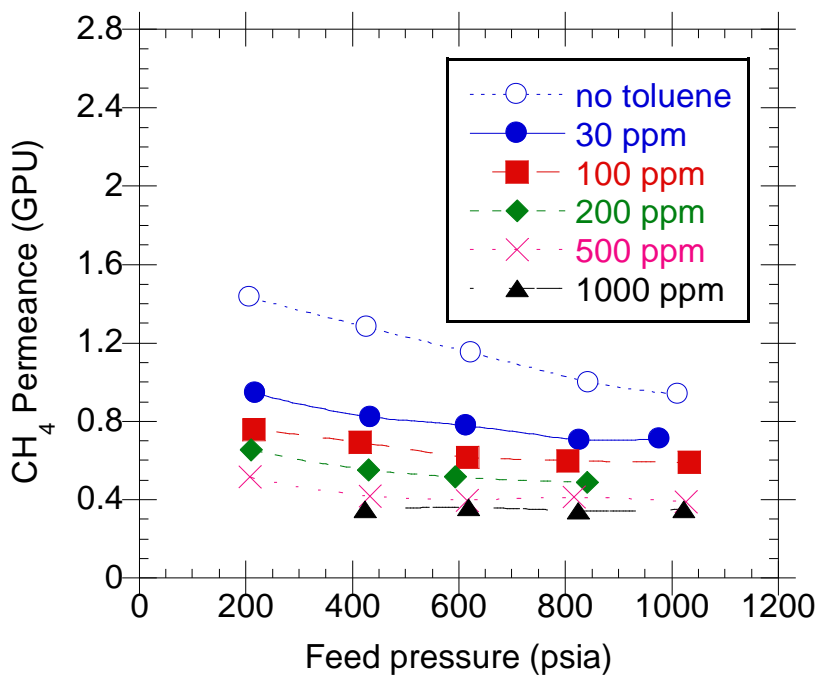


Figure 6.8: Effect of toluene at different feed pressures on the CH₄ permeance using a 200 °C crosslinked PDMC hollow fiber membrane. Test temperature: 35 °C.

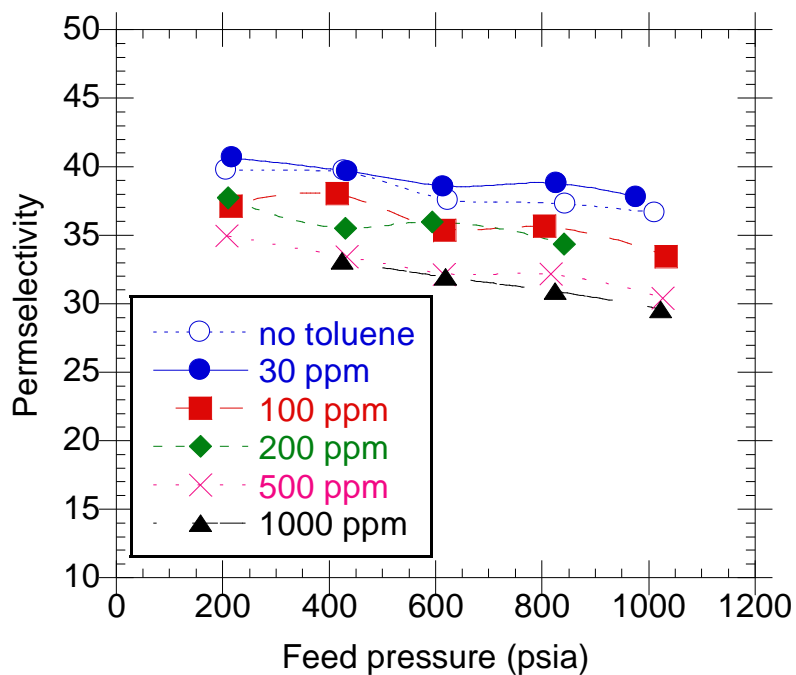


Figure 6.9: Effect of toluene at different feed pressures on the CO₂/CH₄ permselectivity using a 200 °C crosslinked PDMC hollow fiber membrane. Test temperature: 35 °C.

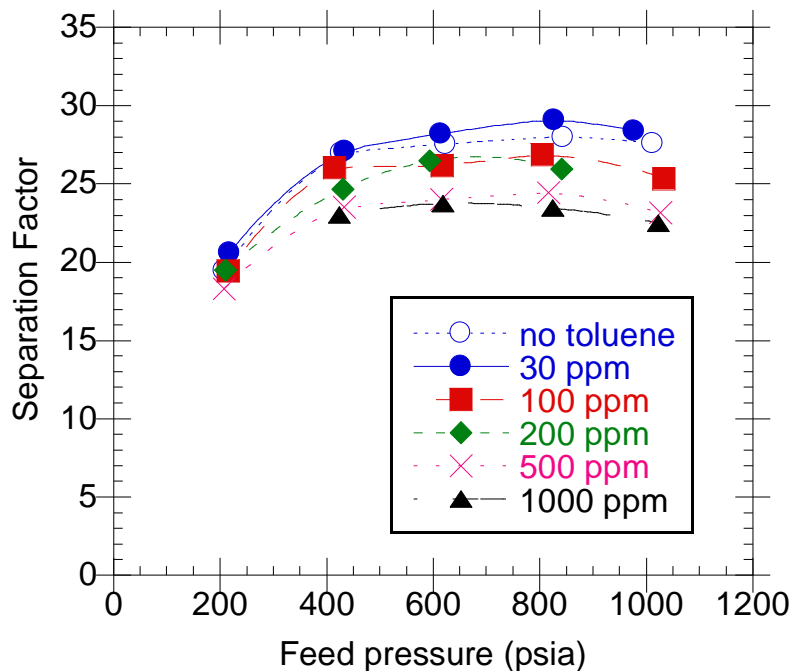


Figure 6.10: Effect of toluene at different feed pressures on the CO₂/CH₄ separation factor using a 200 °C crosslinked PDMC hollow fiber membrane. Test temperature: 35 °C.

From the figures above, it can be seen that there is no plasticization occurring from increased pressures using all the feeds. Instead, the permeance decreases indicative of Langmuir sorption saturation or antiplasticization. The feed with no toluene shows more of a Langmuir mode effect from the increased pressure (steeper decrease in permeances) than the feeds with toluene contamination, which suggests that the membrane sorbs a significant amount of the toluene molecules even at lower pressures. This is indicated by the Langmuir affinity constant, which is about 29 psia⁻¹ for toluene, 0.018 psia⁻¹ for CO₂, and 0.010 psia⁻¹ for CH₄. The separation efficiencies (permselectivity and separation factor) still remain at attractively high values even in the presence of high amounts of toluene. To investigate the effects of Langmuir sorption versus antiplasticization, the equation for the permeance in a multiple feed mixture from the partial immobilization model was used [7]. This is shown in Equation 6.1 below.

$$\frac{P_i}{l} = \frac{D_{D,i} \cdot k_{D,i}}{l} \cdot \left(1 + \frac{F_i \cdot K_i \cdot \frac{f_{i,up}}{f_{i,up} - f_{i,d}}}{1 + \sum_{i=1}^n b_i \cdot f_{i,up}} - \frac{F_i \cdot K_i \cdot \frac{f_{i,d}}{f_{i,up} - f_{i,d}}}{1 + \sum_{i=1}^n b_i \cdot f_{i,d}} \right) \quad (6.1)$$

The model represented by Equation 6.1 accounts for the presence of the excess free volume that exists in glassy polymers. In the case that the excess free volume or Langmuir holes are completely filled up, the permeance approaches the limit where permeation occurs through only the Henry's mode, similar to the case for rubbery polymers. In such a case, the term in parenthesis in Equation 6.1 will approach unity, and

the permeance approaches a constant value, assuming the diffusion coefficients do not change. This limit is described mathematically as $k_{D,i} \cdot D_{D,i} / l$. From values of $D_{D,i} / l$ in Table 5.4 in Chapter 5, and the sorption parameters in Table 5.3 of Chapter 5, values for $k_{D,i} \cdot D_{D,i} / l$ for CO₂ and CH₄ are estimated to be ~37 GPU and 0.8 GPU respectively. As can be seen from the plots in Figures 6.7 and 6.8, the permeances for CO₂ and CH₄, with increasing toluene concentration, are well below these values, and indicate that the diffusion coefficients are changed due to the presence of the toluene contaminant in the feed as would be the case in an antiplasticized membrane. At the highest level of toluene, the CO₂ permeance is ~10 GPU and the CH₄ permeance is ~0.35 GPU. Antiplasticization, in effect, reduces the frequency of molecular motion and the transient gap formation required for the molecules to make a diffusive jump is hindered due to the presence of the heavy impurity. This is illustrated using Figure 6.11 and Equation 6.2. In Equation 6.2, D is the diffusion coefficient for the penetrant molecule, f is the frequency for diffusion jumps and λ is the average jump length created by the transient gap.

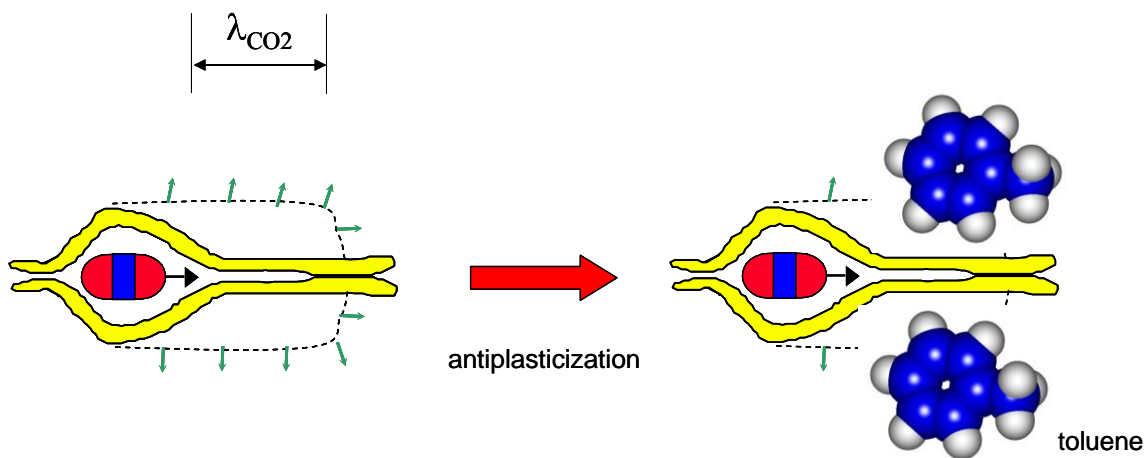


Figure 6.11: Schematic illustrating the effect of antiplasticization on the molecular motions of the polymer and on the gas diffusion.

$$D_i = \frac{f_i \cdot \lambda_i^2}{6} \quad (6.2)$$

The trends from the toluene exposure were compared with the performance of a commercially available polymer, Matrimid[®], courtesy of Madden [8]. This is shown in Figures 6.12–17.

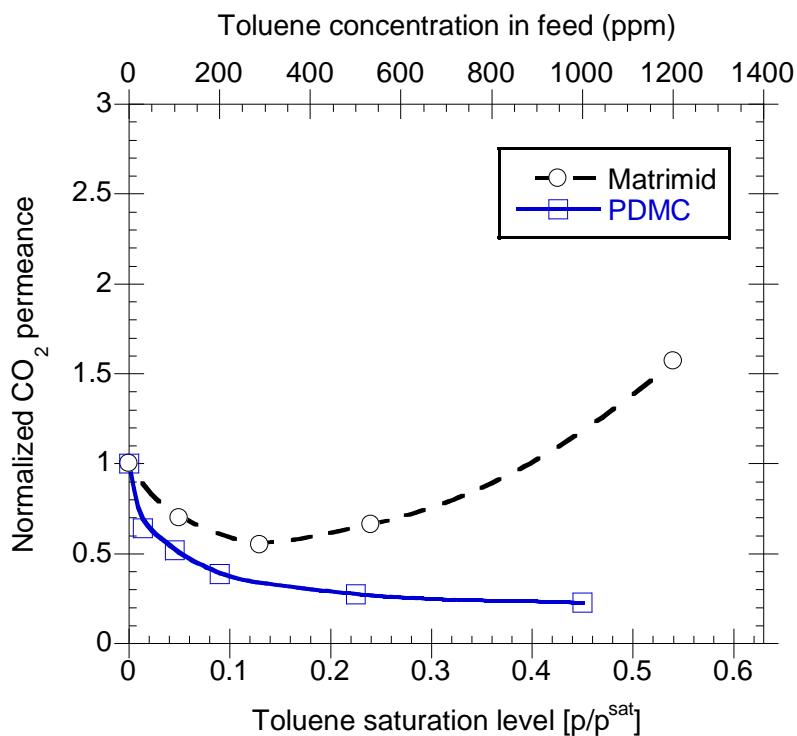


Figure 6.12: Effect of toluene concentration on normalized CO₂ permeance of Matrimid[®] and PDMC crosslinked at 200 °C. Feed pressure ~400 psia, temperature ~35 °C.

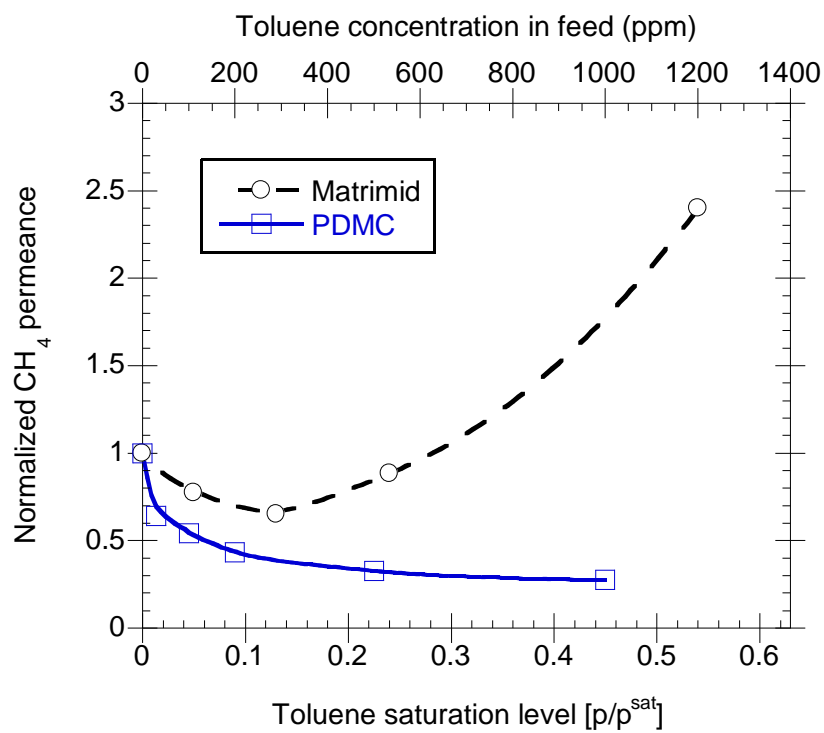


Figure 6.13: Effect of toluene concentration on normalized CH₄ permeance of Matrimid[®] and PDMC crosslinked at 200 °C. Feed pressure ~400 psia, temperature ~35 °C.

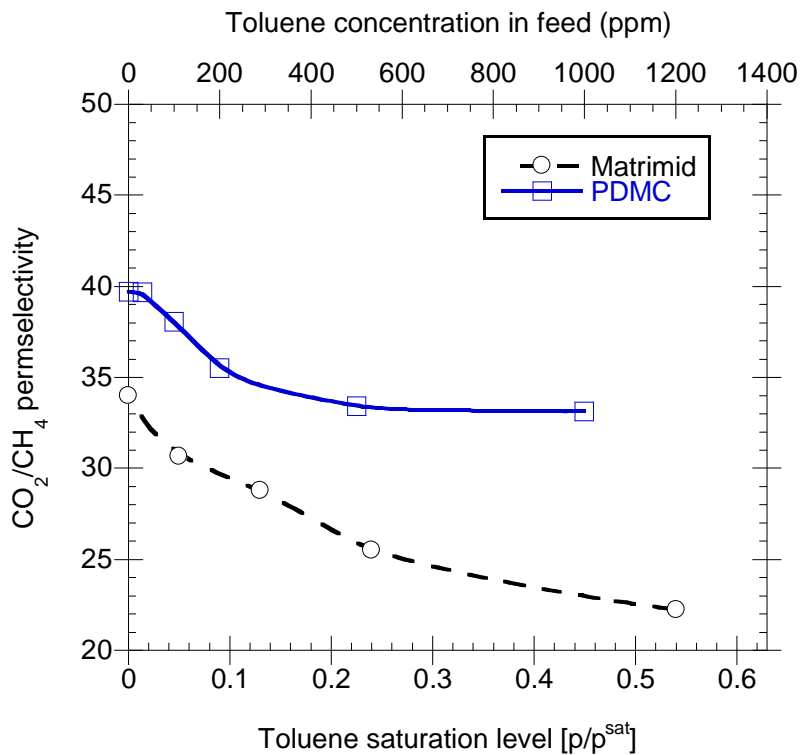


Figure 6.14: Effect of toluene concentration on normalized CH₄ permeance of Matrimid[®] and PDMC crosslinked at 200 °C. Feed pressure ~400 psia, temperature ~35 °C.

Higher toluene levels in testing the PDMC hollow fibers are also shown in Figures 6.15 to 6.17.

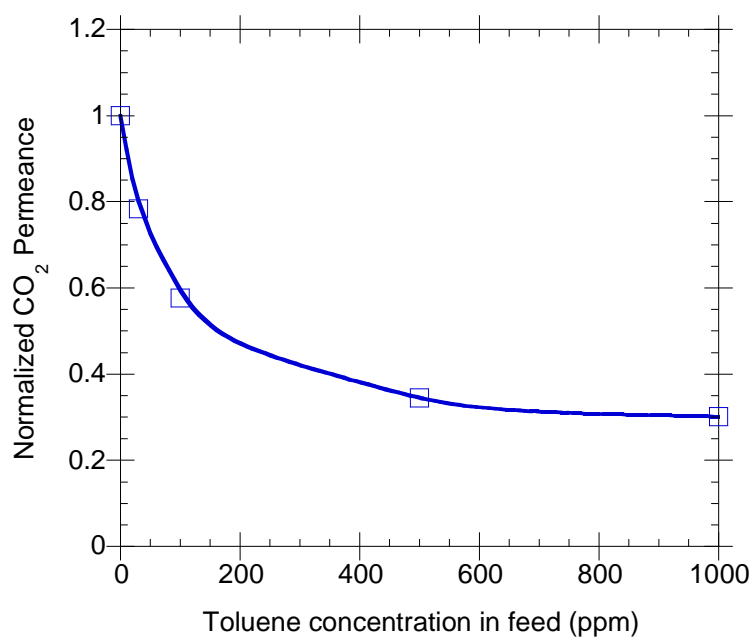


Figure 6.15: Effect of toluene level on normalized CO₂ permeance of PDMC crosslinked at 200 °C. Feed pressure ~1000 psia, temperature ~35 °C.

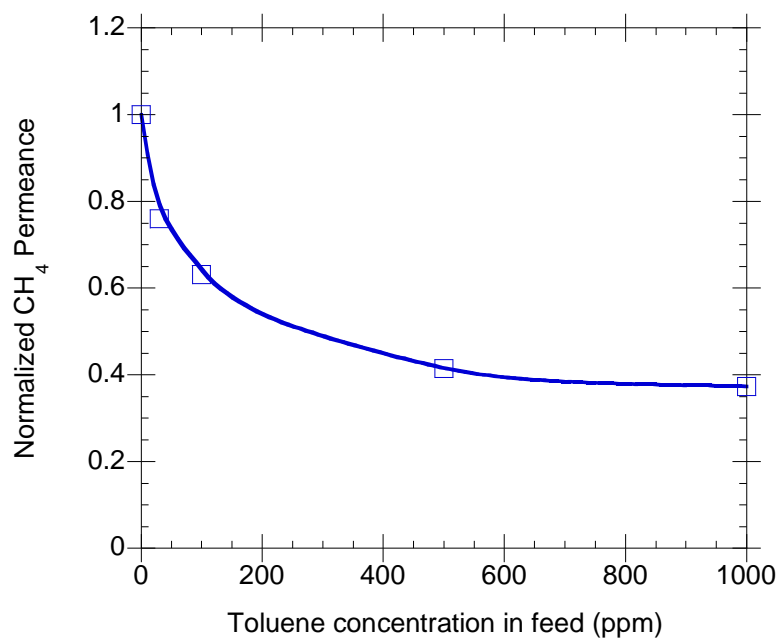


Figure 6.16: Effect of toluene level on normalized CH₄ permeance of PDMC crosslinked at 200 °C. Feed pressure ~1000 psia, temperature ~35 °C.

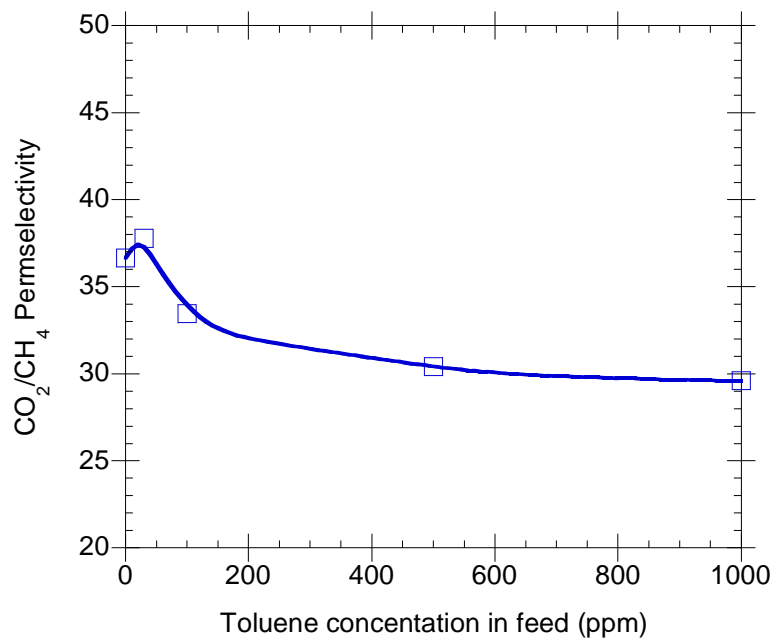


Figure 6.17: Effect of toluene level on CO₂/CH₄ permeability of PDMC crosslinked at 200 °C. Feed pressure ~1000 psia, temperature ~35 °C.

As the toluene levels increase as shown in Figures 6.12 to 6.17, the negative effects from contamination on the productivity and separation efficiency begin to reduce as the performance values level off. This suggests that the antiplasticization effect is dependent on the level of sorption. At the highest toluene contamination level, the CO₂ permeance is ~10 GPU, which is about ~30% of the permeance without toluene at that pressure. The selectivity at this point is ~30. The performance of the PDMC hollow fiber membrane appears viable in the presence of the impurities, since no plasticization was evident. Although the productivity has decreased significantly at these aggressive conditions, conservative estimates show that the permeance value still surpasses the performance of other solvent resistant polymers with relatively high selectivities for CO₂/CH₄ such as Torlon[®] without impurities.

It was also observed that the Matrimid[®] polymer plasticized as the toluene concentration increased, while there was no apparent plasticization using the PDMC polymer. The results here suggest that *antiplasticization* occurs in the PDMC hollow fiber membranes instead. The sorption of toluene in the PDMC polymer was compared with that for Matrimid[®] and can be seen in Figure 6.18.

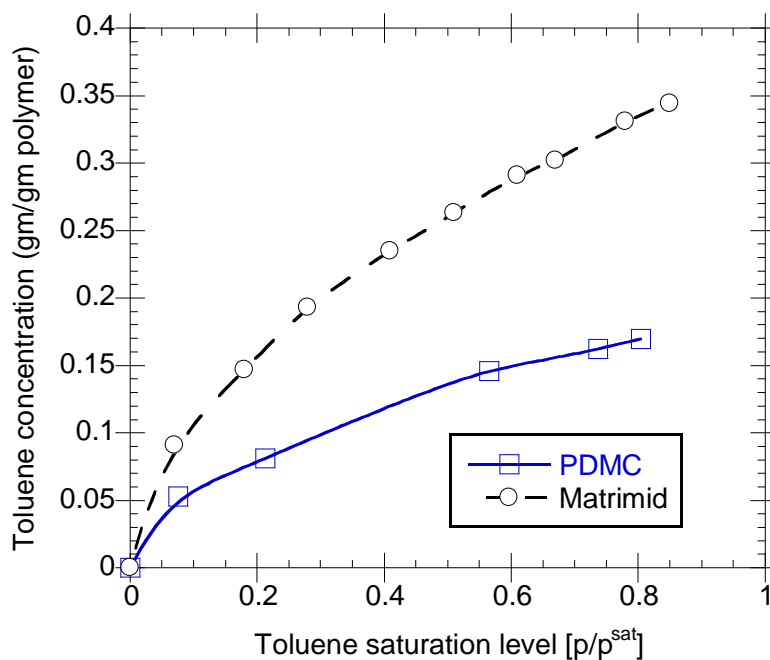


Figure 6.18: Sorption of toluene in crosslinked PDMC hollow fiber membranes and Matrimid[®]. (Matrimid courtesy of Madden).

As can be seen from Figure 6.18, the Matrimid[®] polymer does sorb significantly more than the crosslinked PDMC polymer. This is not a result of the crosslinking, because crosslinking in these crosslinkable polymers actually increases excess free volume and sorption compared to their uncrosslinked counterparts [9]. It is observed from Figure 6.18 that as the activity of toluene approaches unity, the concentration of toluene in Matrimid[®] is almost 40 wt%. The Matrimid[®] fibers were tested up to toluene activities of about 0.55 during the permeation experiments as shown in Figures 6.12–6.14. At this point, the

sorbed concentration in Matrimid[®] is over 25 wt%. However, the PDMC fibers do not seem to sorb nearly as much. This suggests that there may be attractive chemical interactions between the Matrimid[®] polymer and the toluene molecules or less favorable interactions between the PDMC polymer and the toluene molecules that makes the Matrimid[®] polymer sorb more toluene. The Matrimid[®] polymer may have more accessible aromatic groups per unit chain length and this may be the reason for the increased sorption since aromatic groups may engage in pi bond interactions with toluene molecules. This may be the reason why Matrimid[®] plasticizes at such lower activities, and not necessarily because it is not crosslinked. The structure of Matrimid[®] and PDMC are shown in Figure 6.19 for reference.

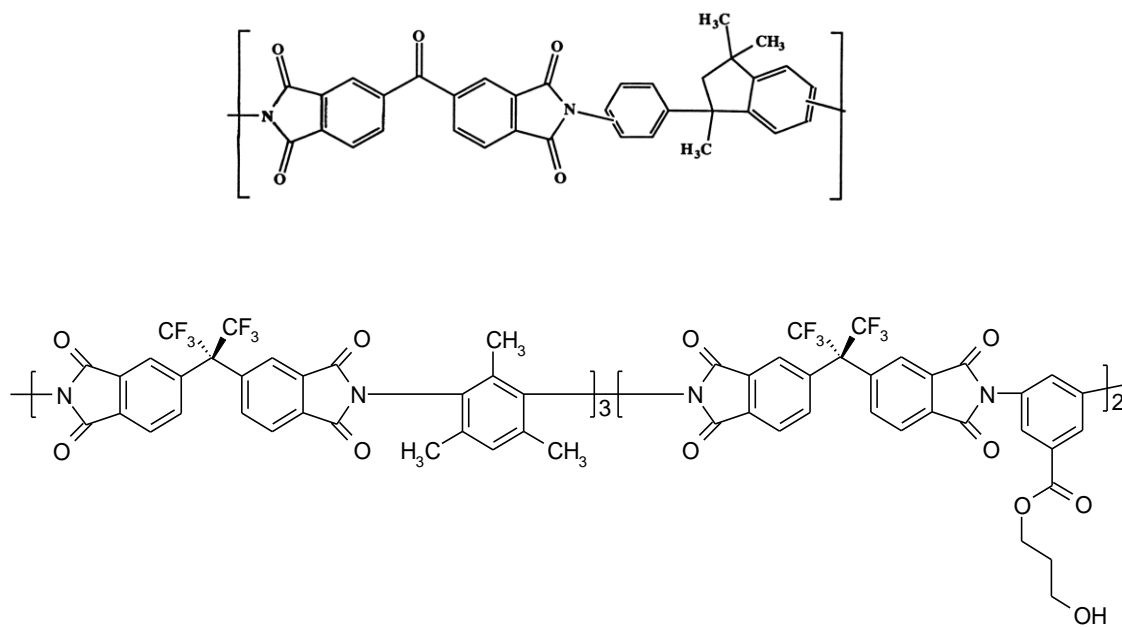


Figure 6.19: Chemical backbone structure of Matrimid[®] polyimide (top) and the PDMC polyimide (bottom).

Madden also demonstrated that the Matrimid[®] hollow fibers antiplasticize in the regions where the permeance decreases, and found that a free volume based model was more appropriate in describing the effects of plasticization/antiplasticization due to the presence of such heavy molecules like toluene and heptane, as opposed to the less heavy permanent gases encountered in Chapter 5 [8].

6.3.2.2 Effect of toluene contamination on uncrosslinked PDMC hollow fibers

Previous studies shown in Chapter 5 demonstrated that the *uncrosslinked* PDMC fibers plasticize in the presence of *high pressure CO₂* in the feed, indicating instability in the polymer matrix from swelling caused from the sorption of CO₂. Complementary studies showed that crosslinking the PDMC fibers reduced these instabilities, simply by heating the fibers at “moderate” temperatures above ~150 °C for ~2 h under vacuum. Fibers crosslinked at 200 °C have been used for membrane characterization, as these fibers showed good stability against high pressure CO₂, especially compared to their uncrosslinked counterpart. This indicates the importance of crosslinking in reducing the effects of plasticization from CO₂ rich streams. In the presence of toluene contaminated feeds, there was no indication of plasticization when the crosslinked fibers were tested. This is contrary to what has been experienced with Matrimid[®] hollow fiber membranes, which plasticize in the presence of small amounts of toluene. To demonstrate that the PDMC polymer’s stability in the presence of the toluene molecules may not necessarily be due to crosslinking, the uncrosslinked versions of the PDMC polymer was tested. The *uncrosslinked* PDMC fibers, which show instabilities due to high CO₂ pressures, were

tested in the presence of the toluene feeds. The results from this experiment can be seen in Figures 6.20–22.

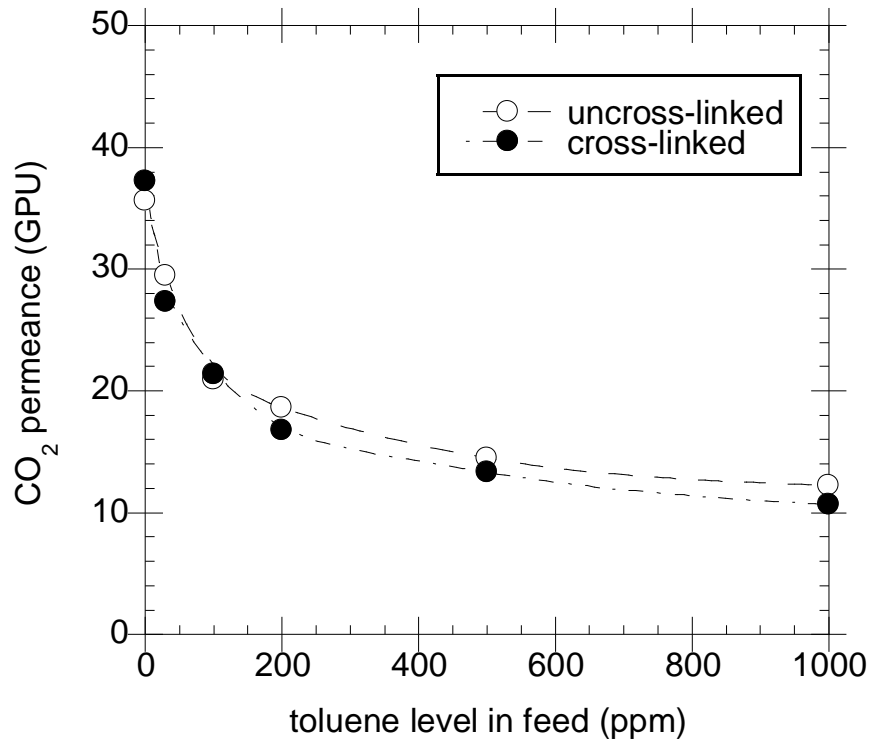


Figure 6.20: CO₂ permeance for uncrosslinked and crosslinked PDMC hollow fiber membranes in the presence of toluene contamination (feed pressure ~800 psia, temperature ~ 35 °C, CO₂ content ~ 10%, CH₄ content ~ balance).

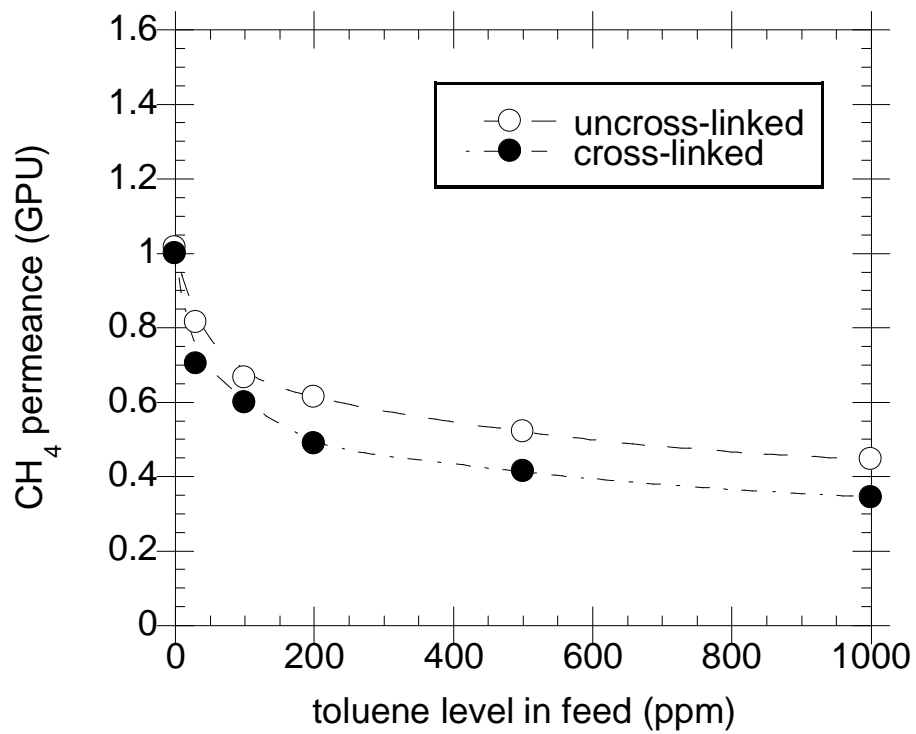


Figure 6.21: CH₄ permeance for uncrosslinked and crosslinked PDMC hollow fiber membranes in the presence of toluene contamination (feed pressure ~800 psia, temperature ~ 35 °C, CO₂ content ~ 10%, CH₄ content ~ balance).

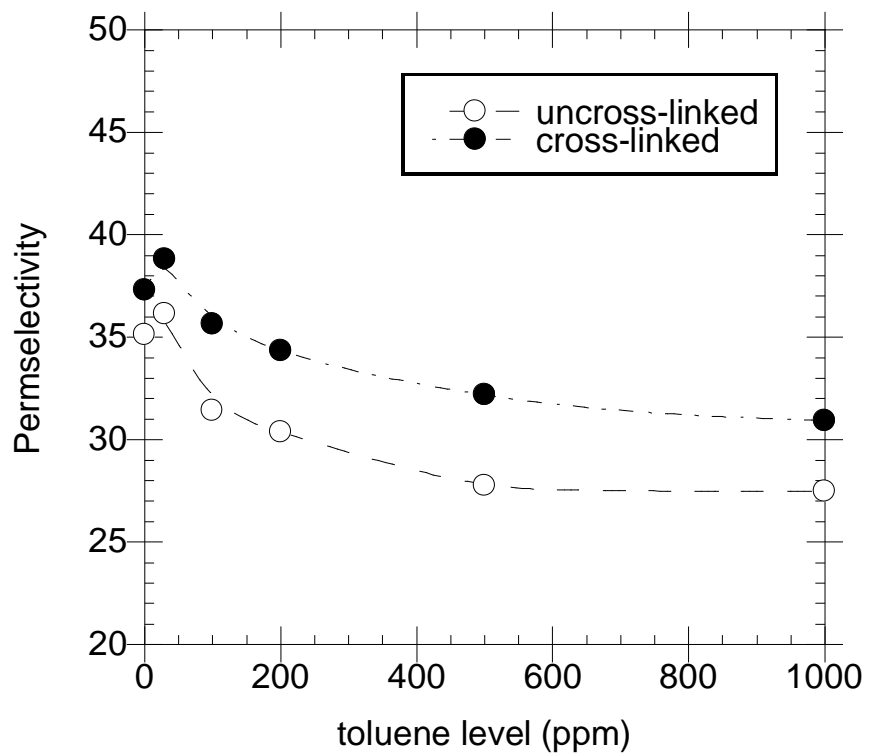


Figure 6.22: CO₂/CH₄ permselectivity for uncrosslinked and crosslinked PDMC hollow fiber membranes in the presence of toluene contamination (feed pressure ~800 psia, temperature ~ 35 °C, CO₂ content ~ 10%, CH₄ content ~ balance).

The results from this study showed that there was no instability typical of plasticization in the uncrosslinked fibers as well using a 10% CO₂ feed with increasing levels of toluene. Instead, suppression in the permeance was observed, with a slight reduction in CO₂/CH₄ permselectivity. The trends were similar to those seen for the crosslinked fibers.

From the Figures 6.20–22, it is observed that the uncrosslinked fibers show a similar trend in separation performance in the presence of toluene as the crosslinked fibers. However, the crosslinked fibers show significantly higher selectivities than the uncrosslinked fibers during the experiment, probably since their intrinsic values are higher. The uncrosslinked fiber was tested again with a high pressure CO₂ feed. If the uncrosslinked fibers are as stable as the crosslinked fibers in the presence of high pressure CO₂ (a known plasticizer for uncrosslinked PDMS), then that would indicate a change in the structure of the uncrosslinked fibers over time or due to the toluene exposure.

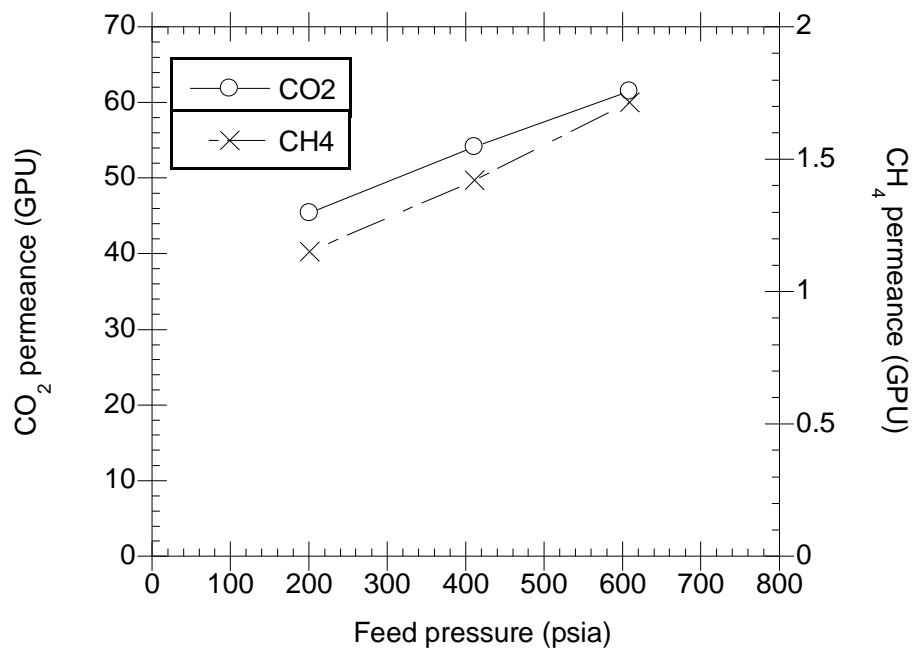


Figure 6.23: CO₂ and CH₄ permeances for uncrosslinked PDMC hollow fiber membranes showing plasticization occurring (Temperature ~ 35 °C, CO₂ content ~ 50%, CH₄ content ~ balance).

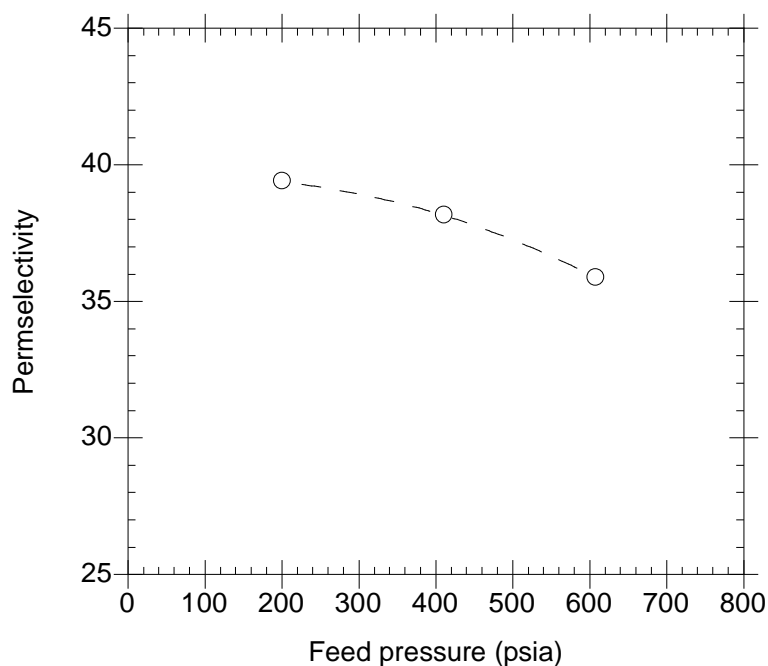


Figure 6.24: CO₂/CH₄ permselectivity for uncrosslinked PDMC hollow fiber membranes from corresponding permeances shown in Figure 6.23, which indicate plasticization (Temperature ~ 35 °C, CO₂ content ~ 50%, CH₄ content ~ balance).

As shown in Figure 6.23 and 6.24, a reexamination of the uncrosslinked fibers shows that they are still unstable in the presence of high pressure CO₂, suggesting that the crosslinking *is* important for stability against aggressive feeds, more importantly with feeds with high CO₂ contents than with toluene.

6.4 Summary

It has been shown that the crosslinked PDMC hollow fiber membranes do not plasticize in the presence of toluene containing feeds at high levels of toluene in the feed. In contrast, the fibers show declines in permeances characteristic of antiplasticization. It appears that the resistance to plasticization from the presence of toluene in the feeds may be due to the chemical structure of the PDMC polymer rather than the presence of covalent crosslinks between chain segments. This is quite different from the case experienced in the presence of high CO₂ content feeds. Therefore, it can be concluded that plasticization resistance is a function of the membrane material as much as it is a function of the sorbed penetrant. The cause of plasticization/antiplasticization may require extensive studies. From the results presented in this chapter, the antiplasticization effects cause significant losses in membrane productivity. This may be alleviated by reducing the effective skin thickness of the membranes (via optimization of the spinning process) or by effective pretreatment of the feeds before exposure to the membrane.

6.5 References

1. UOP. <http://www.uop.com/objects/84CO2RemvbyMembrn.pdf>. 2008 [cited 2008 9-14-2008].
2. Vu, D.Q., W.J. Koros, and S.J. Miller, *Effect of condensable impurity in CO₂/CH₄ gas feeds on performance of mixed matrix membranes using carbon molecular sieves*. Journal of Membrane Science, 2003. **221**(1-2): p. 233-239.
3. Al-Juaied, M. and W.J. Koros, *Performance of natural gas membranes in the presence of heavy hydrocarbons*. Journal of Membrane Science, 2006. **274**(1-2): p. 227-243.
4. White, L.S., et al., *Properties of a polyimide gas separation membrane in natural gas streams*. Journ. Membr. Sci., 1995. **103**: p. 73-82.
5. Felder, R.M. and R.W. Rousseau, *Elementary principles of chemical processes*. 3rd ed. 2000, New York: John Wiley & Sons, Inc. 675.
6. Maeda, Y. and D.R. Paul, *Effect of antiplasticization on selectivity and productivity of gas separation membranes*. Journal of Membrane Science, 1987. **30**(1): p. 1-9.
7. Koros, W.J., et al., *Model For Permeation of Mixed Gases and Vapors in Glassy Polymers*. Journal of Polymer Science, Polymer Physics Edition, 1981. **19**(10): p. 1513-1530.
8. Madden, W.C., *The Performance of Hollow Fiber Gas Separation Membranes in the Presence of an Aggressive Feed Stream*, in *Chemical Engineering*. 2005, Georgia Institute of Technology: Atlanta, Georgia. p. 219.
9. Hillock, A.M.W. and W.J. Koros, *Cross-Linkable Polyimide Membrane for Natural Gas Purification and Carbon Dioxide Plasticization Reduction*. Macromolecules, 2007. **40**: p. 583-587.

CHAPTER 7

SUMMARY AND RECOMMENDATIONS

Based on the objectives described in Chapter 1, the goals of this dissertation are summarized and progress toward those goals achieved in this project is reviewed.

The first objective was to increase the molecular weight of the crosslinkable polymer for hollow fiber spinning. This was addressed in the materials section of Chapter 3. It was found that the crosslinkable polymer, PDMC, had to be synthesized with reduced levels of moisture and with a reduced amount of catalyst. During the monoesterification reaction, moisture in the presence of an acid catalyst causes scissioning of the imide ring on the polymer. This was found to be the source of the molecular weight loss that caused difficulty in subsequent membrane formation processes. It was found that lowering the moisture content and the catalyst concentration helps in eliminating the molecular weight loss, and high molecular weight PDMC batches could be synthesized in large batches.

The second objective, spinning a defect-free asymmetric hollow fiber membrane from the PDMC polymer, required the completion of the first objective. The high molecular weights achievable without molecular weight loss during monoesterification allowed use of more viscous dopes without using excessively high polymer concentrations in the dopes. The spinning process could be optimized due to the resultant spinnability from increased molecular weight polymers. The spinnability allowed an adequate range of experimental conditions. The more important aspect of spinning a defect free PDMC hollow fiber appeared to be from the use of a high molecular weight

polymer. Higher molecular weight polymer solutions enabled spinning at elevated spinneret temperatures, high air gaps, and maintaining a high degree of chain entanglement for skin formation and vitrification to occur. It was also found that the presence of both a volatile solvent and non-solvent helps keep the nascent membrane in one phase during vitrification of the skin layer in the air gap, which helps in forming a dense defect-free skin.

The third objective was to characterize the defect-free hollow fiber membranes in the presence of high CO₂ contents to demonstrate the efficacy of the crosslinking approach. CO₂ partial pressures of up to 400 psia were used with the defect-free crosslinked and uncrosslinked PDMC fibers. It was shown that the crosslinking significantly reduced plasticization. Dual mode analysis and frame of reference effects were considered and showed that some swelling may occur at high CO₂ concentrations, but the crosslinking reduces the level of swelling considerably.

The fourth objective was to determine the performance of the crosslinked hollow fibers in the presence of natural gas feeds with toluene. It was found that the PDMC polyimide hollow fibers were resistant to plasticization from the toluene feeds. It was also found that antiplasticization occurs in the presence of the toluene vapors.

Recommendations for future work

- Thin skin optimization

Further studies on the formation of thinner defect-free, integral skin layers with the crosslinked PDMC polymer should continue. This will greatly increase productivities of the membrane, especially since the productivity is reduced in the presence of contaminants such as toluene. The CO₂ permeances reported in this work were about 40–60 GPU_s for the crosslinked hollow fibers at high pressures (between 200 and 1000 psia binary feed). Dense film studies on the PDMC polymer indicate that high permeabilities (~60 Barrers) are typical of the polymer. This means that there may be room for achieving higher permeances in the hollow fiber membranes. Although high permeances were seen in uncrosslinked fibers after spinning, these permeances decline due to physical ageing effects. Similar trends were seen after annealing/crosslinking. The uncrosslinked permeation data may help in optimization of the spinning process to form a thinner skin layer, but ultimately, the overall optimization process will involve balancing both spinning and subsequent crosslinking processes, since the final crosslinked fibers are used (versus the uncrosslinked). Lower annealing temperatures may be required to preserve the delicate morphology in a thin skinned hollow fiber membrane. Therefore the assistance of a catalyst may be required in such an optimization process. Furthermore, lower annealing temperatures are generally preferred for scale up. The formation of such thin skinned PDMC hollow fibers may be achieved by lowering the volatile component concentration in the dopes, reducing spinneret temperatures, and/or lowering polymer concentrations in the dopes as long as spinnability is not

undermined. A high molecular weight polymer ($M_w > 100,000$) would be beneficial for these reasons.

- Catalyst assisted crosslinking

As mentioned previously, lower annealing temperatures are preferred. However, the degree of crosslinking should not be compromised. To balance this, a catalyst may be used to promote the transesterification reaction at lower annealing temperatures. Some catalysts for crosslinking were identified in this work but effects on crosslinking were not determined. The amount of catalyst imbibed into the fiber will be important, and should be low enough that the catalyst itself only improves plasticization resistance at lower temperatures without reducing absolute separation performance values significantly. Determination of the degree of crosslinking using analytical techniques such as NMR would be very helpful in this aspect. A procedure was written, which may guide the experimenter in such catalyst studies. This procedure is shown below.

Catalyst assisted crosslinking procedure of experiments

The aim here is to increase the degree of crosslinking at lower annealing temperatures, ~150 °C, in order to increase the plasticization resistance of the hollow fibers at such a lower temperature. This may allow the use of lower cost conventional ovens for heating during scale up of the membrane production process.

1. Test uncrosslinked hollow fiber modules using 20/80 CO₂/CH₄ feed at 200 psia, 35 °C

2. Dissolve catalyst in solvent i.e. ethanol
 - a. Catalysts: p-TSA, Tyzor[®] TPT (DuPont), methanesulfonic acid, sulfuric acid, and triflic acid
 - b. Concentration: 2g catalyst in 1 liter of ethanol
3. Pour catalyst solution into module housing and seal module
4. Allow catalyst to imbibe into fiber for 1 h, while pulling vacuum on the bore
5. Drain off catalyst solution
6. Allow module to dry for a few hours and preheat oven to 150 °C
7. Place fiber modules in vacuum oven at 150 °C for ~2 h, then let cool
8. Remove fiber modules and retest using 20/80 CO₂/CH₄ feed at 200 psia, 35 °C (determine effects of catalyst on absolute transport properties)
9. Test with 50/50 CO₂/CH₄ feed at elevated pressures (determine effects of catalyst on plasticization resistance)

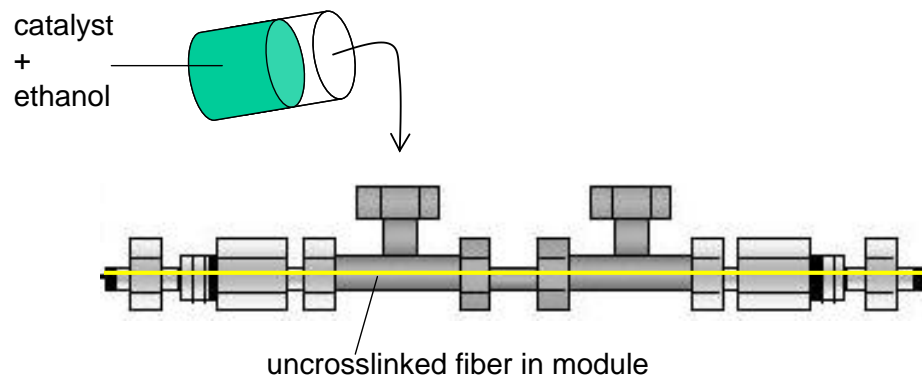


Figure 7.1: A depiction showing catalysts imbibed into uncrosslinked hollow fibers in a module, useful for permeation testing.

- Characterization of crosslinking degrees

Analytical determination of the degree of crosslinking will be necessary for catalyst optimization experiments. ^{13}C NMR was used in this work to some degree. It was found that determination of the crosslinking degree may also be dependent on the monoesterification yield. Since crosslinking can occur either between two esters or between an ester and an unconverted acid group, monitoring the presence of the monoester alcohol moiety in determining degree of crosslinking requires that a sufficient ester yield be achieved. If the ester yields are low (less than 80%), crosslinking may occur via the ester/acid route and water would be evolved rather than the diol. This may cause underestimations in the degree of crosslinking if such a method, as used in Chapter 5 of this work, is applied.

- Dual layer hollow fiber spinning

The PDMC polymer is considered a high performance polymer. However, the monomers used in synthesizing PDMC are costly. Membrane material cost reductions may be achieved by using dual layer spinning technology. In this case, the high performance PDMC polymer can be used in the sheath layer and less expensive polymers may be used as the core layer in the hollow fiber. This is described in Figure 7.2.

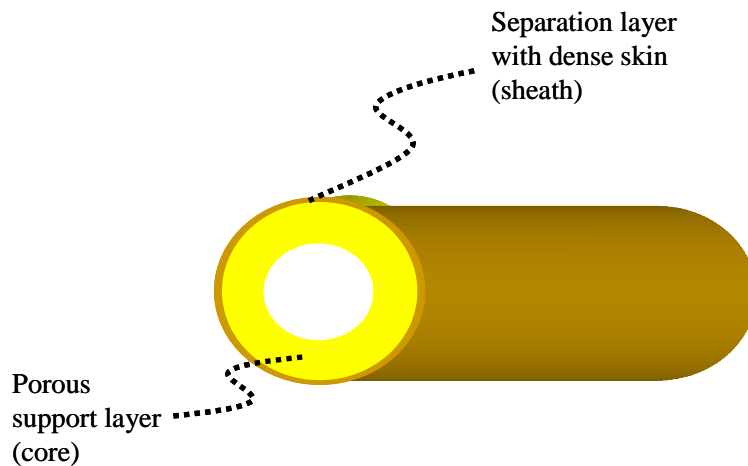


Figure 7.2: Schematic illustrating a dual layer hollow fiber showing the sheath and core layers.

This dual layer spinning approach would also be advantageous if the PDMC polymer is used in mixed matrix membranes. The development of a functional dual layer hollow fiber would require compatibility between the sheath and core polymers. Some miscibility tests were performed in this work to determine possible candidate core polymers. These are described below. As seen from the figure, cellulose acetate seems to be the only promising candidate core polymer from the polymer tested.

Polysulfone : PDMC (1:1 wt ratio)



Cellulose Acetate :
PDMC (1:1 wt ratio)

Matrimid® : PDMC
(1:1 wt ratio)

- CA mixture was quite homogeneous
- PSF & Matrimid® did not form a good film
- Ultem® did not mix in solution with NMP

Figure 7.3: Illustration showing effects of mixing various polymers in solution with PDMC (tests performed in February 2007).

- Continued testing with impurities in feed (H_2S , H_2O)

Continued performance evaluation studies of the crosslinked PDMC hollow fiber membranes in the presence of impurities would determine the viability of the crosslinked membranes in realistic feed conditions. The effect of H_2S and H_2O during permeation was not studied in this work. These components may preferentially permeate through the membrane (versus CH_4), but their effects on the PDMC material should be determined. As acidity increases in the feed or if the PDMC membrane has significant quantities of residual catalyst, the effects of moisture may be more pronounced, and hydrolytic degradation may occur on the esters or the imide rings.

- Studies on ageing without exposure vs. ageing during exposure

Studies on ageing effects in this project were carried out on fibers that were left dormant during the times when they were not tested. These studies showed that there is a significant decrease in the membrane permeance over time when the membrane is not in use. Such studies may give a good indicator on the membrane shelf life, beyond which the productivity becomes unimpressive. However, the performance of the membrane may differ when the module is continuously exposed to the feed stream. Certain feeds such as CO₂ at moderate pressures may condition the membrane. Such feeds, hypothetically, may serve as a means to preserve the permeance of the hollow fiber membrane. This was not investigated in this project, but would be worth investigating. A schematic describing a setup where such an experiment may be performed is shown in Figure 7.4.

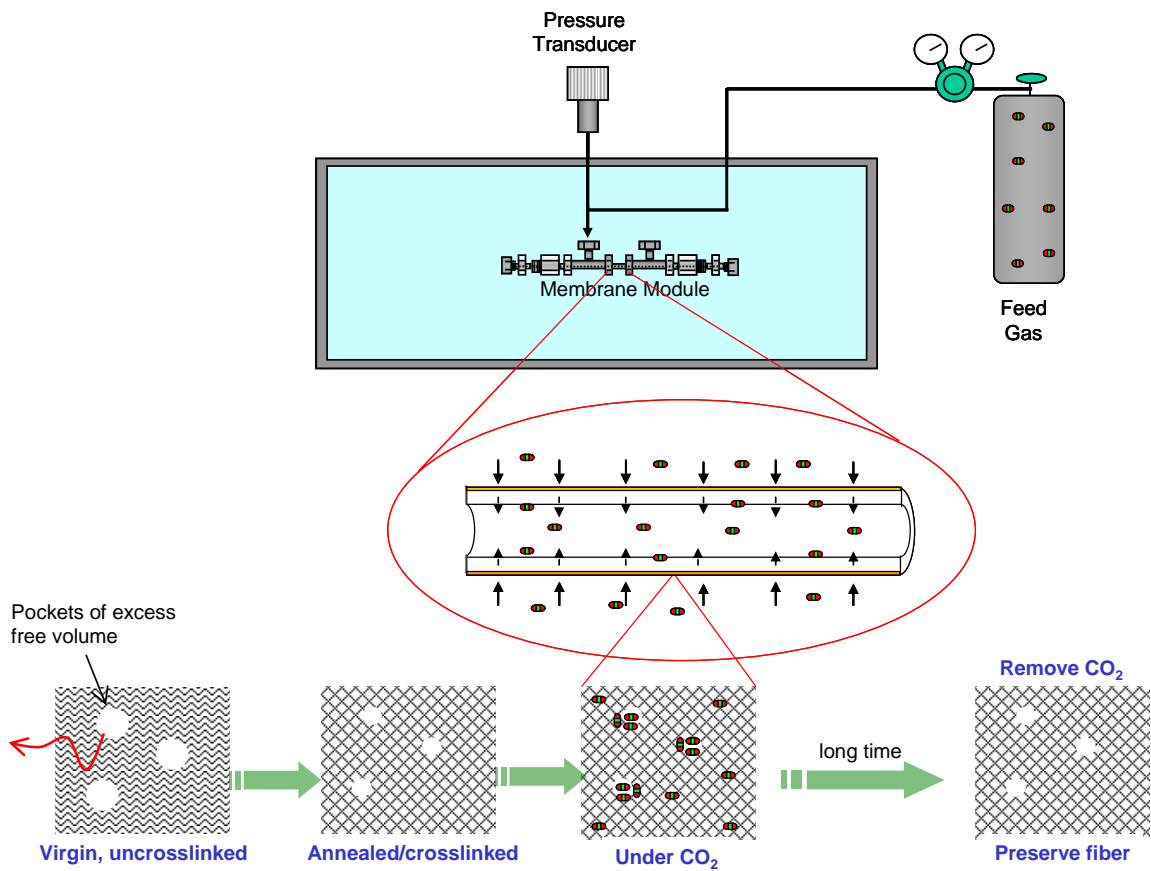


Figure 7.4: Depiction of a fiber storage process using CO₂ to preserve the membrane's productivity.

APPENDIX A

Manufacture of lab-scale hollow fiber modules [1, 2]

Hollow fiber modules are required for permeation testing of asymmetric hollow fibers. The module serves as the interface between the permeation system (gas cylinder, tubing, valves, etc.) and the polymeric membrane.

This appendix lists off the Parts, Procedure and Notes for constructing a double-ended hollow-fiber module for laboratory-scale experiments. This design has been used in a number of prior studies and is reported in work by Djoekita [3].

A.1 PARTS

The table below lists the main parts needed to make a hollow fiber module.

Name	Manufacturer	Notes
Ferrules	Swagelok [®]	Brass or Stainless Steel
Nut	Swagelok [®]	Brass or Stainless Steel
Female Adapter	Swagelok [®]	Brass or Stainless Steel
Male Adapter	Swagelok [®]	Brass or Stainless Steel
Tee	Swagelok [®]	Brass or Stainless Steel
Metal Tubing	Swagelok [®]	Brass or Stainless Steel
Cap	Swagelok [®]	Brass or Stainless Steel
Plug	Swagelok [®]	Brass or Stainless Steel
ID Tag		
Tygon Tubing	Fisher Scientific	
“5 Minute” Epoxy	GC Electronics or Devcon	

Table B.1: Parts required for manufacture of double-ended lab scale permeator

A.2 PROCEDURE

Summary: A ‘blank’ module is first prepared as shown in Figure B.2. Fibers are then put into the module and the ends sealed with Teflon tape and epoxy. Finally, the module is prepared to be put into the permeation testing system.

1. The “Blank” Module

- a. Stainless Steel (S.S.) Parts.
 - i. Cut an 11.5cm piece of ¼” S.S. tubing.
 - ii. Bore out the ends with a ¼” countersink tool used as the bit in a drill press.
 - iii. Test the ends for burrs with a Q-tip.
 - iv. Add a S.S. nut, ferrule and tee to each end.
- b. Brass Parts
 - i. Attach a Brass nut and ferrule to a Brass female ¼” NPT adapter.
 - ii. Attach the S.S. tee from step 1a(iv) to the Brass nut on the female adapter.
 - iii. Repeat steps (i) and (ii) for the other end of the module. Both ends should be identical.
- c. Attach an ID tag to the S.S. tubing.

Figure B.1: Parts for a “Blank” Module

Figure B.2: The “Blank” Module.

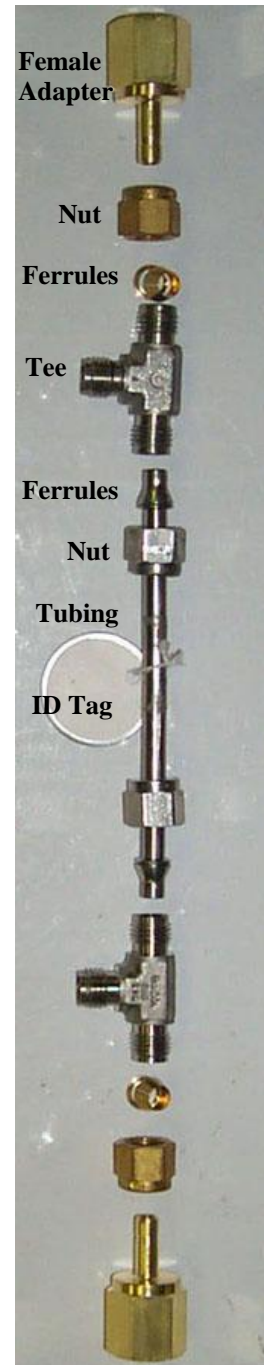


Figure B.3: Brass Male adapter with Tygon® tubing piece.



2. Adding the Hollow Fibers.

- a. Separate out nominally 25 1-meter long hollow fibers from the main hank of fibers. More fibers leads to less variability between modules, but any number can be used.
- b. Recount the fibers.
- c. Tie a 2-ft. long string to the middle of the 25 fibers.
- d. Slide the string through the Blank Module, pulling the fibers through as well. (NOTE: Be careful and slow while pulling the fibers through - they break easily.)
- e. Cut the string so that only ~3 inches remain.
- f. Tape the other, non-tied, end of the fibers together with Scotch tape so that they can easily be threaded through ¼” tubing.
- g. Slide the fibers so that equal length sections extend from each end of the module.
- h. For particularly fragile fibers, it is often helpful to simply tape the ends together and then use tape to attach the fibers to the string before pulling the fibers through the module. This avoids the need for the fibers to remain intact while bending sharply to fit through the module bore.

3. Sealing the Module.

- a. Pack a Teflon[®] tape “worm” into one of the Female Adapters and around the fibers. Be careful not to crush the fibers, yet still assure a good seal between the fibers and the brass wall of the female adapter. (A “worm” is a 5-cm long roll made up of ~16 layers of Teflon[®] tape.)

- b. Put a 1-cm piece of 3/16" Tygon[®] Tubing onto a Brass Male 1/4" NPT Adapter. (Figure B.3).
- c. Add a 1:1 ratio of the GC electronics epoxy Hardener and Resin into a disposable container. Mix for 30 seconds. (NOTE: Once mixed, the epoxy becomes 'unworkable' after 2 minutes.) (Stycast[®] brand epoxy may be used as well, see notes.)
- d. Pour the epoxy into the Brass Female Adapter, filling it slightly beyond the top.
- e. Slide the fibers through the Brass Male Adapter and Tygon tubing piece. Screw the Male Adapter into the Female Adapter until the epoxy fills the Tygon tubing piece.
- f. Wait ~10 minutes, then flip the module and repeat steps 3a-e for the other end of the module.

4. Prepare the Module for Permeation Tests

- a. Once the epoxy has fully cured (30 minutes after mixing for the GC Electronics '5 minute' epoxy.), break off the Tygon tubing piece by tapping it on the countertop or striking sharply with a hammer. The fibers should be all open, with an encapsulating seal of epoxy around them.
- b. Put a Brass nut and ferrule on the Male Adapter on each end of the module.
- c. As seen in Figure B.4, put a Plug into one end of the module, and a Cap on the nearest Tee fitting, and a Port connector on the furthest Tee fitting.

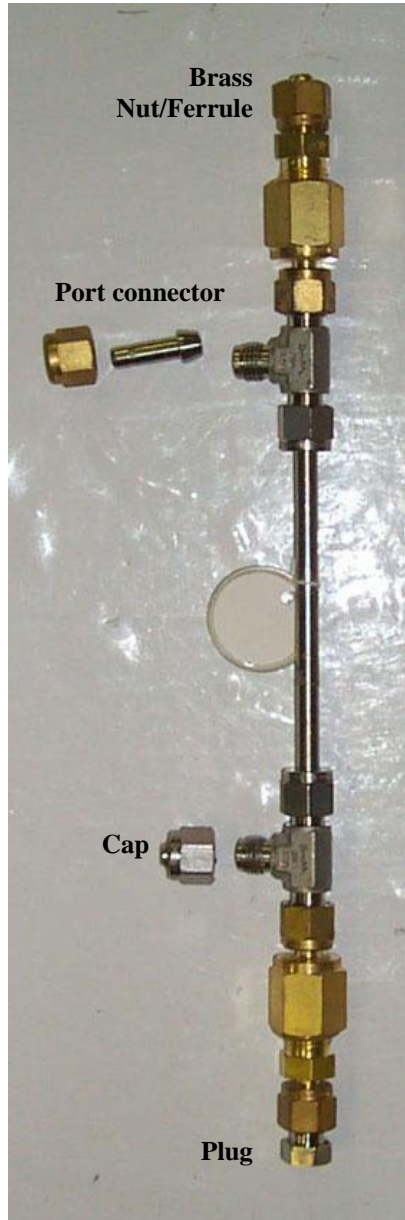


Figure B.4: Final Module- ready for permeation tests.

A.3 NOTES

Type of Epoxy: The GC Electronics '5 minute' epoxy may be used for general purpose modules. It is easy to use, inexpensive and cures quickly (within 30 minutes). For a more durable seal, Stycast[®] 2651 from Emerson & Cuming, Billerica, MA may be used. Stycast has excellent adhesion to a wide range of substrates, lower viscosity to fully encapsulate the fibers, high tensile strength (> 6500 psi) after curing for high-pressure applications and a high upper temperature tolerance (130°C). However, Stycast requires 24 hrs to cure at room temperature, is somewhat more difficult to use and mix, and is slightly more expensive.

A.4 REFERENCES

1. Carruthers, S.B., *Integral Skin Formation in Hollow Fiber Membranes for Gas Separations*, in *Chemical Engineering*. 2001, University of Texas--Austin: Austin, TX. p. 233.
2. Wallace, D.W., *Crosslinked Hollow Fiber Membranes for Natural Gas Purification and Their Manufacture from Novel Polymers*, in *Chemical Engineering*. 2004, The University of Texas at Austin: Austin, Texas. p. 202.
3. Djoekita, G., D.Q. Vu, and W.J. Koros, *Pervaporative Introduction of Organic Vapors into High-Pressure Gas Feeds*. *Journ. Applied Polymer Sci.* **80**(2): p. 311-315.

APPENDIX B

Permeation testing of hollow fiber modules[1]

This appendix includes the procedures used in this work for pure and mixed gas testing. All tests are run in a temperature-controlled ‘black-box’.

B.1 Pure Gas Permeation Testing [2]

B.1.1 Setup

Bore vs. Shell Feed

Testing can be done by feeding the gas on either the bore or shell side of the module. Bore feed is generally more reproducible and may give slightly higher permeation rates. Shell feed will hold higher pressures, but the pressure drop down the bore may introduce error for very fast gases in highly permeable fibers.

The “Christmas Tree”

Set up Swagelok fittings (Union Crosses and Female-Female Unions) to attach the feed inlet of the modules to the feed gas port in the permeation system. Be certain that a pressure transducer is hooked up to the feed as well. The only restriction on the number of modules is the space available. The whole unit with Swagelok[®] fittings and modules hanging off of it sometimes looks like a “Christmas Tree”.

B.1.2 Purge the System

1. Zero the pressure transducer.

2. Open the Retentate outlet on all the modules. (Only *Slightly* open if Shell Feeding)
3. Open the gas cylinder and pressurize the entire system.
 - a. Gas should be flowing through the entire system and exiting through the Retentate of each module.
 - b. Let the gas flow for at least 5 seconds.
4. Close the main cylinder valve.
 - a. The pressure should slowly drop in the system.
5. Open the cylinder valve when the regulator pressure reads ~20 psi.
6. Repeat steps 4 and 5 three more times.
 - a. The entire system has been purged, or 'rinsed', a total of four times with 'clean gas'.
7. Close the Retentate of each module.
8. Adjust the feed pressure as desired, close the door to the permeation system.
9. Wait 15 min. The permeation flowrates and inner box temperature should equilibrate.

B.1.3 Testing

1. (*0-15 minutes*) During the 15 min. equilibration, the following steps should be done:
 - a. Record the Active Length of each module
 - b. Record the # of fibers in each module
 - c. Record the Box Temperature
 - d. Wet the bubble flowmeter.

2. (> 15 minutes) Measure each module's Permeate Flowrate w/ a Bubble Flowmeter.
 - a. Let the bubble travel for at least 15 seconds, and preferably an easily measured distance.
 - i. GOOD--10.00 mL in 17.67 seconds
 - ii. GOOD--200 mL in 31.27 sec
 - iii. BAD--10.00 mL in 11.21 seconds (too short, too much error).
 - b. Smallest measurable flowrate is ~ 0.5 mL / minute.
 - c. Electronic Flowmeters do NOT seem to be as accurate or precise at low flowrates (< 100 ml/min). A Bubble Flowmeter should be used.
 - d. Record the Feed Pressure for each flowrate measurement.
3. (> 45 minutes) Test the modules *again* 45 min after equilibration (1 hr after pressurization).
 - a. If there's greater than a **5%** difference between the '45 minute measurement' and the '15 min measurement', wait another 45 minutes and measure a 3rd time.
 - b. Keep testing until there is less than a **5%** change over 45 minutes. Only 2 measurements are generally necessary if the system was purged well.
4. Calculate permeances and selectivities for the membranes. Retest as desired.
5. Close all cylinder valves, turn off the pressure transducer, clean up.

B.2 MIXED GAS PERMEATION TESTING

B.2.1 GC Set-up

1. Turn on helium and set regulator to 50 psi
2. Using knobs on the GC, adjust the flowrate from both columns to 30 mL/min
3. Turn on GC and set column temperature to 65. (WARNING: DO NOT turn on the GC without helium running through the columns. The columns may be severely damaged.)
4. Set the Bridge Setting knob to “Thermistor”, the Output knob to “1024”, and the Readout knob to “Left Column”
5. Turn on integrator, enter date and time at prompts.
6. Wait a while (usually several hours).
7. Push the “level” button on the integrator. The level should be 1000 after the system has had time to warm up. Use the coarse and fine adjustment knobs to set the level to 1000. Press “level” after each adjustment to see the effect. If no number prints, the GC needs some more time to warm up. The system will likely take 1-3 hours to stabilize enough to take a reading.

B.2.2 Module Set-up

Note: This set-up assumes only one module is being tested.

1. Modules can be set up in either bore or shell fed configurations. Be sure that they are operating in counter-current flow (retentate and permeate are taken from different ends of the module).
2. Attach the feed to the module.
3. At the retentate exit, attach a fine control needle valve

4. Cap the permeate side closest to the retentate exit.
5. Attach a T-valve to the permeate side closest to the feed. One exit from the valve should lead to the GC, the other to a flowmeter.
6. Purge the module in the same way as in pure gas testing (this should be made easier by the existence of the retentate valve).
7. Set the retentate valve to the desired flowrate (higher retentate flowrates = lower stage cuts = higher selectivity).
8. Make certain that the permeate T-valve is directing the permeate to the GC and that the GC sampling valve is in the “sample” position.

B.2.3 Testing

1. Allow at least 15 minutes of equilibration after the GC has completely warmed up and the gas has been flowing.
2. Press level on the integrator and adjust to 1000.
3. Turn the GC sample valve to “load” and press “Inj A” on the integrator. Do these simultaneously.
4. The GC is now independent of the module. Turn the permeate T-valve to the flowmeters.
5. Measure and record the following
 - a. Module ID
 - b. Feed composition
 - c. Feed pressure
 - d. Retentate flow
 - e. Retentate pressure (normally atmospheric)
 - f. Permeate flow
 - g. Permeate pressure (normally atmospheric)

- h. Module temperature
- 6. When all peaks have eluted, press “Inj A” on the integrator again to stop the run.
- 7. Turn the sample valve back to “sample” and the permeate T-valve back to the GC.
- 8. Wait 45 minutes and repeat steps 2-7. If the two runs are close, the measurement can be considered valid. If not, wait again and repeat. Waiting now can be minimized by waiting earlier and making sure everything is warmed up before beginning testing.

B.2.4 Calibration

1. Calibration is done external to the GC
2. Run calibration tests in the same way as shown above, eliminating the module. Pipe calibration gases directly to the GC, make sure everything's equilibrated, and take the sample (steps 3 and 6 from “Testing Procedure”)
3. Make sure that everything matches by doing at least three injections of each calibration gas to certify reproducibility.
4. Make sure the correct retention time is known for each gas. This can be checked by injecting pure gas samples.
5. Once 3-5 calibration gases have been run, take the data and construct a calibration curve, composition on one axis and GC area percentage on the other.

B.3 REFERENCES

1. Wallace, D.W., *Crosslinked Hollow Fiber Membranes for Natural Gas Purification and Their Manufacture from Novel Polymers*, in *Chemical Engineering*. 2004, The University of Texas at Austin: Austin, Texas. p. 202.
2. Carruthers, S.B., *Integral Skin Formation in Hollow Fiber Membranes for Gas Separations*, in *Chemical Engineering*. 2001, University of Texas--Austin: Austin, TX. p. 233.

APPENDIX C

Hollow fiber post-treatment [1, 2]

Hollow fibers can be treated to “plug” minor defects in the fiber skin. This treatment usually involves coating the fibers with a second layer of a highly permeable, flexible polymer that can prevent Knudsen flow through the fibers as outlined by Henis and Tripodi [3].

In this research, a crosslinkable polydimethylsiloxane, Sylgard 184[®] available from Dow Chemicals was used to post-treat the fibers. The procedure is outlined as follows:

1. A 3 wt % solution of Sylgard[®] in heptane was heated at 75 °C for 1 hour to obtain branching and chain extension.
2. The fiber module was filled with the heptane solution and the module shaken to swirl the contents. The fibers were then allowed to soak in the solution for 5 minutes. The solution was drained out of the module.
3. Step 2 was repeated.
4. The module was placed in a vacuum oven at 75 °C for 2 hours under full vacuum.

REFERENCES

1. Husain, S., *Mixed Matrix Composite Hollow Fibers for Gas Separation*, in *Chemical Engineering*. 2003, Georgia Institute of Technology: Atlanta, GA.

2. Wallace, D.W., *Crosslinked Hollow Fiber Membranes for Natural Gas Purification and Their Manufacture from Novel Polymers*, in *Chemical Engineering*. 2004, The University of Texas at Austin: Austin, Texas. p. 202.
3. Henis, J.M.S. and M.K. Tripodi, *Composite Hollow Fiber Membranes for Gas Separation: The Resistance Model Approach*. *J. Membr. Sci.*, 1981. **8**: p. 233-246.